

Ph.D Thesis

ANALYSIS OF MIXING PROCESSES IN LIQUID AND
VAPORIZED DIESEL SPRAYS THROUGH LIF AND
RAYLEIGH SCATTERING MEASUREMENTS

Presented by

JULIEN MANIN

At

CMT - MOTORES TÉRMICOS
UNIVERSIDAD POLITÉCNICA DE VALENCIA

For the degree of

DOCTOR OF PHILOSOPHY

Valencia, February 2011

Ph.D Thesis

ANALYSIS OF MIXING PROCESSES IN LIQUID AND VAPORIZED DIESEL SPRAYS THROUGH LIF AND RAYLEIGH SCATTERING MEASUREMENTS

Presented by: Mr. Julien Manin
Supervisor: Prof. Raúl Payri Marín

TRIBUNAL OF EVALUATION:

President: Prof. José M. Desantes Fernández
Secretary: Dr. José M. García Oliver
Examiners: Dr. Lyle Pickett
Dr-Ing. Lucio Araneo
Dr. José E. Juliá Bolívar

Valencia, February 2011

Resumen

Desde su introducción, los motores de combustión interna alternativos han sido desarrollados con el fin de reducir el consumo y mejorar el rendimiento y facilidad de conducción. Con el tiempo, la contaminación se ha convertido en un factor crítico para los gobiernos y como consecuencia se han introducido regulaciones para reducir las emisiones contaminantes de los motores.

Con el constante progreso tecnológico requerido por las normas contra la contaminación, la inyección directa se ha vuelto indispensable en cuanto a los motores Diesel. La introducción de combustible en la cámara de combustión permite un alto nivel de control sobre la liberación de energía del proceso de combustión. Con las novedosas estrategias de combustión empleadas, el proceso de inyección se ha convertido en el tema principal y el chorro es el factor principal.

El trabajo realizado a lo largo de este estudio para analizar el proceso de mezcla aire-combustible se basa en el desarrollo de técnicas láser de diagnóstico. Inicialmente, la inyección de Diesel se ha estudiado en una atmósfera isoterma para evitar la evaporación del combustible (n-dodecano) a través del uso de una iluminación estructurada para medir la distribución de la mezcla mediante el control de la dispersión de Mie. La aplicación de la dispersión de Rayleigh en la parte evaporada del chorro inyectado en una cámara a alta temperatura ha permitido la obtención de la distribución de combustible en una situación equivalente a la existente en un motor real.

El análisis y comparación de los distintos parámetros del chorro inyectado en condiciones de baja o alta temperatura da la posibilidad de entender mejor lo que es el proceso de mezcla en los motores Diesel. Por otra parte, según el estado del fluido inyectado, líquido o gaseoso, las condiciones experimentales tendrán diferentes efectos y la mezcla aire-combustible también tendrá un comportamiento distinto.

Resum

Des de la seua introducció, els motors de combustió interna alternatius han sigut desenrotllats amb el primer objectiu de reduir el consum i millorar el rendiment i facilitat de conducció. Amb el temps, la contaminació s'ha convertit en un factor crític per als governs i com a conseqüència s'han introduït regulacions per a reduir les emissions contaminants dels motors.

Amb el constant progrés tecnològic requerit per les normes contra la contaminació, la injecció directa s'ha tornat indispensable quant als motors Dièsel. La introducció de combustible en la cambra de combustió permet un alt nivell de control sobre l'alliberament d'energia del procés de combustió. Amb les noves estratègies de combustió empleades, el procés d'injecció s'ha convertit en el tema principal i el doll és el factor principal.

El treball realitzat al llarg d'este estudi per a analitzar el procés de mescla aire-combustible es basa en el desenrotllament de tècniques làser de diagnòstic. Inicialment, la injecció de Dièsel s'ha estudiat en una atmosfera isoterma per a evitar l'evaporació del combustible (n-dodecà) a través de l'ús d'una il·luminació estructurada per a mesurar la distribució de la mescla per mitjà del control de la dispersió de Mie. L'aplicació de la dispersió de Rayleigh en la part evaporada del doll injectat en una cambra a alta temperatura ha permès l'obtenció de la distribució de combustible en una situació equivalent a l'existent en un motor real.

L'anàlisi i comparació dels distints paràmetres del doll injectat en condicions de baixa o alta temperatura dóna la possibilitat d'entendre millor el que és el procés de mescla en els motors Dièsel. D'altra banda, segons l'estat del fluid injectat, líquid o gasós, les condicions experimentals tindran diferents efectes i la mescla aire-combustible també tindrà un comportament distint.

Abstract

Thermal engines have become a monopoly and uncompromising regarding transportation systems. Since their introduction, the internal combustion engines have been developed with the first objective to reduce consumption and improve performance and drivability. Over the time, pollution has become a critical factor for governments resulting in the introduction of regulations to reduce pollutant emissions of combustion engines.

With constant technological progresses required by the anti-pollution standards, direct injection has become indispensable as regards Diesel engines. The introduction of fuel directly into the combustion chamber allows a high level of control on the energy released by the exothermic process that is combustion. With the emergence of new combustion strategies, the process of injection took the lead and the spray has become the main factor.

The work done throughout this study to analyze the process of fuel-air mixing was based upon the development of powerful laser diagnostic techniques. As a first step, the Diesel spray has been studied in an isothermal atmosphere in order to avoid the evaporation of the fuel (n-dodecane) through the use of structured illumination to get the mass distribution of mixing by controlling the multiple Mie scattering. The application of Rayleigh scattering in the vaporized region of a jet injected into a high temperature chamber has allowed the extraction of the mixing field of the jet under evaporative conditions.

The analysis and comparison of the jet introduced in vaporizing conditions or not permits to understand better the process of mixing during a Diesel injection event. In addition, depending on the state of the fluid, liquid or gaseous, the experimental conditions have different effects and therefore the air-fuel mixing behaves in distinct ways.

Résumé

Les moteurs thermiques ont aujourd'hui un monopole sans concession en ce qui concerne les moyens de transports. Depuis leur apparition, les moteurs à combustion interne ont été développés avec comme objectif premier de réduire la consommation et d'en améliorer les performances et l'agrément de conduite. Avec le temps, la pollution est devenue un facteur primordial pour les gouvernements résultant en l'introduction de réglementation visant à réduire les émissions contaminantes des moteurs thermiques.

Avec l'avancement technologique constant requis par ces normes anti-pollution, l'injection directe est devenue incontournable en ce qui concerne les moteurs Diesel. L'introduction de carburant directement dans la chambre de combustion permet un contrôle accru de la libération énergétique du processus exothermique qu'est la combustion. Avec les nouvelles stratégies de combustion, l'injection a pris le premier rôle et le jet en est le principal acteur.

Le travail réalisé tout au long de cette étude visant à analyser le processus de mélange air-carburant s'est basé sur le développement de techniques de diagnostic laser performantes. Dans un premier temps, le jet Diesel a été étudié dans une atmosphère isotherme dans le but d'éviter l'évaporation du carburant (n-dodécane) grâce à l'utilisation d'une illumination structurée pour obtenir la distribution massique de mélange en contrôlant la diffusion multiple de Mie. L'application de la diffusion de Rayleigh dans la région vaporisée d'un jet injecté dans une chambre à haute température a permis l'extraction de la distribution de mélange du même jet en milieu évaporatoire.

L'analyse et la comparaison du jet introduit en milieu évaporatif ou non permet de comprendre plus complètement le processus de mélange lors de l'injection Diesel. Par ailleurs, selon l'état liquide ou gazeux du jet, les conditions expérimentales vont avoir différents effets et le mélange air-carburant résultant présente de ce fait un comportement dissemblable.

*To my family
and friends*

*In memory of
Père and Loulou*

*There are in fact two things,
Science and opinion;
the former begets knowledge,
the latter ignorance.*

Hippocrates

First of all, I would like to express my gratitude to my supervisor Raúl Payri, whose expertise, understanding and patience considerably improved my graduate experience. I have to emphasize my acknowledgments for his continuous help while redacting the final document of my thesis and all along the work achieved here at CMT - Motores Térmicos.

My thanks should also go to Francisco Payri and José María Desantes for giving me the opportunity to pursue my doctorate in this world-recognized research institute along with the experimental facilities to carry out all the necessary steps required by such a work. I would like to thank José Vicente Pastor for his precious help concerning optical diagnostics and his accurate comments related to scientific publications.

Thanks to his enrollment for various projects at CMT - Motores Térmicos, I am very thankful to get the opportunity to work with Lucio Araneo, who aroused my curiosity to the understanding, the fuel of an engineer. I must also thank all my friends and colleagues of the injection team for the good times spent together, particularly, Joaquín, Gabriela, Jaime, Michele, Jorge, Oscar, Vlad and many more, including José Enrique for the strong-arm conversations in the lab and Javier Salvador for his fine help anytime I needed.

I cannot forget to acknowledge people at Lund Institute of Technology and Sandia National Laboratories where I spent valuable time learning a lot in two of the best places working in the vast field of engines. Specially I would like to thank Lyle Pickett for being open to any kind of discussion, Caroline, Ryan, Dave and all the others; I really appreciated my time in Livermore and I am looking forward to working with them again.

I also thank my parents and family for the support they provided me with through my entire life and the last years; they have always been here and ever will. My last thanks are going to Carla for being comprehensive with the requirement imposed by such a work and for having been here everyday to make me feel better.

Contents

Contents	i
List of Figures	v
List of Tables	xiii
Nomenclature	xv
1 Introduction	1
1.1 Subject and motivations of the work	1
1.2 Previous studies and objectives of this investigation	4
1.3 Outline of the Thesis	7
Bibliography	8
2 Injection Process In Diesel Engines	11
2.1 Introduction	12
2.2 Injection system in Diesel engines	13
2.2.1 Background	13
2.2.2 The common-rail system	18
2.2.3 The injector and the nozzle	20
2.3 Internal liquid flow	23
2.3.1 Orifice geometry and related parameters	23
2.3.2 Characteristics of the flow	24
2.3.3 Pressure drop and cavitation	26
2.3.4 Influence of nozzle geometry on the internal flow	32
2.4 Formation of Diesel sprays	35
2.4.1 General properties of sprays	36
2.4.2 Disintegration process and droplet formation	41
2.5 Characteristics of Diesel sprays	47

2.5.1	Spray tip penetration	47
2.5.2	Spreading angle of the spray	50
2.5.3	Droplet size distribution and prediction	51
2.5.4	Velocity and concentration profiles	54
2.6	Conclusions	57
	Bibliography	58
3	Experimental techniques applied in this study	65
3.1	Introduction	66
3.2	Injection system	67
3.3	Internal geometry and flow characterization	69
3.3.1	Internal geometry determination	70
3.3.2	Rate of injection measurements	73
3.3.3	Spray momentum flux	77
3.4	Equipment used for isothermal spray analysis	82
3.4.1	Optically accessible cold spray facility	82
3.4.2	Direct visualization of the liquid phase	84
3.4.3	Laser imaging	86
3.5	Experimental apparatus under evaporative conditions	90
3.5.1	Engine Combustion Network	90
3.5.2	Schlieren imaging	93
3.5.3	Rayleigh scattering diagnostics	95
3.6	Available methods to overcome multiple scattering effects	96
3.6.1	X-Ray absorption	98
3.6.2	Ballistic imaging	100
3.6.3	Structured Laser Illumination Planar Imaging (SLIPI)	103
3.7	Conclusions	105
	Bibliography	106
4	Mixture fraction measurement in isothermal spray	115
4.1	Introduction	116
4.2	Propagation of light in media containing scatterers	117
4.2.1	Mie scattering and fluorescent emission of a single droplet	117
4.2.2	Light radiation propagation in turbid media	123
4.3	Technique development and calibration	126
4.3.1	Design of a specific experiment	128
4.3.2	Evaluation of the conventional PLI in known situation	130
4.3.3	Scattering correction via Structured Planar Laser Imaging	133
4.3.4	Further considerations for quantitative measurements	136
4.4	Application to sprays	141

4.4.1	Experimental setup	142
4.4.2	Fluorescence properties of the dyed fuel	146
4.4.3	Theoretical evaluation of the PDS parameters	151
4.5	Quantitative measurements in a spray	154
4.5.1	Spray sizing via Structured Planar Laser Imaging	154
4.5.2	Light extinction between illumination and acquisition	159
4.5.3	Mixture fraction	162
4.6	Conclusions	169
	Bibliography	170
5	Rayleigh scattering measurements in vapor phase	179
5.1	Introduction	180
5.2	Rayleigh scattering theory	183
5.2.1	General formulation	184
5.2.2	Rayleigh cross-section	186
5.2.3	Rayleigh scattering in jets	189
5.3	Calibration of the experiments	190
5.3.1	Specific optical arrangement	190
5.3.2	Estimation of the cross-sections	192
5.3.3	General diagnostic protocol	195
5.4	Data processing and corrections	198
5.4.1	Image post-processing	199
5.4.2	Further corrections and improvements	201
5.4.3	Uncertainty analysis	202
5.5	Mixture fraction and temperature distributions	204
5.5.1	Single jet analysis	205
5.5.2	Mixture fraction in vaporized jets	206
5.5.3	2-D temperature distribution	211
5.6	Conclusions	212
	Bibliography	213
6	Results and experimental conditions influence	219
6.1	Introduction	220
6.2	Hydraulic characterization of the injector	221
6.2.1	Internal geometry of the nozzle tip	221
6.2.2	Rate of injection	223
6.2.3	Momentum flux of the spray	226
6.2.4	Additional characteristic parameters	228
6.2.5	Summary table of the hydraulic parameters	231
6.3	Mixing evolution in isothermal sprays	232

6.3.1	Macroscopic parameters of the liquid spray	233
6.3.2	Discussion on radial distribution profile	236
6.3.3	Influence of experimental conditions on mixing	240
6.4	Mixing evolution of vaporized jets	245
6.4.1	Vapor jet boundary	247
6.4.2	Mixing measurements and parameters influence	249
6.5	Comparative study of isothermal and evaporative sprays	255
6.5.1	Spray tip penetration	256
6.5.2	Spray opening	258
6.5.3	Mixing of isothermal and evaporative sprays	260
6.6	Conclusions	264
	Bibliography	266
7	Conclusions and further developments	271
7.1	Conclusions	272
7.2	Suggestions for future works	276
	Bibliography	279
	Appendices	305
A	Estimation of the error made on droplet sizing	305
B	Structured Planar Laser Imaging (SPLI-2P) function	309
C	Planar Laser Rayleigh Scattering function	317

List of Figures

2.1	Schematic of an indirect injection system.	14
2.2	Schematic of a pump-injector system. This system is electronically controlled.	17
2.3	Representation of a complete common-rail system.	19
2.4	Global schematic of a solenoid actuated common-rail injector (Injector type: Bosch CRI2.4).	20
2.5	Working principle of a typical solenoid actuated common-rail injector.	21
2.6	Geometric parameters to define the orifice of a Direct injection nozzle.	23
2.7	Schematic of the <i>Vena Contracta</i> and recirculation zone at the orifice entrance.	26
2.8	Comprehensive scheme of Nurick's model for cavitation [163]. General parameter definition.	30
2.9	Collapsing of the mass flow at the outlet of a cylindrical orifice (source Gimeno [93]).	31
2.10	Evolution of the discharge coefficient C_d as a function the cavitation number in a cylindrical orifice (source Gimeno [93]).	32
2.11	Evolution of the static pressure along an injection orifice for two L/D ratios. The prime symbol designates a higher L/D ratio (source Ramamurthi and Nandakumar [199]).	34
2.12	Illustration of the structure of the spray in the atomization regime (source [87]).	37
2.13	Representation of the Probability Density Function (PDF) or droplet size distribution as an histogram.	52
3.1	Global schematic of the injection system together with the injector temperature control apparatus.	68
3.2	Picture of the injector and technical drawing of the tip of the single-hole nozzle used in the experiments (source Bosch).	68

3.3	Images of the silicone molds extracted from multi-holes (a) and single-hole (b) nozzles obtained through SEM measurements. . . .	71
3.4	Imaging of some geometrical parameters: (a) Entrance radius and inlet diameter, (b) half-distance diameter, (c) outlet diameter and (d) global view.	72
3.5	Flow rate meter using the Bosch or long tube method [37].	74
3.6	Original and corrected signals of the rate of injection measured by the Bosch method. ($p_{inj} = 150$ MPa, $p_b = 6$ MPa).	77
3.7	Sectional representation of the flow at the outlet of a cavitating orifice.	77
3.8	Definition of the effective velocity and area (b) from the actual flow (a) at the outlet of an orifice.	79
3.9	Measurement principle of the momentum flux of the spray.	81
3.10	Global sketch of the cold spray visualization test rig.	83
3.11	Cold spray testing section with single-hole nozzle injector and optical accesses.	84
3.12	Combustion vessel used to perform experiments at high temperature (Engine Combustion Network - ECN)	91
3.13	Combustion vessel and high-speed Schlieren imaging setup. Mirror spacing and angles are not scaled.	94
3.14	Schematic representation of the experimental setup for fuel mass fraction measurements (Powell 2004 [195]).	99
3.15	Deduction of the liquid volume fraction (LVF) represented as a mass/area ratio for a water spray using X-ray measurements (Wang 2006 [252]).	100
3.16	Optical configuration used for ballistic imaging in a spray (source [140]).	101
3.17	Typical image obtained through ballistic measurement of the steady period of a spray (source [140]).	102
3.18	Experimental setup used in the SLIPI method to correct multiple scattering in high-speed flows (source Berrocal et al. [26]).	103
3.19	Illustration of the technique: set of 3 images (dephased of $2\pi/3$), related equations and resulting images for regular planar imaging and SLIPI (source Berrocal et al. [27]).	104
4.1	Schematic of the directions and angles of the incident and scattered photons.	119

4.2	Mie scattering phase function of a spherical fuel droplet illuminated at $\lambda = 532$ nm from the left side (Calculated from Bohren and Huffman's code [35]). Droplet diameter is $20 \mu\text{m}$, incident radiation is unpolarized and the scattered intensity is on log-scale.	120
4.3	Scattering efficiency factor of a spherical droplet ($n = 1.42$) as a function of the droplet diameter. Incident radiation wavelength is 532 nm.	121
4.4	Conceptual diagram of fluorescent emission process (Jablonski [115]).	122
4.5	Illustration of the propagation of light in an optically thick medium with significant effects produced by multiple scattering.	124
4.6	Schematic of the conventional and Structured Planar Laser Imaging (SPLI-2P) methodologies. The signals are shifted by half a period.	128
4.7	Schematic of the experimental arrangement used to acquire Structured Planar Laser Imaging signals in controlled test situation. The Cuvette is moved to change section position ($2, 12, 22$ and 32 mm).	129
4.8	Sample images recorded with the Structured Planar Laser Imaging setup used for Mie (left) and LIF (right). The intensity profile of the laser-sheet is displayed on the left side of the image.	130
4.9	Conventional planar resulting signals for Mie (left) and LIF (right). Particle diameter is $15 \mu\text{m}$, optical depth (τ) is 4 and illumination is placed at 12 mm from front wall.	131
4.10	Intensity profiles along laser path for Mie (<i>left</i>) and LIF (<i>right</i>). Vertical summation of the illumination region. ($15 \mu\text{m}$ and $\tau = 4$).	132
4.11	Sauter Mean Diameter map for the conventional Planar Droplet Sizing (PDS) technique. The laser-sheet is at 2 mm from the front wall. ($15 \mu\text{m}$ and $\tau = 4$).	132
4.12	Two-dimensional signals extracted from the Structured Planar Laser Imaging technique for Mie (left) and LIF (right). Particle diameter is $15 \mu\text{m}$, τ is 4 and laser-sheet is at 12 mm from front wall.	134
4.13	Intensity profiles recorded for Mie and LIF extracted by SPLI-2P technique compared to the theoretical decay (Beer-Lambert law). Illumination plane is at 12 mm from front wall.	135
4.14	Example of Sauter Mean Diameter map obtained by PDS when the SPLI-2P technique is applied. Laser-sheet is at 22 mm from the front wall. ($15 \mu\text{m}$, $\tau = 4$).	135
4.15	Measured optical depth (τ) in the cuvette between the illumination plane and the collection system for both Mie and LIF. ($15 \mu\text{m}$, $\tau = 4$).	137

4.16	Normalized profiles for Mie and LIF along laser-sheet path. Theoretical decay computed with the experimental τ . Vertical summation of the illumination region. (15 μm and $\tau = 4$).	138
4.17	2-D number density maps for Mie (left) and LIF (right) at 22 mm from front wall. Number density profiles along laser path (bottom), theoretical has been calculated by actual optical depth. (15 μm , $\tau = 4$).	141
4.18	Schematic of the optical layout of the Nd:YAG laser source. (<i>Source : Continuum</i>)	143
4.19	Illustration of the optical setup used in this study. The Nd:YAG laser is on the right (gray) and the testing section on the left (drawing lines).	144
4.20	Molar Absorptivity and fluorescence emission spectra of the Sulfo-rhodamine B. Note that the signals are presented on distinct intensity scales.	148
4.21	Scattered light intensity as a function of droplet diameter for n-dodecane doped with Sulfo-rhodamine B. The curve has been fitted to measure the exponent on the droplet diameter.	152
4.22	Fluorescence intensity as a function of droplet diameter for n-dodecane doped with Sulfo-rhodamine B. The curve has been fitted to measure the exponent on the droplet diameter.	153
4.23	Example of a spray image illuminated by a sinusoidal modulation (false color). This is an average over 100 images of the Mie scattering process. The spray is illuminated from the bottom.	155
4.24	Mie (left) and LIF (right) signals extracted via SPLI-2P in a real Diesel spray. Incident illumination comes from the bottom of the image.	155
4.25	Radial profiles of SPLI-2P resulting signals for Mie and LIF at 25 and 45 mm downstream. Illumination source is on the right side.	156
4.26	2-D map of LIF/Mie ratio (SMD) in a Diesel spray calibrated through PDPA measurements of the volume mean diameter d_{30} (left). Radial profiles of volume mean diameter via PDS when applying SPLI-2P method and PDPA at 25 and 45 mm (right).	158
4.27	Scheme of the extinction process between the illumination plane and the acquisition system in a spray.	159
4.28	Measured and calculated radial profiles of the optical depth at 25 and 45 mm from the injector tip.	161
4.29	Concept of the 3-D methodology to correct the SPLI-2P signal from extinction between illumination plane and imaging system.	162

4.30	Illustration of the procedure to extract the mixture fraction from the Mie and LIF Structured Planar Laser Images. The images have been replicated by symmetry according to the axis of the spray. . .	164
4.31	Resulting 2-D map of the mixture fraction with symmetry according to spray axis for the LIF signal. ($p_{inj} = 150$ MPa and $\rho_g = 22.8$ $kg.m^{-3}$).	164
4.32	Schematic of the one-dimensional discrete control volume for transient jet model (Musculus [157]).	165
4.33	Experimental and computed mixture fraction on the spray centerline. ($p_{inj} = 150$ MPa and $\rho_g = 22.8$ $kg.m^{-3}$).	167
4.34	Experimental and computed radial profiles of the mixture fraction at 25 and 45 mm from the tip. ($p_{inj} = 150$ MPa and $\rho_g = 22.8$ $kg.m^{-3}$).	168
4.35	Comparison of the experimental and computed mean mixture fraction along the axis of the spray. ($p_{inj} = 150$ MPa and $\rho_g = 22.8$ $kg.m^{-3}$).	168
5.1	Metal port with fused-silica window insert ($7 \times 58mm$) for laser-sheet transmission.	192
5.2	Calibration curve of the adiabatic mixing temperature as a function of the number density ratio N_{fuel}/N_{amb}	197
5.3	Calibration curve of the recorded intensities ratio (I_{mix}/I_{amb}) as a function of the number density ratio (N_{fuel}/N_{amb}).	197
5.4	Sample images of the raw signal acquired by the acquisition system and the N_{fuel}/N_{amb} map obtained after correction procedure. . . .	199
5.5	Composite image of Mie (left) and Rayleigh (right) scattered signals. This images show that the signal of the ambient gases is recorded through Rayleigh scattering and not with Mie.	200
5.6	Example of the image correction procedure influence on the original image (left). The corrected image (right) is obtained after particle inpainting and median filtering (6×6 pixels).	202
5.7	Sample two-dimensional signals of the fuel over ambient ratio in terms of number density. The two maps are different events of the same testing condition dataset.	205
5.8	Spreading angle and jet axis experimentally evaluated on a single-shot image. The outlet of the injector is not imaged by the acquisition system.	207
5.9	Two-dimensional distribution of the quantitative mixture fraction on the jet axis plane.	208
5.10	Experimental and computed mixture fraction on the jet centerline.	210

5.11	Experimental and computed radial profiles of the mixture fraction at 25 and 45 mm from the tip of the injector.	211
5.12	Ensemble-average of 2-D map of adiabatic mixing temperature of a liquid fuel jet injected into hot gases.	211
5.13	Axial and radial profiles of the adiabatic mixing temperature of the jet. The axial profile is recorded on the center-line and the radial distributions are extracted at 25 and 45 mm.	212
6.1	Sample SEM images of the silicone mold with computer-processed measurements of the single-hole nozzle used in this study: (a) inlet diameter and entrance radii, (b) half-distance diameter, (c) outlet diameter and (d) general view.	222
6.2	Temporal evolution of the rate of injection recorded by the flow rate meter. The electronic signal is plotted at the top and the pressure signal measured at 70 mm from the injector is represented in the middle.	224
6.3	Steady mass flow rate as a function of the square root of the pressure difference.	225
6.4	Discharge coefficient C_d as a function of the Reynolds number. Reynolds number has been calculated thanks to the theoretical velocity of Bernoulli (eq. 2.11).	225
6.5	Momentum flux of the spray measured as a function of time.	226
6.6	Mean value of the momentum flux in the steady period as a function of the pressure difference.	228
6.7	Momentum coefficient C_m as a function of the Reynolds number.	228
6.8	Effective velocity of the flow at the orifice exit as a function of the square root of the pressure difference.	229
6.9	Velocity coefficient C_v as a function of the Reynolds number.	230
6.10	Effective diameter of the orifice as a function of the Reynolds number.	230
6.11	Temporal evolution of the tip penetration for non-vaporizing sprays. The plots represent the influence of ambient density (left) and injection pressure (right).	233
6.12	Spreading angle as a function of time for non-vaporizing sprays. The influence of ambient density is plotted on the left and injection pressure on the right side.	234
6.13	Comparison of the measured and modeled spray tip penetration rates for the reference condition. The dashed line is the predicted penetration for the measured spreading angle and the dot line the prediction obtained by tuning the spreading angle to match penetration rate.	235

6.14	Measured mixture fraction and model predictions of the isothermal spray on centerline and for radial profiles at two axial distances for the reference condition: $p_{inj} = 150$ MPa, $\rho_g = 22.8$ $kg.m^{-3}$	237
6.15	Experimental and computed mean mixture fraction for the reference condition along with the axis of the spray. Spreading angle has been adjusted by matching penetration rate.	238
6.16	Comparison of the measured mixture fraction with model predictions assuming two distinct distribution profiles: Abramovich [1] and exponential [55]. This sample corresponds to the reference condition. Centerline is plotted on the left side of the figure and radial profiles on the right.	239
6.17	Measured mixture fraction and model predictions of the isothermal spray on centerline and for radial profiles at two axial distances. Experimental conditions: $p_{inj} = 150$ MPa, $\rho_g = 7.6$ $kg.m^{-3}$	241
6.18	Measured mixture fraction and model predictions of the isothermal spray on centerline and for radial profiles at two axial distances. Experimental conditions: $p_{inj} = 150$ MPa, $\rho_g = 45.6$ $kg.m^{-3}$	241
6.19	Measured mixture fraction of the isothermal spray on the centerline (left) and radially at 25 mm downstream. This graph shows the influence of ambient density on fuel-ambient mixing at constant injection pressure: $p_{inj} = 150$ MPa.	242
6.20	Measured mixture fraction on the centerline (left) and at 25 mm downstream (right) for different injection pressures. These results corresponds to the reference ambient density condition: $\rho_g = 22.8$ $kg.m^{-3}$	243
6.21	Graphical representation of the mixture fraction evolution as a function of ambient density for all injection pressures tested. The values are taken on the centerline at 25 mm from the tip.	244
6.22	Sample image extracted from high-speed Schlieren for the reference condition with computed vapor boundary plotted in green. Raw image (top) and corrected image (bottom) are shown according to image processing (sec. 3.5.2).	247
6.23	Spreading angle of the vapor region of the jet as a function of time for different ambient densities.	248
6.24	Temporal evolution of the vapor-phase penetration measured through Schlieren imaging. The predicted penetration rates are also represented (dashed lines).	249

6.25	Measured mixture fraction and model predictions of the vapor region of the jet on centerline and for radial profiles at two axial distances. Experimental conditions: $p_{inj} = 150$ MPa, $\rho_g = 15.2$ $kg.m^{-3}$ and $T_g = 1100$ K.	250
6.26	Measured mixture fraction and model predictions of the isothermal spray on centerline and for radial profiles at two axial distances. Experimental conditions: $p_{inj} = 150$ MPa, $\rho_g = 7.6$ $kg.m^{-3}$ and $T_g = 1400$ K.	251
6.27	Measured mixture fraction of the isothermal jet on the centerline (left) and radially at 25 mm downstream (right). The predictions are also plotted as references along the centerline (dashed lines). The injection pressure is the reference one ($p_{inj} = 150$ MPa). . . .	253
6.28	Measured mixture fraction on the centerline (left) (with model predictions) and at 25 mm downstream (right) for different injection pressures. This sample corresponds to the reference ambient density condition: $\rho_g = 22.8$ $kg.m^{-3}$	254
6.29	Graphical representation of the mixture fraction evolution as a function of ambient density for all injection pressures tested. The values are taken on the centerline at 25 mm from the tip.	255
6.30	Spray tip penetration vs. time at different ambient densities for vaporizing (dashed) and non-vaporizing (solid) sprays. The injection pressure is set to $p_{inj} = 150$ MPa.	257
6.31	Stabilized spreading angle for ambient density from 7.6 to 22.8 $kg.m^{-3}$ as a function of injection pressure for vaporizing and non-vaporizing sprays.	259
6.32	Comparison of the mixture fraction on the centerline (left) and radial distribution at 25 and 45 mm from the tip (right) for different ambient densities ($\rho_g = 15.2$ and 22.8 $kg.m^{-3}$, $p_{inj} = 150$ MPa). . .	261
6.33	Comparison of the mixture fraction on the centerline (left) and radial distribution at 25 and 45 mm from the tip (right) for different injection pressures ($p_{inj} = 50$ and 150 MPa, $\rho_g = 22.8$ $kg.m^{-3}$). . .	264
A.1	Radial profiles of the different definitions concerning droplet mean diameter. Adjusted d_{30} has been extracted from LIF/Mie ratio adjusted with PDPA volume mean diameter assuming constant relative difference between Sauter and volume mean diameter definitions.	307

List of Tables

2.1	General characteristics of the disintegration regimes (source [209]).	42
2.2	Breakup regimes of a single droplet. Recompilation proposed by Pilch and Erdman [192].	46
2.3	The different notations to express mean diameters according to Mugele and Evans [156].	53
3.1	General fluid characteristics of n-dodecane.	69
4.1	Standard deviation of the Sauter Mean Diameter for the conventional PDS technique.	133
4.2	Standard deviation of the Sauter Mean Diameter for the PDS technique when Structured Planar Laser Imaging is applied.	136
4.3	Results of the precision of the Structured Planar Laser Imaging technique for both Mie and LIF. The reference decay has been recorded at 2 mm.	139
4.4	Estimation of the accuracy of the Structured Planar Laser Imaging technique for both Mie and LIF. The reference decay has been calculated with Beer-Lambert law.	139
4.5	Chemical structure and general characteristics of the Sulforhodamine B molecule.	147
5.1	Molar fractions and Rayleigh cross-sections of the species in the combustion chamber at the time of injection.	195
6.1	Internal geometry and dimensionless parameters extracted from silicone molding of the nozzle.	223
6.2	Summary of the measured hydraulic parameters for the reference conditions ($p_{inj} = 150$ MPa) as well as flow coefficients to be used to potentially adjust model predictions.	231

6.3	Summary of the resulting spreading angles from experiments and through fitting of the measured penetration rate.	236
6.4	Summary of the spreading angles obtained through Schlieren experiments and thanks to an evaluation of the jet opening on two-dimensional individual mixing fields.	248
6.5	Rayleigh cross-sections for different linear alkanes together with stoichiometric mixtures. The equivalent cross-sections for stoichiometric mixture fraction are also presented.	252
A.1	Mean diameter using different definitions: d_{10} , d_{20} , d_{30} and d_{32} or SMD. The droplets have been measured with the PDPA instrument (TSI) at 45 mm downstream and are given in micrometer.	305
A.2	Estimation of the error induced by adjusting the volume mean diameter with to Sauter Mean Diameter (d_{32}). Measurements provided in table A.2.	306

Nomenclature

Latin Symbols and Abbreviations

- A Molar refractivity of the molecule [m^3/mol].
- A_c Section of the injection chamber of the rate meter.
- A_i Cross-sectional area at the inlet of the orifice.
- $a_m(x, y)$ 2-D normalized amplitude of the modulated illumination signal.
- A_o Cross-sectional area at the outlet of the orifice.
- a_s Arbitrary constant for tip penetration (Naber and Sieber [158]).
- A_{eff} Effective area of the orifice (eq. 3.10).
- A_{geo} Geometrical area of the orifice.
- AR Area reduction of the orifice (eq. 3.1).
- $ASOE$ Time from start of electronic command of injector.
- $ASOI$ Time from start of injection.
- k_{mod} Amplitude of signal modulation.
- c Concentration of fluorescent dye [mol/L].
- C_a Area contraction coefficient (eq. 3.13).
- C_d Discharge coefficient (eq. 3.14).
- C_m Momentum coefficient (eq. 3.15).
- C_v Velocity coefficient (eq. 3.12).
- $C_{p,amb}$ Heat capacity of the ambient gases [J/K].
- $C_{p,fuel}$ Heat capacity of the fuel [J/K].
- C_{R1} Spray radial distribution coefficient (Correas [55]).

C_{R2}	Spray radial distribution coefficient (Abramovich [1]).
D	Orifice diameter.
d	Droplet diameter.
D_i	Orifice inlet diameter.
D_m	Orifice diameter at half distance between entrance and exit.
D_o	Orifice outlet diameter.
d_{10}	Geometrical mean Diameter.
d_{20}	Surface area mean Diameter.
d_{30}	Volume mean Diameter.
d_{32}	Sauter Mean Diameter (SMD).
D_{eff}	Effective diameter of the orifice (eq. 3.11).
d_{part}	Nominal diameter of the fluorescent particles.
DI	Direct Injection.
e	Absolute roughness of the orifice [μm].
ET	Electronic time for solenoid excitation.
F	Dimensionless function of the scattered light direction.
F_K	King correction factor.
$FWHM$	Full Width Half Maximum.
$H_{vap, T_{vap}}$	Enthalpy of vaporization [J].
I_0	Incident radiation intensity.
I_C	Intensity of the conventional planar laser image.
I_f	Intensity of the fluorescent emission.
I_R	Recorded intensity.
I_r	Intensity radiated by the laser-sheet.
I_S	Intensity of the spatially modulated image (SLIPI).
I_s	Intensity of the scattered light.
I_t	Transmitted intensity.
I_{amb}	Intensity of the signal emitted by the ambient gases.
I_{mix}	Intensity of the signal emitted by the mixture.
I_{Ray}	Intensity of the Rayleigh scattered signal.

k -factor	Conicity factor of the orifice (eq. 2.1).
K	Number of cavitation (eq. 2.18).
K_B	Boltzmann constant.
k_f	Constant for fluorescent signal - droplet diameter dependency.
k_s	Constant for tip penetration adjustment.
K_{crit}	Critical cavitation number.
k_{fric}	Friction coefficient.
k_{LIF}	Constant for fluorescent intensity dependency.
k_{LL}	Constant for liquid length correlation.
k_{Mie}	Constant for intensity dependency of the scattered light.
k_{PDF1}	Shape parameter for the probability density function.
k_{PDF2}	Scale parameter for the probability density function.
k_{sa}	Constant for spreading angle correlation.
k_{SMD}	Constant for SMD correlation.
L	Orifice length.
l	Distance from the scatterer (particle).
L_{opt}	Optical path length.
LL	liquid length of the vaporizing spray.
\dot{m}	Mass flow rate.
$\dot{M}(x)$	Momentum flux at distance x from the tip.
\dot{M}_o	Momentum flux at the outlet.
\dot{M}_{theo}	Theoretical momentum flux (see eq. 3.15).
\dot{m}_{theo}	Theoretical mass flow (eq. 2.12).
m_f	Mass of fuel.
m_g	Mass of ambient gases.
N	Number density [part/mm ³].
n	Refractive index.
N_0	Loschmidt constant.
N_A	Avogadro number.
n_D	Refractive index at Sodium D line.

- N_T Total number density.
 N_{amb}, N_a Number density of the ambient gas molecules.
 N_{fuel}, N_f Number density of the fuel molecules.
 N_{mix} Number density of the molecules of the mixture.
 NO_x Generic term for the mono-nitrogen oxides NO and NO_2 .
 Oh Ohnesorge number.
 Δp Pressure difference between the two sides of the orifice.
 P Scattering phase function.
 $P(d)$ Probability density function.
 p_b Discharge pressure.
 p_i Pressure at the inlet of the orifice.
 p_o Pressure at the outlet of the orifice.
 p_{inj} Injection pressure.
 p_{vap} Pressure for vaporization of the fluid.
PDPA Phase Doppler Particle Analyzer (TSI instrument).
PDS Planar Droplet Sizing (Also LSD).
PLIF Planar Laser-Induced Fluorescence (Planar LIF).
 Q_e Extinction efficiency factor.
 Q_s Scattering efficiency factor.
 R Total radius of the spray or jet at corresponding axial distance.
 r Radial position within the spray or jet.
 r_e Entrance connecting radius of the orifice.
 R_r Relative rate of radiative process.
 R_{dipole} Radius of the sphere including the dipole.
 R_{nr} Relative rate of non-radiative process.
ROI Rate of injection [g/s].
 S Amplitude scattering function.
 s Spray tip penetration.
 Sc Schmidt number.
SLIPI Structured Laser Illumination Planar Imaging technique.

SMD	Sauter Mean Diameter (d_{32}).
SNR	Signal-to-noise ratio.
$SPLI - 2P$	Structured Planar Laser Imaging technique (2-Phase).
t	Time from start of injection (ASOI).
t_b	Time until full atomization of the spray.
T_g	Temperature of the gases in the chamber.
t_{Γ}	Time from fluorescence excitation for lifetime measurements.
T_{fuel}	Fuel temperature.
t_{inj}	Real hydraulic injection time.
T_{mix}	Temperature of the mixture.
T_{vap}	Boiling temperature.
u_B	Theoretical velocity of Bernoulli (eq. 2.11).
u_f	Mean velocity of the flow.
u_i	Mean velocity at the inlet of the orifice.
u_o	Mean velocity at the outlet of the orifice.
u_x	Axial component of the flow velocity.
u_{eff}	Effective velocity at the orifice outlet (eq. 3.10).
u_{jet}	Velocity of the jet.
V	Volume.
v_c	Speed of sound in the fluid.
V_M	Molar volume.
W_R	Total power recorded by the imaging system.
W_T	Total power scattered by the dipole.
We	Weber number.
X	Molar fraction.
X_{amb}	Molar fraction of the ambient gases.
X_{fuel}	Molar fraction of fuel.
Y_f	Fuel mass fraction.
Z	Mass fraction of the mixture.

Greek Symbols

α	Polarizability of the molecule [cm^3].
$\bar{\alpha}$	Trace of the polarizability tensor of the molecule [cm^3].
β	Azimuth angle of the scattered light.
$\bar{\chi}_f$	Mean volume fraction of fuel.
χ_f	Fuel volume fraction.
η_T	Dimensional total efficiency factor [cm].
η_{opt}	Global efficiency of the acquisition system.
ε	Molar absorptivity of the fluorescent dye [m^2/mol].
ε_0	Vacuum permittivity [F/m].
γ_f	Surface tension of the fluid [mN/m].
κ_D	Mass diffusivity coefficient.
Λ	Period of the disturbances in liquid sprays.
μ_a	Absorption coefficient [m^{-1}].
μ_e	Extinction coefficient [m^{-1}].
μ_f	Dynamic viscosity of the fluid [$Pa.s$].
μ_g	Dynamic viscosity of the ambient gases [$Pa.s$].
μ_m	Mass absorption coefficient [m^{-1}].
μ_s	Scattering coefficient [m^{-1}].
ν	Spatial frequency.
ν_f	Kinematic viscosity [m^2/s].
Ω	Collection angle of the acquisition system.
Φ	Fluorescence quantum yield.
ϕ_0	Arbitrary initial phase of the modulated signal.
Ψ	Anisotropy of the molecule polarizability [cm^3].
φ	Scattering angle.
ϖ	Number of particle in considered volume.
ρ_f	Density of the fuel [kg/m^3].
ρ_g	Density of the gases in the discharge volume [kg/m^3].
ρ_{eq}	Equivalent density of the fluid at the outlet [kg/m^3].

$\rho_{loc}(x, r)$	Two-dimensional local density in the spray.
ϱ_p	Depolarization ratio of the molecule for polarized illumination.
σ_a	Absorption cross-section [m^2].
σ_e	Extinction cross-section [m^2].
σ_R	Rayleigh cross-section [cm^2].
σ_s	Scattering cross-section [m^2].
σ_{amb}	Rayleigh cross-section of the ambient gases [cm^2].
σ_{fuel}	Rayleigh cross-section of the fuel [cm^2].
σ_{mix}	Rayleigh cross-section of the mixture [cm^2].
τ	Optical depth.
θ	Spreading angle of the spray [$^\circ$].
ξ	Relative radial position in the spray ($\xi = r/R$).

Chapter 1

Introduction

Contents

1.1 Subject and motivations of the work	1
1.2 Previous studies and objectives of this investigation	4
1.3 Outline of the Thesis	7
Bibliography	8

1.1 Subject and motivations of the work

At the end of the XIXth century, the motored vehicles designed for transporting passengers saw the light of the day. The evolution of ground, marine or air transportation required a source of energy other than human or animal to be animated. The thermal engine represents since the beginning the preferred mechanical power source to move these vehicles, no matter the size and no matter the type, the thermal engine has supplanted all the other methods for its easiness of application and its durability. That is why the thermal engines have been developed and investigated by all the transportation manufacturers for more than a century now and the latter improvements mainly concern fuel energy conversion efficiency and reduction of the pollutant emissions.

The environmental contamination has become more and more a matter of concern for people and governments, it now represents one of the most important topic and as such, many efforts have been done to increase the air quality. Still, there is a lot to do to reduce these emissions because they affect the ecosystem everyday and particularly the atmospheric pollution that results

in a destruction of the ozone layer and a global warming of Earth that would drive to major climatic changes according to the scientific opinion. As thermal engines use combustion to transform the chemical power contained in the fuel, either gaseous or liquid, to mechanical power through a combustion process, they are also responsible for the emission of many pollutants.

Even if some injection systems use gaseous fuel as a source of energy, the most part of the fuels used to generate power through combustion are liquid and injected as sprays. The new combustion strategies developed in the last years are based on new injection processes and improvements made to inject liquid fuel. The injection strategy has become one of the main parameters concerning engine efficiency and pollutant emissions such as NO_x , hydrocarbons and soot for example. More recently, the authorities have shown their interest in controlling also the CO_2 emissions, responsible of the greenhouse effect. This explains why the studies concerning sprays are so extended today in all the research centers, which work on the field, when it was inexistent 40 years ago. Nowadays, international conferences are fully devoted to the understanding of sprays and their atomization processes. The law of combustion is now mainly controlled by the law of injection and this demonstrates why most of the research concerning sprays are devoted to those driving the combustion process.

The general knowledge concerning sprays is that a lot of phenomena influence their developments leading to a misunderstanding of the global process and an inability to predict it. Spatial and temporal variations, mainly during the transients, of droplets size and concentration are the symbol of the unsteadiness of sprays. This unsteadiness is really important at the beginning and at the end of the injection, during these phases, the interactions between the two phases of the flow are responsible for a high level of instability and makes the turbulent process of injection a non-predictable event.

This unsteadiness basically means a lack of control over the injection process and consequently a reduction in combustion performance by causing unexpected fluctuations of local air/fuel ratio. As the characteristics of the droplets generated result from the level of turbulence, physical fluctuation or vibration induced by the contact between the fluids, a slight change in the conditions could lead to a major change in the atomization process.

A lot of experimental techniques are available and used throughout the different institutes to study sprays. Most of them are already applied to evaluate the sprays injected in the combustion chamber of a thermal engine. It has to be

said that almost all the researches carried out concerning injection in thermal engines are dedicated to direct injected sprays. However, the measurements of liquid spray from fuel injectors presents many challenges for any experimental technique. The main problem for any sampling method is that the spray is a dynamic system and any mechanical sampling process may either modify the droplet size or concentration or may not collect a representative fraction leading to hazardous results.

Because of their non-intrusive nature, optical techniques have been widely used and developed to serve spray diagnostics. During the past three decades, the development and improvements of new laser-based techniques has been particularly extensive. The fruit of all these investigations is a wide variety of instruments capable of performing measurements in sprays. Obviously, none of these instruments is perfect and can provide all the necessary information but only local and/or specific experimental data such as droplet size, velocity, trajectory; but these techniques, generally labeled as microscopic analysis, are mainly punctual and give information at one location at a time [1]. Other techniques analyze the spray macroscopically to get a two-dimensional global information map, which basically consists in visualizing the spray with a digital camera and a flash lamp. One simple example of the enhancement of the technology, the conventional camera has been replaced by a high-speed digital video camera capable of acquiring hundreds of pictures during the short process of injection.

Planar Laser Imaging solution is an alternative as it can provide macroscopic and microscopic information of the studied spray at the same time. A technique developed almost 20 years ago and improved by many researchers, called Planar Droplet Sizing (PDS), showed its capability to simultaneously determine the liquid volume and droplet surface-area distribution in an illuminated cross-section of a spray [2,3]. This experimental technique was very promising due to its double approach which, according to the authors, gives a map of Sauter Mean Diameters and a global visualization of the spray. However, the multiple scattering effects introduced by the dispersion of light in a medium containing many scatterers like liquid fuel droplets dramatically decrease the ability of the technique and the quality of the results. To obtain coherent measurements, some strong corrections had to be implemented during the post-processing of the experimental data.

In the same way, when the same spray is injected at high temperature (and pressure), this is to subserve the upcoming event, i.e. the combustion process. Several experimental solutions are available to analyze the fuel mass fraction in the vaporized region of the spray, but only a few of them have demonstrated

to provide trustful results. Most of the techniques developed at the end of the past century were based on the illumination of the cross-section of the spray by a pulsed laser. Depending on the method, particular care must be taken to reduce the scattering effects in the Mie regime, i.e. the scattering induced by liquid fuel droplets still present in the sample of interest.

The purpose of this work is to provide quantitative and reliable data concerning the liquid and vaporized fuel mass fraction in the spray. Two different laser-based techniques will be applied to obtain 2-D fuel concentration maps of a DI Diesel spray in the aim of better understanding the process of injection and fuel-air mixing. A total comprehension of these processes is necessary to fulfill with the future regulations regarding the quality of the gases rejected by the vehicles. This simply goes on the same direction of the last years world interest: Take care of our planet.

1.2 Previous studies and objectives of this investigation

The use of Planar Laser techniques to study sprays is a topic that has been investigated since the beginning of the 80's [4]. The principle of the Planar Laser imaging is to study a section of the spray thanks to a thin laser-sheet that crosses it generally along its axis. To overcome the background noise due to the strong scattered light signal, the fluorescence can be visualized to provide concentration maps [5]. This methodology generally called Laser-Induced Fluorescence (LIF) has been widely used in the last two decades. The Planar Laser-Induced Fluorescence (PLIF) is the two-dimensional version of the LIF technique and is one of the most applied laser techniques nowadays. An alternative developed further is to make the ratio between fluorescence and Mie scattering signals, which theoretically should give a map of droplet size [2]. This method was first called Laser Sheet Dropsizing (LSD) but it is most common to find it as Planar Droplet Sizing (PDS) now, this last name will be used all along this thesis.

The fluorescence is induced by the light of the laser-sheet and can occur naturally, due to inclusions present in liquids [3,6], or can be introduced by adding a known concentration of fluorescent dye to the liquid under study [7]. Assuming that the elastically scattered light is proportional to the droplet surface-area and the fluorescence to its volume (or basically the quantity of

dye in the droplet), the ratio of both images would determine the spatial Sauter Mean Diameter (SMD) distribution on an illuminated cross-section of the liquid spray.

One advantage of the Planar Droplet Sizing is that it considers the ratio of two intensity signals, which should eliminate the influence of laser light attenuation in its path through a dense cloud of particles as it is present on both images. One important thing to consider is that the light could have been multiply scattered by thousands of droplets and the signal of the light in the considered cross-section is really weak and almost totally covered by the multiply scattered light.

There are, however, a number of key issues with this technique:

- The PDS method specifically requires d^2 and d^3 dependencies with Mie scattering intensity signal and fluorescence signal. And even if the d^2 dependency in the range of droplets diameters generally analyzed in a typical spray injected in an engine ($d > 5\mu m$) has been verified in the past, the dependency to d^3 is sensitive to fluorescent tracer concentration and the absorption length within the droplets. This issue can be solved by a rigorous study of the fluorescence emission and absorption of light when the concentration of dye in the liquid changes.
- It uses two different properties of light, elastic scattering of the incident light and fluorescent emission, which is an inelastic light scattering process. The Mie scattering having a preferred direction, in opposition to the fluorescence emission, the signal observed by the camera will not be the same depending on the position in the image. In other words, the number of photons coming from one location will not be the same even if the droplet surface-area is equal if the angle of the elastically scattered light is different. Due to the anisotropy of the Mie scattered light, the technique would provide different ratios when observing the same droplet at different angles, thus limiting the accuracy two-dimensionally.
- Most of the applications of the LIF technique are based on the single scattering approximation assuming that the detected photons have experienced only one scattering event prior to arrival at the system of detection. This assumption remains valid while the particles number density is low and when the total photon path in the liquid region of the spray is short. However, in an optically dense medium like the studied sprays are, a large amount of photons have been scattered more than once before reaching the detector and so the single scattering assumption

is no longer valid. In such a situation, the multiple light scattering blurs and attenuates the original light emitted by the droplets on the illuminated cross-section, introducing significant uncertainties in the detected optical signal.

In this study, a new illumination technique will be applied together with a purposely designed imaging system. The combination of these two methodologies will show their potential for quantitative measurements of fuel concentration in optically thick media like Diesel sprays. The illumination technique is inspired by the Structured Illumination Microscopy (SIM) but is implemented here in a larger scale with a planar laser imaging configuration similar to the PLIF setup but by using a sine modulated light. The spatial modulation of the input light is used to remove the out-of-focus photons, which cause blurring effects and attenuation on the resulting image. These unwanted effects observed in PLIF caused by multiple scattering of light can be suppressed during the processing of the images. The assumption behind this technique is that photons that have experienced several scattering events in the sample will lose the original modulation information on their way to the imaging system; while singly scattered photons will not. The imaging system aim is to reduce the contribution of multiple scattering as well, by reducing the diaphragm (increasing $f/\#$), a large part of the multiply scattered photons can be blocked, thus increasing the efficiency of the technique.

Concerning the vapor phase of the spray, the Planar Laser Rayleigh Scattering (PLRS) will be used to get the fuel-vapor concentration in a DI Diesel jet quantitatively [8]. Rayleigh scattering is an attractive diagnostics method since it requires no doping of the media under investigation [9]. Due to the simple linear dependence of the Rayleigh scattered light signal on the molecular number density, the interpretation of the intensity of the signal obtained is almost direct and no complex system calibration are necessary. This method still requires sufficient care in the optical setup to minimize the other light sources of elastic scattering whereas the Rayleigh signal from the vaporized fuel molecules will suffer from interferences from other particles and background scattered light.

Planar Laser Rayleigh scattering will provide quantitative fuel-vapor concentration and will be compared to the quantitative measurements obtained in the liquid phase of the spray injected under non-evaporative conditions. This work is part of an international project, whose aim is to serve the industries by providing unique injector and spray diagnostic. This study and

quantitative characterization of the spray either liquid or vaporized will assist in development of improved spray models.

1.3 Outline of the Thesis

To assist the reader and to make this thesis as easy as possible to understand and follow, it has been divided in seven sections, this general introduction being the first chapter of the document. The main target of this dissertation is to carry out the various objectives cited in the last paragraphs. In that way, along the six next chapters of this document, the results and comments will always be discussed and compared to the knowledge and the understanding concerning sprays at this point.

The next coming section (chap. 2) will provide the reader with the characteristics and generation process of sprays with a particular emphasis to Direct Injected Diesel sprays that are injected in the latest technology on the market. This review of the literature will give the results of decades of investigation in this field until today through a detailed description of sprays, the formation of the droplets and the vaporization of droplets in high temperature ambient conditions. The study of the characteristics of sprays have been made feasible thanks to the use of the available experimental techniques.

Chapter 3 will describe the numerous experimental apparatus used in order to perform all the necessary analyses required to achieve this work. First of all, the experimental techniques to obtain the internal shape and the hydraulic characteristics of the injector used will be presented. The equipment used to carry out optical measurements in sprays will be described in this chapter for both isothermal and evaporative conditions. The different techniques used to analyze the liquid spray and the vapor region will be detailed with the corresponding processing methodologies. The limitations concerning optical measurements in the liquid region of a Diesel spray due to multiple scattering will be introduced. Finally, a presentation of different experimental solutions to overcome multiple scattering effects in liquid sprays will be drawn together with their advantages and drawbacks.

The following chapter (chap. 4) will present in details the development and application of a new planar laser imaging technique in a DI Diesel spray. An evaluation of the technique will be driven to confirm the validity and the quantitative aspect of the results. The results will reinforce the fact that the multiple scattering affects optical measurements using visible light in the

dense region of the liquid spray. The limitations and the uncertainties of such measurements will also be discussed in this chapter and an evaluation of the results in sprays will be made through confrontation to a validated model.

In chapter 5, the application of the Rayleigh scattering in the vaporized region of the spray will be described, the tests will be done in the aim of further comparing liquid and evaporative sprays. All the necessary steps to setup this kind of experiment and how to apply it to a vaporized Diesel jet will be given in this section. The post-processing will also be explained and an analysis will be done to present an evaluation of the quality and reliability of the results. Note that the term jet in this document refers to as the vaporized region of a liquid spray injected under high temperature conditions or simply as a gas-jet. Spray is a generic term to symbolize a stream of droplets entraining the surrounding gas. As the fuel injected in this thesis is liquid, the initial stream will be called spray until complete evaporation, after what it will be defined as a jet.

All the experimental results will be provided in chapter 6 in order to see the influence of the different parameters such as gas density and injection pressure on the fuel mass fraction in the liquid and vaporized part of the spray. The results of the hydraulic characterization of the injector will be presented together with the internal geometry measurements. Two-dimensional results of fuel concentration will be presented for both the liquid region (isothermal sprays) and the vapor-phase of the sprays. Preliminary comparison will be done regarding development of sprays injected under evaporative conditions or not. The results concerning the mixture fraction in the spray under isothermal and high temperature conditions will be compared and the validity of the gas-jet model to predict Diesel spray mixing will be discussed.

The last chapter of this thesis (chap. 7) will present the general conclusions over all the work done during this project of doctoral thesis and will also provide some recommendations for future researchers proceeding in this field.

Bibliography

- [1] Vlad Soare. *Phase doppler measurement in diesel dense sprays: optimisation of measurements and study of the orifice geometry influence over the spray at microscopic level*. PhD thesis, E.T.S. Ingenieros Industriales. Universidad Polit cnica de Valencia, Valencia, 2007.

-
- [2] C.N. Yeh, H. Kosaka, and T. Kamimoto. A fluorescence/scattering imaging technique for instantaneous 2-D measurement of particle size distribution in a transient spray. *3rd International Congress on Optical Particle Sizing, Yokohama, Japan*, pages 355–361, 1993.
- [3] Jose Enrique Julia. *Medida de concentraciones de combustible en chorros Diesel mediante tecnicas de fluorescencia inducida por laser*. PhD thesis, E.T.S. Ingenieros Industriales. Universidad Politécnica de Valencia, 2003.
- [4] G.S. Settles. Flow visualization techniques for practical aerodynamic testing. *Flow Visualization III*, pages 306–315, 1985.
- [5] P. Andresen, G. Meijer, H. Schluter, H. Voges, A. Koch, W. Hentschel, W. Oppermann, and E. Rothe. Fluorescence imaging inside an internal combustion engine using tunable excimer lasers. *Applied Optics*, 29(16):2392–2404, 1990.
- [6] J.V. Pastor, J.J. Lopez, J.E. Juliá, and J.V. Benajes. Planar laser-induced fluorescence fuel concentration measurements in isothermal diesel sprays. *Optics Express*, 10(7):309–323, 2002.
- [7] P. Le Gal, N. Farrugia, and D.A. Greenhalgh. Development of laser sheet drop sizing (lsd) for spray characterization. *IMEchE conference transactions*, pages 113–120, 1998.
- [8] F.Q. Zhao and H. Hiroyasu. The applications of laser rayleigh scattering to combustion diagnostics. *Progress in Energy and Combustion Science*, 19(6):447–485, 1993.
- [9] H. Zhao and N. Ladommatos. Optical diagnostics for in-cylinder mixture formation measurements in ic engines. *Progress in Energy and Combustion Science*, 24(4):297–336, 1998.

Chapter 2

Injection Process In Diesel Engines

Contents

2.1	Introduction	12
2.2	Injection system in Diesel engines	13
2.2.1	Background	13
2.2.2	The common-rail system	18
2.2.3	The injector and the nozzle	20
2.3	Internal liquid flow	23
2.3.1	Orifice geometry and related parameters	23
2.3.2	Characteristics of the flow	24
2.3.3	Pressure drop and cavitation	26
2.3.4	Influence of nozzle geometry on the internal flow	32
2.4	Formation of Diesel sprays	35
2.4.1	General properties of sprays	36
2.4.2	Disintegration process and droplet formation	41
2.5	Characteristics of Diesel sprays	47
2.5.1	Spray tip penetration	47
2.5.2	Spreading angle of the spray	50
2.5.3	Droplet size distribution and prediction	51
2.5.4	Velocity and concentration profiles	54
2.6	Conclusions	57
	Bibliography	58

2.1 Introduction

Depending on the kind of application it is used for, the characteristics of sprays and the way the liquid has to be dispersed could be fundamentally different. Droplet size, velocity, air entrainment, these characteristic parameters of a spray are directly related to where it will be injected and the purpose of it. Sprays are used in many domains, and this becomes truer day after day through all type of application from the most common use to the new ones. During the last decades, the most research efforts in spray generation and analysis have been driven to focus on liquid fuel injection to produce combustion. Leading to several crucial improvements on the injection process responsible of making the combustion more efficient and reducing pollutant emission. Even if liquid spray injected could mean car engines for many people, liquid fuels are injected in rocket engines, gas turbines, spark ignition engines, Diesel engines for boats, aircrafts, cars and an extensive list of system in which they will provide power through combustion.

Liquid fuels are easy to store, to transport, and they present the main advantage to contain more energy per unit volume than gas fuels. These powerful fluids are injected through specifically designed nozzles in order to be transformed in a very large amount of droplets as liquid fuels are not volatile enough to vaporize in the combustion chamber without a successful mass dispersion. This process of disintegration ensures a better evaporation and thus a great air/fuel mixing to permit a complete and fast energy conversion as the rate of evaporation is inversely proportional to the size of the droplets generated. More than droplet size only, the structure of the spray plays a major role in the mixture preparation and will affect the quality of combustion and pollutant emissions.

As the purpose of this thesis is to provide from both points of view, i.e. macroscopically and microscopically, a complete understanding of sprays is needed. For this reason, after an introduction of the technology used in Diesel engines to make such improved sprays, the next part of this chapter will start with a description of the internal liquid flow. In the following section the sprays will be presented, together with a description of the way a liquid flow can be transformed into thousands of droplets: the disintegration processes. Finally the different characteristics of Diesel sprays will be presented, from a theoretical approach.

2.2 Injection system in Diesel engines

Fuel sprays are injected into the combustion chamber of any of kind of thermal engines as a result of the pressure difference between both sides of the nozzle orifice. The high pressure of the fuel that feeds the injector drives the fluid through the orifices of the nozzle at relatively high speed. The velocity of the internal flow and the behavior of the fuel stream at the outlet are a direct consequence of the injection system used and the operating conditions.

The function of the fuel injection system is to supply the engine with fuel in quantities exactly metered in proportion to the load and power required and timed with the highest possible accuracy. The injected quantity as well as the quality of the injected fuel stream are crucial parameters for the engine to deliver the energy while keeping the pollutant emissions within the limits prescribed by governmental regulations. The injection system must complete the three following steps:

- To introduce the fuel in the combustion chamber according to the desired injection law, which determines the behavior of the upcoming combustion process.
- To disintegrate the liquid flow into an ensemble of small droplets, this process is called atomization as the injection pressure is relatively high.
- To mix the fuel and gases present in the combustion chamber through air entrainment to permit better mixing and thus complete combustion.

Depending on the operating mode of the engine, the injection strategy can be either indirect or direct. These two configurations do not require the same kind of technology regarding to the injection system and, the direct injection, which was earlier used basically in big and slow engines, is now used in small and fast.

2.2.1 Background

The engines developed in automotive require such a level of versatility that the engines are small and fast, in comparison to truck engines for example. Thus the indirect injection was the solution used to ensure complete combustion in this small period of time between two cycles.

Indirect injection system

In indirect injection engines, the combustion chamber is divided in two parts: the pre-combustion chamber and the main chamber, in which the complete combustion occurs and delivers the output power. During the compression phase of the 4-stroke cycle, the air gets into the small connecting orifice between main chamber and pre-combustion volume generating turbulences of the gas stream. This turbulence helps the mixing process when the fuel is injected through a single-hole nozzle in the pre-combustion chamber thus igniting when the adequate thermodynamical conditions are reached. In such systems, the quality of the injected spray is not as important as it is in direct injection engines, that is why the injection pressures are relatively low (around 20 to 40 MPa). The mixing process is enhanced by the first stage of the combustion within the pre-combustion chamber which projects the rich fuel-air mixture toward the main chamber to "complete" the combustion process.

The pre-combustion chamber also called prechamber is generally designed and intergrated in the cylinder head as shown in figure 2.1. In this geometry, the fuel is injected tangentially to surface of the chamber in order to increase the turbulent behavior of the air-fuel mixture.

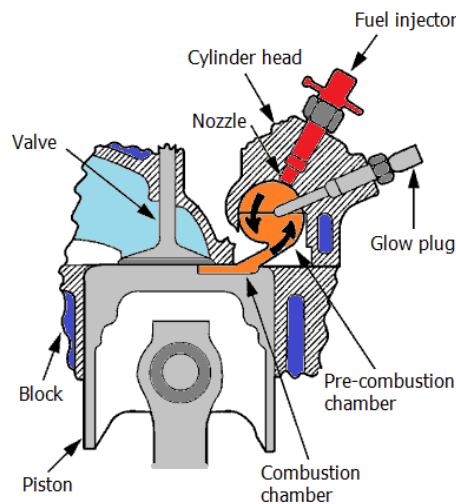


Figure 2.1: Schematic of an indirect injection system.

Indirect injection system has the following advantages:

- Due to the turbulence in the pre-chamber, a good dispersion of the spray

is achieved, thus granting a high-quality macro-mixing.

- A good air-fuel mix, which is necessary to have a good combustion. As a consequence, in this type of engines violent pressure increases are avoided as well as great production of noise. Moreover, the good combustion grants a small production of smoke and NO_x.

On the other hand, the following list presents the main disadvantages of the indirect injection in Diesel engines:

- As a direct consequence to the chamber division, ventilation of the pre-combustion chamber is bad because of the small section of the connecting orifice.
- Due to presence of two chambers, the surface/volume ratio is high, thus leading to great heat dispersion and, as a consequence, a lower efficiency.
- Because of the heat dispersion, a pre-heating spark must be included in the pre-chamber (see Glow plug on fig. 2.1) to ease engine start in cool conditions.
- The global efficiency of this engine type is lowered also by the pressure losses in the throttling between pre-combustion and main chamber.

With the advancements done concerning injection system technology, the indirect injection became obsolete in most of the applications and is now employed for specific use that do not require high level of performance. Therefore, the direct injection earlier used for high volume engines has been developed for smaller engines and demonstrated to perform better in most of the conditions.

Mechanical direct injection and pump-injector

The direct injection means that the fuel is directly injected into the combustion chamber; hence, no pre-combustion is required and so, this technological solution reduces (or cancels) the drawbacks of the indirect injection system listed above. The systems using direct injection were mechanically actioned in the past decades. This means that the high pressure pump was in charge of metering the exact fuel quantity to inject with the correct timing. With this technology, the start of injection is governed by the pressure in the injector which counteracts the force of the preloaded spring.

The main disadvantages of these systems are:

- The fluctuations of the injection pressure as this depends upon the engine speed and time of injection.
- Because the injector opening is mechanically driven, a consequence of the pressure fluctuations is a lack of control on the real start of injection

In order to control better the start of injection and the quantity injected in the combustion chamber, the pump injector has been introduced and represented a big improvement in this field. In this technology, the injector is the element in charge of metering the fuel quantity to inject as well as the level of atomization of the spray, i.e. the injection pressure. The fuel pump only pressurizes the fuel up to the consign of the system and then holds it constant. The injector opening can be driven either mechanically or thanks to the new devices aiming at controlling the different parameters of the engine, electronically. Note that the mechanically controlled systems are mainly used in constant speed engines as the fuel quantity injected decreases when the engine goes faster.

The systems in which the opening and closing of the injector are controlled electronically exist for decades [1] but until 1995, no system has been installed on large-scale car production due to cost and reliability.

The pump-injector is fixed directly in the cylinder head as described in figure 2.2. This technology groups the high pressure pump, injector and nozzle in a unique system actioned by an additional cam on the cam-shaft generally in the cylinder head as well. Each pump-injector is equipped with a fast solenoid valve to control the start and end of the injection.

The solenoid valve of the pump-injector is normally opened, which allows the fuel to go back to the fuel tank via the return line. At the same time, the fuel fills the pumping chamber, in normal operation during the admission stroke. Once the solenoid valve closes, the fuel cannot exit the injector except through the nozzle into the combustion chamber when the pressure goes over the consign load of the spring. Therefore, the start of injection is defined by the solenoid valve closing and the quantity injected by the closing of the injector, related to the re-opening of the solenoid valve.

The electronic signal is controlled by the ECU (Electronic Central Unit) which computes the exact timing as a function of the different parameters received and according to the engine maps. This means that the start and the end of injection are programmable and independent upon the position of the piston and engine speed.

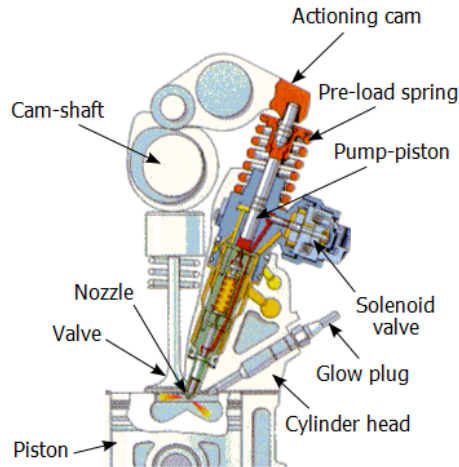


Figure 2.2: Schematic of a pump-injector system. This system is electronically controlled.

Thanks to this system, the fluid is at high pressure in a small region inside of the pump-injector. This offers the consequent advantage to increase the injection pressure as it is not limited by the high pressure pipes between the pump and the injector. The high pressure (somewhere over 200 MPa for the last generation systems) combined with the control on the start and end of injection leads to a dramatic reduction of the pollutant emissions concerning Diesel engines. This system offers another advantage it allows disconnecting some cylinders at low and mid-loads.

The disadvantages of the pump-injector system, making it no longer used for automotive engines are:

- Because of the location and size of the system, a specific and complex cylinder head must be designed, thus increasing cost and production difficulties.
- The pressure being generated by the actioning-cam connected to the cam-shaft, it is not constant along the cycle.
- Another consequence of the injection pressure is the reduced time of the injection possibilities, thus making more than two injections per cycle impossible.

Because of the requirements of the regulations regarding pollutant emissions, injection strategies using more than two injections per cycle have been

implemented, thus dooming this technology. For these reasons, the car manufacturers had to consider other solutions, presenting the same advantages while avoiding the disadvantages, the accumulation systems or common-rail are the answer.

2.2.2 The common-rail system

For many years, realizing a flexible injection system for Diesel engines has been an important target. With the constant request in terms of fuel economy and emissions regulations, the following parameters must be easily and accurately controlled:

- The start of injection
- The mass of fuel to inject
- The rate of injection
- The injection pressure

With this purpose many injection designs were studied, the ultimate solution applied in most of the engines used in automotive production today is the common-rail. The common-rail system allows controlling the initial time of the injection, its end, as well as the injection pressure (in a range of 20 up to 200 MPa) and the number of injections (multi injection). With a high level of accuracy thanks to a fully and integrated electronic control over the multiple parameters influencing the injection process.

Unlike in conventional systems, in this technology, the pressure in the injector does not govern the injection process directly but through an electronic command. The injection pressure is generated by an external pump mechanically driven by the engine and the pressure is regulated by a special device implemented onto the rail. The common-rail acts as an accumulator and ensure only small variations of the injection pressure along the cycle in which up to seven injections can be performed. Figure 2.3 is a schematic representation of the common-rail injection system as it is implemented in modern Diesel engines.

In a typical common-rail system, a low pressure pump generally placed in the fuel tank provides the high pressure pump mechanically connected to the engine with the fuel. The high pressure pump pressurizes the fuel for the common-rail acting like an accumulator as introduced earlier and to the injectors, connected to the rail thanks to high pressure lines. One part of the fuel is directly injected into the combustion chamber through the nozzle of

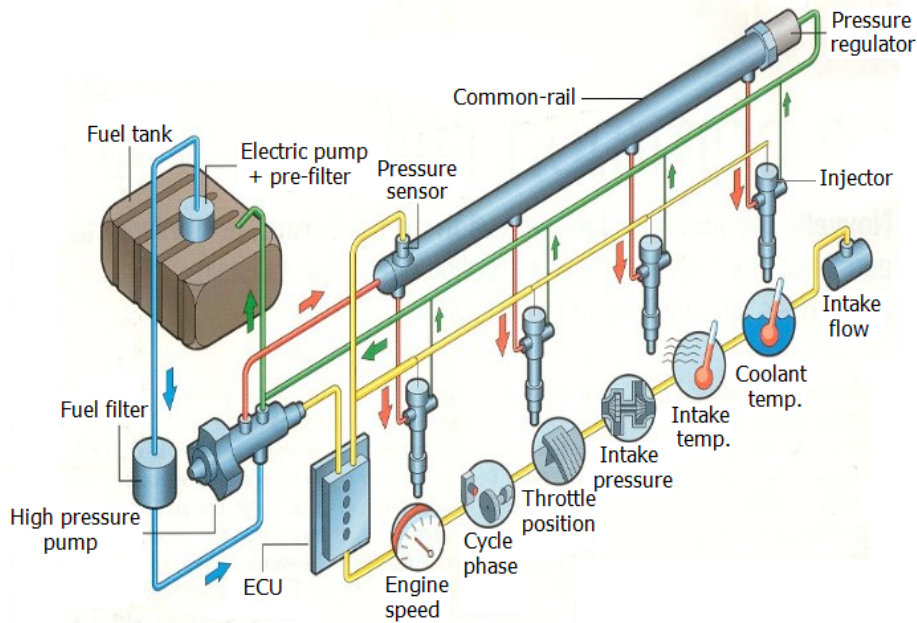


Figure 2.3: Representation of a complete common-rail system.

each injector, another part is used to hydraulically drive the injector opening and closing and is then traveling back to the fuel tank.

The volume of the rail and the different pipes between the high pressure pump and the rail or between the rail and the injectors is used to damp out the fluctuations generated by the pump but also the pressure slope produced by the sudden fuel discharge when the injector opens. Thanks to this concept, the fluctuations are only of a few megapascals (MPa) [2], which is relatively small compared to the high pressure capability of such systems (up to 200 MPa).

The pressure in the rail and therefore in all the system is held by a pressure regulator and controlled by the Electronic Central Unit (ECU) through a pressure transducer. If the value sets by the ECU is not that measured by the sensor, the regulator opens the outlet of the rail toward the fuel tank and the pressure decreases. The pressure is generated by a radial pump for small and fast engines, and a linear pump is generally used for bigger engined vehicles. The radial pump presents the advantage of being compact while producing high pressure with a regulated flow rate, thus being efficient as it adapts itself to the engine demand.

2.2.3 The injector and the nozzle

The injector certainly represents the most complex and important organ of this kind of injection system. A common-rail injector is composed of several elements shown in figure 2.4 and described below from bottom to top:

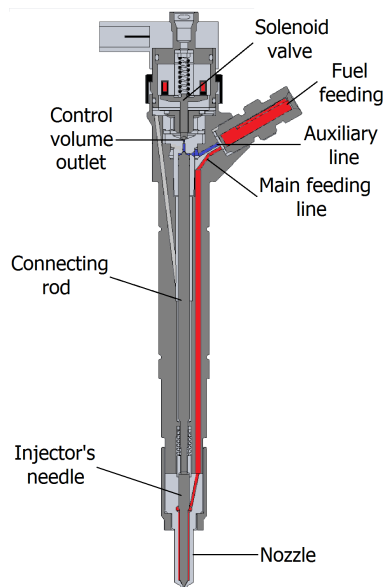


Figure 2.4: Global schematic of a solenoid actuated common-rail injector (Injector type: Bosch CRI2.4).

- A specially designed nozzle. The nozzle generally has several orifices, up to eight in production injection system for passenger cars. This part goes together with the needle, which acts as a valve to open or close the injector.
- A connecting rod which moves together with the needle. The movement of the needle begins at the top of this part.
- An auxiliary fuel feeding line. This fuel entrance feed the control volume with the high pressure fuel at the top of the connecting rod.
- A fuel exit at the top of the control volume. Closed by the solenoid valve, this controls the injector opening and closing thanks to a pressure difference.

This type of injector uses the high pressure generated by the pump and always available as long as the engine is running as a source of energy to move the needle up and down. This hydraulic control of the injector is the key as it only requires a small quantity of energy to open or close the injector while a direct action on the needle would require hundreds of times more.

The following description of the working principle of this technology is supported by figure 2.5 in which the different phases of the injector during an injection cycle are schematically represented.

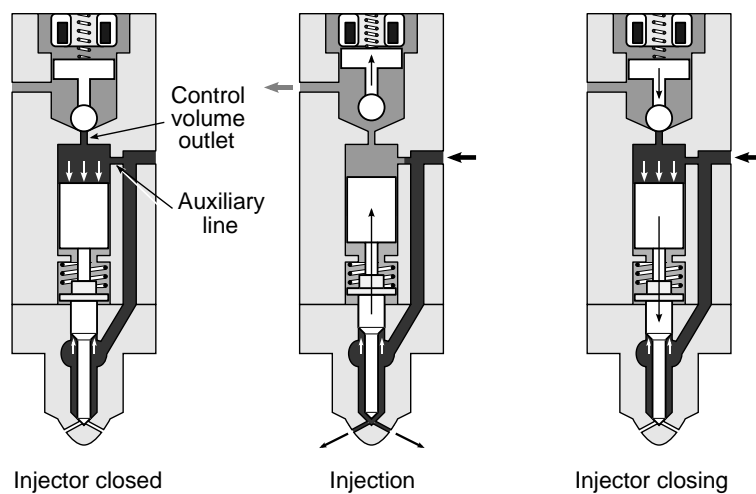


Figure 2.5: Working principle of a typical solenoid actuated common-rail injector.

The fuel is provided at the entrance by the high pressure pump through the common-rail and the distribution lines. Right after the entrance, the fuel is divided into two channels, one goes down toward the nozzle, this fuel is the one to be injected and another goes to the control volume. To access the control volume located at the top of the connecting rod, the fuel goes through the auxiliary line on which a calibrated orifice has been manufactured.

When the solenoid is not activated, the valve is closed and no flow can go through the control volume outlet, also equipped with a calibrated orifice. Therefore, the pressure of the fluid in the control volume is the static pressure of the injection system and the area at the top of the connecting rod is higher than that of the needle, the pressure pushes the rod-needle down, thus closing the orifices. Note that a pre-loaded spring keeps the injector closed when there is no pressure.

Once the solenoid is activated, the valve goes up and the outlet of the control volume opens, hence the pressure at this location suddenly drops down. In this situation, the pressure at the top of the connecting rod is lower and the high pressure at the bottom of the needle makes the system rod-needle to go up. This action opens the nozzle and the orifices start to inject. The injection lasts until the solenoid is deactivated, this closes the volume control and the pressure at the top of the connecting rod increases, thus getting stronger than that at the bottom of the needle. The system rod-needle then goes down and the orifices of the nozzle are closed again, thus ending the injection.

In newer generations, the solenoid has been replaced by a piezo-electric system offering a better control for smaller injection timings and allowing faster action, thus increasing the number of injection per cycle potentially. The difference resides in the opening of the control volume now performed by the deformation of a material with piezo-electric characteristics.

The nozzle also represents a crucial part of the injection as its shape mainly determines the behavior of the flow at the outlet and therefore the spray development and atomization. There is a high degree of international standardization concerning injector nozzles and most are derived from the original Bosch designs and are interchangeable, although internal features may vary.

Direct-injection systems employed in the automotive production mostly use long-stem hole-type nozzles as shown at the bottom of the injector schemed in figure 2.4. The extended small-diameter tip reduces the space required to accommodate it between the cylinder head valves, generally placed in the center of the combustion chamber for a better mixing process.

A large amount of parameters influence the manufacturing of the nozzle, based upon the specificities required by the manufacturer concerning the engine performances. The number, diameter and position of the orifices represent part of the most important parameters concerning nozzle design. The ratio of the diameter of the valve guide and seat called the differential ratio also plays a role on the dynamic of the injector, as well as the mobile mass of the needle. The diameter and volume of the sac are other of the numerous parameters to take into account as they certainly have an impact on the performances of the injection system. It must be said however that in addition to all these factors, the shape of the orifice shall be the most important when looking at spray development and disintegration process as for a same orifice diameter, the behavior of the flow may be fundamentally different.

2.3 Internal liquid flow

The characterization of the liquid flow inside the orifice of the nozzle is fundamental for a complete understanding of the breakup processes responsible of the disintegration and full atomization and thus development of the liquid spray. The study of the parameters that influence the internal flow is a challenge as all the processes occurs inside the orifice, at microscopic scales and relatively high velocities [3–7].

An extensive work has been performed by Gimeno [8] in 2008 on internal flow characterization and the objective of this section is to summarize and add recently published support to this work.

2.3.1 Orifice geometry and related parameters

The orifice of a Diesel injection nozzle is not a simple straight pipe but has several specificities that strongly affect the flow of the liquid inside [9–11]. Figure 2.6 defines schematically the important characteristic dimensions of a typical orifice that can be found in a Direct injection nozzle.

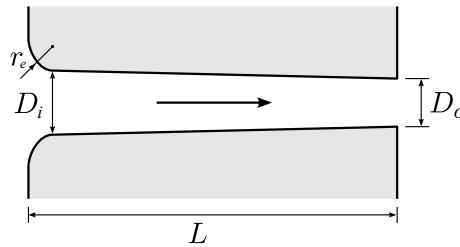


Figure 2.6: Geometric parameters to define the orifice of a Direct injection nozzle.

The geometric parameters generally used in fluid mechanics applied to Diesel nozzle injectors are: inlet and outlet diameters D_i and D_o respectively, orifice length L and entrance radius r_e . From these dimensions, some parameters can be defined, they characterize the shape of the nozzle's orifice and are dimensionless:

- Length - diameter relation: L/D_o
- Entrance radius - inlet diameter: r_e/D_i
- Inlet - outlet diameter ratio: D_i/D_o

This last ratio gives conicity or convergence (note that it can also be divergence) of the orifice, this ratio is equal to the unity 1 for cylindrical nozzles. To determine the convergence of an orifice, the *k-factor* is generally found throughout the literature and is defined as follows [12, 13]:

$$k\text{-factor} = \frac{D_i - D_o}{10 [\mu\text{m}]} . \quad (2.1)$$

Nevertheless, this parameter presents the disadvantage not to make any difference between actual orifice diameter. For example, an orifice with $D_i = 210 \mu\text{m}$ and $D_o = 200 \mu\text{m}$ will have the same *k-factor* as another hole with $D_i = 110 \mu\text{m}$ and $D_o = 100 \mu\text{m}$; while the geometrical areas and therefore the flow characteristics will be different.

2.3.2 Characteristics of the flow

The fluid mechanic has been studied for years and a lot of models and equations are known to predict and analyze every kind of process. As a first approach, the flow regime can be or must be determined to know in which situation the flow is and therefore which theory has to be applied in the studies case [14]. Two flow regimes with quite accurate theories are commonly accepted: Laminar and turbulent that are distinguished for specific values of Reynolds number [15], a dimensionless parameter that gives a measure of the ratio between inertial forces and viscous forces:

$$Re = \frac{\rho_f u_f D_o}{\mu_f} . \quad (2.2)$$

In this expression, ρ_f is the fuel density, u_f the velocity of the flow, D_o the specific diameter, concretely the nominal outlet diameter of the pipe and μ_f the dynamic viscosity of the fluid. For cylindrical straight ducts, internal experimental observations show that the flow is laminar for values of Reynolds number below $Re \approx 2300$ and turbulent for values above $Re \approx 4000$. The interval $2300 < Re < 4000$ is considered as a transition zone where both laminar and turbulent regimes are possible, depending on several parameters like pipe roughness or flow uniformities. Nonetheless, care must be taken with respect to this definition because it appears to be valid only for fully developed flows, this means after a certain distance in the pipe. When a fluid is traveling into a pipe, a sudden change of direction can produce local uniformities of the flow due to the fact that the boundary layer has to thicken to wall and

it takes time (distance) to be stabilize. It is generally consider that it takes several diameter to be stable, in the case of the orifice introduced before, it would be stable at high L/D (either D_i or D_o). This distance needed to get a stabilized flow also depends on the regime (laminar or turbulent) and would never be long enough in an injector's orifice as this ratio is generally lower than $L/D \approx 10$. In practice, the length of the orifice necessary to consider the flow as stable in the laminar regime is also function of the Reynold number [16]:

$$\frac{L}{D} = 0.03 Re \text{ When } Re < 2300. \quad (2.3)$$

Other values of the coefficient in this equation can be found in the literature going from 0.03 to 0.06 [17]. In this formulation, for example if $Re = 2000$, the length should be around 60 times the diameter D to consider the flow fully developed.

When the regime is turbulent ($Re > 4000$), the mixing intensity induced by the turbulence itself makes the necessary length shorter to get a developed flow. The formulation proposed by White [17] to calculate the length necessary to consider the flow stabilized in turbulent regime is:

$$\frac{L}{D} = 4.4 Re^{1/6} \text{ When } Re > 4000. \quad (2.4)$$

As an example, for Reynolds number commonly used in the orifice of an injector ($10000 < Re < 100000$), the length should be between 20 and 30 times the orifice diameter to get a fully developed turbulent flow.

This leads to the following conclusion that neither in laminar regime condition nor in turbulent, the orifices used in Diesel injectors are long enough. This means that in none case the flow will be fully developed and thus the analysis of the flow in such orifices would require the following considerations to be taken into account:

- The behavior of the flow will be directly related to the geometry of the entrance of the orifice and will affect the flow characteristics, e.g. thickness of the boundary layer (or separation), local pressure losses, etc. In this way, the velocity profiles and head losses in the orifice will strongly depend on the flow behavior at the entrance.
- As the flow is not completely developed, the standard limits used to characterize the regime as laminar or turbulent ($Re > 4000$) will not be valid in such an orifice [18]. As a consequence, the Reynolds number is

not the only parameter to take into account to characterize the regime and therefore the intensity of the turbulence.

- The fluid mechanic theories based on fully developed flow cannot be applied in this case. For example, the velocity profiles at the orifice outlet will not be almost constant in the whole section of the orifice exit as it would be if flow were stabilized [19].

2.3.3 Pressure drop and cavitation

On its way through the orifice, the fuel will lose part of its energy. This energy loss, generally called pressure drop, is the result of several parameters and causes a decrease of the flow outlet velocity. There are two types of pressure losses in the orifice of an injector's nozzle: The minor losses generated by the geometry of the orifice entrance and the major losses produced by the friction of the fluid against the walls.

Due to a sudden change of section at the entrance of the orifice, the fluid cannot easily follow the way guided by the internal shape in this region and a separation of the boundary layer may occur. This separation results in the apparition of a recirculation zone that restrains the flow in a smaller section commonly called *Vena Contracta*. This restriction makes the flow to speed up (and the pressure to drop down) locally around the *Vena Contracta*; then the flow slows down at the end of the recirculation zone to reach the orifice walls again. Figure 2.7 represents schematically this process at the entrance of an orifice.

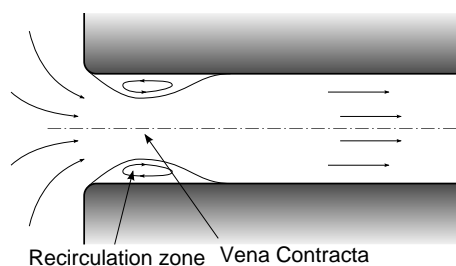


Figure 2.7: Schematic of the *Vena Contracta* and recirculation zone at the orifice entrance.

From a physical point of view, this deceleration of the flow produces a large

viscous dissipation that yields to the following pressure drop presented in [19]:

$$\Delta p_i = \xi \frac{\rho_f}{2} \bar{u}_f^2, \quad (2.5)$$

where ρ_f is the fuel density and \bar{u}_f the mean velocity of the flow. The minor loss coefficient ξ ranges from 0 and upward; 0 meaning that there is no loss and when $\xi = 1$, the pressure drop is equal to the dynamic pressure. Note that the minor loss coefficient can also be greater than 1 for some components.

The minor loss is also called singular head loss, this termination might be more adapted to the orifice of an injector's nozzle. The minor loss can actually be significant there compared to the major loss that refers to the pressure drop due to friction because as explained before, the orifice of an injector's nozzle is generally short.

So the major loss induced by friction Δp_{fric} against the walls in the orifice is dependent on the length of the hole L and is defined by the following expression:

$$\Delta p_{fric} = k_{fric} \frac{L}{D} \frac{\rho_f}{2} \bar{u}_f^2. \quad (2.6)$$

Here, k_{fric} is the friction coefficient that depends on Reynolds number and wall roughness, and D is the orifice diameter. To evaluate the friction coefficient k_{fric} , once again, the regime must be known; however, if the flow is considered fully developed and within the laminar regime, the pipe roughness can then be neglected and the friction coefficient only depends on Reynolds number:

$$k_{fric} = \frac{64}{Re}. \quad (2.7)$$

When the regime is turbulent, the roughness affects the flow and the friction coefficient can then be expressed as the following function:

$$k_{fric} = f(Re, e/D). \quad (2.8)$$

where e/D is the relative roughness with e the absolute roughness and D the orifice diameter. The Colebrooke equation presents an analytical solution of the friction coefficient [9]:

$$\frac{1}{\sqrt{k_{fric}}} = -2 \log \left(\frac{2.51}{Re \sqrt{k_{fric}}} \right) + \frac{e/D}{3.72}. \quad (2.9)$$

Since k_{fric} is on both sides of the equation, it has to be solved by iteration; if Reynolds number, length and diameter of the orifice, roughness, fluid density and mean velocity of the flow in the orifice are known, the pressure drop induced by friction can be calculated. Moody's diagram is a graphical representation of the Colebrooke equation in which the friction coefficient can be found if Reynolds number and pipe roughness are known.

At some conditions, the shape of the orifice can lead the fluid to reach the vapor pressure in the recirculation zone. This phenomenon called cavitation represents the change from liquid to vapor phase of the fluid inside the orifice [20,21]. When the separation of the boundary layer is too sudden, the static pressure can go down to the critical vapor pressure of the fluid and gas bubbles are produced that maybe dragged through the orifice till the exit.

The phenomenon of cavitation is quite common in Diesel injector orifices as the pressure differences used presently are relatively higher. To control this effect, the shape of the orifice has been purposely designed to prevent the apparition of cavitation; whether it is harmful or not, cavitation is not desirable in fuel injection nozzles. To do so, convergent orifices and larger entrance radius have been manufactured as a response to the constantly increase in injection pressures. Such a shape also proved to keep the orifice cleaner due to a better internal dragging; however, they started to be widely used only a few years ago [12,22].

One of the first study that commented the apparition of cavitation in an orifice has been presented by Bergwerk [10]. In this work, small transparent orifices have been used to observe the apparition of cavitation under certain conditions. Since then, a lot of studies have been performed to experimentally visualize cavitation in the aim of analyzing which parameters were controlling its apparition and characteristics.

The apparition of cavitation produces a fundamental change of the flow characteristics in the orifice; the main consequence being indisputably the discharge loss that the orifice suffers when the flow is cavitating. The fact that part of the fluid has been vaporized in the orifice makes the mean density smaller and leads to a decrease of the mass flow rate. This aspect has also been observed by Bergwerk [10] and means that cavitation is always associated with a reduction of the mass flow rate.

This decrease of the mass flow rate has a direct effect on the discharge coefficient, which is one of the most used parameters to characterize the flow through the orifice of an injector's nozzle. It is defined as the ratio of the real

mass flow and the maximum theoretical value of the flow at these conditions. The theoretical mass flow is calculated by Bernoulli's equation assuming that the orifice does not suffer from pressure losses and that the flow velocity before the studied orifice is negligible:

$$\frac{p_{inj}}{\rho_f} = \frac{p_b}{\rho_f} + \frac{1}{2} u_B^2 . \quad (2.10)$$

p_{inj} and p_b are the injection and discharge pressure respectively. Simplifying the pressure drop as $\Delta p = p_{inj} - p_b$, the maximum theoretical velocity of Bernoulli after combination is expressed as:

$$u_B = \sqrt{\frac{2 \Delta p}{\rho_f}} . \quad (2.11)$$

Now, assuming that the flow is driven all the way through the orifice and that all the geometrical area of the outlet A_o is used by the fluid, the theoretical mass flow rate would be given by the following expression:

$$\dot{m}_{theo} = A_o \rho_f u_B . \quad (2.12)$$

And finally, the discharge coefficient can be written as:

$$C_d = \frac{\dot{m}}{\dot{m}_{theo}} = \frac{\dot{m}}{A_o \rho_f u_B} = \frac{\dot{m}}{A_o \sqrt{2 \rho_f \Delta p}} . \quad (2.13)$$

A simple one dimensional model can be used to extract the calculation of the mass flow rate when the orifice is cavitating. Nurick [21] developed an interesting model through testing transparent scaled orifices in which several phenomena coming from cavitation can be explained. The parameters used in this model are represented in figure 2.8 together with a schematic view of the cavitation in an orifice.

In this sketch, i is one point upstream, where the conditions are steady enough to consider the velocity of the flow negligible. Point c corresponds to the exact location where the *Vena Contracta* has the smallest sectional area. Finally, b is a point at the outlet of the orifice. On this figure, the cavitation (or fuel vapor phase) is observed close to the entrance and sticks to the wall again, the rest being the liquid fluid flowing toward the exit. With this model, the difference between a cavitating flow or not are more obvious and the process can be better understood.

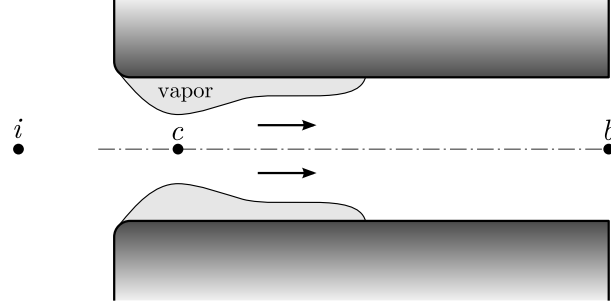


Figure 2.8: Comprehensive scheme of Nurick's model for cavitation [21].
General parameter definition.

Under cavitating conditions, the mass flow rate at the outlet of an orifice would be:

$$\dot{m} = A_c \rho_f u_c, \quad (2.14)$$

where A_c and u_c are the sectional area and velocity at location c on figure 2.8 respectively. A_c can also be written as a function of A_o by the implementation of an area contraction coefficient C_a such as $A_c = C_a A_o$. Its value depends on the geometry of the entrance of the orifice and may vary from 0.61 to 1, where the lowest value is observed for sharp edges [23]. Note that the contraction coefficient can also be used for non-cavitating orifices if the edges are sharp.

On the other hand, it can be assumed that the pressure loss between the inlet of the orifice and the chamber is negligible because of the vapor layer against the wall that makes the efforts lower. Besides, both liquid and vapor are present in section c which allows assuming that the pressure at this location is the vapor pressure p_{vap} . These hypotheses lead to another formulation of the Bernoulli's equation between points i and c :

$$p_i = p_{vap} + \frac{1}{2} \rho_f u_c^2. \quad (2.15)$$

After combination of last two equations (2.14 and 2.15), the following expression of the mass flow rate is obtained:

$$\dot{m} = A_o C_a \sqrt{2 \rho_f (p_i - p_{vap})}. \quad (2.16)$$

The mass flow rate under cavitating conditions is independent of the pressure downstream (discharge pressure p_b), but only depends on the injection

and vapor pressures. This means that when the flow is cavitating, the orifice is collapsed and the mass flow rate does not increase anymore when the discharge pressure goes down. Soteriou et al. [24] verified this experimentally, either with scaled nozzles or real sized orifices. The mass flow rate as a function of pressure drop is given in figure 2.9, it can be observed that when the p_b goes down, the mass flow rate does not increase as the orifice is collapsed. This plot indicates that the flow is not increasing anymore, no matter the pressure drop. This is a typical behavior of cavitating orifices, from these results, it can be concluded that there is contraction of the mass flow because of the cylindrical geometry of the orifice.

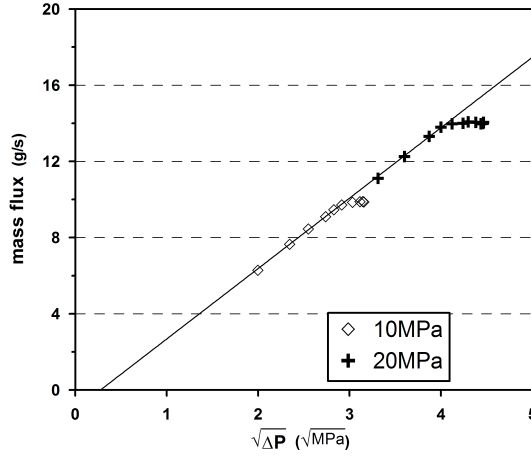


Figure 2.9: Collapsing of the mass flow at the outlet of a cylindrical orifice (source Gimeno [8]).

Another parameter comes from the last expression (2.16), the discharge coefficient can be calculated if the area contraction coefficient is known:

$$C_d = C_a \sqrt{\frac{p_i - p_{vap}}{p_i - p_b}} . \quad (2.17)$$

The quotient under the square root in this equation is the cavitation number. Introduced by Nurick [21], it gives an indication of the cavitation level of the flow in the orifice:

$$K = \frac{p_i - p_{vap}}{p_i - p_b} . \quad (2.18)$$

The cavitation number controls the characteristics of the flow whereas they are more controlled by the Reynolds number when the flow is not cavitating. This non-dimensional parameter conceptually compare the convective forces as an indicator of the cavitation, with an inhibitor effect: the difference between discharge and vapor pressure. This last statement signifies that an increment of the injection pressure will increase the level of cavitation while an increment of the back pressure will inhibit it. As defined, a low value of K indicates a high level of cavitation. The beginning of the cavitation can be defined then as the critical cavitation number: K_{crit} . This means that when K is going down, the probability of cavitation of the flow is higher; consequently, for K lower than K_{crit} , the flow will be cavitating. Several studies carried out on the critical cavitation number found that it was mainly dependent on orifice geometry (entrance radius, convergence or diameter of the orifice [25]), but also on the injection pressure [26–28].

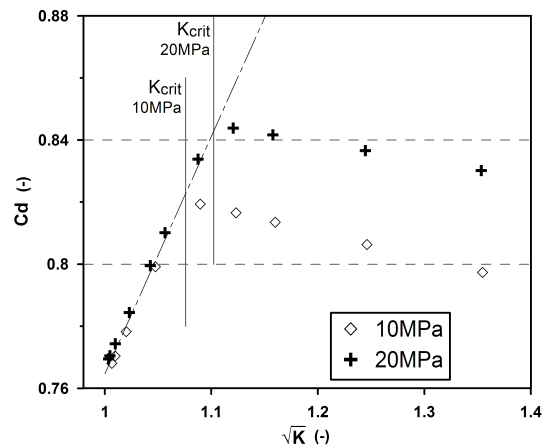


Figure 2.10: Evolution of the discharge coefficient C_d as a function the cavitation number in a cylindrical orifice (source Gimeno [8]).

Figure 2.10 represents the discharge coefficient according to the cavitation number (same nozzle as used in fig. 2.9). The critical cavitation number K_{crit} is depicted on this graph, it can be seen that when the flow is cavitating, the results match the predictions of Nurick’s model.

2.3.4 Influence of nozzle geometry on the internal flow

The internal geometry of the nozzle has a fundamental effect on the characteristics of the flow in the orifice. There are different aspects of the internal

nozzle shape that can affect the flow and their influence may change depending on the conditions of the injection process. The geometrical parameters that influence the internal liquid flow are described qualitatively together with the resulting effects of the different internal shapes.

Length - Diameter relation

A distinction has to be made on the effects of the length - diameter relation depending if the flow is cavitating or not. If the flow is not within the cavitation regime, an increase of the L/D ratio will induce higher losses due to friction against the walls. This will obviously affect the discharge coefficient (C_d), Lichtarowitz et al. [29] made a compilation of the results published by several researchers who studied the flow under non-cavitating conditions. These works found that the maximum discharge coefficient obtained at high Reynolds number, was decreasing as the L/D ratio was increasing. Note that the authors also pointed out that for L/D values below 2, the discharge coefficient is lower because the separation of the flow makes the effective area smaller.

First thing to say about the apparition of cavitation is that a higher L/D ratio leads to lower values of K_{crit} ; the consequence is a shifting in the apparition of cavitation to lower cavitation number K , making its apparition more difficult. In fact, a higher head loss due to the increase of the L/D produces that for similar discharge pressure and mass flow, the pressure at the entrance is higher, thus leading to a lower probability of reaching the vapor pressure. This effect is schematically depicted in figure 2.11 presented by Ramamurthi and Nandakumar [30] to justify this phenomenon.

Convergence of the orifice

The convergence of the orifice is the relation between both inlet and outlet sectional areas. When the orifice is convergent, this means that its inlet diameter is larger than that of the outlet. For this reason, the mean velocity of the flow at the entrance section u_i will be lower than the outlet mean velocity u_o for such an orifice. The relationship between convergence, velocity and diameter can be expressed as:

$$\frac{u_i}{u_o} = \frac{A_o}{A_i} = \left(\frac{D_o}{D_i} \right)^2 . \quad (2.19)$$

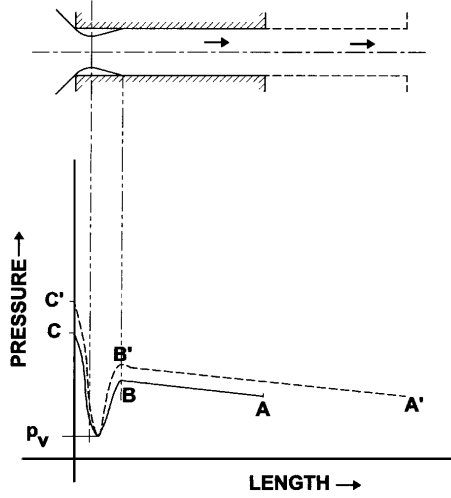


Figure 2.11: Evolution of the static pressure along an injection orifice for two L/D ratios. The prime symbol designates a higher L/D ratio (source Ramamurthi and Nandakumar [30]).

In this equation, density, pressure and velocity are considered to be uniform in both entrance and exit sections of the orifice. By applying Bernoulli's equation between entrance and exit of the nozzle, the following equivalence is obtained:

$$p_i + \frac{1}{2} \rho_f u_e^2 = p_o + \frac{1}{2} \rho_f u_o^2, \quad (2.20)$$

where p_i and p_o are the inlet and outlet pressure respectively. A combination of this expression (eq. 2.20) with the previous equation (2.19) and substituting u_o , the following expression is obtained:

$$\frac{p_i - p_o}{1/2 \rho_f u_o^2} = 1 - \left(\frac{A_o}{A_i} \right)^2 = 1 - \left(\frac{D_o}{D_i} \right)^2. \quad (2.21)$$

As demonstrated in this last equation, a higher convergence (higher D_i/D_o) induces a higher increment of the static pressure at the orifice entrance. This leads to several consequences: first, higher pressure at the entrance shifts the apparition of cavitation as seen before, due to a lower K_{crit} . Secondly, a higher pressure in the entrance section means a lower pressure difference with the pressure upstream and thus, a diminution of the minor head loss at the entrance. Finally, the result of these two consequences has a direct effect on

the injected mass. If the pressure loss is lower through the orifice, the mass flow rate is higher and in the same way, the discharge coefficient as well.

For these reasons and to better control the injection, almost all the nozzles implemented nowadays in Diesel engines use convergent nozzles, some shapes are even able to cancel the cavitation phenomenon for all operating conditions [31, 32].

Entrance radius

The main cause of the head loss at the orifice entrance has been detailed previously in this section as a separation of the boundary layer produced by high velocities and sudden change of the direction of the flow. One solution to decrease this separation is to increase the curvature of the radius of the edges at the entrance. This has the following effect which is to reduce the sudden change of the fluid flow and therefore the head loss engendered in this area is going down and could be considered as negligible for $r_e/D_i \geq 0.2$ [19].

This reduction of the pressure losses leads to higher values of the discharge coefficient but also to a diminution of the apparition of cavitation [19]. This can be explained by a higher pressure at the entrance due to smaller separation of the boundary layer and thus larger section area for higher r_e/D_i ratio.

The work published by Gimeno [8] treats the different aspects of the geometry as well as their influence on the flow at the outlet of the orifice. The reader may be interested in this thesis to find additional information concerning internal flow behavior.

2.4 Formation of Diesel sprays

After a review of the characteristics of the internal flow inside the orifice of an injector's nozzle and the properties of the flow at the outlet, this section presents the main aspects known at present about Diesel sprays. The structure of the sprays and the different parameters that influence them are detailed now as all this represents the main purpose of this work. The atomization regimes are described together with their parametric characteristics and the effects on droplet formation. Finally, special attention is paid to the parameters used, from an experimental point of view, for the characterization of sprays injected in Diesel engines. This part presents two different approaches to analyze sprays: the macroscopic point of view for the basic geometrical aspects

of the spray and the microscopic one which is more dedicated to analyzing the internal and dense region of the spray when possible.

2.4.1 General properties of sprays

Sprays are known to be complex fluid mechanical structures born from the disintegration of a liquid flow into numerous droplets. This flow interacts with the ambient gases and the aerodynamic forces induced by the inter-facial frictions between liquid and gas produce liquid structures to be extracted from the liquid core. Depending on both the liquid and surrounding gas conditions, several disintegration regimes can be identified [33]. These regimes will be detailed in the next coming section focusing on the last regime: the atomization, which mainly corresponds to DI Diesel engines sprays.

Spray structure

Directly injected Diesel sprays aim is to achieve the best atomization, that is why the following description will support spray structure under atomization regime and continuous reference will be made toward Diesel injection. As it has been seen for the internal flow, a lot of parameters are involved in the process of spray formation as well. The injected liquid core is mainly affected by the same properties that control the internal liquid flow; the surrounding gas will also play a major role in spray behavior. The effects of the surrounding medium will be studied and evaluated throughout this section as several parameters have to be used to characterize its influence.

The structure of a spray under the atomization regime is sketched in figure 2.12, where macroscopic parameters and microscopic properties can be identified.

A global point of view provides information about the spreading angle of both the near nozzle field and the more dilute region. Looking at the spray in detail, several fluid mechanical zones can be identified [33, 34]:

- The liquid core is an extension of the internal liquid flow not yet perturbed that remains compact and intact for a short distance in the discharge chamber.
- The multi-phase mixing layers refer to relatively large liquid structures generated by the primary disintegration of the boundaries of the liquid core.

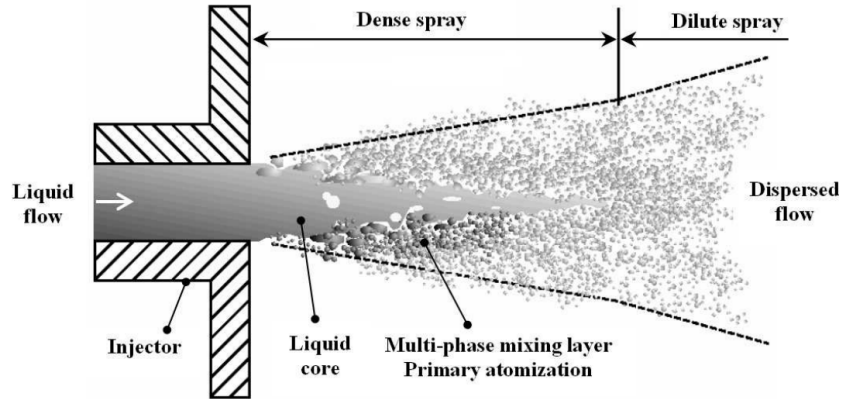


Figure 2.12: Illustration of the structure of the spray in the atomization regime (source [34]).

- The dispersed flow is the largest part of an atomizing spray where small and round droplets are formed.
- The vaporization zone downstream, whose location mainly depends upon temperature. Note that the evaporation process actually starts once the spray is injected in the high temperature chamber.

Under non-evaporative conditions, the complete process of atomization is that an incoming liquid flow exits from the exit and is subject to perturbations driving the spray to disintegrate into numerous small droplets. The disintegration of a liquid body into structures due to contacts between gas and liquid generating interfacial instabilities is known as the primary breakup. This first step of the disintegration process only occurs in the dense region of the spray where the disturbances are periodic [35] and lead to break the liquid core into smaller but geometrically irregular structures. The second breakup is the disintegration of these structures into small round droplets mainly due to a balance between aerodynamic forces and surface tensions.

The characterization of the dilute spray is obviously easier than that of the denser part, near the nozzle outlet. The irregular structures present in the near nozzle field make the measurements difficult and that is why there is a lack of information in this region. The complexity of the disintegration processes in the dense core can be schemed by the fact that there is not a fixed terminology to describe the biphasic flow or ligaments until they are droplets. A lot of studies have been done to analyze the dilute region of the spray which is generally situated from 200 to 500 outlet diameters at normal temperature

and pressure according to [6]. A specific study showed that for Diesel sprays, the average breakup length was comprised between 10 and 30 mm for spray velocities of around 200 m/s. Downstream along the axis, the spray is becoming more and more dilute and the volume fraction is decreasing as the distance between droplets is increasing. The liquid volume fraction is an important parameter as it gives the air/fuel ratio in the spray. It mainly depends on position, either axially or radially and starts from 1 in the liquid core to go below 0.1 at the edges of the spray and shall be 0 in the ambient [34].

When the droplets are small and dispersed and traveling into the surrounding gas, they will evaporate due to contact with the airflow. The temperature of the ambient gases is the main parameter that affects the rate of evaporation; nonetheless, the size of the droplets and the relative velocity also have to be taken into account. All the parameters described before have their importance on the evaporation rate of the droplets, some other parameters like fluid properties will be detailed in the forthcoming paragraphs.

Properties affecting spray behavior

Whether it is injected under high temperature conditions or not, the final structure of the spray is the result of the combination of a large amount of parameters. From the characteristics of the internal flow to the properties of the surrounding gases, every parameter plays a role in the development, atomization and evaporation of the spray. This section gives a summary of the numerous physical and chemical characteristics that influence the formation of a spray.

As seen previously, the internal flow is influenced by fluid properties, the injected flow will be also affected but additional effects are observed. The most representative fluid characteristics that play a role in the generation of sprays are density, viscosity and surface tension. It has to be said that these characteristics are strongly affected by temperature and under evaporative conditions for example, they would be really different.

Fluid density is the first parameter to come in mind, it is easy to measure and its effect is easily understandable. A denser fluid transports more mass, but the injected flow has a lower velocity as well and this should lower the disintegration rate. It has been reported that denser fluids generally disintegrate less due to the formation of bigger ligaments that present higher resistance to segregation [36]. The relative lower velocity is also an important parameter and recent studies made with biodiesels confirm this trend [37].

The viscosity presents the quantity of the resistance for a liquid to flow and a higher viscosity means a higher resistance. Its influence on sprays lies on flow rate, geometrical shape of the spray and droplet size. A lower flow rate when the viscosity increases leads to hamper the development of the liquid core. The disintegration process is then delayed and larger droplets are present in the dilute region. From a macroscopic point of view, higher viscosity means narrower sprays [37]. Note that it has been observed that denser fluids generally have higher viscosity and it is not always straightforward to conclude about one of these fluid characteristics.

Despite the fact that there are no real studies dedicated to the analysis of the surface tension influence on spray developments, it is certainly the most important parameters when the spray is being disintegrated. The surface tension is the property of a liquid to keep its molecules together at an interface, in this context, between air and fuel. Higher surface tension generally leads to larger droplets because the fluid has a better capability of countering the aerodynamic, centrifugal and pressure forces.

The velocity and in a similar way the level of turbulence of the flow studied earlier directly affects the spray structure and its disintegration. A high speed flow entrains a large amount of gas during spray penetration due to the transfer of momentum [38]. The velocity could come from the outlet flow but also from the gas in the chamber, in the end, the relative velocity is the characteristic parameter of importance. The turbulence also influences the disintegration of the spray due to a higher level of disturbance. Care must be taken when talking about turbulence in such orifices, as seen earlier, all theoretical studies regarding the turbulence of the flow are really risky.

The surrounding gas must also be taken into considerations as it presents physical properties that affect the development and mixing of the spray. The density of the ambient gases is the most important factor of influence from both a macroscopic point of view or a microscopic one. The interaction of the fluid and the gas at relatively high opposite velocity generates a kind of fluid hammer which is responsible of the disintegration, a higher density means a more intense fluid hammer and thus smaller droplets. At the same time, the axial velocity is reduced by a higher density and therefore, the radial one has a stronger effect, this leads to get wider sprays.

The temperature is essential to characterize the structure of the spray as it influences the fluid mechanical properties of the injected liquid. In addition to the effect on fluid properties, it controls dramatically all the chemical processes potentially happening in such event. For example, under high temperature, the

rate of evaporation is higher and the vaporization of the droplets starts from the first exit of the orifice. This makes hard the comparison of sprays under evaporative conditions or not as the disintegration processes are dramatically different and in most cases, the droplets would be fully vaporized even before the end of respective atomization. However, due to strong changes in physical and chemical properties of both fluids, any conclusion is then complicated. This aspect is discussed later in this thesis (Chapter 6).

Spray physical parameters

It is commonly accepted that the behavior of the spray breakup processes is the relative importance of fluid inertia compared to its surface tension. To analyze fluid flows in which there is an interface between two fluids (e.g. liquid and gas), a dimensionless number is often used: the Weber number, defined as:

$$We = \frac{\rho_f u^2 l}{\gamma_f} . \quad (2.22)$$

In this expression, which is useful to analyze droplet formation, ρ_f is the density of the fluid (liquid), u is the relative velocity of the flow, l the characteristic length of the liquid structure, in this case the diameter of the droplets. Finally, γ_f is the surface tension between the fluid and the medium, here Diesel fuel in air. The Weber number in its common form is principally used to classify the disintegration regimes as well as the breakup regimes of a single droplet in a smaller scale. It is also utilized as the determination coefficient of a droplet to breakup via the definition of a critical Weber number that gives a threshold value where above it, the droplet is supposed to breakup whereas for lower values, it should remain stable in the flow.

Another dimensionless parameter is also important to define sprays; the Ohnesorge number (Oh [39]) relates the viscous forces to inertial and surface tension forces, it is defined as follows:

$$Oh = \frac{\mu_f}{\sqrt{\rho_f \gamma_f l}} = \frac{\sqrt{We}}{Re} . \quad (2.23)$$

Defined earlier in this section, μ_f is the dynamic viscosity of the fluid. A higher Ohnesorge number means a greater influence of the viscosity, and this leads to the conclusion that an increase of the inertial forces is necessary for breakup to occur. From these two physical parameters (Weber and Ohnesorge numbers),

semi-empirical correlations can be built to get the spreading angle of the spray, liquid breakup length, average droplet diameter and number density for a given spray. After further development and adjustment of these correlations, they can be used for spray modeling by introducing some more parameters like orifice geometry or discharge density.

The internal flow is highly responsible of the behavior of the spray and breakup processes, nozzle geometry will be one of the main parameter that controls the injection process. However, the physical properties included in the dimensionless parameters described above also influence the spray and breakup due to the interaction with the ambient gases. The disintegration process of a spray and the breakup of droplets are influenced by numerous parameters that will affect the development of the spray in different ways.

2.4.2 Disintegration process and droplet formation

Disintegration of the spray is a complex process in which all the characteristics and parameters, either geometric or physical, will affect the whole development at different scales. A spray comes from the injection of a fluid into a medium (generally fluid as well), the disintegration is the result of the injection and is controlled by the balance between two groups of forces: consolidating and disruptive. On one side, the consolidating forces, represented mainly by viscosity and surface tension, will make the molecules of a droplet to remain together. On the other side, the aerodynamic forces will make the droplet to vibrate resulting in a separation or breakup of a large droplet into smaller ones. To this group, the centrifugal forces and the initial turbulence could be added as disruptive forces.

Disintegration regimes

As quickly introduced in the previous section, the disintegration process of a spray can be classified in four different regimes [33,39]: The Rayleigh regime, the first and second wind-induced regimes and finally the atomization regime reached at high injection velocities. It is common to use the Weber number as a specific parameter to classify the flow among these regimes; Table 2.1 gives a summary of the characteristics of the four disintegration regimes:

The first regime, known as Rayleigh regime occurs at really low injection speeds while the aerodynamic forces are considered insignificant. The breakup during this regime appears due to axi-symmetric surface waves formed by the

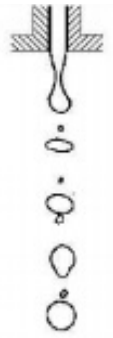
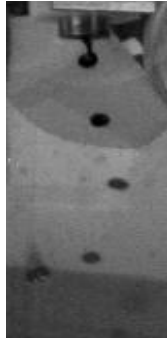



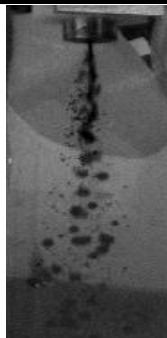

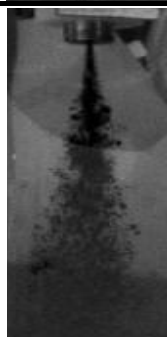
Breakup regimes	Intensity range (We number)	Dominant breakup property	Illustration	Sample picture
Rayleigh	$We < 0.4$	<ul style="list-style-type: none"> • Surface tension force • Capillary waves 		
first wind-induced	$0.4 < We < 40$	<ul style="list-style-type: none"> • Surface tension force • Dynamic pressure of ambient air 		
Second wind-induced	$40 < We < 100$	<ul style="list-style-type: none"> • Dynamic pressure of ambient air opposed by surface tension force initially 		
Atomization	$We > 100$	<ul style="list-style-type: none"> • Aerodynamic and shear forces • Turbulence • Expansion • Surface tension force initially 		

Table 2.1: General characteristics of the disintegration regimes (source [33]).

interaction of primary disturbances in the liquid core and surface tension. The period Λ of these disturbances could be an indicator of the breakup: When Λ is small, the forces generated by the surface tension tend to damp out the oscillations whereas they will increase when Λ gets higher, also due to surface tension. The consequence is that these deformations will increase until the liquid core breaks-up and will result in droplets with quite similar diameters.

When the velocity of the spray is higher, the period of the disturbances Λ increases and makes the amplitude of the disturbances to get higher as well. The aerodynamic forces are no longer negligible and this corresponds to the first wind-induced breakup regime. The particularity of this regime is that the droplets produced during breakup are of the same size as the spray diameter and breakup generally occurs at a distance of several hole diameter downstream from the exit.

At higher injection speeds, the aerodynamic forces are the main responsible for surface waves of short wavelength (or period Λ) and their amplitude is growing with the turbulences produced at the orifice exit. This regime, called the second wind-induced breakup regime is as its name indicated, an extension of the previous one and occurs closer but still at several hole diameter after the exit. The breakup distance is function of the injection velocity and decreases while injection speed increases. During this process, the aerodynamic forces makes the perturbations of the liquid flow higher until breakup and produce small droplets with a diameter of about the period of the surface waves.

The last step of disintegration is reached at high injection pressures, the atomization regime is characterized by a breakup which occurs every time closer to the nozzle exit. At its highest level, the disintegration can start directly at the orifice exit due to the high velocity and turbulence of the flow or other effects like cavitation or flash boiling generated in the orifice and also right at the exit.

Because of the high injection pressures used in Diesel engines, the operative conditions are generally leading to this disintegration regime, which has not been fully explained due to the difficulty of the analysis in and close to the orifice.

The aerodynamic instabilities are certainly the most important factor that affects breakup in the atomization regime. The liquid core suffers from relatively high frequency deformations leading to the separation of ligaments or structure from the non-perturbed liquid flow. This reduction of size of the liquid core makes it to get closer to the orifice exit while the disruptive forces,

embodied by the turbulences, increase. Several studies can be found in the literature to predict the breakup process [40, 41]; some, based on Taylor's linear analysis [42–44] work quite well at relatively low injection speeds, close to the second wind-induced breakup regime. However, other important parameters influence this phenomenon when the injected flow goes too fast and make the analysis not exhaustive enough to get accurate predictions.

One of these parameters is the turbulence of the flow generated in the orifice. The radial component of the flow velocity makes the liquid to be extracted from the liquid core after exiting the conduct where the flow was guided by the walls. This aspect of the turbulence inside the orifice has been studied by Ruiz [45] and explains part of the atomization process but the effect of the discharge density showed that it cannot be the only important parameter.

The cavitation also influences disintegration of the spray and its effect can be explained from two points of view: first, it could increase the turbulence, which in its turn increases the atomization. Secondly, the cavitation generates gas bubbles that can go all through the orifice to the exit making the flow biphasic [21, 24, 25, 27, 32]. The discontinuities in the liquid flow make the separation of the structures easier, due to a reduced action of the surface tension, and thus the level of atomization is higher.

The last mechanism that can potentially atomizes the liquid core at the exit is the modification of the velocity profiles at this location [8]. The fluid friction along the orifice suddenly disappear, together with the viscous forces. The consequence is an acceleration of the external layer of the liquid flow producing instabilities and increasing turbulences. This has been explained by Ruiz [45] who observed that a modification of the velocity profiles at the exit increased the radial component and therefore make the atomization level higher.

Under higher discharge temperature, the disintegration process is globally accelerated due to several parameters such as decrease of the fluid-mechanic property values (e.g. viscosity, surface tension or density) but also because of immediate flash boiling atomization. It has been observed that the effect of temperature on spray breakup process was higher at elevated value of injection pressure due to the faster evaporation of smaller droplets [46].

Formation of droplets

After the first process of the disintegration that breaks up the liquid core into liquid structures, a second stage is the breakup of droplets into smaller round ones. This secondary breakup occurs while droplets are traveling at relatively high speed into the discharge volume thus suffering from deformation due to gas density, in other terms aerodynamic forces. These smaller droplets favor the evaporation rate as they are of smaller size and it is said that this secondary breakup controls the mixing rate of the dilute spray in the evaporation zone [47]. The droplet breakup process is generally influenced by several parameters, like the first breakup is, which are:

- Droplet size.
- Droplet-gas relative velocity.
- Liquid and gas densities.
- Fluid viscosity.
- Surface tension.

Depending on the values of these parameters, their influence permits to classify the disintegration of a droplet into five breakup regimes, widely related to the Weber number also. The first regime is called deformation or fluttering, it is generally observed for Weber number below 12. Between 12 and 80, the droplet is disintegrated according to the bag breakup process. At values of We around 80, a boundary breakup process occurs, also called shear breakup, the extremity of the bag created by the aerodynamic forces are disintegrated into small droplets. For values from 80 to 800, the breakup is called stripping, the droplet is broken into several smaller and this gives consequence to the catastrophic breakup for values of We above 800. Table 2.2 provides a quick summary of the different breakup regimes recompiled by Pilch and Erdman [48]. The breakup of a droplet is a complex process as well that can be divided into up to twelve steps [49], however, the simplification presented by Lee and Reitz [50] is usually preferred and is composed by two stages only.

The first stage is a change in shape from an original round form to a thin disk due to the action of the gas density on the front side of the droplet. The second stage is a result of the aerodynamic forces as the droplet is deformed and fluttered; it brakes up depending on the conditions and according to the different regimes described above. In Diesel sprays, the high injection pressures lead to Weber number higher than 100 and even values above 800 are presently reached with the last generation injection systems. In such conditions, the process of breakup of droplets corresponds to stripping and catastrophic regimes.

Deformation or breakup regimes	Intensity range (We)	Illustration
Deformation and flattening	$We < 10$	
Bag breakup	$10 < We < 80$	
Boundary or shear breakup	$80 < We < 100$	
Stripping breakup	$100 < We < 350$	
Catastrophic breakup	$We > 350$	

Table 2.2: Breakup regimes of a single droplet. Recompilation proposed by Pilch and Erdman [48].

During the stripping breakup process, the droplet is deformed and oscillates because of strong aerodynamic forces, density gradient and surface tensions. The growth of these oscillations makes the droplet to disintegrate into an extensive system of liquid ligaments, protruding from the periphery. Numerous small and round droplets are then formed at the end of these ligaments in the near downstream whose sizes mainly depend on viscosity rather than surface tension [51]. The next level of disintegration is the catastrophic breakup and shares some similarities with the stripping breakup process. The frequency of the oscillations increases on the droplet surface due to interaction with the ambient and their amplitude is growing with the global deformation of the droplet. This combination of deformations is responsible for shattering the drop into a cloud of liquid fragments that further disintegrate into a mist of small round droplets [52].

2.5 Characteristics of Diesel sprays

Diesel sprays have been a topic of great interest for the last forty years now. On the other hand, the progresses made in technologies aiming to improve the injection process to make the engines cleaner and/or more efficient also made the spray more and more complicated to study. To perform a complete study of the spray, a large amount of parameters are required. The macroscopic parameters are no longer providing enough information and science of combustion needs a deeper analysis of the spray or additional knowledge in the near nozzle-field where the spray is denser. This section will present the different parameters used to characterize the liquid and vaporized spray distinguishing macroscopic and microscopic approaches.

First, from a macroscopic point of view, the information used to characterize a spray are basically reduced to its geometrical characteristics. These parameters are still widely used and present paramount information for engine designers, either under evaporative conditions or not.

2.5.1 Spray tip penetration

The penetration of sprays versus time or crank angle is one of the most obvious and used parameters to determine its characteristics. It is conceptually defined as the distance between the orifice exit and the head of the spray. As seen before, the spray is injected in the discharge chamber, in this case the combustion chamber and will disintegrate and mix with the ambient gases. A

quick estimation of the air/fuel mixing can be extracted from the penetration before and after evaporation.

The fundamental parameters that affect the spray tip penetration are spray momentum at the outlet and spreading angle as confirmed by the numerous studies found in the literature [53,54]. Spray momentum is commonly assimilated as the force or energy of the spray delivered at the exit of the orifice and is conserved along penetration. So the parameters that influence the flow at the outlet automatically affect the penetration of the spray. The density of the ambient gases is one of the most preponderant parameters as the spray has to develop into the chamber. The theoretical spray tip penetration obeys the following proportionality when the Buckingham π theorem [55] is applied [56]:

$$s(t) = k_s \rho_g^{-1/4} \dot{M}_o^{-1/4} t^{1/2} \tan^{-1/2} \left(\frac{\theta}{2} \right), \quad (2.24)$$

k_s is a constant that depends on spray internal distribution. Not included in the momentum, some authors found that for $k_s = 1.29$ [56], the penetration was correctly estimated for a wide range of Diesel sprays. ρ_g is the gas density, \dot{M}_o is the momentum flux of the spray, t is the time since start of injection (Time ASOI) and θ is the spreading angle of the spray.

This last expression showed its accuracy but a measure of the momentum flux is required. Some correlations have been presented that include other parameters to predict spray penetration like the one presented by Wakuri in equation 2.25 [57].

$$s(t) = \frac{(2 C_d^3)^{1/4}}{\tan^{1/2}(\frac{\theta}{2})} \rho_g^{-1/4} \Delta p^{-1/4} D_o^{1/2} t^{1/2} \quad (2.25)$$

In this correlation, C_d is the discharge coefficient defined earlier, Δp is the pressure difference between ambient gases and injected fluid, and D_o is the nominal orifice diameter.

Lately, a closer analysis showed that the penetration was affected by other parameters in the near-nozzle field where the atomization is not complete and has led to a 2 stages model [58]. More recently, Naber and Siebers [59] found a similar behavior and built another correlation which takes into account the characteristic parameters of the flow like velocity and area coefficients (respectively C_v and C_a , see sec. 3.3.3 for more information). The following expression can therefore be extrapolated to a wide range of conditions:

For $t < t_b$:

$$s(t) = C_v \sqrt{\frac{2 \Delta p}{\rho_f}} t . \quad (2.26)$$

and for $t \geq t_b$:

$$s(t) = \frac{C_v^{1/2} (2 C_a)^{1/4}}{a_s \tan^{1/2}(\frac{\theta}{2})} \rho_g^{-1/4} \Delta p^{-1/4} D_o^{1/2} t^{1/2} . \quad (2.27)$$

Here t_b is the breakup time or the time when the spray is fully atomized and is expressed as:

$$t_b = \frac{(2 C_a)^{1/2}}{C_v a_s \tan^{1/2}(\frac{\theta}{2})} \frac{\rho_f D_o}{(\rho_g \Delta p)^{1/2}} . \quad (2.28)$$

Note the introduction of an arbitrary constant a_s for the correlation proposed by Naber and Siebers [59], they found that a value of 0.66 provided successful penetration predictions.

A quick analysis of this correlation shows that within the breakup time, the penetration is linear with the time and that neither ρ_g nor D_o affect the development of the spray. However, when the spray is considered to be fully atomized, the penetration becomes proportional to the square root of the time; an increase of ρ_g leads to a slower development, some more parameters like those seen in the previous correlation presented also affect the spray penetration.

A different behavior in the first part of the spray tip penetration has been observed by several researchers, nevertheless, the explanations differ slightly. As said before, Hiroyasu and Arai [58] justified this by the fact that the spray is not atomized yet and still has a cylindrical shape making its velocity constant during the first instants. Naber and Siebers [59] argued that in the first part, the penetration is more controlled by the injected fluid, although later, the air/fuel mixing process dominates more. Some authors claimed that this difference could come from the increase in the rate of injection in the first instants, which would obviously affect momentum flux and thus spray penetration. This hypothesis has been partially discarded by Naber and Siebers [59] as they experimentally compared rate of injection and penetration and concluded that the transient was relatively short to justify such results.

Under evaporative conditions, the injected fuel is vaporized after a certain amount of time in the discharge chamber. This time, can also be expressed as a penetration distance, called liquid length and is strongly affected by temperature. Some correlations have been reported in the literature and they generally show the dependence of some other parameters like nozzle diameter, ambient density or pressure drop. The following correlation, presented by Payri et. al [60], provides values of liquid length valid for last generation Diesel sprays:

$$LL = k_{LL} D_o^a C_a^b \rho_g^c T_g^d \Delta p^e, \quad (2.29)$$

where k_{LL} is a constant and T_g the temperature of the ambient gases. This correlation is versatile and can be adjusted to fit the experimental data by changing the values of the coefficient a , b , c , d and e . The authors proposed different values for this correlation depending on the shape of the nozzle. The exponents found for better fitting show a great influence of the temperature and as an opposition to the penetration, the effect of the injection pressure (or pressure drop) is almost negligible as reported by several authors [58–60].

For the complete spray under evaporative conditions, first liquid and then gaseous, a reduction of the penetration has been observed and found to be as high as 20 % for low discharge densities. This trend gets lower as the discharge density increases and almost no difference are observed at high back density for a certain time ASOI (After Start Of Injection). The comparison of the evaporative and non-evaporative sprays carried out by Naber and Sieber [59] showed that the difference was maximum where the spray is completely vaporized. Garcia [61] observed similar behavior and their explanation is that the injected fuel is cooling the ambient, thus increasing the density of the gas mixture. The result of this higher density is a slower progression of the newly injected fuel progressing in the chamber and therefore, the velocity of the spray tip penetration is reduced.

2.5.2 Spreading angle of the spray

A really basic representation of the spray could be a cone and a semi-sphere placed in the end in which the cone is considered to be the steady part and the semi-sphere or spray head is generally considered to be more transient. The spreading angle is then formed by the two lines of the edges of the cone and is supposed to be constant when the spray is fully atomized. However, this assumption is not valid during the first part of the spray penetration when the breakup is not complete [62]. This is coherent with the behavior observed

for spray tip penetration, the development of the spray is different within the breakup time for both penetration and spreading angle.

Several expressions of the spreading angle can be found in the literature based on either theoretical or experimental considerations [41,63,64]. A large part shows the influence of both liquid and gas densities, which demonstrates that the phenomenon is controlled by liquid-gas aerodynamic interactions. Some authors observed an influence of the nozzle geometry as well [58,59] but the studies did not quantify this clearly. After all, a general expression of the spreading angle can be built up that finally takes into account gas and liquid densities and injection pressure:

$$\tan\left(\frac{\theta}{2}\right) = k_{sa} \left(\frac{\rho_g}{\rho_f}\right)^a p_i^b, \quad (2.30)$$

where a and b are exponents that have to be found through previous experiments and correlations. The measure of the spreading angle is not as trivial as the penetration could be and care must be taken. Its determination can be affected by numerous parameters such as: the visualization technique used, the intensity and homogeneity of light, the fluctuation of the spray pattern, etc. Another parameter might be of importance also for experimental measurement: the criterion chosen to perform the boundary determination on the images [65]. These factors obviously influence the accuracy of the measured spreading angle and they make the experiment difficult to compare between one test rig and another and thus from different sources.

Under high temperature conditions, the spreading angle of the liquid spray tends to be narrower [66]. However, only a few experimental studies have been performed to quantify this tendency and almost no work have been reported which intended to evaluate the angle of the spray of the vapor-phase.

By getting closer to the spray, some more information can be obtained. The microscopic parameters used to determine the spray are not as easy to analyze as the macroscopic ones. Nevertheless, the support of modeling has been a great help and this explains why the theoretical approaches are numerous and lead to different results.

2.5.3 Droplet size distribution and prediction

The size of the droplets provides good indication on the quality of the atomization process. In the meantime, under evaporative conditions, the size of the

droplets decreases until complete evaporation somewhere around the liquid length location. Due to the spontaneous or catastrophic behavior of the atomization process in Diesel sprays, this mechanism leads to droplets of a large range of diameters. This aspect commonly called polydispersity means that the spray is composed by a droplet size distribution either simple or complex. The droplet size distribution is often represented by a histogram and when this distribution is known it is then possible to plot the Probability Density Function (PDF) for a sample or for the entire spray. In such a case (see fig. 2.13), each bin of the histogram represents the fraction of the total droplet number within the diameter range covered by the bin. Note that the total number of droplets can be plotted instead of the fraction as it provides an indication of the quality of the experimental data, a low droplets number means poor accuracy.

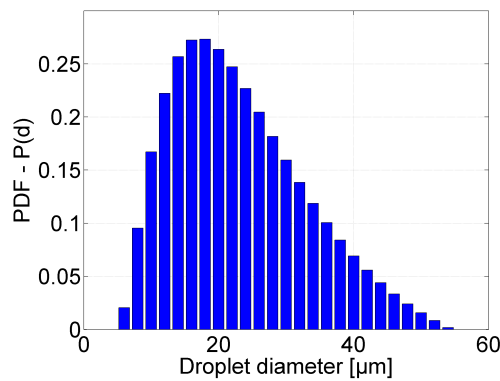


Figure 2.13: Representation of the Probability Density Function (PDF) or droplet size distribution as an histogram.

The distribution of the droplet size in a spray has been studied and several empirical expressions have been developed to match experimental data. The most used regarding Diesel sprays is the log-normal shaped and therefore, the probability for every droplet to have a diameter value (d) is given by:

$$P(d) = \frac{1}{k_{PDF1} \sqrt{2\pi} d} \exp\left(-\frac{(\ln(d) - k_{PDF2})^2}{2 k_{PDF1}^2}\right), \quad (2.31)$$

where k_{PDF1} and k_{PDF2} are the shape and scale parameters respectively. The distribution of droplet size requires a lot of hypotheses and does not provide crucial information except regarding spray non-uniformity.

Nonetheless, one solution to characterize the quality of the atomization is to get the value of mean diameters of the complete droplet distribution. This average droplet size is actually really important as it provides information concerning the upcoming evaporation process. According to Mugele and Evans [67] who initially developed different notations for mean diameters, droplet size can be classified in four different categories depending on which aspect the application is focused on (see tab. 2.3).

Symbols	Dominant factors	Physical meaning	Formulation
d_{10}	Number of length	Average geometrical diameter	$\frac{\sum_{i=1}^{\infty} N_i d_i}{\sum_{i=1}^{\infty} N_i}$
d_{20}	Surface area	Average surface area	$\left(\frac{\sum_{i=1}^{\infty} N_i d_i^2}{\sum_{i=1}^{\infty} N_i} \right)^{1/2}$
d_{30}	Volume	Average volume or mass	$\left(\frac{\sum_{i=1}^{\infty} N_i d_i^3}{\sum_{i=1}^{\infty} N_i} \right)^{1/3}$
d_{32}	Surface - volume (SMD)	Surface - Volume related to mass transfer	$\frac{\sum_{i=1}^{\infty} N_i d_i^3}{\sum_{i=1}^{\infty} N_i d_i^2}$

Table 2.3: The different notations to express mean diameters according to Mugele and Evans [67].

Table 2.3 provides the different notations of mean diameters together with their method of calculation. The most simple one is called the geometrical mean diameter d_{10} (said "d one - zero"), also called arithmetic mean diameter (noted \bar{d}). The surface area mean diameter, d_{20} , the volume mean diameter, d_{30} and , finally the volume surface mean diameter, commonly called Sauter Mean Diameter (SMD) also noted d_{32} .

Hiroyasu engaged a campaign to extensively study the size of the droplets in the spray under non-evaporative conditions [58, 68]. His work provided an expression of the Sauter Mean Diameter valid for a location in the far-field where the disintegration process is considered to be complete (65 mm

downstream) such as [68]:

$$\frac{SMD}{D} = k_{SMD} Re_d^{0.75} We_d^{-0.32} \left(\frac{\mu_f}{\mu_g} \right)^{0.37} \left(\frac{\rho_f}{\rho_g} \right)^{0.47} \quad \text{with } k_{SMD} = 0.38. \quad (2.32)$$

In this equation, D is the nominal orifice diameter, Re_d and We_d are the Reynolds and the Weber number of the droplets in the flow, respectively. μ_f and μ_g are the fuel and gas dynamic viscosities in this order and the densities are noted ρ_f for the fuel and ρ_g for the ambient gases. Some authors found that for short injection times (1 ms), this expression was not suitable to predict SMD [69]. In a specific study to relate the first expression with the injection time [58], Hiroyasu found another formula to predict droplet diameter. In the following expression, he introduced the mass injected up to that specific instant of droplet size calculation (m_q):

$$SMD = k_{SMD} \Delta p^{-0.135} \rho_g^{0.121} m_q^{0.131}, \quad (2.33)$$

Δp being the difference between injection and discharge pressures. This equation might be easier to apply but still requires the rate of injection to expect accurate results. Other correlations are found throughout the literature [70, 71] and they generally used the same parameters such as orifice diameter, injection pressure, gas density, etc.

Care must be taken with these correlations because large variations are obtained on the predictions, certainly due to the weak amount of experimental data used to build the correlation. It is then hazardous to extend an expression to other nozzle shapes or diameters, injected fuels; they maybe used only as a starting point and adjusted to fit well the experimental data under consideration.

2.5.4 Velocity and concentration profiles

In sprays injected in gasoline or Diesel engines, the fuel concentration is one of the most important and studied parameters as it drives mixing with ambient gases and therefore combustion. This aspect provides important information concerning the mixing process and local fuel mass fraction. The velocity is often related to concentration as it has been observed and concluded by Abramovich that, in a gaseous jet, velocity and concentration have similar distribution profiles in any axial cross-section [3]. For liquid fuel sprays, some

works reported the use of a diffusivity parameter to relate velocity and concentration profile in the fully atomized region [4, 72]. This dimensionless parameter, called the Schmidt number (Sc), represents the ratio of spray momentum diffusivity and mass diffusivity of the injected fluid such as:

$$Sc = \frac{\nu_f}{\kappa_D}, \quad (2.34)$$

where ν_f is the kinematic viscosity of the fluid such that: $\mu_f = \nu_f \rho_f$, which refers to the momentum diffusivity and, the mass diffusivity coefficient κ_D theoretically solved thanks to the Fick's laws of diffusion. This coefficient is proportional to the molecular diffusivity in a medium and mainly depends on kinetic energy, droplet diameter and viscosity of the medium. This means that temperature and pressure of both the liquid and the gases affect the mass diffusivity coefficient and thus the Schmidt number.

Due to the chaotic behavior of the atomization process, air entrainment is fundamentally different according to the location in the spray, and so is the fuel concentration. In a certain section of the spray, a relation can be established between velocity and concentration; Spalding proposed the following expression for a gaseous jet, including the Schmidt number [4]:

$$\frac{Y_f}{Y_{f,axis}} = \left(\frac{u_{jet}}{u_{jet,axis}} \right)^{Sc}. \quad (2.35)$$

Y_f and u_{jet} are respectively fuel concentration and jet velocity at a specific location, they are given with respect to the values found on the axis ($Y_{f,axis}$ and $u_{jet,axis}$), the fuel mass fraction Y_f is defined as:

$$Y_f = \frac{m_f}{m_g + m_f}. \quad (2.36)$$

m_f and m_g are the masses of fuel and gas in a control volume respectively. Equation 2.35 could be a starting point for application regarding Diesel sprays, it is generally assumed that both velocity and concentration profiles of a liquid spray are Gaussian-shaped also. Nonetheless, the spreading angle for a given nozzle geometry, strongly depends on discharge density while it is not affected for a gaseous jet [3]. Correas [73] adjusted the mathematical expressions proposed by Hinze [74] to determine the profiles of both velocity and

concentration for a liquid spray:

$$\frac{Y_f}{Y_{f,axis}} = \exp\left(-Sc C_{R1} \left(\frac{r}{R}\right)^2\right) \text{ and } \frac{u_{jet}}{u_{jet,axis}} = \exp\left(-C_{R1} \left(\frac{r}{R}\right)^2\right), \quad (2.37)$$

where C_{R1} is a coefficient that defines the percentage of the velocity or concentration on-axis in order to define the angle of the spray. It basically represents the shape of the Gaussian profile and good agreement with isothermal liquid sprays have been found for $C_{R1} = 4.6$ [73]. The ratio r/R is the normalized radial position from the axis to the boundary of the spray where the value of the ratio is 1. Note that the nomenclature is not modified for consistency, as these expressions are based on gas-jet mixing, the term "jet" also refers to liquid sprays. For vaporized jets, the most commonly used definition has been proposed by Abramovich [3] and is described in equation 2.38.

$$\frac{\bar{\chi}_f}{\bar{\chi}_{f,c}} = (1 - \xi^{C_{R2}})^2, \quad (2.38)$$

where $\bar{\chi}_f$ is the turbulent mean volume fraction, the subscript *axis* denotes that the value is on the centerline of the jet. $\xi = r/R$ is the relative radial position where r is the actual position and R half the jet width such as: $R = x \tan(\theta/2)$ with θ the full spreading angle of the spray and x the axial distance from the orifice exit. The exponent C_{R2} is the radial profile coefficient giving the distribution its shape resembling a Gaussian-error function. Note that the definition and utilization of this coefficient is different to that of parameter C_{R1} defined by Correias [73], care must be taken when using such radial distribution coefficients.

The momentum flux is necessary to calculate velocity and concentration wherever in the spray, the conservation of momentum makes the following expression valid in the whole section of a gas-jet or Diesel spray [75]:

$$\dot{M}_o = \dot{M}(x) = \int_0^R 2 \pi \rho_{loc}(x, r) r u^2(x, r) dr. \quad (2.39)$$

Here $u(x, r)$ is the axial velocity at this specific location and $\rho_{loc}(x, r)$ the two-dimensional local density in the spray expressed as [76]:

$$\rho_{loc}(x, r) = \rho_f \frac{1}{Y_f(x, r) \left(1 - \frac{\rho_f}{\rho_g}\right) + \frac{\rho_f}{\rho_g}}. \quad (2.40)$$

After rearrangement of the equations presented before, the momentum at any axial distance from the outlet of the injector can be expressed as [75]:

$$\dot{M}(x) = \frac{\pi}{2 C_{R1}} \rho_g \tan^2 \left(\frac{\theta}{2} \right) x^2 u_{jet,axis}^2 \sum_{i=0}^{\infty} \frac{\frac{2}{Sc}}{\frac{2}{Sc} + i} \left(\frac{u_{jet,axis}}{u_o} \frac{1 + Sc \frac{\rho_f - \rho_g}{\rho_f}}{2} \right)^i. \quad (2.41)$$

In this equation, θ is the spreading angle of the spray. After simplification, the velocity on the centerline can be calculated, assuming that the local density is that of the ambient, the following expression is obtained:

$$u_{jet,axis} = \frac{M^{1/2}}{\rho_g^{1/2} \left(\frac{\pi}{2 C_{R1}} \right)^{1/2} x \tan \left(\frac{\theta}{2} \right)}. \quad (2.42)$$

It has been observed that this last expression is valid in the far-field, several diameters downstream from the orifice exit (around $30 D_o$), where the predictions showed good agreement with the experimental data (error has been reported to be lower than 3 %) [76]. This last expression allows to calculate the velocity at any location in the spray by assuming a radial distribution profile, and if the Schmidt number is known, the concentration can be deduced.

2.6 Conclusions

The thousands of droplets composing a direct-injection Diesel spray represent the state-of-the-art in terms of spray generation. The march of technological progress realized in the last decades aiming at making the sprays better produced the last generation injection systems widely mounted in present Diesel engines: the common-rail. The system is electronically controlled, allowing to vary not only the time of the injection but also to split the injection in several smaller quantities like pilot, main and post injections. These systems are also capable of injecting sprays up to 200 MPa injection pressure, thus intensifying the disintegration process of the liquid flow in order to improve fuel vaporization and mixing with the ambient gases.

The very end of the injection system or the element seen from the combustion chamber is the nozzle. The nozzle geometry, more specifically the orifices determine the flow inside the nozzle and therefore the behavior of the flow at the outlet, entering the combustion chamber. The main parameter of

an injection nozzle is the discharge coefficient, which is dependent upon the internal feature of the orifice such as: Length - diameter ratio, convergence of the orifice (*k-factor*) and entrance radius. The phenomenon of cavitation, which reduces the discharge coefficient of the injection system may occur under certain conditions but can be controlled or canceled thanks to appropriate internal design of the nozzle's orifices.

The conditions of the flow at the outlet, velocity, turbulence, cavitation, etc. determine the behavior of spray development. When penetrating in the discharge chamber, the liquid flow injected at high velocity encounters the ambient gases that are comparatively still. Due to aerodynamic forces principally, the liquid core disintegrates into liquid structures during the first break up process and into small and round droplets with the second break up. Depending on the temperature of the ambient gases, the spray may experience vaporization. In this case, the spray penetrates in the chamber like a gas-jet after a constant distance (liquid length) in which the spray is still liquid. The characteristics of the spray depends mainly on the density of the ambient gases but also on spreading angle and momentum flux of the spray itself.

Thanks to extensive research in the field of sprays, several correlations are available to predict spray penetration, droplet velocity and diameter or also fuel concentration. Because of the nature of these models, generally based on the gas-jet theory and further adjusted empirically, tuning of the parameters has to be done to adjust the model to the particular experimental conditions. The vast knowledge on gas-jet and the hypothesis that liquid penetrating sprays may present similar behavior, the velocity and concentration profiles can be assumed to be of a Gaussian-like profile as stated by a large number of works.

Bibliography

- [1] P. Lauvin, A. Löffler, A. Schmitt, W. Zimmermann, and W. Fuchs. Electronically controlled high pressure unit injector system for diesel engines. *SAE Paper 911819*, 1991.
- [2] G. Stumpp and M. Ricco. Common rail - an attractive fuel injection system for passenger car DI diesel engines. *SAE Paper 960870*, 1996.
- [3] G.N. Abramovich. The theory of turbulent jets. *MIT Press, Cambridge, Massachusetts*, 1963.

-
- [4] D.B. Spalding. Combustion and mass transfer. *Pergamon international library of science, technology, engineering, and social studies*, 1979.
- [5] H. Hiroyasu, M. Shimizu, and M. Arai. The breakup of high speed jet in a high pressure gaseous atmosphere. *ICLASS 1982*, pages 69–74, 1982.
- [6] M. Arai, M. Tabata, and M. Shimizu. Disintegrating process and spray characterization of fuel jet injected by a Diesel nozzle. *SAE Paper 840275*, 1984.
- [7] T.A. Fox and J. Stark. Characteristics of miniature short-tube orifice flows. *Proc. Inst. Mech Engrs*, 203:351–357, 1989.
- [8] Jaime Gimeno. *Desarrollo y aplicacion de la medida del flujo de cantidad de movimiento de un chorro Diesel*. PhD thesis, E.T.S. Ingenieros Industriales. Universidad Politécnica de Valencia, 2008.
- [9] C.F. Colebrook. Turbulent flow in pipes, with particular reference to the transition region between the smooth and rough pipe laws. *Journal of the ICE*, 11(4):133–156, 1939.
- [10] W. Bergwerk. Flow pattern in Diesel nozzle spray holes. *Proc. Inst. Mech. Engrs*, 173, n. 25., 1959.
- [11] DC Bogue. Entrance effects and prediction of turbulence in non-newtonian flow. *Industrial & Engineering Chemistry*, 51(7):874–878, 1959.
- [12] D. Potz, W. Chirst, and B. Dittus. Diesel nozzle: The determining interface between injection system and combustion chamber. *THIESEL 2000 Conference on Thermo and Fluid-dynamic Processes in Diesel Engines, Valencia, Spain*, 2000.
- [13] R. Payri, F.J. Salvador, J. Gimeno, and V. Soare. Determination of diesel sprays characteristics in real engine in-cylinder air density and pressure conditions. *Journal Of Mechanical Science And Technology*, 19(11):2040–2052, 2005.
- [14] G.G. Stokes. On the effect of the internal friction of fluids on the motion of pendulums. *Trans. Cambridge Philos. Soc*, 9(8), 1851.
- [15] O. Reynolds. An experimental investigation of the circumstances which determine whether the motion of water shall be direct or sinuous, and of the law of resistance in parallel channels. *Philosophical Transactions of the Royal Society of London*, 174:935–982, 1883.

-
- [16] H. Schlichting. Boundary layer theory. *McGraw-Hill, Series in Mechanical Engineering*, 1979.
- [17] F.M. White. Fluid mechanics. *McGraw-Hill Science/Engineering/Math, 5th edition*, 2004.
- [18] P. Gravesen, J. Branebjerg, and O.S. Jensen. Microfluidics - A review. *Journal of Micromechanics and Microengineering*, 3:168, 1993.
- [19] A. Barrero and M. Perez-Saborid. Fundamentos y aplicaciones de la mecanica de fluidos. *McGraw-Hill Interamericana de España*, 2005.
- [20] R.T Knapp, J.W. Daily, and F.G. Hammitt. Cavitation. *McGraw-Hill, New York*, 1970.
- [21] W. H. Nurick. Orifice cavitation and its effects on spray mixing. *Journal of fluids engineering*, 98:681–687, 1976.
- [22] C. Soteriou, S. Zuelch, M. Lambert, and D. Passerel. The flow characteristics of high efficiency diesel nozzles with enhanced geometry holes. *THIESEL 2006 Conference on Thermo and Fluid-dynamic Processes in Diesel Engines, Valencia, Spain*, 2006.
- [23] D.P. Schmidt and M.L. Corradini. The internal flow of diesel fuel injector nozzles: a review. *ImechE, Int. J. Eng. Res.*, 2(6), 2001.
- [24] C. Soteriou, R. Andrews, and M. Smith. Direct injection diesel sprays and the effect of cavitation and hydraulic flip on atomization. *SAE Paper 950080*, 1995.
- [25] V. Macián, R. Payri, X. Margot, and F. J. Salvador. A CFD analysis of the influence of diesel nozzle geometry on the inception of cavitation. *Atomization and Sprays*, 13:579–604, 2003.
- [26] R. Payri, C. Guardiola, F. J. Salvador, and J. Gimeno. Critical cavitation number determination in diesel injection nozzles. *Experimental Techniques*, 28(3):49–52, 2004.
- [27] F. Payri, V. Bermúdez, R. Payri, and F.J. Salvador. The influence of cavitation on the internal flow and the spray characteristics in diesel injection nozzles. *Fuel*, 83:419–431, 2004.
- [28] R. Payri, X. Margot, and F.J. Salvador. A numerical study of the influence of diesel nozzle geometry on the inner cavitating flow. *SAE Paper 2002-01-0215*, 2002.

-
- [29] A. K. Lichtarowicz, R. K. Duggins, and E. Markland. Discharge coefficients for incompressible non-cavitating flow through long orifices. *Journal of Mechanical Engineering and Science*, 7(2):210–219, 1965.
- [30] K. Ramamurthi and K. Nandakumar. Characteristics of flow through small sharp-edged cylindrical orifices. *Flow Measurement and Instrumentation*, 10(3):133–143, 1999.
- [31] V. Macián, V. Bermudez, R. Payri, and J. Gimeno. New technique for determination of internal geometry of a diesel nozzle with the use of silicone methodology. *Experimental Techniques*, 27(2):39–43, 2003.
- [32] R. Payri, F.J. Salvador, J. Gimeno, and J. de la Morena. Study of cavitation phenomena based on a technique for visualizing bubbles in a liquid pressurized chamber. *International Journal of Heat and Fluid Flow*, 30:768–777, 2009.
- [33] Rolff Reitz. *Atomization and other breakup regimes of a liquid jet*. PhD thesis, Princeton University, 1978.
- [34] G.M. Faeth, L.P. Hsiang, and P.K. Wu. Structure and breakup properties of sprays. *International Journal of Multiphase Flow*, 21:99–127, 1995.
- [35] J.C. Lasheras and E.J. Hopfinger. Liquid jet instability and atomization in a coaxial gas stream. *Annual Review of Fluid Mechanics*, 32(1):275–308, 2000.
- [36] Nader Rizk. *Studies on liquid sheet disintegration in airblast atomizers*. PhD thesis, Cranfield University, Cranfield, UK, 1976.
- [37] J.M. Desantes, R. Payri, A. Garcia, and J. Manin. Experimental study of biodiesel blends' effects on Diesel injection processes. *Energy & Fuels*, 23:3227–3235, 2009.
- [38] R. Payri, S. Ruiz, F.J. Salvador, and J. Gimeno. On the dependence of spray momentum flux in spray penetration. *Journal of Mechanical Science and Technology*, 21(7):1100–1111, 2007.
- [39] W. Ohnesorge. Formation of drops by nozzles and the breakup of liquid jets. *eitschrift für Angewandte Mathematik und Mechanik (ZAMM)*, 16(4):355–358, 1936.
- [40] R. Reitz and F. Bracco. Mechanism of atomization of a liquid jet. *Physics of Fluids*, 25(10):1730–1742, 1982.

-
- [41] F. Ruiz. A few useful relations for cavitating orifices. *ICLASS 1991, Gaithersburg, Maryland*, pages 595–602, 1991.
- [42] R. Reitz and R. Diwakar. Effect of drop breakup on fuel sprays. *SAE Paper 860469*, 1986.
- [43] R. Reitz and R. Diwakar. Structure of high-pressure fuel sprays. *SAE Paper 870598*, 1987.
- [44] R. Reitz and F. Bracco. Mechanism of breakup of round liquid jets. *Encyclopedia of Fluids Mechanics, Gulf publishing*, 3, 1994.
- [45] F. Ruiz. Turbulence inside a cavitating injector orifice: a different animal. *ILASS-Americas*, pages 133–137, 1998.
- [46] R. Morgan, J. Wray, D.A. Kennaird, C. Crua, and M.R. Heikal. The influence of injector parameters on the formation and break-up of a diesel spray. *SAE Transactions*, 110(3):389–399, 2001.
- [47] L.P. Hsiang and G.M. Faeth. Near-limit drop deformation and secondary breakup. *International Journal of Multiphase Flow*, 18(5):635–652, 1992.
- [48] M. Pilch and C.A. Erdman. Use of breakup time data and velocity history data to predict the maximum size of stable fragments for acceleration-induced breakup of a liquid drop. *International journal of multiphase flow*, 13(6):741–757, 1987.
- [49] Z. Dai and G.M. Faeth. Temporal properties of secondary drop breakup in the multimode breakup regime. *International Journal of Multiphase Flow*, 27(2):217–236, 2001.
- [50] C.S. Lee and R.D. Reitz. Effect of liquid properties on the breakup mechanism of high-speed liquid drops. *Atomization and Sprays*, 11(1):1–20, 2001.
- [51] W.H. Chou, L.P. Hsiang, and G.M. Faeth. Temporal properties of drop breakup in the shear breakup regime. *International Journal of Multiphase Flow*, 23(4):651–669, 1997.
- [52] A.A. Ranger and J.A. Nicholls. Aerodynamic shattering of liquid drops. *AIAA Journal*, 7(2):285–290, 1969.
- [53] P. Hay and P.L. Jones. Comparison of the various correlations for spray penetration. *SAE Paper 720776*, 1972.

-
- [54] J.C. Dent. A basis for comparison of various experimental methods for studying spray penetration. *SAE Paper 710571*, 1971.
- [55] E. Buckingham. Model experiments and the form of empirical equations. *Trans. ASME*, 37:263, 1915.
- [56] J.M. Desantes, R. Payri, F.J. Salvador, and A. Gil. Development and validation of a theoretical model for diesel spray penetration. *Fuel*, 85(7-8):910–917, 2005.
- [57] Y. Wakuri, M. Fujii, T. Amitani, and R. Tsumeya. Studies of the penetration of a fuel spray in a diesel engine. *JSME*, 3(9):123–130, 1960.
- [58] H. Hiroyasu and M. Arai. Structures of fuel spray in Diesel engines. *SAE Paper 900475*, 1990.
- [59] J. Naber and D. Siebers. Effects of gas density and vaporization on penetration and dispersion of diesel sprays. *SAE Paper 960034*, 1996.
- [60] R. Payri, F.J. Salvador, J. Gimeno, and L.D. Zapata. Diesel nozzle geometry influence on spray liquid-phase fuel penetration in evaporative conditions. *Fuel*, 87(7):1165–1176, 2008.
- [61] Jose Maria Garcia. *Aportaciones al estudio del proceso de combustion turbulenta de chorros en motores Diesel de inyección directa*. PhD thesis, E.T.S. Ingenieros Industriales. Universidad Politécnica de Valencia, Valencia, 2004.
- [62] J.M. Desantes, R. Payri, F.J. Salvador, and J. De la Morena. Cavitation effects on spray characteristics in the near-nozzle field. *SAE Paper 2009-24-0037*, 2009.
- [63] T. Dan, T. Yamamoto, J. Senda, and H. Fujimoto. Effect of nozzle configurations for characteristics of non-reacting Diesel fuel spray. *SAE Paper 970355*, 1997.
- [64] R. Reitz and F. Bracco. On the dependence of spray angle and other spray parameters on nozzle design and operating conditions. *SAE Paper 790494*, 1979.
- [65] J.V. Pastor, J. Arrègle, and A. Palomares. Diesel spray images segmentation using a likelihood ratio test. *Applied Optics*, 40(17):2876–2885, 2001.

- [66] D.L. Siebers. Scaling liquid-phase fuel penetration in diesel sprays based on mixing-limited vaporization. *SAE Paper 1999-01-0528*, 1999.
- [67] R.A. Mugele and H.D. Evans. Droplet size distribution in sprays. *Industrial & Engineering Chemistry*, 43(6):1317–1324, 1951.
- [68] H. Hiroyasu, M. Arai, and M. Tabata. Empirical equations for the sauter mean diameter of Diesel spray. *SAE Paper 890464*, 1989.
- [69] N. Levy, S. Amara, and J.C. Champoussin. Simulation of a diesel jet assumed fully atomized at the nozzle exit. *SAE Paper 981067*, 1998.
- [70] J. Arrègle, J.V. Pastor, and S. Ruiz. Influence of the injection parameters on Diesel spray characteristics. *SAE Paper 1999-01-0200*, 1999.
- [71] F. Di Giorgio, D. Laforgia, and V. Damiani. Investigation of drop size distribution in the spray of a five-hole, vco nozzle at high feeding pressure. *SAE Paper 950087*, 1995.
- [72] J. M. Desantes, R. Payri, F. J. Salvador, and J. Gimeno. Measurements of spray momentum for the study of cavitation in Diesel injection nozzles. *SAE Paper 2003-01-0703*, 2003.
- [73] David Correas. *Estudio teórico-experimental del chorro libre Diesel isoterma*. PhD thesis, E.T.S. Ingenieros Industriales. Universidad Politécnica de Valencia, Valencia, 1998.
- [74] J.O. Hinze. Turbulence: an introduction to its mechanism and theory. *McGraw-Hill, New York*, 162, 1959.
- [75] J.M. Desantes, R. Payri, J.M. Garcia, and F.J. Salvador. A contribution to the understanding of isothermal Diesel spray dynamics. *Fuel*, 86(7-8):1093–1101, 2007.
- [76] J.M. Desantes, R. Payri, F.J. Salvador, and A. Gil. Deduction and validation of a theoretical model for a free Diesel spray. *Fuel*, 85:910–917, 2006.

Chapter 3

Experimental techniques applied in this study

Contents

3.1	Introduction	66
3.2	Injection system	67
3.3	Internal geometry and flow characterization	69
3.3.1	Internal geometry determination	70
3.3.2	Rate of injection measurements	73
3.3.3	Spray momentum flux	77
3.4	Equipment used for isothermal spray analysis	82
3.4.1	Optically accessible cold spray facility	82
3.4.2	Direct visualization of the liquid phase	84
3.4.3	Laser imaging	86
3.5	Experimental apparatus under evaporative conditions	90
3.5.1	Engine Combustion Network	90
3.5.2	Schlieren imaging	93
3.5.3	Rayleigh scattering diagnostics	95
3.6	Available methods to overcome multiple scattering effects	96
3.6.1	X-Ray absorption	98
3.6.2	Ballistic imaging	100
3.6.3	Structured Laser Illumination Planar Imaging (SLIPI)	103
3.7	Conclusions	105
	Bibliography	106

3.1 Introduction

All the knowledge regarding sprays is the result of years of investigation. This experience is the fruit of extensive developments in experimental techniques aiming at analyzing and discovering the complex processes of injection and spray disintegration. There is a large amount of methods to study injected sprays nowadays; depending on which aspect of the process is under investigation, one or maybe several techniques will be available. The internal flow, near nozzle-field, spray breakup, droplet size and number density etc. are among the studied topics in this field and each of them might require a different experimental installation. All these efforts lead to one general purpose: improving the general knowledge to make engines better. Engine manufacturers know that the process of injection is basically controlling the next coming combustion process and to improve engine efficiency or reducing contamination, this first stage must be controlled.

The characterization of sprays can actually be divided into two purposes or steps: since the beginning, experimental techniques have been developed in order to test and improve sprays, mainly those injected to produce combustion. Their goal is to obtain the complete spray properties to evaluate the effects of modifying the different parameters of the injection process. Over the years, this capacity has been given to research as well in order to understand the physics of spray formation and disintegration through experimental and theoretical analysis. The complex fluid dynamical processes involved in spray development require intensive and devoted studies to be related to physical phenomena due to its inherent turbulent behavior.

Sprays have been studied during the past years using numerous techniques. Photographic, mechanical and electrical were applied at the beginning but due to their non-intrusive nature, laser diagnostics have been extensively developed and are now widely applied for spray characterization. Since their apparition, 30 years ago, laser techniques have been highly developed and improved, through optical sensors sensitivity, computer performance and software development. With the new technologies, laser techniques have also been introduced and with the time they improved the science of making measurements in sprays. As injection systems are getting better everyday, the diagnostics have to follow the trend, and smaller droplets at higher velocity is a continuous challenge for experimental techniques developers.

The methods applied in this work to experimentally evaluate the different

aspects of sprays described in the previous chapter are presented here. The injection system used all along this study to generate the sprays is presented first. The characterization of the internal flow will be introduced next through orifice geometry determination, the rate of injection and momentum flux of the spray will also be addressed here as they represent parameters of the internal flow more than anything else. Thirdly, the regular visualization methods used to characterize the spray macroscopically will be presented, the liquid and vapor phases can be seen thanks to these techniques. The laser-based diagnostics will be the object of the following section as they present a large part of this study in terms of setup and calibration. Finally, an overview of some other available methods will be done; these techniques are still under development and they present another approach in terms of spray characterization.

3.2 Injection system

The system used to deliver high-pressure fuel to the injector is a normal automotive production series common rail system adapted to laboratory use and featuring temperature control. This is necessary on one side because it is obviously better to have all the variables under control when conducting an experiment and on the other side because the fuel consumption is very low and thus there is a higher proportion of fuel returning to the main tank, causing a gradual temperature rise up to 100°C and more if no fuel cooling system was employed. All elements involved in the injection system can be identified in figure 3.1. The high pressure pump is driven by an electric motor at constant speed, which can also be adjusted.

The injector used in this study has been purposely designed by Bosch (see technical drawing on fig. 3.2), it is based on second generation Common-Rail systems. The needle is indirectly moved by a solenoid coil and the injector is equipped with a single-hole nozzle of diameter 0.09 mm coaxially positioned with the injector's body. The orifice internal geometry is of conical shape with *k-factor* of 1.5, hydro-erosion has been performed to reach the desired mass flow rate and thus reducing cavitation (this has been described in sec. 2.3.4). The signals required to initiate the needle opening and held it in this position are provided by a Genotec pulse generator, which can handle up to nine injections per cycle. A frequency generator is used to trigger both the Genotec and all the equipment and acquisition system.

In order to perform all the tests under the same conditions, in addition to that of the fuel, the temperature of the body of the injector has been controlled

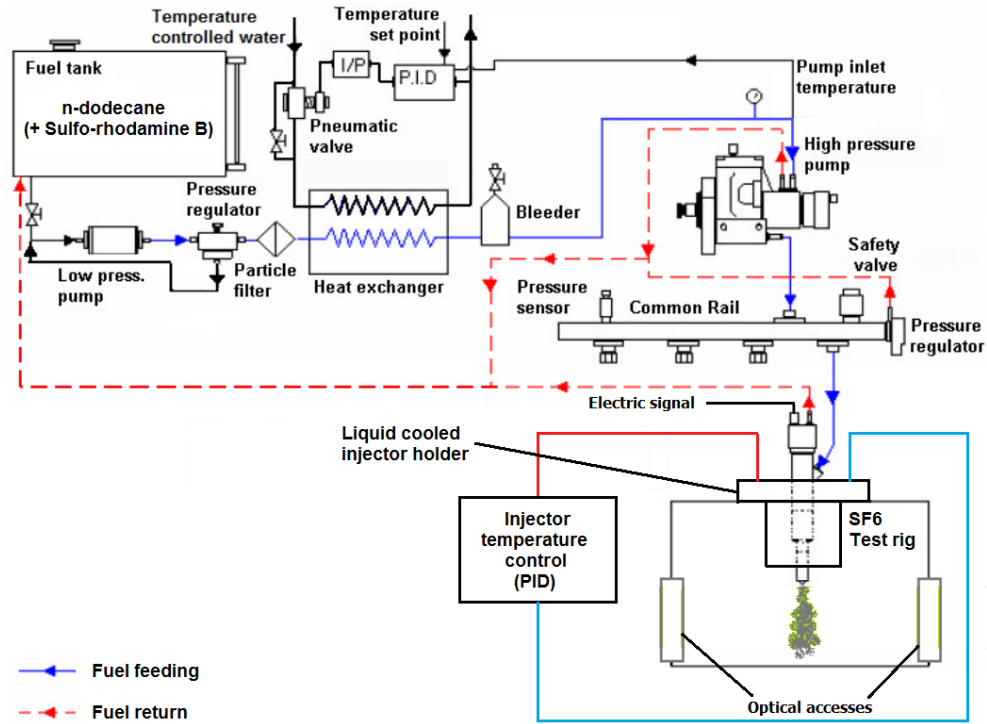


Figure 3.1: Global schematic of the injection system together with the injector temperature control apparatus.

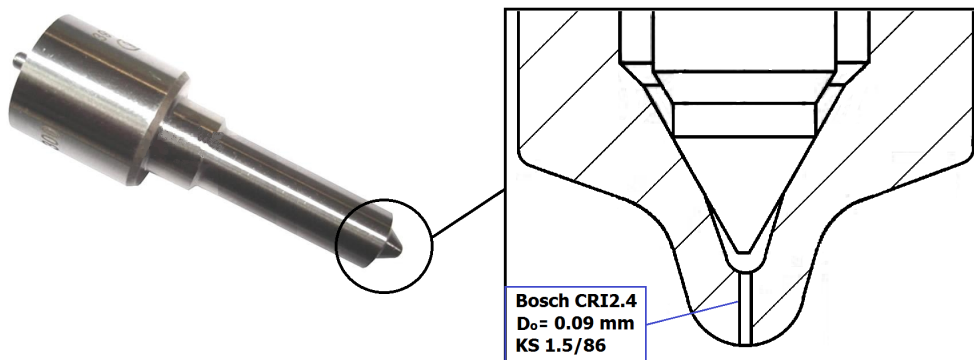


Figure 3.2: Picture of the injector and technical drawing of the tip of the single-hole nozzle used in the experiments (source Bosch).

and held at a constant 70°C (343 K). The injector has been placed in a specific liquid-cooled holder in which temperature controlled water flows; the system sets and holds the injector temperature via a Proportional-Integral-Derivative controller (PID) by heating or cooling the injector's body depending on the testing condition.

As an objective of being consistent within all the different installations used along this work, a pure alkane has been injected; high purity n-dodecane ($C_{12}H_{26}$) has been chosen to be the reference fuel in this study. Table 3.1 presents the main properties of the n-dodecane fuel used in this study.

Properties	Values	Units
Chemical formula	$C_{12}H_{26}$	[-]
Purity	> 99	[%]
Molar weight	170.34	[g/mol]
Density	0.748	[g/cm ³]
Viscosity	1.342	[mPa.s]
Melting point	261	[K]
Boiling point	488	[K]
Refractive index (n_D)	1.422	[-]

Table 3.1: General fluid characteristics of n-dodecane.

3.3 Internal geometry and flow characterization

Knowing the geometrical characteristics of the inner part of an injector's nozzle, in other terms the orifice, is really important to characterize the spray. As described in the previous chapter, the internal flow has to be evaluated separately as the fluid dynamic processes are really different from what occurs after the orifice exit. Nevertheless, studying the internal flow is still under investigation as the orifice is relatively small and the velocity of the flow relatively high and represents a challenge for any kind of measurement technique.

From a rational point of view, the best way to analyze the internal flow would be to look into it; several researchers investigated the aspect of cavitation through visualization methods [1,2]. These works used nozzles or only orifices manufactured in transparent materials, the refractive index of the fluid has also been adjusted to perfectly match that of the material used [3,4]. Walther

et al. [5] carried out some tests aiming at measuring the velocity of the flow inside a Diesel nozzle injector using Fluorescent Particle Image Velocimetry (FPIV). But the low injection pressures involved by the material used do not make complete comparison possible with real injectors as the velocity and thus Reynolds number will not be the same. To overcome this problem and study similar operative conditions, some works have been done with scaled orifices [6–9]. Nevertheless, some used real sized transparent orifice [3, 10–15], but the cost of the experiment is obviously really different. From an experimental point of view, the use of scaled orifices that reproduces the actual internal geometries makes the flow visualization technically easier. Nevertheless, as pointed out by some authors [3, 10], the results obtained with such orifices cannot be completely generalized to real scale orifices.

An alternative is available to characterize the internal flow by studying it right at the exit of the orifice as both the injector and the conditions can be reproduced. This does not evaluate precisely where the cavitation is or what the velocity profiles look like, however it gives precious information like rate of injection or momentum flux of the spray. By combining both measurements, several additional parameters can be deduced that determine qualitatively the injected spray [16–20]. The aim of this work being to analyze fully developed sprays, no extensive information about the internal flow is required and an hydraulic characterization is more than enough. For that, the geometrical shape of the orifice will be determine through silicone molds and the flow will be characterize at the outlet thanks to rate of injection and spray momentum measurements.

3.3.1 Internal geometry determination

The manufacturing process of a nozzle require high precision devices and is completed after several stages. First, after mechanization of the core of the nozzle, the needle room is drilled and adjusted for the needle to sit perfectly. Then, the orifice is mechanized through mechanical drilling, electrical eroding or more recently laser "drilling". Finally, the orifice is submitted to hydro-erosion whose main objective is to reach the desired flow; in multi-hole nozzles, the flow between orifices is equaled. During the drilling of the orifice, some imperfections are left behind that would affect the flow and potentially engine performances. This process considerably increase the discharge coefficient of the orifice as the flow restriction goes down while the edges and imperfections are smoothed by the abrasive fluid flowing through. The hydro-erosion is stopped when the mass flow rate, for a specific pressure drop condition (gener-

ally $p_{inj} = 10$ MPa and $p_b = 0.1$ MPa), reaches the target value, which mainly depends on engine specifications. [21, 22].

Nozzle manufacturers would have a hard time trying to control all the internal geometric parameters of the orifice during and after the manufacturing process. Nonetheless, as described before, the geometry has a huge effect on the flow at the outlet and all the disintegration process from the liquid core to thousands of droplets. That is why the silicone mold technology has been used to determine the internal geometry of the nozzle of the different injectors [23]. This technology uses the ability of the silicone to be fluid at first and then to be an elastic deformable solid. The silicone is introduced in the nozzle, previously taken apart from the injector's body, the needle is removed and after some time, the silicone is carefully taken out from the nozzle. The samples are then coated with a thin layer of gold (about $0.01 \mu\text{m}$ thick) as the Scanning Electron Microscope (SEM) visualization method requires electrical conductivity of the material.

The mold of the nozzle is photographed from a large amount of points of view and zooming levels like shown in figures 3.3 and 3.4 to get the specificities of the complex geometry. At the bottom left hand corner of the images, a scale is displayed that allows to measure the geometrical parameters by using a CAD software accurately.

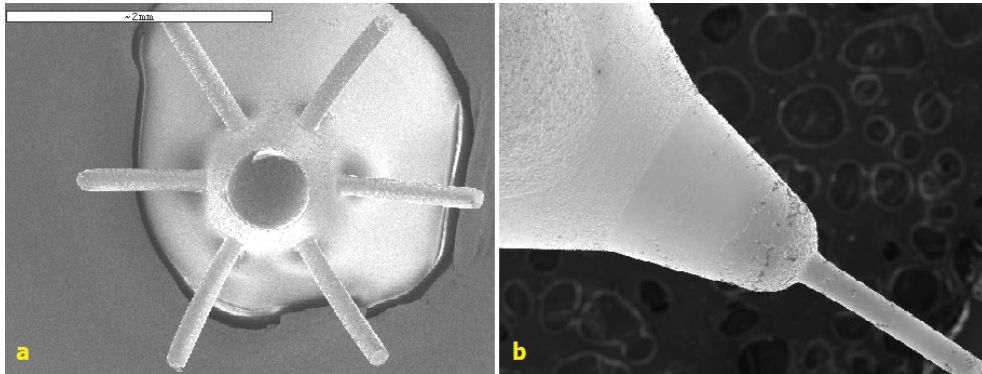


Figure 3.3: Images of the silicone molds extracted from multi-holes (a) and single-hole (b) nozzles obtained through SEM measurements.

The geometrical characteristics measured from the molds are numerous and give necessary information to understand how the flow behaves in the orifice but also at the exit, thus influencing spray development.

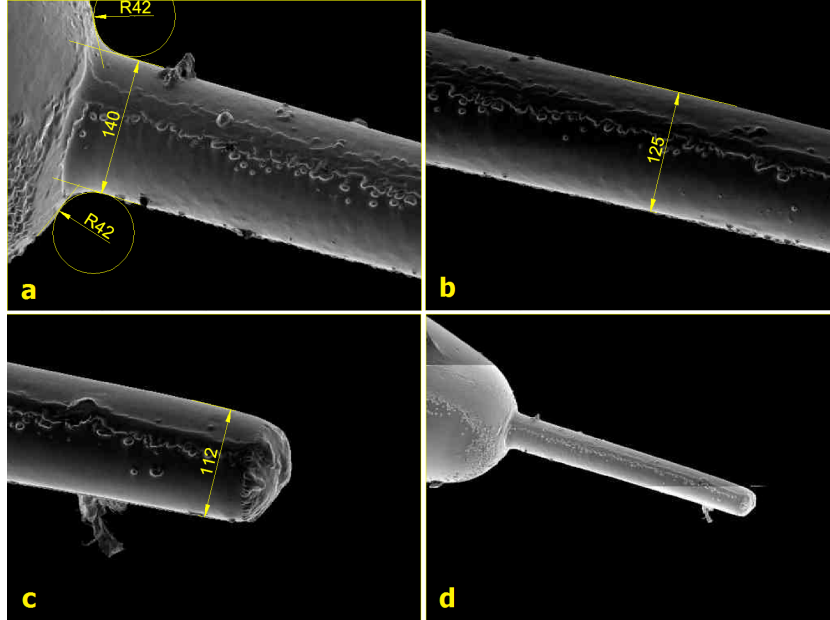


Figure 3.4: Imaging of some geometrical parameters: (a) Entrance radius and inlet diameter, (b) half-distance diameter, (c) outlet diameter and (d) global view.

Characteristic parameters measured

The different points of view imaged through SEM allow getting geometrical parameters that can depend slightly from one to another. The measured geometrical features can be seen on figure 3.4. The geometrical parameters defined previously in 2.3.1 are detailed in the following nomenclature:

- ψ : Orifice angle. Angle formed by nozzle and orifice axes. $\psi = 0$ for single-hole axi-symmetrical nozzles.
- r_e : Curvature radius between the orifice and the mini-Sac.
- D_i : Inlet diameter of the orifice.
- D_m : Diameter in the middle section of the orifice.
- D_o : Outlet diameter of the orifice.
- D_i' , D_m' , D_o' : Same conceptual parameters but measured at 90° .

As the orifices are visualized from two different perspectives and therefore some differences can be observed on the geometrical parameters of interest, an equivalent value is taken to get a general characterization of the nozzle.

In that way, the diameters at the entrance, middle and outlet of the orifices are the geometric means of both values previously defined. The value of the diameter being different depending on the point of view, this gives the orifice an elliptic shape. Even if this has been observed through other experimental methods, as its origin has not been fully explained yet, no studies mentioned this clearly.

The conicity of the orifice can be defined by two parameters thanks to the measurements: The *k-factor* [24] is the most commonly used parameter by injectors manufacturers, it has been defined in the previous chapter (eq. 2.1). The other parameter used to define the conicity is the area reduction, which makes the relation between the areas instead of the diameters as follows:

$$AR = \frac{A_i - A_o}{A_i}, \quad (3.1)$$

A_i and A_o being the cross sections of the entrance and outlet areas respectively. This definition presents the advantage of giving a relative idea of the reduction and thus the velocity variations can be directly related.

Technique validation

The methodology of both silicone molding and image processing has been validated in two ways. First, the precision of the process has been evaluated by comparing the results of two molds of the same nozzle made. This study showed an error as low as 2 % on the diameters and about 8 % on the curvature radius. A higher value of the error on the curvature radius can be explained by the difficulty to estimate this radius with the CAD software.

The second important aspect studied was the accuracy of the technique by comparison of the mold of an orifice and the original orifice itself visualized by SEM. The error found on several orifices oscillated between 0.5 % and 1 % making this method one of the most accurate for this kind of measurements [23,25]. As this value has been found to be lower than the error of the precision of the manufacturing, it can be assumed that the deviation from original orifice shape to silicone mold is negligible.

3.3.2 Rate of injection measurements

The rate of injection (commonly ROI) is certainly the most used parameter to characterize the flow at the outlet of the orifice. The equipment used in

this study to determine this characteristic is based on the long tube method or Bosch method [26]. Within the techniques available to determine the instantaneous mass flow rate, this method is known to be the most exhaustive as it provides a time-resolved signal of the injected flow [27].

Figure 3.5 is a sketch of the flow rate meter used in this experiment. The tip of the injector is placed in the chamber designed for it to fill the entire rate meter with the fluid to inject. A mechanical valve holds the discharge pressure to the target value to simulate the pressure in the combustion chamber of a real engine for example.

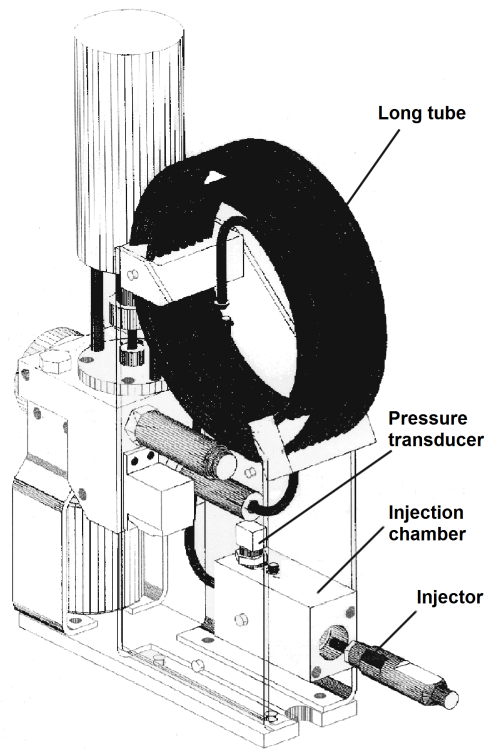


Figure 3.5: Flow rate meter using the Bosch or long tube method [26].

When the injection begins, the needle moves up and the fluid contained in the injector starts flowing toward the exit thanks to the pressure difference. This produces a pressure wave that travels at the speed of sound in the medium (the fuel) in the long tube till a small tank. The pressure variation is recorded by a high-speed piezoelectric transducer placed close to the injector tip, in the

injection chamber.

At the end of the long tube, a wave pressure will be generated by the section change and will be traveling in the opposite direction. This second wave of pressure can potentially disturb the measurements, that is why the tube is long enough to avoid any reflection to interact with the injection signal. In the same time, with the length of the tube and the final tank, the signal is attenuated in order not to affect the original signal.

The experimental conditions, like injection pressure, injected fluid, nozzle geometry and many more are the main responsible for the signal amplitude. A valve can be user-controlled to change the section at the end of the long tube and can then damp the secondary pressure waves depending on the testing conditions.

Theoretical point of view

The signal recorded by the piezoelectric transducer in this kind of measurement device is the pressure wave generated by the injection itself, which travels downstream in the injection chamber. Through processing of this signal, it is possible to obtain the instantaneous mass flow rate of the injection.

This process begins with a theoretical study of the propagation of a pressure wave in a pipe with constant section. The wave travels at a velocity corresponding to the speed of sound v_c and induce a punctual variation of both the velocity of the flow Δu and the pressure Δp . The pressure difference is then measured by the high-speed pressure transducer.

Considering the volume of the injection chamber as a cylinder with section A_c and length dx , where the pressure wave is traveling. Assuming that the gravity effects are negligible in this case, the only forces are those induced by the pressure difference. Then, applying the law of the conservation of the linear momentum in the direction of the pipe, the next expression is obtained:

$$(p_b + \Delta p) A_c - p A_c = \rho_f A_c v_c \Delta u, \quad (3.2)$$

where p_b is the discharge pressure of the injection chamber or pressure in the tube and ρ_f the fluid density. By simplification of this expression, the pressure drop can be extracted:

$$\Delta p = \rho_f v_c \Delta u . \quad (3.3)$$

At the same time, the variation of the mass flow rate \dot{m} induced by the pressure wave can be expressed as:

$$\dot{m} = \rho_f A_c \Delta u . \quad (3.4)$$

From the two last equations, the variation of the mass flow rate is finally obtained as a function of the pressure variation recorded by the sensor:

$$\dot{m} = \frac{A_c}{v_c} \Delta p . \quad (3.5)$$

If the section A_c of the long tube of the rate meter and the speed of sound v_c in the fluid under the experimental conditions are known, the mass flow rate can be determined. Nevertheless, the speed of sound in the fluid depends upon pressure and temperature and must be measured or calculated to get an accurate value of the mass flow rate. In this work, the speed of sound has been measured at different conditions until 200 MPa from 293 K up to 353 K applying the experimental technique described by Payri et al. [28]. The fluid temperature in the rate meter T_f is measured by a sensor placed in the injection chamber and the pressure of the fluid p_b is measured in the rate meter by a piezo-resistive transducer.

Calibration and corrections

Once the pressure signal has been acquired, in the aim of getting a more accurate instantaneous mass flow rate, it is adjusted in such a way that its integral corresponds to the injected mass of one single injection. This injected mass per cycle is obtained by measuring the injected mass along time; the mass flow rate is then obtained and as the frequency of the injection is known (normally set to $10Hz$), the injected mass per stroke is calculated.

It has been observed that the signal suffers from an accumulation phenomenon coming from an increase of the pressure in the rate meter due to the injection. Assuming that this accumulation is proportional to the signal recorded, i.e. the pressure or injected mass, and considering that the accumulation behaves like a first order system, it is possible to correct the mass flow rate. The algorithm uses the final part of the signal, after the end of injection to do the correction [29]. A study showed that this phenomenon must be corrected as the signals would be incoherent instead [29]. Figure 3.6 shows the original signal recorded by the pressure transducer but given as mass flow rate and the corrected signal.

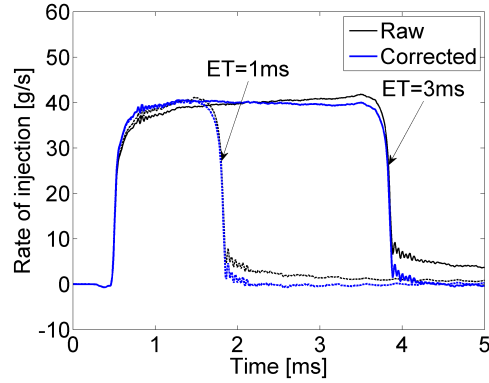


Figure 3.6: Original and corrected signals of the rate of injection measured by the Bosch method. ($p_{inj} = 150 \text{ MPa}$, $p_b = 6 \text{ MPa}$).

3.3.3 Spray momentum flux

The measure of the momentum flux is of primary interest as it provides basic information of the spray and its development when the measure is merged together with the rate of injection. It is defined as the product of the mass and the velocity at one specific instant. In the application of sprays, the concept would be the product of the mass flow rate and the mean velocity of the spray. The flow at the exit of the orifice is generally not continuous and both density and velocity could be irregular. Figure 3.7 represents the flow at the outlet of the orifice of an injection's nozzle under cavitating conditions.

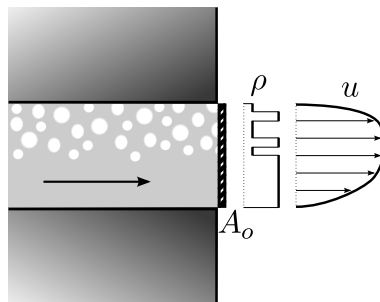


Figure 3.7: Sectional representation of the flow at the outlet of a cavitating orifice.

In this specific case and considering the axial component only, the following expression of the momentum flux through the geometrical area of the orifice

is obtained:

$$\dot{M} = \int A_o \rho_{eq} u_x^2 dA . \quad (3.6)$$

The geometrical area is defined as A_o , u_x is the axial component of the flow velocity and ρ_{eq} is the density profile which corresponds to the fuel density except if cavitation appears.

Information provided by the measurements

As introduced briefly before, the spray momentum flux has to be treated with the mass flow rate, which is defined as follows for the particular case of the orifice of an injector's nozzle (see fig. 3.7):

$$\dot{m} = \int A_o \rho_{eq} u_x dA . \quad (3.7)$$

The mass flow rate \dot{m} gives important information concerning the energy delivered to the engine through injected mass of fuel. The velocity of the flow at the outlet u_f , for example, could be expressed as follows [30–32]:

$$u_f = \frac{\dot{m}}{\rho_f A_o}, \quad (3.8)$$

where ρ_f is the fuel density. It is obvious that in this formulation, the density and velocity of the flow at the exit are considered as uniform. If these conditions are not fulfilled, when the flow is cavitating for example, the error on the measure could be important [16, 17]. One more drawback of this calculus is that the outlet area is required and a little variation on the orifice diameter engender a large error on the final result [23].

From the spray momentum and mass flow rate measurement, two important parameters can be determined: the effective velocity of the spray and the effective area of the outlet of the orifice [18, 33, 34].

The real flow at the orifice exit is then determined by the velocity profile and fuel density (fig. 3.8). By application of the effective area and velocity on the spray momentum and rate of injection, the integral equations become:

$$\dot{m} = A_{eff} \rho_f u_{eff} \text{ and } \dot{M} = A_{eff} \rho_f u_{eff}^2 . \quad (3.9)$$

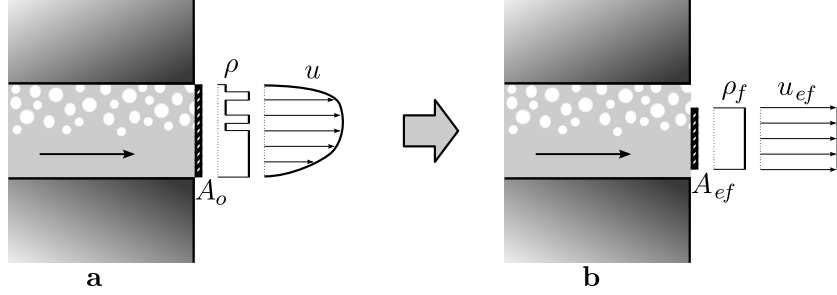


Figure 3.8: Definition of the effective velocity and area (b) from the actual flow (a) at the outlet of an orifice.

Rearranging these equations, the effective velocity and area can be extracted, and are expressed as follows:

$$u_{eff} = \frac{\dot{M}}{\dot{m}} \text{ and } A_{eff} = \frac{\dot{m}^2}{\rho_f \dot{M}} . \quad (3.10)$$

If the orifice is considered circular, the effective diameter can then be calculated:

$$D_{eff} = \sqrt{\frac{4 A_{eff}}{\pi}} . \quad (3.11)$$

The difference between geometric area and effective area are generally due to losses caused by the non-uniformity of the velocity profile, a cavitating behavior of the flow or an hydraulic flip of the flow. In the expression of the effective velocity, the geometric area is not required, avoiding any kind of error induced by its measurement.

Several dimensionless parameters can be defined from these last expressions: the velocity, area and discharge coefficients [25].

- *Velocity coefficient.* It represents the relation between effective velocity and theoretical one obtained by resolving Bernoulli's equation, it is defined as:

$$C_v = \frac{u_{eff}}{u_B} = \frac{u_{eff}}{\sqrt{2 \Delta p / \rho_f}} . \quad (3.12)$$

- *Area coefficient.* This evaluates the area reduction with respect to the geometrical one, its formulation is:

$$C_a = \frac{A_{eff}}{A_{geo}} . \quad (3.13)$$

- *Discharge coefficient.* Introduced in the previous chapter 2, the discharge coefficient is the ratio between the actual mass flow rate and the theoretical one. The theoretical mass flow rate is calculated with the maximum theoretical velocity and through the entire geometric area, it is calculated by:

$$C_d = \frac{\dot{m}}{\dot{m}_{theo}} = \frac{\dot{m}}{A_o \sqrt{2 \rho_f \Delta p}} . \quad (3.14)$$

- *Momentum coefficient.* In a similar way, the measured momentum flux is compared to the theoretical one, based on the same assumptions used to calculate the theoretical mass flow rate, it is defined as:

$$C_m = \frac{\dot{M}}{\dot{M}_{theo}} = \frac{\dot{M}}{2 A_o \Delta p} . \quad (3.15)$$

Measurement principle

The momentum flux of the spray is measured by a piezo-electric force transducer placed perpendicularly to the spray, large enough to collect it all. The sensor measures the force of the impact of the spray which is equivalent to the total momentum flux at the outlet of the orifice, due to the conservation of this magnitude in the axial direction. The measurement principle of the momentum flux is depicted in figure 3.9.

The conservation of the momentum flux equation can be resolved by making the following considerations into the control volume:

- The gravitational forces are assumed to be negligible.
- The discharge pressure is uniform in the control volume of the chamber and results in taking into account the only force exercised by the spray on the sensor.

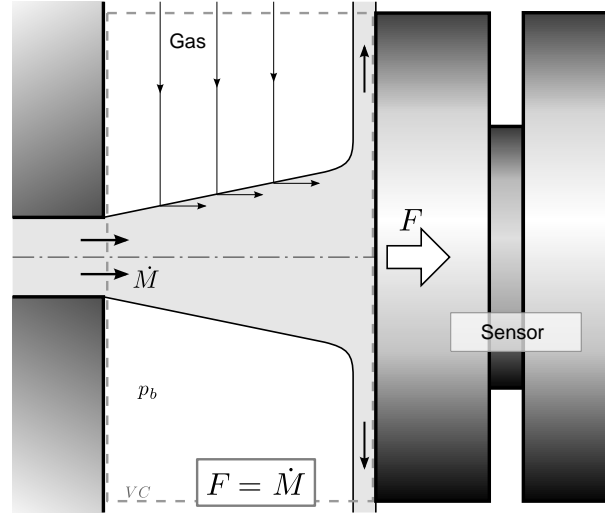


Figure 3.9: Measurement principle of the momentum flux of the spray.

- The air is entrained perpendicularly to the spray axis, and the fuel is evacuated perpendicularly as well resulting in balancing the radial momentum and assuming that there are no viscous forces in the axial direction.

A study demonstrated that these assumptions have minor impact on the measurements and it has been concluded that the error was within the uncertainty of the overall precision of the experiments. Applying these hypotheses to the equation of the conservation of the momentum flux and considering the system under steady conditions, the following expression is obtained:

$$F = \dot{M}, \quad (3.16)$$

where F is the force of the impact of the spray measured by the sensor. This last equation means that whenever all the assumptions are fulfilled the force of the spray against the transducer is equivalent to the momentum flux at the outlet of the orifice.

3.4 Equipment used for isothermal spray analysis

To achieve quantitative measurements in the liquid spray injected under isothermal conditions (293 K), several techniques have been used to compare and evaluate its behavior. The installations used to visually analyze the liquid spray are described in this section. The spray is injected in a purposely designed chamber that simulates the ambient densities of a real engine environment during the injection process but avoiding fuel evaporation. Regular visualization techniques are generally used as one of the first stages of a global study concerning spray penetration. The basic parameters provided by this kind of visualization are mainly spray tip penetration distance and spreading angle along time and are widely used to characterize the spray. The ability of laser-based techniques to provide microscopic information combined with macroscopic information of the spray cannot be denied. This special capacity makes them as a first choice to obtain useful parameters like fuel mass fraction or droplet size wherever in the spray.

As it is one of the most important organ of this experiment for its specificity, the cold spray test rig will be described first. The equipment used to visualize the liquid spray will be presented then, together with the image processing and the parameters obtained. Finally, the Planar Laser Imaging system and the associated diagnostics will be briefly presented, as it requires deeper development, the setup and calibration of this technique will be the object of chapter 4.

3.4.1 Optically accessible cold spray facility

The visualization test rig is a closed-loop installation designed in order to simulate the air density in the combustion chamber of an engine prior to injection. The advantage of such a test rig is the optical access that allows better visualization of the spray than in a real engine where the moving elements make any kind of visual measurement highly challenging. A global sketch of the installation is given in figure 3.10.

The rig is filled with sulfur hexa-fluoride (SF_6), which is an inert gas and has similar characteristics like air in terms of viscosity and optical properties [35]. The high molecular weight of SF_6 (146 g/mol) allows simulating engine-like densities with relatively low pressure. For example, a gas density of 30 kg/m^3 is reached with pressures of about 0.5 MPa at ambient temperature. It has been seen that spray tip penetration and spreading angle generally depend on ambient density and not on pressure [33, 36] (See sec. 2.5.1 and 2.5.2).

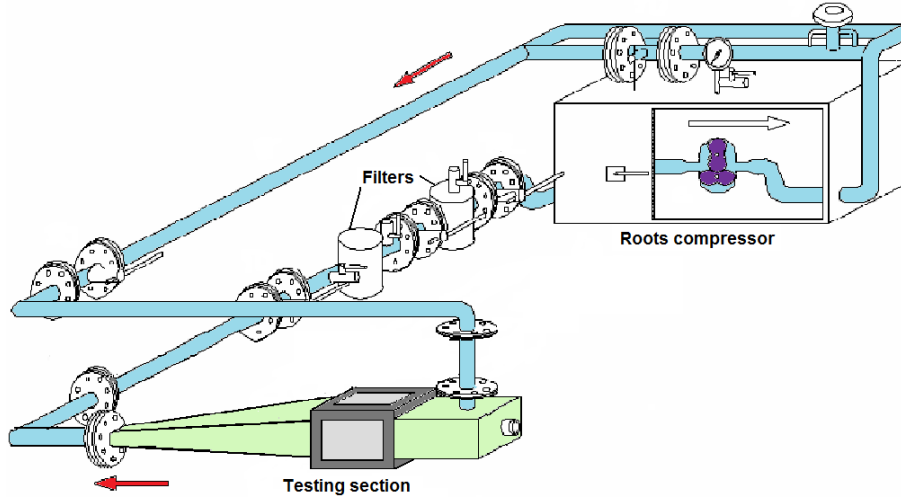


Figure 3.10: Global sketch of the cold spray visualization test rig.

This means that the experiments made in this test rig will be completely representative of the behavior of the spray under the same given conditions [37].

A constant gas stream flows in the closed-loop at a velocity lower than 3 m/s to ensure complete scavenging of the testing volume between two injection events. The maximum rate of the flow stream is 5000 L/min and the bigger particles (or droplets) are removed by a cyclonic filter while the smaller ones are stopped by a high efficiency cartridge filter. The temperature of the gas flow is controlled and all the experiments have been done at a constant temperature set to 293 K to avoid evaporation. The testing section of the rig is shown in figure 3.11 where its dimensions are displayed, the three windows are placed on both side of the injector and at the top ensuring wide optical accesses to the spray.

This rig has been designed especially to operate single-hole nozzles, and despite the fact that multi-hole injectors (generally no more than 3 orifices) can be tested, window contamination is still hard to avoid. A special cap is used to collect all but the spray under study that can therefore penetrate freely in the testing section. Single-hole nozzles with orifice coaxial with the injector axis have been preferred for this study as they present a great advantage when optical diagnostics have to be applied.

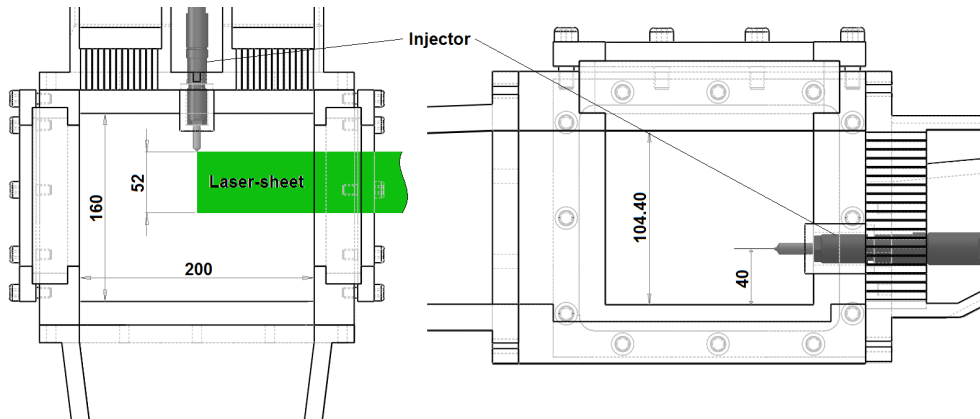


Figure 3.11: Cold spray testing section with single-hole nozzle injector and optical accesses.

3.4.2 Direct visualization of the liquid phase

Spray visualization in ambient conditions is a useful parameter as it gives the evolution of the liquid spray in terms of tip penetration and spreading angle versus time. To visualize the liquid phase does not require specific optical arrangement or equipment except a fast-shuttered or high-speed camera and the associated illumination system. The fast-shuttered camera, generally acquires one picture per event or injection and the sequence is recorded by moving the shutter in time along the development of the spray; flashes are used to freeze the image with a time gate as low as possible. On the other hand, high-speed imaging is carried out by recording a movie of one complete injection at high frame rate (generally more than 20000 frames per second).

Optical arrangement for liquid spray visualization

The large optical accesses offered by the test rig allow to perform different type of visualization:

- Direct visualization with side illumination with the camera placed perpendicularly to the lights.
- Line-of-sight visualization with diffuse back illumination.

This last technique has been chosen because it has been observed less influence of the illumination with respect to the side lighting. The line-of-sight

optical setup makes the light rays going toward the camera to be attenuated while they cross the liquid spray. The direct visualization however illuminates the spray and the reflection of light is recorded by the acquisition system. To obtain a more homogeneous background, an optical diffuser has been placed between the continuous light used and the spray, making the light more diffuse.

The image acquisition has been performed with a 12-bits CMOS-based high-speed camera (Vision Research - Phantom v12) at a frame rate of more than 40000 frames per second and a resolution of 512 x 256 pixels. The time step at this frame rate is as low as 25 μ s; and 10 injections or spray developments for each condition have been acquired.

Image processing and useful information

The image processing is one fundamental stage as it provides spray tip penetration and spreading angle versus time and is described next. As the spray is a biphasic system (liquid - gas), the difference between spray and background is difficult to evaluate and so is the spray pattern. First the background is taken and adjusted to every single image global intensity to compensate slight variations of the illumination system. Then, the adjusted backgrounds are removed from the respective individual image for the spray to be easily identified. Then, through a computer-assisted processing methodology, the spray pattern is detected.

Finally, as the boundaries of the spray are known, the definitions proposed by Naber and Siebers [33] is used to presented the different macroscopic parameters as listed below:

- *Spray boundary detection.* The spray pattern is determined as the geometrical threshold previously calculated.
- *Spray axis.* The axis is estimated as the angle bisector of the two regression lines calculated for the spreading angle.
- *Penetration distance and full cone angle.* These parameters require an iterative process as they are both inter-dependent. The penetration is the distance along the spray axis to a location where 50 % of the pixels of the half angle are inside the boundary of the spray [33]. The spreading angle of the spray is defined by:

$$\tan(\theta) = \frac{A_{ps/2}}{(s/2)^2}, \quad (3.17)$$

where $A_{ps/2}$ is the projected area of the upstream half of the spray evaluated by the spray boundary detection.

- *Local spray dispersion angle.* It is estimated as the arctangent of the spray width divided by the correspondent axial location calculated as discrete spray bins of fixed length to average out some of the turbulent structures [33].

3.4.3 Laser imaging

The domain of laser-based techniques and their number are so vast that their classification remains a problem. The information provided can be of help to categorize them: droplet size, velocity, number density, etc. The optical principle used or the nature of the method applied as well (direct or indirect) may also be other classification criteria.

Nevertheless, some techniques have been developed and widely used while they only provide results in one dimension or even for a single measuring location.

- *Fraunhofer diffraction.* This line-of-sight method was first developed by Swithenbank in 1976 [38] and an instrument (Malvern Particle Sizer - MPS) has been commercialized to measure droplet size and number density of a liquid spray. One region of the spray is illuminated by a coherent collimated monochromatic light source and the scattered signal in the near forward direction is analyzed. For different spherical droplet diameters, the Fraunhofer diffraction of the light creates a series of concentric light rings that can be related to the particle diameter. The technique presents the advantage of being easy to apply, relatively cheap and, the instrument generally provides accurate results for simple droplet distribution. However, the poor spatial resolution coming from the integration along the line-of-sight and the complex implementation in dense sprays requiring multiple scattering correction make this method inappropriate for Diesel spray analysis [39, 40].
- *Point interferometry.* This technique was first developed 45 years ago by Yeh and Cummins [41] for the measurement of flow velocity. The method has been then improved to provide the particle size, liquid flux and number density. It consists of dividing a coherent laser beam into two beams which intersect in the liquid spray with a given angle to create an interference pattern due to superposition of the two electrical fields.

When a droplet crosses the pattern, it scatters light toward a receptor that focuses the light onto a photo-detector to convert scattered light into voltage fluctuations. The signal frequency is the Doppler frequency and is directly related to droplet velocity as long as the spacing between fringes is known. By adding a second detector and under certain hypotheses, the particle diameter can be measured as the phase shifting, induced by the different detection angles, is almost linearly dependent to the diameter down to just a few micrometers [42]. The sphericity of the droplets can somehow be verified by adding a third detector. The latest advancements of the technique also named Phase Doppler Interferometry (PDA and PDPA being product names of PDI tools) have been to use the intensity of the signal as a function of droplet diameter to validate data [43, 44]; or technically to use two wavelengths ($\lambda = 514.5$ and 488nm) and two pairs of detectors [45].

The advantages of the method are the accuracy provided without complex calibration as well as the ability to measure several parameters simultaneously. On the other hand, the limitations are that it is time consuming when spray mapping is wanted as the method is point specific, there is a lack of accuracy in dense sprays and the complete equipment is expensive [39, 46].

The interferometric technique has been employed in this study to calibrate and experimentally compare the results. The instrument used is a TSI PDPA system with FSA4000 digital processor. The main specifications of the setup are:

- Laser source: Argon-ion continuous laser, $\lambda = 514.5$ nm.
- Fringe spacing: 1.8 μm .
- Scattering angle: 70° from incident direction.
- Diameter range: Up to 70 μm with refractive index of $n = 1.42$.

Full description of the PDPA equipment is provided in [47] together with the measurement strategy used for accurate results. As the main objective consists in quantitative 2-D fuel mass fraction measurements in sprays under both non-evaporative and evaporative conditions, these experimental technologies are not considered as global solutions.

For the purpose of this thesis, the Planar Laser Imaging techniques (PLI) seem to be the most suitable as they provide macroscopic and microscopic information simultaneously. The concept is quite basic as it consists in a

thin laser-sheet which traverses the spray and the photons scattered by the liquid droplets can be acquired by an acquisition system, generally placed perpendicularly. Several techniques have been developed on this basis, they potentially give a description of the spray on a macroscopic scale such as cone angle, spray tip penetration, general shape, etc. At the same time, droplets characteristics (e.g. diameter or number density) and spray dynamic (e.g. droplet velocity or vortices) can also be extracted depending on the specificity of the diagnostic applied. The techniques used in this work to study the liquid spray are briefly presented in the paragraphs below, for more details, these laser-based techniques are more extensively developed in the next chapter 4.

Planar Mie imaging

Mie scattering in sprays refers to the elastic light scattered by droplets bigger than the incident wavelength. The term "elastic scattering" defines the light emitted by particles (or molecules) at the same wavelength of the incident radiation. The electromagnetic signal scattered by the droplets is the dominant source of light in laser diagnostics for sprays under non-evaporative conditions [48,49]. It has been observed that the intensity of the light elastically scattered by a droplet of size much bigger than the wavelength was linearly dependent to the square of the droplet diameter d^2 [50–52]. Note that this is no longer valid when the particles or droplets are smaller and correction procedures are required. The theory as well as a novel experimental solution are described in chapter 4.

Planar Laser-Induced Fluorescence (PLIF)

This technique is based on the initial absorption of part of the incident radiation and the reemission of a new electromagnetic radiation at a longer wavelength. In opposite to the Mie scattering, the principle of fluorescence is inelastic as the wavelength of the emitted light is not that of the incident one. Fluorescing compounds are naturally present in commercial fuels, however, the signal emitted is difficult to quantify and a specific dye is generally added. The intensity of signal generated by the absorber (the dye) is a function of the concentration of absorber, the temperature and the ambient pressure. If the doping has been carried out appropriately, the signal emitted is isotropic and proportional to the incident light intensity. Under such assumptions, the fluorescence signal would be volume dependent and therefore linear to d^3 for spherical droplets [53,54]. To guarantee the proportionality, the range of the

size of the droplets must be known and the dye concentration carefully adjusted. More explanation concerning the parameters that affect the cubic dependency with droplet diameter is given in chapter 4.

Planar Droplet Sizing (PDS)

Also called Laser Sheet Dropsizing (LSD), this technique is based on the combination of the planar Mie imaging and Planar Laser-Induced Fluorescence [55–58]. The concept is that for a droplet excited by a laser-sheet, the volume will be given through the fluorescence signal intensity emitted by the dye contained by the liquid droplet; whereas the intensity of the Mie scattered light will represent the surface area of the same droplet. By ratioing those two signals, the Sauter Mean Diameter should be deduced:

$$SMD = \frac{S_{LIF}}{S_{Mie}} \propto \frac{\sum_i d_i^3}{\sum_i d_i^2}, \quad (3.18)$$

where S_{LIF} and S_{Mie} are respectively the signals emitted through fluorescence process and Mie scattering and d , the droplet diameter. If two cameras are used to record the fluorescence and Mie scatter signals simultaneously, fast 2-D SMD measurements can be achieved. The experimental technique presented in chapter 4 is a modification of the standard PDS, an evaluation of both is presented in the following chapter.

Laser-based measurements in sprays present obvious advantages, however, the amount of multiple light scattering detected is particularly significant due to the high number density and the wide acceptance angle of the optics required for good detection. The planar imaging methods are promising, but they also suffer from multiple scattering and large correction procedures must be implemented to get satisfying results. The main point of the PDS technique is to reduce the difference in terms of scattering behavior of the elastic and inelastic radiations. Several alternatives exist to overcome the multiple scattering matters, some of the solutions applied or potentially applicable to sprays are presented in section 3.6.

3.5 Experimental apparatus under evaporative conditions

The installations used to study the spray injected under high temperature condition will be presented in this section. A constant-volume combustion vessel with specific and large optical accesses has been used to visualize the vaporized jet. Shadowgraphy [59, 60] or Schlieren imaging [33, 61, 62], are sensitive to gradients in refractive index, formed by either density or composition differences along the line-of-sight. This technique is exclusively applied together with high-speed imaging mainly because the spray is injected under high temperature condition, and many injections are needed by regular cameras making the experiment longer and more expensive. Like for the liquid spray, quantitative results can be provided by laser measurements in the evaporative spray as well; they are now widely used and several methods are available.

This installation to simulate high pressure and high temperature conditions is called the Engine Combustion Network and is managed by Dr. Lyle Pickett (CRF - Sandia National Laboratories). This equipment is described first in this section and an analysis of the internal conditions in the core region where the spray is injected and evaporated due to high temperature (more than 900 K) is presented. The optical setup to perform Schlieren imaging of the penetrating spray is outlined then together with the process done on the high-speed movies recorded. Finally, a laser-based technique is presented as well; like for the liquid spray, this technique is developed and evaluated in chapter 5.

3.5.1 Engine Combustion Network

The disposal equipment is able to provide a wide range of ambient (charge-gas) environmental conditions that can be simulated at the time of fuel injection, allowing the effect of each variable to be assessed. With a full optical access, it can be processed ambient gas temperatures from 450 K to 1400 K, densities from 3 to 60 kg/m³ and oxygen concentrations from 0 to 21 %. These conditions fit or exceed those generally encountered in a Diesel engine.

Figure 3.12 shows a schematic cross-section of the combustion vessel. The characteristic dimension of the cubic-shaped volume section is 108 mm and each side of the combustion chamber has a round port with a diameter of 105 mm.

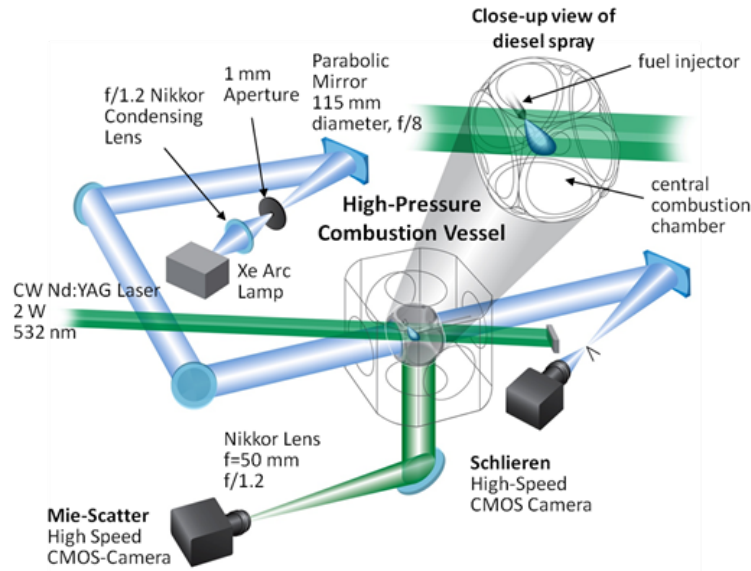


Figure 3.12: Combustion vessel used to perform experiments at high temperature (Engine Combustion Network - ECN)

Optical accesses and operation

This Engine Combustion Network in its "basic" configuration is equipped with 3 sapphire windows of 102 mm diameter to allow maximum optical access to the spray. Only two of those are used in this setup for entrance and exit of the parallel rays of light, the last one can be eventually used as a camera access. Two other metallic windows are permanently setup with the injector and its internal cooling system, which control the flow to maintain a constant temperature of 90°C and one at the top where the spark plugs are. The last window is optional and can be used for some specific experiments such as front visualization (by using another sapphire window) or soot sampling for example (with a metallic window and a purposely-designed soot collector).

Before a set of experiments, the vessel is heated up at 455 K and the ambient conditions are reached thanks to a premixed, combustible-gases mixture, which is ignited to increase pressure and temperature in the vessel. The admitted mixture is at the desired density and after premix burn, when the internal conditions match the present one, the experiment can begin and so the spray is injected into the vessel. A fan, placed in one corner of the vessel, mixes the gases so that the conditions are assumed homogeneous during injection

and spray development while the gases velocity is as low as 0.7 m/s in the core region. Reminding that spray velocity can reach around 600 m/s in the first millimeters, it is presumed that the injected spray is not veered off. The vessel is also equipped with pressure and temperature transducers to record those parameters during the experiments; the temperature being also checked by the pressure drop to adjust the cool down process.

The reactants of the pre-burn used to fill the vessel consist of acetylene (C_2H_2), hydrogen (H_2), oxygen (O_2) and nitrogen (N_2) and the molar fraction is adjusted so that complete-combustion can be assumed. After the premix combustion, the ambient conditions are changing over a relatively long time (about a second) due to heat transfer to the vessel walls, and the pressure slowly decreases. Other environments, such as exhaust-gas-recirculation used in engines, or an inert ambient (0 % O_2), were simulated by changing the reactant O_2 and N_2 concentrations. Some tables are used to calculate the amount of those different species in order to reach the ambient conditions when the fuel is injected. Two methods have been used to determine the influence of the premix burn on the left over products after combustion: gas sampling of the exhaust and closed-reactor simulation. The results of the tests indicated that for typical Diesel conditions (around 800 K to 1000 K), the products of the combustion except CO_2 , H_2O , O_2 , and N_2 were less than 0.02 %. This means that the molar fractions of the species used for generating the combustion mixture are close approximations for boundary conditions at the time of Diesel injection. In order to better control this pre-burn process, a cool down history is often recorded when the vessel is working. Actually, the vessel internal conditions may vary and that can affect the cool down, which produces some dispersions during the measurements.

Internal conditions

Specific tests have been performed in order to evaluate the temperature variation inside the combustion vessel, and more precisely, in the core region of the spray. In this aim, type R thermocouples have been used, the platinum-rhodium junction is made with really thin wires (50 μm), this leads to have a fast response in temperature and the time-resolved decay can be acquired. Those tests performed over several premix burns revealed a standard deviation along the spray region and its neighborhood of 2.1 % of the mean (about 20 mm radially from spray axis). These temperature fluctuations are one likely explanation for any variation in system performance from injection to injection.

3.5.2 Schlieren imaging

Contrary to visualization of the isothermal liquid spray, the vapor phase requires a purposely-designed optical setup. Due to their sensitivity to density gradients, shadowgraph and Schlieren imaging when applied to vaporizing fuel sprays are capable of identifying the vapor phase of the spray [33, 62]. Shadowgraphy/Schlieren techniques therefore provide important information concerning spray development when associated to high-speed imaging of Diesel sprays [63]. These visualization methods are mainly designed to record the vapor phase of the injected spray at evaporative conditions.

Optical setup for high-speed Schlieren imaging

The optical arrangement to perform high-speed Schlieren imaging of the evaporative jet in the combustion vessel is depicted in figure 3.13. In this setup, a 150 W (electrical power) mercury-xenon arc lamp with a small arc distance (1.5 mm) system was used as a continuous white light source. A white light is generally preferred in Schlieren and shadowgraph imaging as it avoids diffraction or speckle effect generated with the use of coherent light sources [33]. The light was collected with a 50 mm focal length camera lens (f/1.2 Nikkor), providing better broad wavelength performance compared to a simple achromatic lens. The light was then passed through a 1 mm aperture to form a clear point source and was then reflected by a 115 mm diameter parabolic mirror obtaining parallel rays. The light was steered into the vessel and, after crossing the testing section where the spray evaporates, the light was collimated by another parabolic mirror to be focused again at about 100 mm before entering the high-speed recording system.

A 12-bits CMOS-based high-speed camera (Vision Research - Phantom v7.1) has been used to record spray development at a frame rate of more than 45000 fps and a resolution of 256 x 128 pixels. This leads to an inter-framing time of about 22 μ s, the exposure time has been selected to use the dynamic range of the camera and was as low as 2 μ s demonstrating the quality of the light source.

Image correction and analysis

To measure the very outer part of the spray, in other terms its boundary, it is necessary to setup a system with high sensitivity to refractive index gradients. In the meantime, the heated combustion vessel will engender natural

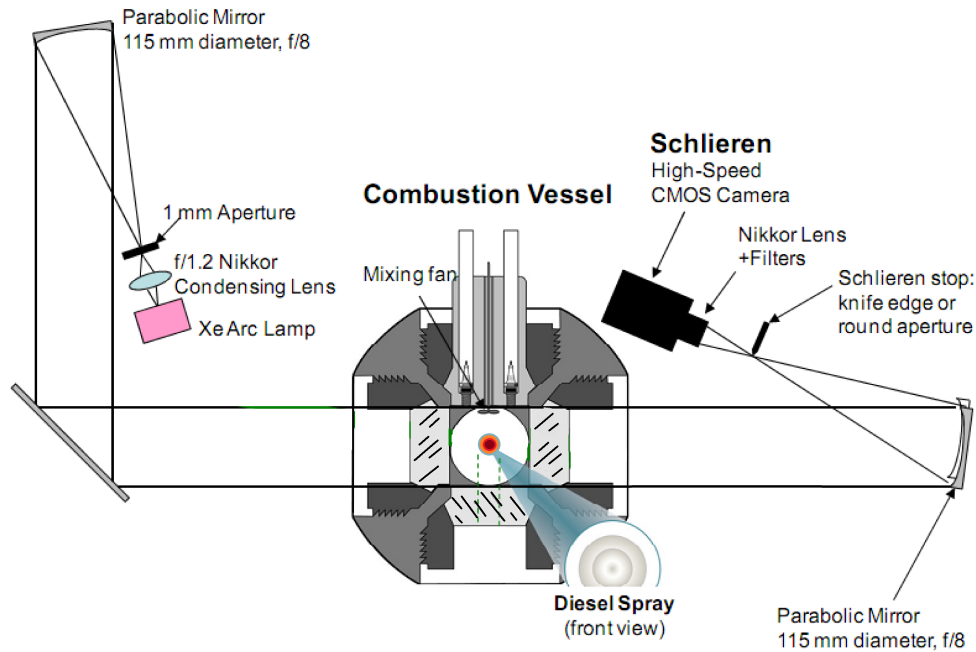


Figure 3.13: Combustion vessel and high-speed Schlieren imaging setup. Mirror spacing and angles are not scaled.

temperature gradients due to boundary layers and so this will generate refractive index inhomogeneities as well. The consequence is that the images will suffer from background moving non-uniformities as the gases are mixed with the fan to reduce temperature fluctuations within the core region. The image intensity before injection is subtracted from the image intensity at any time during injection as a background correction.

The result is that the background of the Schlieren movies appears more flat as the density gradients are well removed by the correction [64]. Any kind of analysis is now easier and more interesting characteristics of spray tip penetration under evaporative conditions can be observed. The spray analysis began with a threshold level selection to separate ambient and penetrating jet. The intensity of this threshold has been calculated as the middle of the two peaks that appeared on the histogram of the cumulative intensity as one corresponds to the spray and the other to the ambient.

Thanks to this correction, every single image of the complete development of the sprays can be treated with better accuracy. The process provides the user with the same parameters defined earlier for liquid penetrating sprays [33]:

Spray boundary, axis, penetration rate, spreading angle and local dispersion. Nevertheless, only penetration rate versus time and spreading angle are used further in this study.

3.5.3 Rayleigh scattering diagnostics

Due to many physical confines and their non-intrusive approach, optical-laser-based technologies of diagnostics have become the method of choice for quantitative measurements in vaporizing sprays. The analysis of the vapor phase of an injected spray could seem more complex as it is not visible by human vision, but it actually presents less matters than in the liquid phase. Through the years, several methods have been developed to study this part specifically, the most relevant information being the fuel to air ratio in the spray also presented as the mixture fraction.

A discussion over which technique seems to be the most suitable to get the fuel mass fraction under evaporative conditions is given in chapter 5. At first, as it does not require additive, the Rayleigh scattering technique has been preferred for quantitative measurements of the fuel concentration for this study. Another reason is that from an illumination point of view, the setup is very similar to the one used for planar laser imaging described earlier for measurements in liquids 3.4.3 which makes more sense when the objective is to compare the behavior of the spray under evaporative and non-evaporative conditions. A brief introduction of the Rayleigh scattering technique is given here, a distinction is done between the information provided by the technique: mixture fraction or temperature distributions. The theory, calibration and an exhaustive description of the technique for quantitative measurements is the object of chapter 5.

Concentration measurement via Rayleigh scattering

The Laser Rayleigh Scattering (LRS) is preferentially used for density measurement and vapor concentration studies. As for Mie, this scattering process is elastic and thus, the emitted radiation is at the same wavelength as the incident light (or almost due to Stoke shift like for Raman scattering). When a perpendicularly polarized electromagnetic radiation penetrates a medium containing particles small compared to the wavelength, the light is isotropically scattered by the particles. The signal emitted in the normal direction to the scattering plane will contain weighted information about the gas concentration or density. The Rayleigh scattering diagnostic does not require addition

of a tracer to the fuel, it is not dependent upon pressure, temperature or surrounding gases composition, as it is the case in any technique using fluorescence. The signal comes from direct interaction of the incident light and the molecules and therefore, the technique provides accurate results. As the signal is relatively strong compared to Raman for example, 2-D imaging is possible and the optical setup is very similar to that used for planar laser imaging in liquid sprays. The main downside of this method is that it may suffer from Mie scattering interferences and spurious scattering. Another matter could be that incident light and emitted signal have the same wavelength that could interfere and thus skew the results. Hence the difficulty lies in finding a way to avoid as much as possible the unwanted scatter and reflection effects from various sources. Some examples of optical noise sources could be: particles in the fuel or in the ambient, fuel droplets, and flare coming from the windows and laser-blade delivery optics.

Rayleigh thermometry

From the concentration, another parameter can be deduced from the Rayleigh scattering signal: the local temperature. Actually, when gas composition and pressure are known Rayleigh imaging allows to measure planar temperature fields, this technique called Rayleigh thermometry comes from the ideal gas law. Conceptually, if the local molar fraction of a known injected gas has been measured, then, the results of the number density can be used to determine the local temperature:

$$T = \frac{p}{K_B N} . \quad (3.19)$$

Here, T is the temperature, p the pressure of the gases or ambient pressure, N the molecular number density of the gases mixture previously measured and finally, K the Boltzmann constant. From this simple relation, a 2-D map of molar fraction measured via Planar Laser Rayleigh Scattering (PLRS) allows obtaining a similar 2-D map of adiabatic mixing temperature of the sample.

3.6 Available methods to overcome multiple scattering effects

Multiple scattering of the light crossing a medium containing scatterers like fuel droplets is a real matter. The regular techniques used to characterize the

liquid and atomized spray are known to be reliable in the dilute region, where the scattering regime is so high. However, in the dense region of the spray, due to the small distance between droplets, these techniques are not capable of measuring accurately because of the large number of photons that have been multiply scattered within the medium [65].

To overcome this multiple scattering problem, a lot of solutions are available throughout the literature. Some are computational operations, which in some way could increase the quality of the results with the use of theoretical analysis of the light scattered by the particles [66]. On the other hand, several laser-based diagnostics have been recently developed and proposed to go deeper in such turbid media like last generation Diesel sprays:

- *The interferometric laser imaging.* This technique developed for droplet sizing [67] has been first applied to sprays by Glover et al. in 1995 [68]. It is based on imaging droplets illuminated by a laser-sheet; due to interaction between reflection and refraction of the light, some fringes are created and can be imaged with adequate defocusing length. The distance between the fringes depends on droplet diameter, as long as the wavelength of the incident light is known, angle of detection and relative refractive index. The first limitation of this technique is the number of droplets that can be imaged to count the fringes with accuracy. An improvement has been done in this way [69], by a set of lenses placed between the imaging plane and the collective optics, the fringes are imaged as a line instead of a disk. This reduces the overlapping of the droplets and measurements can be done within the dense region of the spray. Still, even if the droplet size is accurately measured, this easy-to-calibrate technique requires only spherical droplets and the small size of the testing area ($4 \times 4 \text{ mm}^2$ in [69]) make it not suitable for complete real sprays analysis.
- *The double extinction.* This technique presents the same disadvantage as it can measure only small probes (line-of-sight). This method, also called 2λ or two color technique, has been developed for sprays by Parker et al. [70] and offers a measurement of the droplet size distribution along a line-of-sight based on the Beer-Lambert law (see eq. 4.10). Two collinear beams with different wavelengths (in the far infrared domain - several micrometer - to reduce scattering efficiency) cross the spray and their extinction are independently deduced from the intensity of the light with and without the spray. Assuming mono-disperse droplets or an analytical distribution of droplet size, the extinction ratio gives a unique solution of

the droplet diameter. The disadvantages of this technique, in addition to the small probed area at a time, are the size range that can be measured (droplets bigger than 20 μm can give identical extinction ratio even if their diameters are different) and the use of empirical functions for droplet size distribution that could induce errors or at least limitations.

There are, however, other methods to globally analyze the dense region of the spray; these techniques require some interest and they will be described in this section. They have been developed recently and are now applied to Diesel sprays; as they present the highest atomization regime, their analysis is a challenge of everyday for the numerous researchers working on this field.

3.6.1 X-Ray absorption

First method and certainly the most impressive one because of the so expensive equipment that it requires, the X-ray absorption has been recently applied to high pressure fuel sprays (Argonne National Laboratories). It is quite common to see X-ray radiography of broken bones, nonetheless, its application to high speed two phase flows is a lot more complicated and has been introduced in 1990 [71]. Ten years later, Powell et al. [72] were the first to perform quantitative measurements of liquid mass fraction in a fuel spray.

The main organ of the technique is a monochromatic synchrotron which generates an X-ray beam to illuminate the spray. In a line-of-sight configuration, the fuel mass fraction can be determined by the level of X-ray beam attenuation measured by a high speed Pixel Array Detector (PAD). Figure 3.14 presents a sketch of the experimental installation to perform X-ray measurements in sprays.

The particularity of the X-ray compared to the visible light is that the radiations are attenuated when going through a medium containing particles as well, but they are not deviated or scattered. This attenuation can be calculated thanks to the Beer-Lambert law [74] according to:

$$\frac{I_t}{I_0} = \exp(-\mu_m m), \quad (3.20)$$

where I_t and I_0 are the transmitted and incident X-ray intensities, μ_m the mass absorption coefficient of the fuel and m the mass of fuel in the beam. The mass absorption coefficient of the fuel μ_M is previously calibrated, an absorber has to be added to the fuel in order to increase the absorption and tests can be

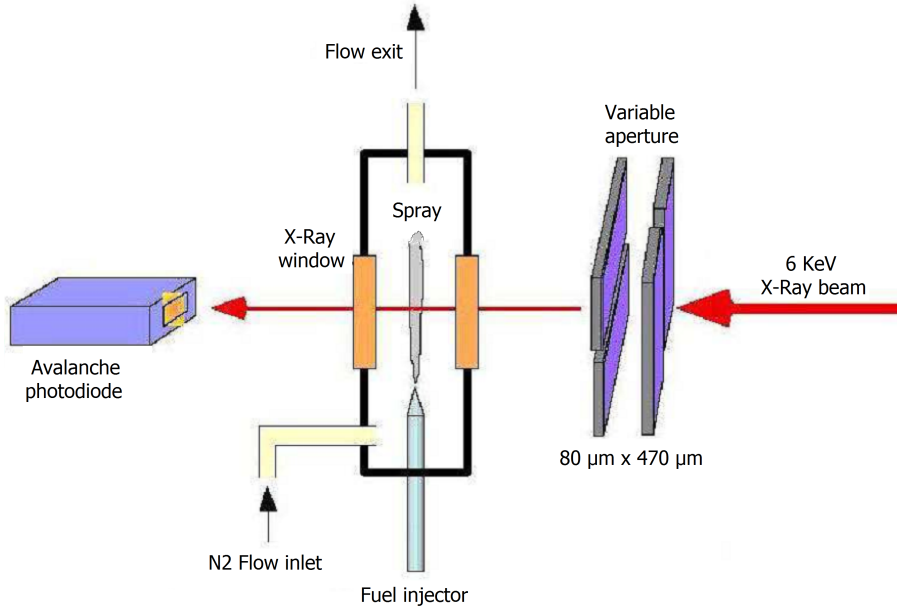


Figure 3.14: Schematic representation of the experimental setup for fuel mass fraction measurements (Powell 2004 [73]).

done on the sample to get a reference point. The mass of fuel along the path of the X-ray beam is then easily deduced from the I_t/I_0 ratio at each location on the radiography. As commented before, X-rays are not affected by multiple scattering phenomena and are highly penetrative in materials with low atomic numbers.

The technique has demonstrated several interesting parameters recently like the fact that a high pressure Diesel spray can travel at supersonic speed and the shock waves generated can be quantitatively measured [75]. Other crucial information provided by X-ray measurements is the presence of a liquid core in the near-nozzle field and the determination of its length, this has an impact on the whole breakup process (see fig. 3.15 [76]).

The use of X-ray has demonstrated to provide quantitative measurements in dense sprays because it does not suffer from multiple scattering, however, it presents some limitations. The first one is the cost of such an installation, as a synchrotron source is required, the diagnostics can be applied by only a few research institutes. The technique is not completely non-intrusive as an absorber has to be added to the fuel, the fluid properties can be altered during this process. The low signal-to-noise ratio (SNR) coming from the sensitivity of

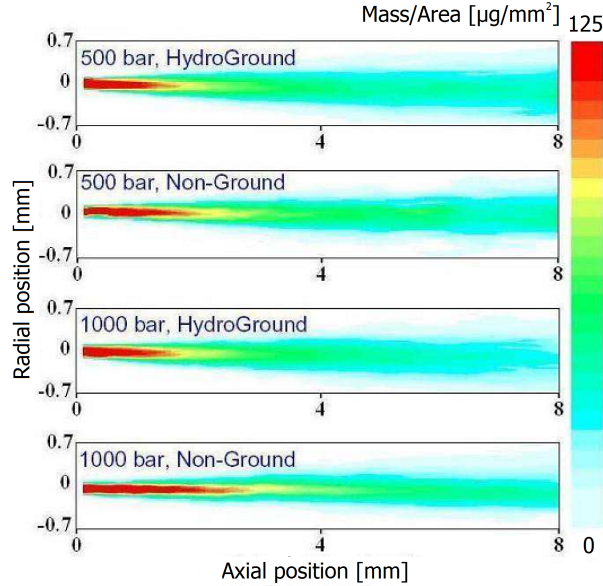


Figure 3.15: Deduction of the liquid volume fraction (LVF) represented as a mass/area ratio for a water spray using X-ray measurements (Wang 2006 [76]).

the detector and the possibility to damage it makes the experiment of a single shot almost impossible and thus results are an average over several injection cycles.

3.6.2 Ballistic imaging

Together with the X-ray absorption, the ballistic imaging technique represents a recent advance in diagnostics devoted to analyze the dense region of liquid sprays. This technique has been developed in bio-medical applications and was originally applied for imaging through tissues [77]. In 1995, Galland et al. [78] applied it to image sprays, but the limited spatial resolution led to a lack of interest within the scientific community. Almost 10 years later and the huge improvements in terms of imaging that come along with, Paciaroni and Linne [79] decided to adapt the ballistic imaging technique to obtain single shot images of a water spray with high spatial resolution (between 20 and 50 μm depending on the location). Since then, the group used the diagnostics to study a turbulent water spray, a steady spray in cross-flow and the transient part of a Diesel fuel spray [80]. The optical configuration of a typical ballistic

imaging system is proposed in figure 3.16.

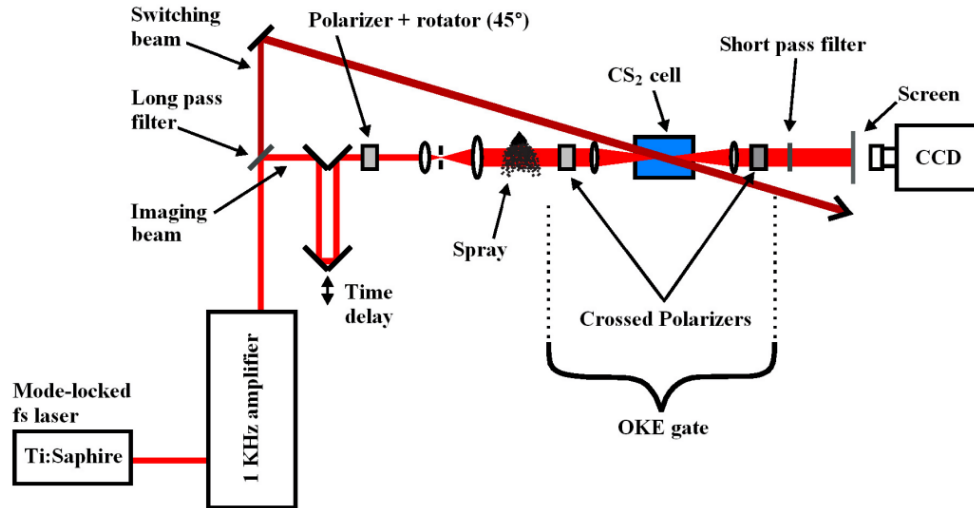


Figure 3.16: Optical configuration used for ballistic imaging in a spray (source [80]).

Ballistic imaging relies on the fact that when the light goes through a turbid medium, like the dense region of a spray, some photons pass straight while the others are multiply scattered. These non-deviated photons, called "ballistic", exit the midst with the same solid angle that they entered as they did not suffer from scattering while they were traveling in the medium. Their name comes from the fact that they travel the shortest distance as their way has not been significantly changed. A second group of photons, called "snake", travels longer as the light is scattered several times (from 1 to 9 times according to Linne et al. [80]) within the forward direction. As these photons are scattered while they travel in the midst, the distance covered is larger and they exit with a delay with respect to the ballistic photons.

It has been observed that ballistic and early snake photons (scattered from 1 to 3 times within the forward direction) conserve the structure of the media in their memory. They can be used then to rebuild the media, in this case a spray, by acquiring these photons only. In the same way, the late snake photons scattered more than 3 times lose memory of the initial structure within the medium. Some photons, scattered 10 times and more conserve no information of the structure they passed through and are called "diffuse" photons.

The difficulty of the technique, except perfect alignment of the optics, consists in extracting the ballistic and early snake photons from the laser

light signal exiting the spray. As sketched in figure 3.16, the ballistic imaging technique relies on a line-of-sight setup where an ultra-fast detection system has been used to cutoff the undesired light (late snake and diffuse photons) together with a femtosecond laser light source.

Another important property of the ballistic and early snake photons is that they keep the polarization of the incident beam when exiting the spray. This governed the researchers to use an Optical Kerr Effect (OKE) gate as high speed shutter to be placed in front of the camera because it uses the polarization properties of light. The Kerr active liquid chosen to perform such measurements was a CS_2 which offers a gate time as low as 2 ps [79]. The resulting images (see fig. 3.17) present shadowgraph properties but with a much higher spatial resolution due to the coherent characteristic of the light as the diffuse photons have been cutoff.

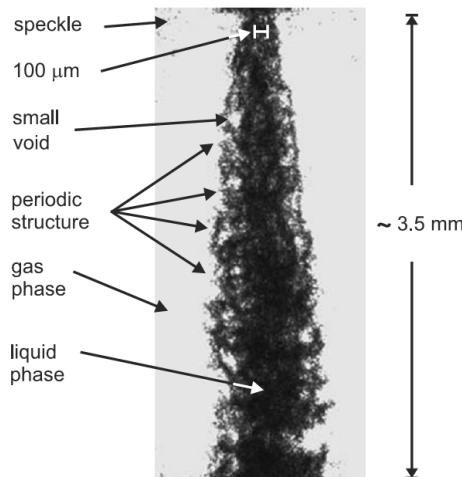


Figure 3.17: Typical image obtained through ballistic measurement of the steady period of a spray (source [80]).

Thanks to the great optical efficiency offered by the technique, ballistic imaging can be used to study the transient part of a high speed flow with instantaneous images. The near nozzle field can also be visualized, making possible the study of primary and secondary breakups although other techniques were limited in this dense region. Vector velocities [81], droplet size and extinction measurements [82] have been demonstrated as other capabilities of the ballistic imaging technique. The main drawback of the technique is the difficulty to adjust the correct time gating as it requires the calculation of photons exiting the medium, generally achieved via modeling. Finally, as it

has been commented previously, the complexity of the optical setup can also be a matter as it requires accurate alignment of the numerous elements.

3.6.3 Structured Laser Illumination Planar Imaging (SLIPI)

Planar laser imaging technique can be improved by a new laser-sheet-based diagnostic able to significantly increase the image contrast of a spray by removing the multiple scattering noise contribution. This technique using structured illumination has been first introduced by Kristensson et al. in 2008 [83]. This work demonstrated the capability of the structured illumination to remove blurring effect induced by multiple light scattering in a dynamic two phase flow. A couple of months later, the same group presented its technique as Structured Laser Illumination Planar Imaging (SLIPI) and applied it to the dense region of a hollow-cone water spray [84]. A sketch of the installation used in this work is depicted in figure 3.18.

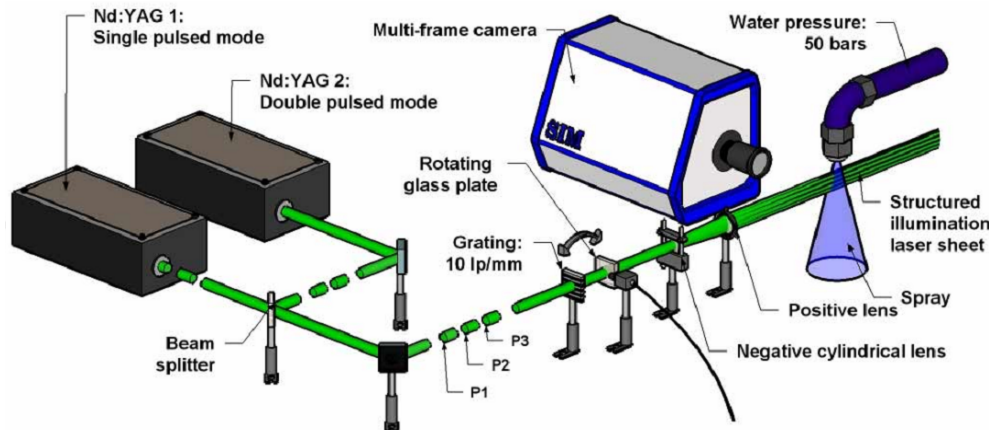


Figure 3.18: Experimental setup used in the SLIPI method to correct multiple scattering in high-speed flows (source Berrocal et al. [84]).

The technique, previously developed for fluorescence microscopy [85], is based on an incident laser-sheet which is spatially modulated along the perpendicular direction of the sheet. Three images are recorded successively while the phase is shifted by a third of a period between acquisition of each image of the set. A specific post-processing of the three images can suppress the similarities between the spatially moved incident light signals, however, the features characterized by the sinusoidal modulation are kept. The base of the method is that a photon which is multiply scattered lose the modulation in-

formation while the singly scattered one preserves it. Through different steps of calculation, the unwanted light is removed from the image leading to an image with single scattering only. A schematic description of the technique with a set of images and the related equations used for the processing is given in figure 3.19.

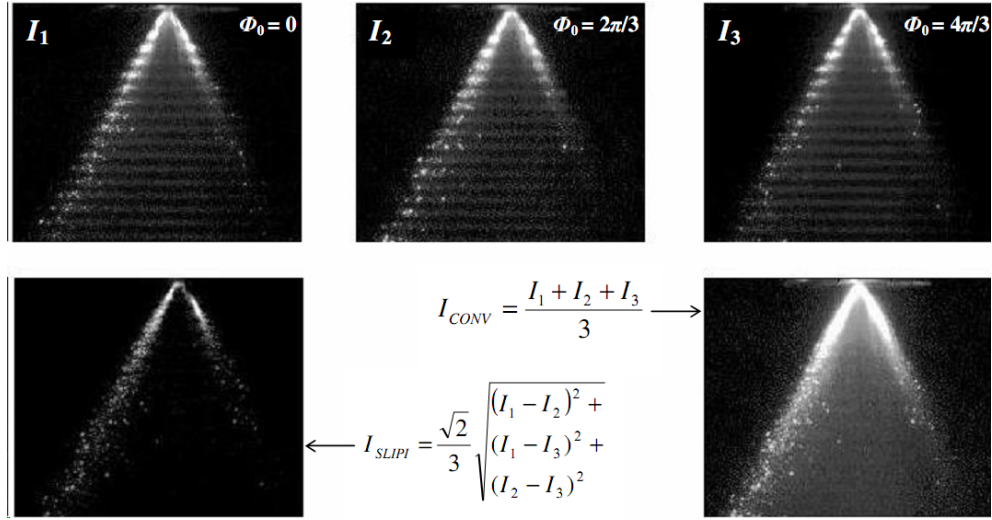


Figure 3.19: Illustration of the technique: set of 3 images (dephased of $2\pi/3$), related equations and resulting images for regular planar imaging and SLIP (source Berrocal et al. [86]).

During the evaluation of the results published in [84], the technique showed to effectively reduce the noise on the images induced by multiple scattering by suppressing up to 44 % of the total detected intensity. An additional work has been done to evaluate the technique better [86], by the implementation of the results in a modern 3-dimensional computational model. Two sprays with different atomization levels have been simulated and the results showed that the technique was still providing reasonable results even at high optical depth [86].

It has to be said that for high values of optical depth, the major part of the light has been multiply scattered, losing the structural information and thus leading to an apparent modulation depth on the individual images near zero. This might be the main limitation of the technique, when the medium is too dense optically, no information of the incident structure of the light can be extracted and the SNR of the resulting image is then too low. One other drawback of this technique is that it requires three images with an exact

phase-shifting, this means that the hardware to analyze individual sprays is quite complex and expensive (e.g. 3 cameras, 3 lasers and accurate phase-shifting).

3.7 Conclusions

Numerous experimental techniques have been used in this work to study the different aspects of the injection and disintegration process of Diesel sprays. The injection system employed to generate the sprays analyzed in this study has been presented, the autonomous equipment has been purposely-designed to drive the last generation common-rail system coupled to it. Thanks to accurate regulation of the injection pressure and control on injection timings, the precision of the injection from shot-to-shot is as high as possible for this kind of experiments. The single-hole nozzle equipping the solenoid injector has been designed for specific studies only and represents the last progresses in terms of nozzle manufacturing.

The equipments used to analyze the flow at the outlet of the injector represent a unique solution to hydraulically characterize the injection system and more particularly the nozzle. Coupled with a technique aiming at giving the internal features of the nozzle's orifice, all this equipment provides crucial information concerning the flow exiting the injector's nozzle. Parameters like time-resolved mass flow rate, momentum flux are of importance when analyzing the flow. Merging these data together with the internal geometry of the injector provide parameters like spray velocity or effective diameter; as well as dimensionless parameters such as discharge and area contraction coefficients.

For the study of isothermal sprays, a constant pressure facility equipped with full optical accesses has been used. This installation filled with an inert gas (SF_6) is capable of simulating the density conditions present in a real engine at time of injection, while keeping the temperature constant at 293 K to avoid fuel evaporation. Two-dimensional macro-visualization with back-illumination of the penetrating sprays provides paramount information with regard to the development and atomization of the injected sprays. The numerous laser diagnostics applied in this work such as laser interferometry (PDI or PDPA), planar Mie scattering or PLIF allows studying the spray from both microscopic (e.g. fuel mass fraction, droplet size) and macroscopic approaches simultaneously.

The Engine Combustion Network designed and managed by Sandia National Laboratories is a constant volume combustion optically accessible vessel. This facility can simulate high temperature and high density conditions in the range of 450 to 1400 K and from 3 to 60 kg/m³, respectively. Schlieren imaging has been performed to record the boundary of the vaporizing sprays in order to obtain spreading angle and penetration rate. Rayleigh scattering diagnostic has been described in this chapter as well in order to quantitatively determine the mixture fraction at any location in the vapor region of the jet.

Due to multiple scattering of the light in the Mie regime, the potential of alternative techniques to overcome this phenomenon is presented in the last section of this chapter. As the goal is to provide quantitative measurements in the liquid phase as well, 2-D techniques such as X-Ray absorption, ballistic imaging and more recently Structured Laser Illumination Planar Imaging (SLIPI) have been evaluated. The requirements in terms of experimental equipment of the X-Ray absorption made this diagnostic available to a few researchers only. The not-quantitative approach of the ballistic imaging removed this technique from the possible solutions to be applied in this study. Therefore, the SLIPI technique represents the best solution to remove multiple scattering in atomized liquid sprays in order to quantitatively evaluate the mixture fraction distribution.

Bibliography

- [1] A. Sou, A. Tomiyama, S. Hosokawa, S. Nigorikawa, and Y. Matsumoto. Visualization of cavitation in a two-dimensional nozzle and liquid jet. *Proc. 5th International Conference on Multiphase Flow*, 2004.
- [2] H. Chaves, C. Kirmse, and F. Obermeier. Velocity measurements of dense Diesel fuel sprays in dense air. *Atomization and sprays*, 14(6):589–609, 2004.
- [3] C. Arcoumanis, M. Badami, H. Flora, and M. Gavaises. Cavitation in real-size multi-hole Diesel injector nozzles. *SAE Paper 2000-01-1249*, 2000.
- [4] H. Li and S.H. Collicott. Visualization of cavitation in high-pressure diesel fuel injector orifices. *Atomization and Sprays*, 16(8):875–886, 2006.
- [5] J. Walther, J.K. Schaller, R. Wirth, and C. Tropea. Characterization of cavitating flow fields in transparent diesel injection nozzles using fluorescent particle image velocimetry (FPIV). *ILASS-Europe*, 2000.

-
- [6] C. Arcoumanis, H. Flora, M. Gavaises, N. Kampanis, and R. Horrocks. Investigation of cavitation in a vertical multi-hole Diesel injector. *SAE Paper 1999-01-0524*, 1999.
- [7] K. Date, H. Nobechi, H. Kano, M. Kato, and T. Oya. Experimental analysis of fuel flow characteristics in the nozzle for direct injection engines. *SAE Paper 931002*, 1993.
- [8] M. Kato, H. Kano, K. Date, T. Oya, and K. Niizuma. Flow analysis in nozzle hole in consideration of cavitation. *SAE Paper 970052*, 1997.
- [9] C. Soteriou, R. Andrews, and M. Smith. Direct injection diesel sprays and the effect of cavitation and hydraulic flip on atomization. *SAE Paper 950080*, 1995.
- [10] H. Chaves, M. Knapp, A. Kubitzek, and F. Obermeier. Experimental study of cavitation in the nozzle hole of Diesel injectors using transparent nozzles. *SAE Paper 950290*, 1995.
- [11] T. Dan, T. Yamamoto, J. Senda, and H. Fujimoto. Effect of nozzle configurations for characteristics of non-reacting Diesel fuel spray. *SAE Paper 970355*, 1997.
- [12] J. Bode, H. Chaves, W. Hentschel, A. Kubitzek, F. Obermeier, K. Schindler, and T. Schneider. Fuel spray in Diesel engines. part I: Spray formation. *ATA 92A065*, 1992.
- [13] M. Blessing, G. König, C. Krüger, U. Michels, and V. Schwarz. Analysis of flow and cavitation phenomena in Diesel injection nozzles and its effects on spray and mixture formation. *SAE Paper 2003-01-1358*, 2003.
- [14] S.H. Collicott and H. Li. True-scale, true-pressure internal flow visualization for Diesel injectors. *SAE Paper 2006-01-0890*, 2006.
- [15] A. Sou, A. Tomiyama, S. Hosokawa, S. Nigorikawa, and T. Maeda. Cavitation in a two-dimensional nozzle and liquid jet atomization. *JSME, International Journal Series B*, 49(4):1253–1259, 2006.
- [16] R. Payri, J.M. Garcia, F.J. Salvador, and J. Gimeno. Using spray momentum flux measurements to understand the influence of diesel nozzle geometry on spray characteristics. *Fuel*, 84(5):551–561, 2005.

- [17] J. M. Desantes, R. Payri, F. J. Salvador, and J. Gimeno. Measurements of spray momentum for the study of cavitation in Diesel injection nozzles. *SAE Paper 2003-01-0703*, 2003.
- [18] J. M. Desantes, R. Payri, J. M. Pastor, and J. Gimeno. Experimental characterization of internal nozzle flow and Diesel spray behavior. part I: Nonevaporative conditions. *Atomization And Sprays*, 15(5):489–516, September 2005.
- [19] J.M. Desantes, J.V. Pastor, R. Payri, and J.M. Pastor. Experimental characterization of internal nozzle flow and Diesel spray behavior. part II: Evaporative conditions. *Atomization And Sprays*, 15(5):517–543, 2005.
- [20] J.M. Desantes, R. Payri, A. Garcia, and J. Manin. Experimental study of biodiesel blends' effects on Diesel injection processes. *Energy & Fuels*, 23:3227–3235, 2009.
- [21] S. Kampmann, B. Dittus, P. Mattes, and M. Kirner. The influence of hydro grinding at VCO nozzles on the mixture preparation in a DI diesel engine. *SAE Transactions*, 105(3):1329–1339, 1996.
- [22] C. Diver, J. Atkinson, B. Befrui, H. J. Helml, and L. Li. Improving the geometry and quality of a micro-hole fuel injection nozzle by means of hydroerosive grinding. *Proceedings of the Institution of Mechanical Engineers - Part B - Engineering Manufacture*, 221(1):1–9, 2007.
- [23] V. Macián, V. Bermudez, R. Payri, and J. Gimeno. New technique for determination of internal geometry of a diesel nozzle with the use of silicone methodology. *Experimental Techniques*, 27(2):39–43, 2003.
- [24] D. Potz, W. Chirst, and B. Dittus. Diesel nozzle: The determining interface between injection system and combustion chamber. *THIESEL 2000 Conference on Thermo and Fluid-dynamic Processes in Diesel Engines, Valencia, Spain*, 2000.
- [25] Jaime Gimeno. *Desarrollo y apliccion de la medida del flujo de cantidad de movimiento de un chorro Diesel*. PhD thesis, E.T.S. Ingenieros Industriales. Universidad Politécnica de Valencia, 2008.
- [26] W. Bosch. Fuel rate indicator is a new measuring instrument for display of the characteristics of individual injection. *SAE Paper 660749*, 1966.

-
- [27] Alejandro Hernán Plazas. *Modelado unidimensional de inyectoros common-rail Diesel*. PhD thesis, E.T.S. Ingenieros Industriales. Universidad Politécnica de Valencia, Valencia (Spain), 2005.
- [28] F. Payri, J.V. Pastor, R. Payri, and J. Manin. Determination of the optical depth of a di diesel spray. *Journal of Mechanical Science and Technology*, 114, 2010.
- [29] R. Payri, FJ Salvador, J. Gimeno, and G. Bracho. A new methodology for correcting the signal cumulative phenomenon on injection rate measurements. *Experimental Techniques*, 32(1):46–49, 2008.
- [30] M. Arai, M. Shimizu, and H. Hiroyasu. Similarity between the breakup lengths of a high speed liquid jet in atmospheric and pressurized conditions. *ICLASS 1991, Gaithersburg, Maryland, 1991*.
- [31] H. Hiroyasu, M. Arai, and M. Shimizu. Break-up length of a liquid jet and internal flow in a nozzle. *ICLASS 1991, Gaithersburg, Maryland, 1991*.
- [32] F. Ruiz. A few useful relations for cavitating orifices. *ICLASS 1991, Gaithersburg, Maryland*, pages 595–602, 1991.
- [33] J. Naber and D. Siebers. Effects of gas density and vaporization on penetration and dispersion of diesel sprays. *SAE Paper 960034*, 1996.
- [34] D.L. Siebers. Scaling liquid-phase fuel penetration in diesel sprays based on mixing-limited vaporization. *SAE Paper 1999-01-0528*, 1999.
- [35] J.V. Pastor, J.J. Lopez, J.E. Juliá, and J.V. Benajes. Planar laser-induced fluorescence fuel concentration measurements in isothermal diesel sprays. *Optics Express*, 10(7):309–323, 2002.
- [36] F. Payri, J. M. Desantes, and J. Arrègle. Characterization of DI diesel sprays in high density conditions. *SAE Paper 960774*, 1996.
- [37] R. Reitz and F. Bracco. On the dependence of spray angle and other spray parameters on nozzle design and operating conditions. *SAE Paper 790494*, 1979.
- [38] J. Swithenbank, J.M. Beer, D.S. Taylor, D. Abbot, and G.C. McCreath. A laser diagnostic technique for the measurement of droplet and particle size distribution. *AIAA, Aerospace Sciences Meeting*, 1976.

- [39] D.A. Greenhalgh and M. Jermy. Laser diagnostics for droplet measurements for the study of fuel injection and mixing in gas turbines and ic engines. *Applied combustion diagnostics*, pages 408–438, 2002.
- [40] J.V. Pastor, R. Payri, L. Araneo, and J. Manin. Correction method for droplet sizing by laser-induced fluorescence in a controlled test situation. *Optical Engineering*, 48:013601, 2009.
- [41] Y. Yeh and H.Z. Cummins. Localized fluid flow measurements with an he-ne laser spectrometer. *Applied Physics Letters*, 4:176, 1964.
- [42] F. Durst and M. Zare. Laser doppler measurements in two-phase flows. *Proceedings LDA-Symposium, Copenhagen*, pages 403–429, 1976.
- [43] S.V. Sankar and W.D. Bachalo. Response characteristics of the phase doppler particle analyzer for sizing spherical particles larger than the light wavelength. *Applied optics*, 30(12):1487–1496, 1991.
- [44] W.D. Bachalo and M.J. Houser. Development of the phase/doppler spray analyzer for liquid drop size and velocity characterizations. *AIAA, SAE, and ASME, Joint Propulsion Conference, Cincinnati, OH*, 1984.
- [45] C. Tropea. Laser doppler anemometry: recent developments and future challenges. *Measurement Science and Technology*, 6(6):605–619, 1995.
- [46] R. Payri, F.J. Salvador, J. Gimeno, and V. Soare. Determination of diesel sprays characteristics in real engine in-cylinder air density and pressure conditions. *Journal Of Mechanical Science And Technology*, 19(11):2040–2052, 2005.
- [47] L. Araneo, V. Soare, R. Payri, and J. Shakal. Setting up a PDPA system for measurements in a Diesel spray. *Journal of Physics: Conference Series*, 45:85, 2006.
- [48] A. D’alessio. Laser light scattering and fluorescence diagnostics of rich flames produced by gaseous and liquid fuels. *Particulate Carbon: Formation During Combustion*, pages 207–259, 1981.
- [49] F. Beretta, A. Cavaliere, and A. D’alessio. Ensemble laser light scattering diagnostics for the study of fuel sprays in isothermal and burning conditions. *Symposium (International) on Combustion*, 20(1):1249–1258, 1985.

-
- [50] M. Kerker. The scattering of light and other electromagnetic radiation. *Academic Press, London*, 1969.
- [51] H.C. Van De Hulst. Light scattering by small particles. *Dover Publications, Inc., New-York*, 1981.
- [52] C.F. Bohren and D.R. Huffman. Absorption and scattering of light by small particles. *Wiley-Interscience, New York*, 1983.
- [53] A.C. Eckbreth. Laser diagnostics for combustion species and temperature. *Abacus, Cambridge, Mass*, pages 249–252, 1988.
- [54] P. Andresen, G. Meijer, H. Schluter, H. Voges, A. Koch, W. Hentschel, W. Oppermann, and E. Rothe. Fluorescence imaging inside an internal combustion engine using tunable excimer lasers. *Applied Optics*, 29(16):2392–2404, 1990.
- [55] C.N. Yeh, H. Kosaka, and T. Kamimoto. A fluorescence/scattering imaging technique for instantaneous 2-D measurement of particle size distribution in a transient spray. *3rd International Congress on Optical Particle Sizing, Yokohama, Japan*, pages 355–361, 1993.
- [56] P. Le Gal, N. Farrugia, and D.A. Greenhalgh. Development of laser sheet drop sizing (lsd) for spray characterization. *IMEchE conference transactions*, pages 113–120, 1998.
- [57] D.A. Greenhalgh. Planar measurements of fuel vapour, liquid fuel, liquid droplet size and soot. *Planar Optical Measurement Methods for Gas Turbine Components*, pages 1–7, 1999.
- [58] M.C. Jermy and D.A. Greenhalgh. Planar dropsizing by elastic and fluorescence scattering in sprays too dense for phase doppler measurement. *Applied Physics B: Lasers and Optics*, 71(5):703–710, 2000.
- [59] N. Chinzei, G. Masuya, T. Komuro, A. Murakami, and K. Kudou. Spreading of two-stream supersonic turbulent mixing layers. *Physics of Fluids*, 29:1345, 1986.
- [60] C. Badock, R. Wirth, A. Fath, and A. Leipertz. Investigation of cavitation in real size Diesel injection nozzles. *International Journal of Heat and Fluid Flow*, 20(5):538–544, 1999.
- [61] D. Papamoschou and A. Roshko. Observations of supersonic free shear layers. *Sadhana*, 12(1):1–14, 1988.

- [62] G.S. Settles. Schlieren and shadowgraph techniques: visualizing phenomena in transparent media. *Springer, Berlin, Heidelberg, New-York*, 2001.
- [63] R. Ochoterena, M. Larsson, S. Andersson, and I.G. Denbratt. Optical studies of spray development and combustion characterisation of oxygenated and fischer-tropsch fuels. *SAE Paper 2008-01-1393*, 2008.
- [64] L.M. Pickett, S. Kook, and T.C. Williams. Visualization of diesel spray penetration, cool-flame, ignition, high-temperature combustion, and soot formation using high-speed imaging. *SAE Paper 2009-01-0658*, 2(1):439, 2009.
- [65] M.B. van der Mark, M.P. van Albada, and A. Lagendijk. Light scattering in strongly scattering media: multiple scattering and weak localization. *Physical Review B*, 37(7):3575–3592, 1988.
- [66] E. Berrocal, I. Meglinski, and M. Jermy. New model for light propagation in highly inhomogeneous polydisperse turbid media with applications in spray diagnostics. *Optics Express*, 13:9181–9195, 2005.
- [67] R. Ragucci, A. Cavaliere, and P. Massoli. Drop sizing by laser light scattering exploiting intensity angular oscillation in the mie regime. *Particle & Particle Systems Characterization*, 7(1-4):221–225, 1990.
- [68] A.R. Glover, S.M. Skippon, and R.D. Boyle. Interferometric laser imaging for droplet sizing: a method for droplet-size measurement in sparse spray systems. *Applied Optics*, 34(36):8409–8421, 1995.
- [69] M. Maeda, T. Kawaguchi, and K. Hishida. Novel interferometric measurement of size and velocity distributions of spherical particles. *Measurement Science and Technology*, 11:L13–L18, 2000.
- [70] T.E. Parker, L.R. Rainaldi, and W.T. Rawlins. A comparative study of room-temperature and combusting fuel sprays near the injector tip using infrared laser diagnostics. *Atomization and Sprays*, 8(5):565–600, 1998.
- [71] J.M. Char, K.K. Kuo, and K.C. Hsieh. Observations of breakup processes of liquid jets using real-time X-ray radiography. *Journal of Propulsion and Power*, 6:544–551, 1990.
- [72] C.F. Powell, Y. Yue, R. Poola, and J. Wang. Time-resolved measurements of supersonic fuel sprays using synchrotron x-rays. *Journal of synchrotron radiation*, 7(6):356–360, 2000.

-
- [73] C. Powell, S. Ciatti, S.K. Cheong, J. Liu, and J. Wang. X-ray characterization of diesel sprays and effects of nozzle geometry. *Proceedings of the Diesel Engine Emission Reduction Conference*, 2004.
- [74] A. Beer. Bestimmung der absorption des rothen lichts in farbigen flüssigkeiten. *Annalen der Physik und Chemie*, 86(2), 1852.
- [75] A.G. MacPhee, M.W. Tate, C.F. Powell, Y. Yue, M.J. Renzi, A. Ercan, S. Narayanan, E. Fontes, J. Walther, J. Schaller, et al. X-ray imaging of shock waves generated by high-pressure fuel sprays. *Science*, 295(5558):1261–1263, 2002.
- [76] J. Wang, Y. Wang, K.S. Im, K. fezzaa, and W. Lee. X-ray vision of an air-assisted sprays: from radiography to quantitative phase-contrast imaging. *ICLASS 2006*, 2006.
- [77] J.C. Hebden, R.A. Kruger, and K.S. Wong. Time resolved imaging through a highly scattering medium. *Applied optics*, 30(7):788–794, 1991.
- [78] P.A. Galland, X. Liang, L. Wang, K. Breisacher, L. Liou, P.P. Ho, and R.R. Alfano. Time-resolved optical imaging of jet sprays and droplets in highly scattering medium. *ASME - HTD*, 321:585–588, 1995.
- [79] M. Paciaroni and M. Linne. Single-shot, two-dimensional ballistic imaging through scattering media. *Applied optics*, 43(26):5100–5109, 2004.
- [80] M. Linne, M. Paciaroni, T. Hall, and T. Parker. Ballistic imaging of the near field in a diesel spray. *Experiments in Fluids*, 40(6):836–846, 2006.
- [81] D.L. Sedarsky, M.E. Paciaroni, M.A. Linne, J.R. Gord, and T.R. Meyer. Velocity imaging for the liquid-gas interface in the near field of an atomizing spray: proof of concept. *Optics letters*, 31(7):906–908, 2006.
- [82] D. Sedarsky, E. Berrocal, and M. Linne. Ballistic imaging for measurement of flow structures in dense multiphase media. *14th International Symposium on Applications of Laser Techniques to Fluid Mechanics, Lisbon*, pages 7–10, 2008.
- [83] E. Kristensson, E. Berrocal, M. Richter, S.G. Pettersson, and M. Aldén. High-speed structured planar laser illumination for contrast improvement of two-phase flow images. *Optics letters*, 33(23):2752–2754, 2008.

- [84] E. Berrocal, E. Kristensson, M. Richter, M. Linne, and M. Aldèn. Application of structured illumination for multiple scattering suppression in planar laser imaging of dense sprays. *Optics Express*, 16:17870–17881, 2008.
- [85] T. Breuninger, K. Greger, and E.H.K. Stelzer. Lateral modulation boosts image quality in single plane illumination fluorescence microscopy. *Optics letters*, 32(13):1938–1940, 2007.
- [86] E. Berrocal, E. Kristensson, D. Sedarsky, and M. Linne. Analysis of the slipi technique for multiple scattering suppression in planar imaging of fuel sprays. *ICLASS 2009, Vail, Colorado, USA*, 2009.

Chapter 4

Mixture fraction measurement in isothermal spray

Contents

4.1	Introduction	116
4.2	Propagation of light in media containing scatterers	117
4.2.1	Mie scattering and fluorescent emission of a single droplet	117
4.2.2	Light radiation propagation in turbid media	123
4.3	Technique development and calibration	126
4.3.1	Design of a specific experiment	128
4.3.2	Evaluation of the conventional PLI in known situation	130
4.3.3	Scattering correction via Structured Planar Laser Imaging	133
4.3.4	Further considerations for quantitative measurements	136
4.4	Application to sprays	141
4.4.1	Experimental setup	142
4.4.2	Fluorescence properties of the dyed fuel	146
4.4.3	Theoretical evaluation of the PDS parameters	151
4.5	Quantitative measurements in a spray	154
4.5.1	Spray sizing via Structured Planar Laser Imaging	154
4.5.2	Light extinction between illumination and acquisition	159
4.5.3	Mixture fraction	162
4.6	Conclusions	169
	Bibliography	170

4.1 Introduction

For more than two decades now, the laser-based techniques are widely used to analyze the specificity and the complexity of sprays. As introduced briefly in section 3.4.3 there are several solutions to go deeper into spray analysis. However, with the improvements or difficulties encountered with the different experimental techniques, some have been preferred by the researchers. The planar imaging offers several advantages, the main one being to generally allow quick and global analysis of the entire spray.

Planar laser imaging relies on the fact that a section of the spray can be cut by a thin laser-sheet. The laser radiation propagates through the droplets and transmits the light according to an elastic scattering process governed by the Lorenz-Mie theory formulated more than a century ago [1, 2]. These independent formulations have been adapted to modern physics [3, 4] and are extensively applied in engine researches mainly to study the liquid part of the spray [5–7].

The Planar Laser Induced Fluorescence (PLIF) [8–12] is an extension of the planar laser imaging technique. Used either for gases or liquids, it assumes that the quantity (or mass) of the substance under study is proportional to the fluorescent emission intensity; since this is true, the concentration of the substance can be obtained.

The relative Sauter Mean Diameter can also be calculated by dividing the two signals obtained, i.e. fluorescence and elastic Mie scattering as introduced in section 3.4.3. Proposed in 1993 by Yeh et al. [13, 14] this 2-D droplet sizing technique assumes surface dependence with droplet diameter for the elastically scattered light signal and volume dependence for the fluorescent emission. To perform this work, TMPD (1% by weight) was used as fluorescent dopant and both images (fluorescent emission and Mie scattering) were acquired simultaneously.

Since then, many researchers concentrated their efforts on this field and spray analysis using the LIF/Mie ratio became more and more important [15–20]. In 2001, Domann and Hardalupas [21] made an evaluation of the parameters that influence the Planar Droplet Sizing (PDS) technique. Two years later, the same authors [22] undertook some works whose purpose was to provide all necessary steps required for quantitative SMD measurements in dense sprays using this PDS technique. Simultaneously, Pastor et al. [23], presented a methodology for concentration measurements of Diesel sprays in

isothermal conditions using the Planar Laser-Induced Natural Fluorescence (PLINF). This work considered the natural fluorescence of a commercial Diesel fuel with an excitation wavelength of 355nm and did not require doping of the system while all previous studies used a fluorescent dye and appropriate excitation wavelength (generally 532 nm).

There are, however, some problems when the objective is to study dense optical media like modern Diesel sprays with planar laser imaging mainly due to multiple light scattering [24–27]. This chapter first presents a theoretical approach of the propagation of the light emitted by a droplet through scattering and fluorescence processes and the scattering of light by an ensemble of small droplets. An evaluation of the planar laser imaging techniques in media containing scatterers is performed and a method to correct multiple scattering issues in optically dense media is proposed and evaluated. The calibration of the technique to measure mixture fraction in non-evaporative Diesel sprays is detailed including the fluorescence properties of the fuel used and the results are presented and compared to other experimental techniques or models. The conclusions concerning the measurement of the fuel mass fraction in a spray injected under non-evaporative conditions are finally drawn.

4.2 Propagation of light in media containing scatterers

The interaction between electromagnetic waves and particles has been studied for many years and represents an important part of the optic physics. The first description of the interaction between light and a single sphere has been described by Lorenz in 1890 [28] without using Maxwell's equations, thus making some assumptions. Almost 20 years later, a formulation resolving the Maxwell's equations is produced by Mie [2] and provides similar results to Lorenz's one. This theory completed by Debye [29], is widely known as the Mie theory (Lorenz - Mie theory (LMT) is also commonly used) and represents the absolute reference to study the diffusion of light by particles.

4.2.1 Mie scattering and fluorescent emission of a single droplet

Before analyzing the propagation of light into a collection of droplets, a quick recall of the theory of the light signals emitted by a single particle for both

elastic or inelastic radiation is presented. First, an introduction of the theoretical concepts of diffusion of an electromagnetic wave when interfering with a particle is provided. A presentation of the concepts of fluorescence follows and a description of the important parameters controlling the intensity of the fluorescent emission is finally proposed.

Quick recall of the theory of light scattering

Scattering refers to light - particle interaction which transforms the incident radiation into a resulting electromagnetic radiation of identical or different properties. When a particle is irradiated by an electromagnetic wave, the electrical charges of the molecules are excited and oscillate due to the electric field of the incident wave. This oscillations depends upon several parameters and may produce a change in the electromagnetic radiation over all directions. The electromagnetic energy emitted is then called scattered radiation [30] and the wavelets emitted interfere one to each other, resulting in several preferential final scattering directions.

The Lorenz - Mie theory describes this physical phenomenon of light scattering by spherical particles and is only valid for homogeneous, isotropic and non-magnetic particles [2]. Gouesbet and Gréhan [31] proposed a generalized version of this theory considering the Gaussian intensity profile of the incident laser beam. Mie's formulation of light diffusion is known to be complex as it requires a solid mathematical development; however, a basic approach of the scattering theory is more than enough to introduce this mechanism.

As a beginning, considering non-absorbing spheres, the total intensity of the incident light will be diffused through an elastic scattering process over all directions. The intensity of the scattered light I_s at any point at a large distance l from a particle can be expressed as [3]:

$$I_s(\beta, \varphi) = \frac{\lambda^2 F(\beta, \varphi)}{4\pi^2 l^2} I_0 . \quad (4.1)$$

Where I_s and I_0 are the scattered and the incident light intensity respectively and λ the wavelength of the electromagnetic radiation. The scattering coefficient $F(\beta, \varphi)$ is a dimensionless function providing the preferential direction of the scattered light expressed in the Cartesian coordinate angles β and φ . Figure 4.1 shows the scattering coordinates used in this formulation.

If the scatterer is spherical, the intensity scattered is independent of φ and

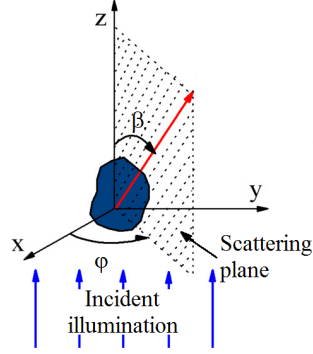


Figure 4.1: Schematic of the directions and angles of the incident and scattered photons.

can be expressed in terms of the amplitude scattering function $S(\beta)$ as:

$$I_s(\beta) = \frac{\lambda^2 S^2(\beta)}{4\pi^2 l^2} I_0 . \quad (4.2)$$

From the amplitude scattering function, the scattering phase function $P(\beta)$ can be defined:

$$P(\beta) = \frac{\lambda^2 S^2(\beta)}{4\pi^2 \sigma_s} . \quad (4.3)$$

The scattering phase function has no physical dimension and its integral over all directions is equal to 1. An example of polar Mie scattering phase function is given in figure 4.2 for a 20 μm fuel droplet, assuming unpolarized illumination.

A new parameter is introduced here, the scattering cross-sectional area or scattering cross-section; it is defined as follows for a spherical particle [3]:

$$\sigma_s = \frac{\lambda^2}{2\pi} \int_0^\pi S^2(\beta) \sin(\beta) d\beta . \quad (4.4)$$

The scattering cross-section σ_s corresponds to the surface-area where the energy of the incident radiation falling on this area equals the total energy scattered in all directions. Another parameter is obtained by dividing the scattering cross-section by the geometrical cross-sectional area projected onto a plane

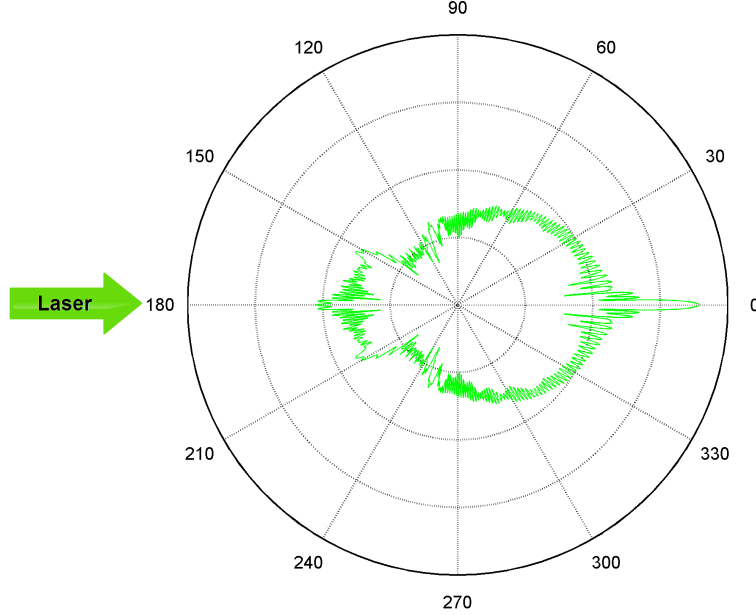


Figure 4.2: Mie scattering phase function of a spherical fuel droplet illuminated at $\lambda = 532 \text{ nm}$ from the left side (Calculated from Bohren and Huffman's code [30]). Droplet diameter is $20 \mu\text{m}$, incident radiation is unpolarized and the scattered intensity is on log-scale.

perpendicular to the incident beam, the scattering efficiency factor Q_s which allows the following formulation of the scattering cross-section:

$$\sigma_s = \frac{\pi d^2}{4} Q_s, \quad (4.5)$$

with d the diameter of the particle so that $\frac{\pi d^2}{4}$ would be its geometrical cross-sectional area. The scattering efficiency factor Q_s can be either lower or higher than the unity 1, this means that for an illuminated particle, the area shadowed can be bigger or smaller than the geometrical cross-section. For droplets bigger than the wavelength (for example $\lambda = 532 \text{ nm}$), the shadowed area is generally bigger than the geometrical cross-section area. This is partially due to the fact that some energy is removed by interference between the scattered radiation and the incident wave. Figure 4.3 shows the evolution of the scattering efficiency factor Q_s as a function of the particle diameter considering an incident illumination wavelength of 532 nm .

By replacing equation 4.5 into equation 4.3 and combining this new expres-

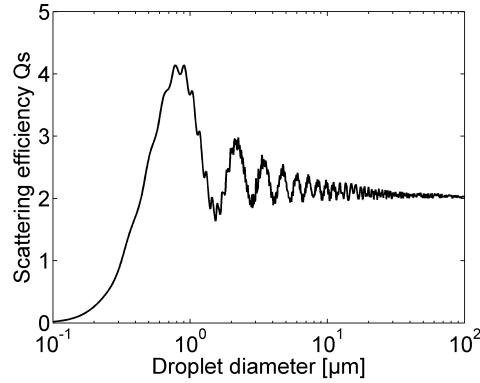


Figure 4.3: Scattering efficiency factor of a spherical droplet ($n = 1.42$) as a function of the droplet diameter. Incident radiation wavelength is 532 nm.

sion of the scattering phase function with equation 4.2, the following expression of the scattered intensity is obtained:

$$I_s = \frac{2\pi}{l^2} \frac{\int_0^\pi P(\beta)}{\frac{\pi d^2}{4} Q_s} I_0 . \quad (4.6)$$

As presented on figure 4.3, the scattering efficiency factor Q_s is oscillating around 2 for droplets bigger than the wavelength. Thus the intensity of the light scattered by a single droplet will be dependent on the square of the diameter of the droplet as shown in equation 4.6.

Concepts of fluorescence

Fluorescence is a member of the luminescence family of processes in which susceptible molecules emit light from electronically excited states created by either a physical (for example, absorption of light), mechanical (friction), or chemical mechanism. Generation of luminescence through excitation of a molecule by ultraviolet or visible light photons is a phenomenon called photoluminescence, which is formally divided into two categories: fluorescence and phosphorescence, depending upon the electronic configuration of the excited state and the emission pathway. If the electronic transition which generates the photon occurs between electronic orbitals with the same spin, the process is called fluorescence; whereas phosphorescence occurs when the electronic transition occurs between orbitals with different spins. When a photon is absorbed, the

energy makes an electron of the molecule to be transferred to an orbital spin of higher energy level. This process is conceptually described in a Jablonski diagram named after its inventor and presented in figure 4.4.

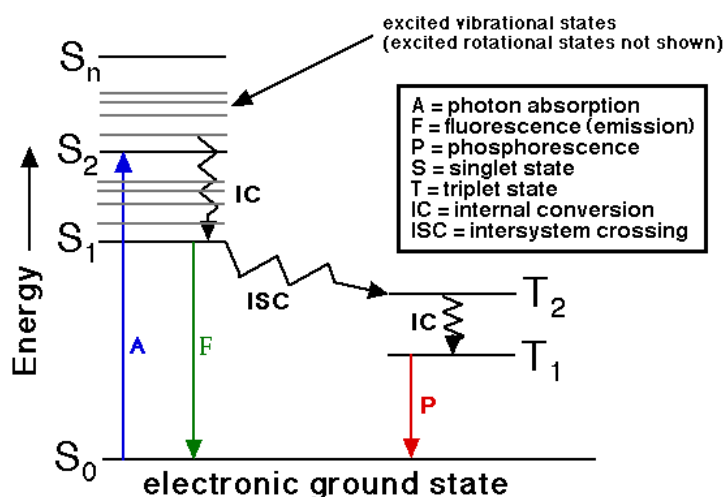


Figure 4.4: Conceptual diagram of fluorescent emission process (Jablonski [32]).

Fluorescence is the property of some atoms and molecules to absorb light at a particular wavelength and to subsequently emit light of longer wavelength after a brief interval, called the fluorescence lifetime. The process of phosphorescence occurs in a manner similar to fluorescence, but with a much longer excited state lifetime. The fluorescence process is governed by three important events, each of them occurs at timescales that are separated by several orders of magnitude. Excitation of a susceptible molecule by an incoming photon happens in femtoseconds (10^{-15} seconds), while vibrational relaxation of excited state electrons to the lowest energy level is much slower and can be measured in picoseconds (10^{-12} seconds). The final process is the emission of photons at a longer wavelength and then the molecule returns to the ground state; this occurs in the relatively long time period of nanoseconds (10^{-9} seconds) called fluorescence lifetime [33], which is as short as a laser pulse.

From a practical point of view, the fluorescence phenomenon can be briefly explained as the re-emission of part of the incident radiation at a longer wavelength when some substances, called fluorophore, are illuminated. According to the Beer-Lambert law [34], it is possible to relate the measured fluorescence

intensity with the concentration of the fluorescent substance, or absorbers. The following formulation of the Beer-Lambert's law gives the intensity of the light signal after absorption into a liquid sample of optical path L_{opt} and dye concentration c [35]:

$$\frac{I_t}{I_0} = \exp(-\varepsilon L_{opt} c) . \quad (4.7)$$

In this equation, I_t is the light intensity at the exit of the sample, I_0 the laser irradiance and ε the molar absorptivity of the dye. This simply leads to the fluorescence intensity emitted along the path of a ray of light inside a droplet for example expressed by the following mathematical expression:

$$I_f = \Phi I_0 (1 - \exp(-\varepsilon L_{opt} c)) . \quad (4.8)$$

The fluorescence quantum yield Φ is the ratio of photons absorbed to photons emitted through fluorescence. In other words the quantum efficiency gives the probability of the excited state being deactivated by fluorescence rather than by another non-radiative mechanism.

Many works affirm that the signal emitted by a droplet containing a fluorescent substance and homogeneously illuminated at a wavelength within the absorption spectrum is dependent to the droplet volume [9,10,12,13,15,16,18,36]. If a cubic volume (droplet) of side dimension d illuminated by a homogeneous beam is considered, the intensity emitted through fluorescence would be dependent to the cross-section of the cube d^2 and its pathlength d . The result is a d^3 dependency of the fluorescent emission intensity. It has been observed that this behavior was similar in spherical droplets under certain conditions [15,17,36–38] and thus the global fluorescent emission intensity can be expressed as:

$$I_f = k_f \Phi I_0(\varepsilon c d^3) . \quad (4.9)$$

Here, k_f is a constant which accounts for the signal extinction inside the droplet mainly due to auto-absorption. This dependency however is the result of different parameters and will be the object of further investigation in section 4.4.2.

4.2.2 Light radiation propagation in turbid media

The propagation of electromagnetic waves into a collection of particles is subject to attenuation and multiple scattering phenomena. Those processes may

induce errors when measurements of droplet size and concentration are performed and depend on the scattering regime, droplet size distribution and optical depth τ principally [26, 27, 39]. Multiple scattering is responsible of changes in the trajectories of the photons as depicted in figure 4.5 which interact with the particles causing losses in the original singly scattered signal emitted by the droplets. This deviation of the photon mainly depends on particle size and refractive indices and can be quantified by the measure of the optical depth.

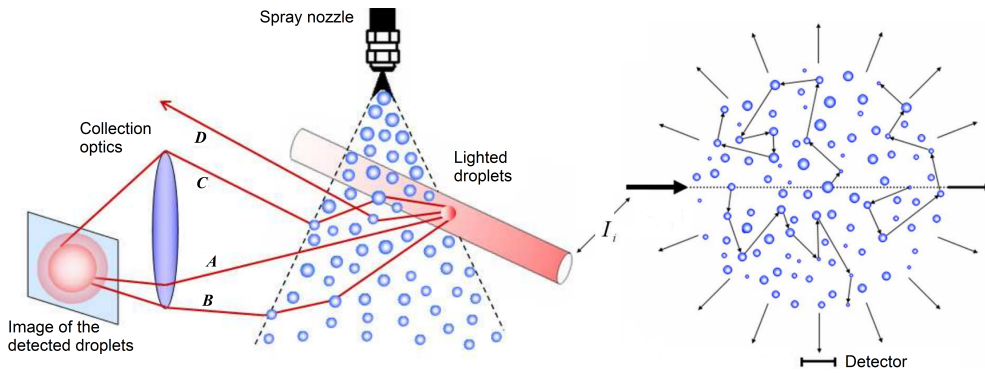


Figure 4.5: Illustration of the propagation of light in an optically thick medium with significant effects produced by multiple scattering.

An other process can affect the light signal which propagates in the medium: the absorption. This process depends upon the physico-chemical properties of the substance under study and is wavelength dependent. When a fluorescent dye is added to the particles or droplets, the signal emitted is directly proportional to the absorption of this substance as described in the previous section 4.2.1. The combined effect of these two processes (scattering and absorption) is called extinction and describes the attenuation of light traveling into a turbid media. The Beer-Lambert law is commonly used to express the extinction of light traveling into an optically thick homogeneous medium with constant extinction along the path such that:

$$I_t = I_0 \exp(-\mu_e L_{opt}), \quad (4.10)$$

where I_0 and I_t are the intensities of the incident radiation and the transmitted light exiting the sample in the original direction, L_{opt} is the pathlength of the sample under study and μ_e is the extinction coefficient which can be expressed

as the sum of the scattering coefficient and the absorption coefficient:

$$\mu_e = \mu_s + \mu_a . \quad (4.11)$$

Each of these coefficients is proportional to the number density N (number of particle per unit volume) and to the respective extinction, scattering and absorption cross-section σ_e , σ_s and σ_a as:

$$\mu_e = N \sigma_e , \mu_s = N \sigma_s \text{ and } \mu_a = N \sigma_a . \quad (4.12)$$

The optical depth τ can be defined from the two previous equations such that:

$$\tau = \mu_e L_{opt} = N \sigma_e L_{opt} . \quad (4.13)$$

The optical depth measures the extinction of light through a turbid media, as shown in equation 4.13, it corresponds to the product of the number density, the cross-section and the distance within the sample. The extinction cross-section σ_e is the result of the scattering and absorption cross-sections such as: $\sigma_e = \sigma_s + \sigma_a$ (see analogy with eq. 4.11).

For polydisperse particles much bigger than the wavelength, an equivalent extinction cross-section σ_e can be introduced which is expressed as follows:

$$\sigma_e = \frac{1}{N} \sum_i^N \frac{\pi d_i^2}{4} Q_{ei} . \quad (4.14)$$

The extinction efficiency Q_e can be considered constant for particles much bigger than the wavelength ($\lambda = 532$ nm) and from this last expression, the intensity of light traveling into a medium of polydisperse droplet can be written as:

$$I_t = I_0 \exp \left(- \sum_i^N \frac{\pi d_i^2}{4} Q_e L_{opt} \right) . \quad (4.15)$$

In the case of mass fraction measurement through LIF technique, the intensity of light exiting an optically thick medium has been attenuated all along its path by both scattering and absorption. However, the multiple scattering phenomenon contorts the signals emitted by the original beam traveling through the cloud of particles. As the photons are deviated, the information of the incident beam is lost during the way until the detection system and some

corrections are needed to recover the original information of the central part of the beam.

4.3 Technique development and calibration

The main idea of the SLIPI technique, presented before (3.6.3), is to remove the multiple scattering that a planar electromagnetic wave suffers in a medium containing scatterers. This technique relies on spatial modulation of the input light to suppress the unwanted interferences caused by multiple scattering. Structured light has been used in fluorescence microscopy for a decade now and it demonstrated to improve image quality and back scattering detection [40]. A couple of years ago, Breuninger et al. [41] applied a structured illumination together with the so called Planar Laser Imaging technique and used it to study the fluorescence spectroscopy of a biological sample.

A similar technique has been developed to suppress multiple Mie scattering in dense two-phase flows relying on the fact that the radiation remains structured if it suffers one scattering event only. In other words, the photons that have experienced several scattering events within the medium will lose the modulation information contained in the excitation light, while singly scattered photons will not. The signal of the electromagnetic plane wave going into the sample results in a normalized amplitude fringe pattern $a_m(x, y)$ of the functional form:

$$a_m(x, y) = 1 + k_{mod} \cos(2\pi \nu y + \phi_0) . \quad (4.16)$$

Where k_{mod} represents the modulation depth, ν the spatial frequency, ϕ_0 is an arbitrary spatial phase while x and y are the two dimension coordinates. This function of illumination will then provide a two dimensional image of intensity $I_R(x, y)$ according to Breuninger et. al [41]:

$$I_R(x, y) = I_C + I_S \cos(2\pi \nu y + \phi_0) . \quad (4.17)$$

In this last equation, a decomposition can be done, I_C is one part of the image in which both single and multiple scattering are present. This picture (I_C) describes how the captured image would be if there were no spatial modulation of the incident light. The second part of the image (I_S) contains mainly singly scattered photons and represents the structured illuminated image. The cosine term is the superimpose fringe pattern of the excitation light and must be

removed to get the clear structured image (I_S). By changing the phase of the modulation, the illumination will be spatially shifted while the multiple scattering will not be affected.

Recent developments of the structured illumination technique use at least 3 phases (images) to recover the spray and suppress multiple scattering by moving the phase a third of a period leading to relative spatial phases of $\phi_0 = 0, 2\pi/3$ and $4\pi/3$. The choice of 3 phases makes sense as the mathematical process of suppression is straightforward (pair-wise difference) and the image is reconstructed directly.

On the other hand, accounting for the equipment available in laboratories working on sprays all over the world (e.g. double-pulsed laser, double-shutter camera), a two-phase solution seems more appropriate. The two phases in this case are shifted by half a period one to each other (relative phases would be: 0 and π). Finally, the following equation, being part of the equation presented by Breuninger et. al [41], is the resulting signal of the Structured Planar Laser Imaging (SPLI-2P) technique:

$$I_S = \sqrt{(I(0) - I(\pi))^2} . \quad (4.18)$$

The resulting image is then obtained by recreating the upper envelope of the signal as the lower envelope should go to absolute 0. In the same time, the signal of the non-structured image referred to as conventional in this thesis would be:

$$I_C = \frac{I(0) + I(\pi)}{2} . \quad (4.19)$$

The fact that both signals are contained in the set of images previously acquired makes all kind of comparison easy. At first, every individual phase-image shows a global blurring effect due to the high optical depth of the dense medium probed and therefore a large probability of multiply scattered photons. On the other hand, the singly scattered photons carry the structural information of the phase shift and are the only left on the post-processed resulting image. This process shown in figure 4.6 operates as a directional filter and extracts most of the singly scattered photons, removing the multiply scattered ones at the same time, leading to significantly improving the definition or contrast of the image.

In addition to less equipment requirement, the two-phase process showed not to be as much affected as by a mis-shifting of the phases and is therefore

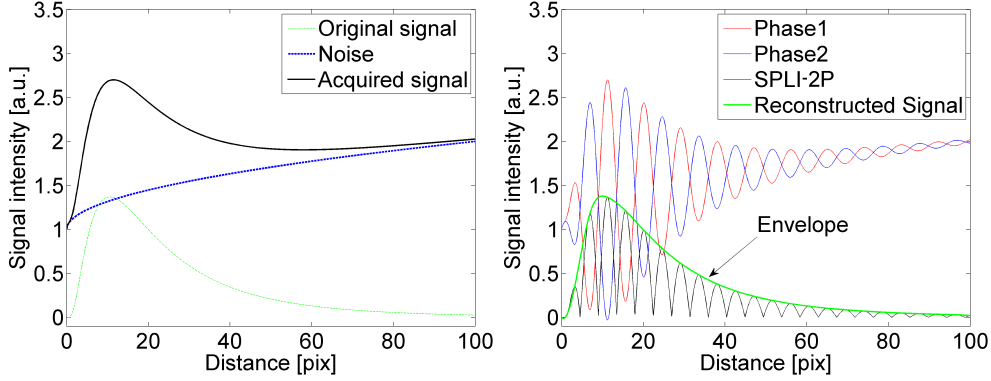


Figure 4.6: Schematic of the conventional and Structured Planar Laser Imaging (SPLI-2P) methodologies. The signals are shifted by half a period.

more robust for multiple scattering removal.

4.3.1 Design of a specific experiment

To evaluate both the conventional and the Structured Planar Laser Imaging techniques, measurements have been performed in a controlled environment, constituted by fluorescent spherical particles of known size. The particles have been homogeneously dispersed in distilled water and the concentration adjusted by weighing the amount of particles and water. The measurement volume consisted of an optical glass cuvette (optical paths: $44 \times 34 \times 100$ mm³) containing a mixture of water and particles of approximately 100 ml; to achieve a homogeneous solution, a magnetic stirrer was used continuously in the cuvette during the experiments. Three particle sizes were studied (7, 15 and 32 μm) and for each solution three different optical depths were investigated (2, 4 and 6). In addition to this, different sections within the cell were probed (2, 12, 22 and 32 mm) to study the influence of the optical thickness between the laser-sheet and the detection system.

Even if there is no time scale specificity for such experiment, in order to hold the relationship with further tests in sprays, a frequency-doubled Nd:YAG laser was used to generate a pulsed laser beam. A laser-sheet has been created by a combination of spherical and cylindrical lenses and the spatial modulation was created by imaging a Ronchi grating (10 lp/mm) onto the sample. Beam blocks have been used to remove the higher order of frequency generated by the Ronchi filter and the phase shifting was managed by tilting a glass plate

placed directly after the Ronchi grating. Another glass plate has been located right before the cuvette to acquire the real intensity of the laser from test to test in order to normalize the signal intensity. A sketch of the experimental setup is presented in figure 4.7. The laser power has been carefully set in order to avoid saturation of the fluorescent signal emitted by the particles as this would affect the propagation of light and therefore induce a deviation from the Beer-Lambert law.

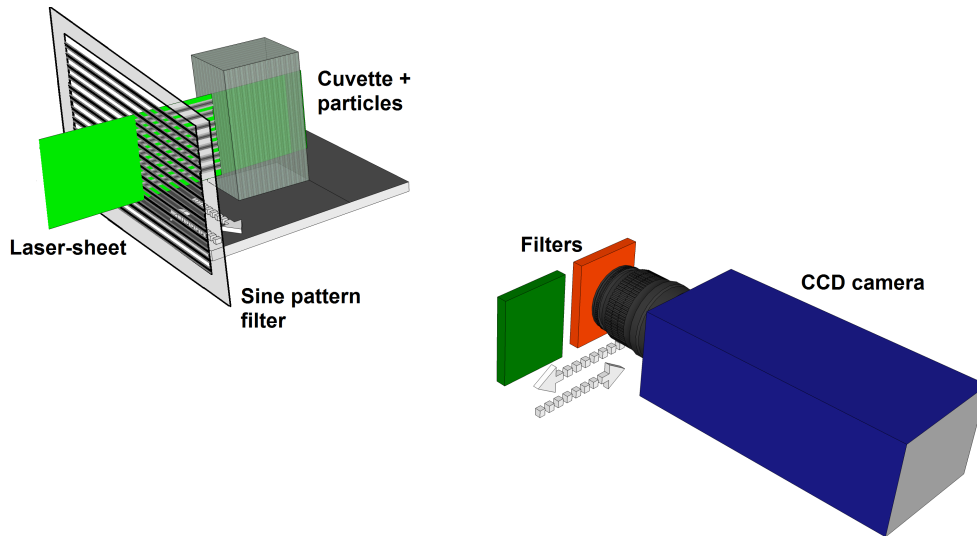


Figure 4.7: Schematic of the experimental arrangement used to acquire Structured Planar Laser Imaging signals in controlled test situation. The Cuvette is moved to change section position (2, 12, 22 and 32 mm).

The images were acquired with a 14-bit Andor iXon camera with a resolution of 512×512 pixels equipped with a 50 mm Nikkor objective. The contribution of the multiple scattering has been kept really low by decreasing the collection angle of the system, this has been achieved by adjusting the diaphragm of the objective to an $f/\# = 8$. Reducing the collection angle actually increases the depth of field, thus limiting the performance of the SPLI-2P technique; however, an improvement has been observed on removing multiple scattering globally. LIF and Mie signal were acquired and the scattering processes were isolated using an interference filter for the elastic scattering (centered on 532 nm) and a long-pass filter for the fluorescent emission (570 nm cut-off, transition width below 5 nm). An amount of 500 images were acquired per phase, meaning a total of 1000 images for each experimental condition in order to get statistically repetitive images. Sample images acquired with this

setup for both Mie and LIF are shown in figure 4.8, note that the power can be recorded only for Mie as the filter blocks the elastically scattered light.

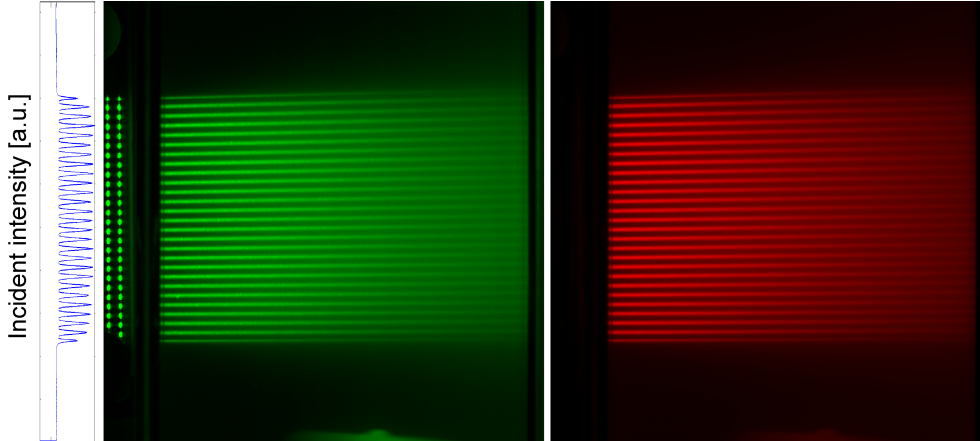


Figure 4.8: Sample images recorded with the Structured Planar Laser Imaging setup used for Mie (left) and LIF (right). The intensity profile of the laser-sheet is displayed on the left side of the image.

The intensity of the incident light is displayed and shows that the profile of the modulated illumination is mainly uniform and can be considered as "top-hat". Due to the number of images used to average the results and the stability of the solid-state laser, the illumination profile should be really similar from one test to another.

As explained in the previous section, either conventional or Structured Planar Laser Imaging processes can be obtained with such an experimental setup, the next two sections present the analysis and comparison of both methodologies.

4.3.2 Evaluation of the conventional PLI in known situation

There are several studies that address the accuracy of the Planar Laser Imaging techniques in turbid media like Diesel sprays pointing out the effects of multiple scattering of light [24, 42]. The concept of the methodology used in this work is to control the medium to have an exact idea of the results and see if the Planar Laser Imaging techniques as they are generally applied provide correct results.

Figure 4.9 presents the resulting conventional images for both scattering processes, i.e. Mie and fluorescence for the 15 μm particles. This sample has

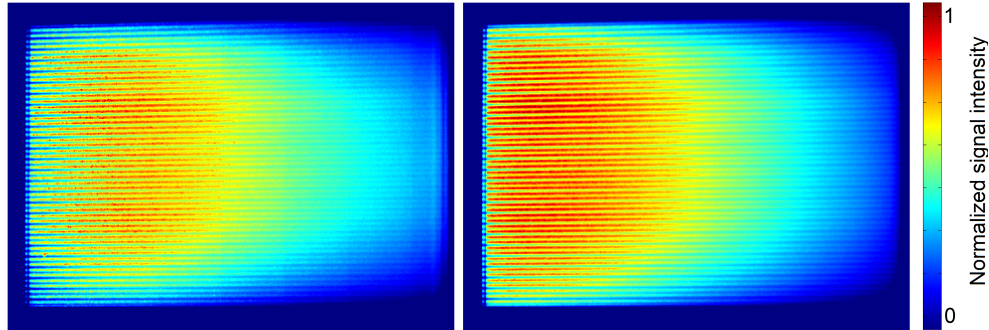


Figure 4.9: Conventional planar resulting signals for Mie (left) and LIF (right). Particle diameter is $15\ \mu\text{m}$, optical depth (τ) is 4 and illumination is placed at 12 mm from front wall.

been extracted from the measurement done at the intermediate concentration, equivalent to τ 4 and when the laser-sheet was at 12 mm from the front wall of the cuvette. As no special process is done to get those images, these two pictures represent the signals obtained by a standard setup to acquire LIF and Mie. At first, it can be noticed that both images show signal variations from one location to another although the illumination and the particle concentration is assumed uniform. As the intensity of the LIF signal is theoretically proportional to the mass of dye illuminated, the signal should be uniform assuming that the concentration of dye is uniform among all the particles and that the particles are evenly dispersed in the cuvette. Figure 4.10 shows the profiles of the intensity recorded along the laser path for the condition presented earlier ($15\ \mu\text{m}$, τ 4); a vertical summation over the illumination area has been done. The four different positions of the laser-sheet in the cell are presented together on these plots referring to the two acquired signals: Mie scattering and fluorescent emission.

The results clearly demonstrate that the signals are not uniform along the cell as introduced before and supported by figure 4.9. When the illumination plane is moved deeper into the cuvette, the multiple scattering and light extinction become more predominant and the signal recorded by the CCD is not uniform. In addition to this, the difference observed between Mie and LIF signals emphasizes the uncertainties concerning eventual LIF/Mie ratio to get maps of particle size. A 2-D map of the droplet size (SMD) is presented in figure 4.11, the size of the particles has been adjusted with the left side of the cell (laser-sheet entrance) as a reference.

The LIF/Mie ratio could be a good example to demonstrate the accuracy

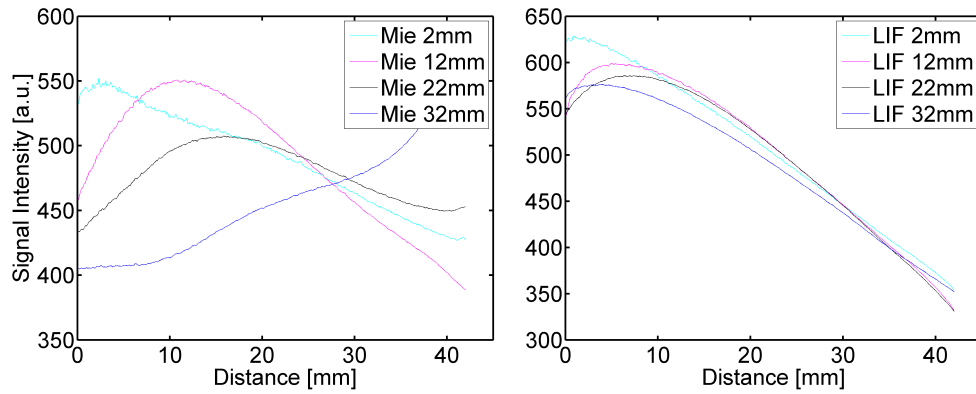


Figure 4.10: Intensity profiles along laser path for Mie (left) and LIF (right). Vertical summation of the illumination region. ($15 \mu\text{m}$ and $\tau = 4$).

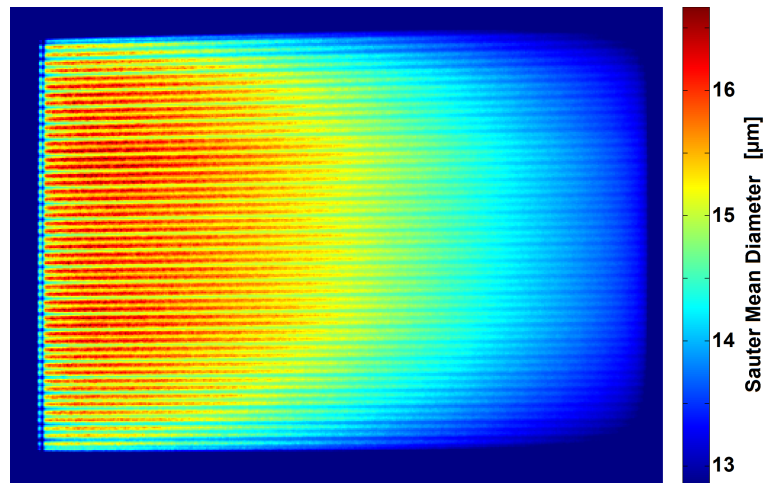


Figure 4.11: Sauter Mean Diameter map for the conventional Planar Droplet Sizing (PDS) technique. The laser-sheet is at 2 mm from the front wall. ($15 \mu\text{m}$ and $\tau = 4$).

of the Planar Laser Imaging techniques in optically thick media. The results show that even at the closest location from the front wall, meaning that the extinction of light between the laser-sheet and the CCD is almost negligible, the ratio of the fluorescent emission and the Mie scattering is not uniform within the illumination plane. Table 4.1 presents the standard deviation of the Sauter Mean Diameter of the particles for the different conditions tested.

Conventional PDS	$d_{\text{part}} = 7 \mu\text{m}$			$d_{\text{part}} = 15 \mu\text{m}$			$d_{\text{part}} = 31 \mu\text{m}$		
	OD2	OD4	OD6	OD2	OD4	OD6	OD2	OD4	OD6
Laser-sheet position									
2 mm [μm]	0.4	0.4	1.3	0.5	0.6	1.2	0.6	1.5	2.9
12 mm [μm]	0.8	1.2	1.9	0.3	1.0	2.1	0.6	2.1	5.1
22 mm [μm]	1.1	1.5	2.8	0.8	1.7	3.0	1.6	2.3	8.0
32 mm [μm]	1.3	2.1	4.1	1.2	2.6	5.4	2.0	3.7	9.8

Table 4.1: Standard deviation of the Sauter Mean Diameter for the conventional PDS technique.

This discrepancy of the results has been observed and analyzed in other works [26, 27] and they show that the error on the LIF/Mie ratio because of the high number density and therefore multiple scattering in such situations can be higher than 25 %. These results are in agreement with table 4.1 and demonstrate that other solutions must be found to perform quantitative measurement in optically dense media.

4.3.3 Scattering correction via Structured Planar Laser Imaging

The effectiveness of the Structured Planar Laser Imaging method has been investigated the same way, using the fluorescent particles and under the exact same situation as explained earlier in this chapter (sec. 4.3.1). By canceling the noise coming from the multiple scattering of light within the medium, the intensity along the laser-sheet can be extracted, therefore this signal should follow an exponential decay as described by the Beer-Lambert's law. Figure 4.12 presents the resulting signals obtained for both Mie and LIF when the SPLI-2P is applied. The conditions are the ones that have been used with the conventional technique presented above, all the images have been corrected from vignetting due to imperfections of the acquisition system. In addition to this, a slight correction has been applied to compensate the signal non-uniformity due to scattering phase function angular dependency, this

produces the intensity scattered in the perpendicular region to be slightly different from one side of the cuvette to another. A scattering phase function can be assumed to adjust the intensity along the path of the laser-sheet, the scattering phase function is not very sensitive to change in diameter within the range considered for Diesel sprays.

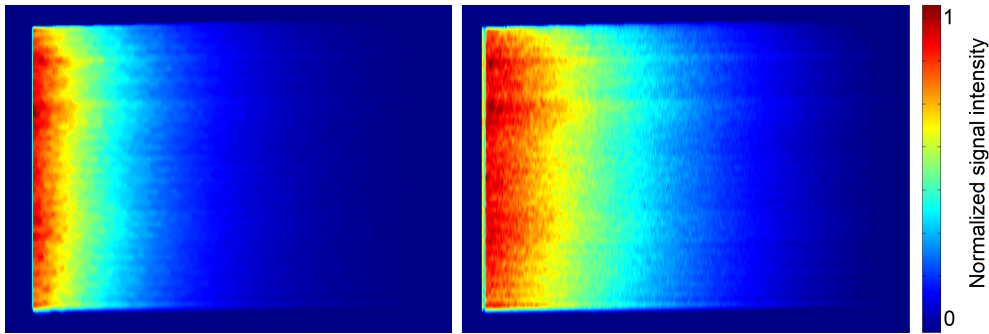


Figure 4.12: Two-dimensional signals extracted from the Structured Planar Laser Imaging technique for Mie (left) and LIF (right). Particle diameter is $15 \mu\text{m}$, τ is 4 and laser-sheet is at 12 mm from front wall.

The images look consistent from the laser entrance (left side) to the exit of the cell (right side); as expected, the intensity of both signals decreases as long as the laser radiation travels into the medium. Figure 4.13 shows the intensity profiles of the two previous images along the laser path, these curves are the result of a vertical summation of the images. The exponential tendency of the decays appear clearly on this figure as expected from the definition of the Beer-Lambert's law.

The intensity of these profiles is different depending on the position in the cell, in other words, the distance from the front wall. It is obvious that the intensity of the light scattered by the laser-sheet at 90° toward the CCD has to go through the particles between the illumination plane and the front wall of the cuvette. The light is therefore extinguished and once again, this decay would follow the Beer-Lambert's law of extinction. As a first approximation, this extinction from the laser-sheet to the CCD can be assumed to be the same, this allows us to make the ratio of the two signals to check if the Planar Droplet Sizing (PDS) technique works in the case of the Structured Planar Laser Imaging. Figure 4.14 shows a 2-D map of droplet size (SMD) when SPLI-2P technique is applied.

The ratio of the two scattering processes looks uniform over all the illumination plane, meaning that the particle diameter is the same anywhere in

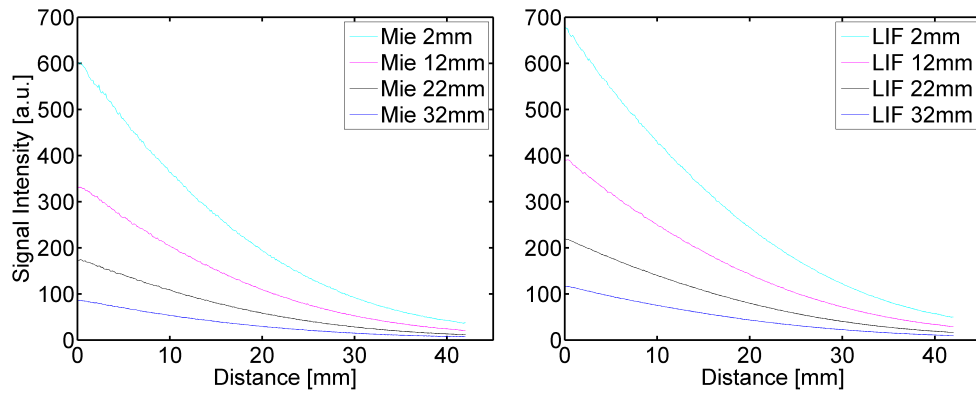


Figure 4.13: Intensity profiles recorded for Mie and LIF extracted by SPLI-2P technique compared to the theoretical decay (Beer-Lambert law). Illumination plane is at 12 mm from front wall.

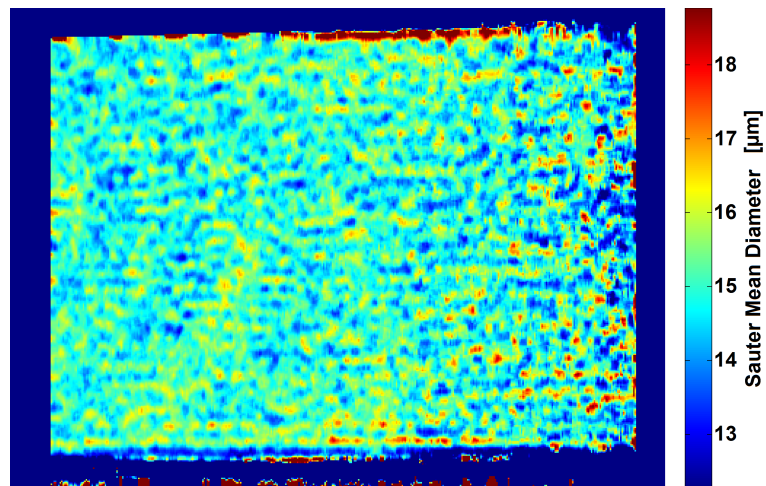


Figure 4.14: Example of Sauter Mean Diameter map obtained by PDS when the SPLI-2P technique is applied. Laser-sheet is at 22 mm from the front wall. ($15 \mu\text{m}$, $\tau = 4$).

the laser-sheet region. This is a great improvement as the SPLI-2P technique seems capable of providing satisfactory results even in optically dense media as shown in table 4.2.

SPLI-2P PDS	$d_{\text{part}} = 7 \mu\text{m}$			$d_{\text{part}} = 15 \mu\text{m}$			$d_{\text{part}} = 31 \mu\text{m}$		
	OD2	OD4	OD6	OD2	OD4	OD6	OD2	OD4	OD6
Laser-sheet position									
2 mm [μm]	0.2	0.2	0.2	0.1	0.4	0.5	1.0	0.6	1.4
12 mm [μm]	0.1	0.3	0.2	0.5	0.5	0.6	0.8	1.2	1.6
22 mm [μm]	0.0	0.2	0.4	0.3	0.7	0.7	1.2	1.4	2.1
32 mm [μm]	0.1	0.3	0.5	0.7	0.4	0.8	1.2	1.7	2.0

Table 4.2: Standard deviation of the Sauter Mean Diameter for the PDS technique when Structured Planar Laser Imaging is applied.

On the contrary to the results presented in table 4.1, the Structured Planar Laser Imaging technique demonstrates its capability for both scattering processes. With a maximum average standard deviation about 5 %, the SPLI-2P method makes possible to measure the size of the particles directly. However, the ratio of fluorescent emission and Mie scattering presents the advantage of being auto-calibrated, some considerations have to be made concerning direct measurements using one signal only.

4.3.4 Further considerations for quantitative measurements

The light intensity radiated by the illumination plane is required for measurements using only one signal, either Mie or LIF. Figure 4.13 presented the acquired intensity profile of the light scattered by the particles on the path of the laser-sheet toward the CCD. The intensity recorded by the camera is different depending on the position of the laser-sheet in the cuvette. The position of the laser-sheet changes the extinction of light between the illumination plane and the CCD, this extinction of light is therefore needed to recover the radiated intensity of the light scattered on the illumination plane.

From its cubic geometry, the cuvette makes this process easy as the light extinction will be the same from the entrance of the laser-sheet (left side) to the exit (right side). Therefore, only two positions of the illumination plane are needed to get the optical depth between laser-sheet and CCD, we choose four positions in order to verify that the optical depth is linear with path length. The following equation gives the optical depth (τ), considering I_0 the

intensity scattered by the laser-sheet toward the collection system and I_t the transmitted intensity detected by the acquisition system:

$$\tau = \ln \frac{I_0}{I_t} . \quad (4.20)$$

The difference between two positions in the cuvette then provides the relative optical depth and as the number density and particle size are held anywhere in the cell, the global optical depth can be calculated. The optical depth along the distance between the laser-sheet and the front wall of the cuvette is plotted in figure 4.15.

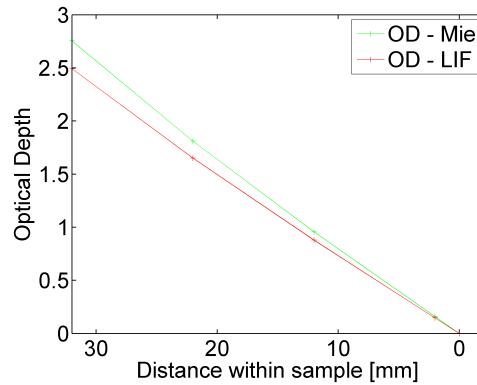


Figure 4.15: Measured optical depth (τ) in the cuvette between the illumination plane and the collection system for both Mie and LIF. ($15 \mu\text{m}$, $\tau = 4$).

The optical depth between the front wall and the closest position of the illumination plane has actually been estimated through a linear fit of the other positions. From this, it is possible to assume that the extinction of light between the cuvette and the CCD is negligible, this seems reasonable as the electromagnetic wave is traveling into air at ambient density.

As the optical depth and therefore the extinction of light between the illumination plane and the collection system is known, the decays presented in figure 4.13 can be adjusted. The decay recorded at 2 mm has been normalized and the other decays have been adjusted with their respective optical depth depending on the relative position to the reference one. Figure 4.16 shows the normalized resulting decays together with the theoretical decay calculated using the Beer-Lambert law for the specific condition tested.

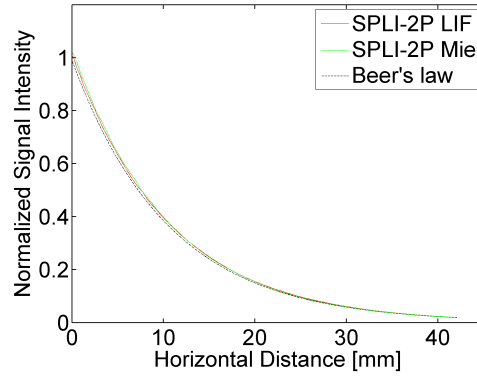


Figure 4.16: Normalized profiles for Mie and LIF along laser-sheet path. Theoretical decay computed with the experimental τ . Vertical summation of the illumination region. ($15 \mu\text{m}$ and $\tau = 4$).

When adjusted with their respective optical depth, the signals appear to be really close. In addition, the theoretical decay extracted from the Beer-Lambert law agrees from the entrance to the exit. The precision and accuracy of the SPLI-2P technique have been investigated for all tested conditions. The concept of precision here is matched between the decays no matter the position of the illumination plane in the cell. The reference is 2 mm from the front wall as the extinction toward the collection system is lower, the other signals corresponding to further position in the cuvette have been then compared to this reference. The results for both Mie and LIF, presented in table 4.3, shows how good the signals match (being 100 % perfect match of the signals all along the cuvette).

The precision of the technique is quite impressive, the decays are coinciding almost perfectly anywhere in the cell. Under some specific conditions, when optical depth is high, the signal recorded goes down to the limit, i.e. close to zero and the precision of the technique starts to decrease. This represents one limitation of the SPLI-2P that when the optical thickness of the medium is too high, there is no signal modulation left and the SNR gets lower.

The accuracy of the technique has been evaluated in a similar way, the reference decays being in this case the results of the theoretical calculation. The normalized and adjusted signals have been compared to the decays extracted from the Beer-Lambert law of extinction; and finally, the results of the SPLI-2P accuracy are presented in table 4.4.

The measured decays are really close to the theoretical one, this demon-

SPLI-2P Precision		$d_{\text{part}} = 7 \mu\text{m}$			$d_{\text{part}} = 15 \mu\text{m}$			$d_{\text{part}} = 31 \mu\text{m}$		
Decay comparison		OD2	OD4	OD6	OD2	OD4	OD6	OD2	OD4	OD6
Mie	2 - 12 mm [%]	100	100	99	100	100	100	100	99	99
	2 - 22 mm [%]	100	99	98	100	99	97	100	99	98
	2 - 32 mm [%]	100	99	92	100	99	98	99	99	99
LIF	2 - 12 mm [%]	100	100	100	100	100	100	100	99	99
	2 - 22 mm [%]	100	100	99	100	100	99	100	98	99
	2 - 32 mm [%]	100	99	97	100	99	99	99	98	99

Table 4.3: Results of the precision of the Structured Planar Laser Imaging technique for both Mie and LIF. The reference decay has been recorded at 2 mm.

SPLI-2P Accuracy		$d_{\text{part}} = 7 \mu\text{m}$			$d_{\text{part}} = 15 \mu\text{m}$			$d_{\text{part}} = 31 \mu\text{m}$		
Decay comparison		OD2	OD4	OD6	OD2	OD4	OD6	OD2	OD4	OD6
Mie	2 - 12 mm [%]	98	98	97	97	96	96	95	96	94
	2 - 22 mm [%]	98	97	95	97	95	93	97	96	94
	2 - 32 mm [%]	96	93	92	94	91	90	94	92	88
LIF	2 - 12 mm [%]	100	99	97	97	97	96	94	94	95
	2 - 22 mm [%]	98	98	97	96	97	92	95	94	92
	2 - 32 mm [%]	99	94	94	96	92	89	92	91	89

Table 4.4: Estimation of the accuracy of the Structured Planar Laser Imaging technique for both Mie and LIF. The reference decay has been calculated with Beer-Lambert law.

strates the effectiveness of the Structured Planar Laser Imaging technique used here. In addition to this, the same comments as can be made concerning the limitation of the SPLI-2P technique in terms of accuracy as those already made regarding the precision of the technique. The accuracy of the resulting intensity radiated by the laser-sheet starts to decrease for high values of the optical depth, i.e. high number density and particle cross-section combination.

Experimental versus theoretical comparison demonstrates the Structured Planar Laser Imaging to provide accurate and precise information concerning the illuminated region in optically thick solutions. From the intensity radiated by the particles present on the illumination plane, the number density can be extracted. Berrocal et al. [43] used SLIPI technique to evaluate the extinction

coefficient μ_e in a spray taking into account the extinction of light between laser-sheet and acquisition system. The extinction coefficient is the product of the extinction cross-section σ_e and the number density N of the particles at a specific location as presented in equation 4.12. Therefore, if the extinction cross-section is known, the number density can be calculated. Considering equation 4.14 for a single element, the extinction cross-section is a function of particle diameter and extinction efficiency Q_e , which is constant for such particles as depicted in figure 4.3. The diameter of the particle is obtained via LIF/Mie ratio as demonstrated earlier in this section (see fig. 4.14 and tab. 4.2). By introducing this concept in the expression of the Beer-Lambert law presented in equation 4.10, the number density of the particles within the sample of interest can be extracted:

$$N = -\ln \frac{I_0 - I_r}{I_0} \frac{1}{L_{opt} \sigma_e}, \quad (4.21)$$

where I_0 and I_r are the intensities of light entering the media and radiated by the laser-sheet respectively, and L_{opt} the length of the sample under study or the dimension of the cuvette in this case. By dividing the cell into several discrete elements of the size of a pixel for example and applying the expression of the number density all along the illumination plane, a 2-D map of the number density N can be generated. This can be achieved by replacing I_0 , I_r and L_{opt} in equation 4.21, I_0 being the intensity entering the pixel, I_r the intensity radiated by the pixel and L_{opt} the size of the pixel. Figure 4.17 shows the results of the number density calculated from the decays (Mie and LIF) extracted from the SPLI-2P technique.

These profiles are vertical averages of the images on the laser-sheet region. The results demonstrate the capability of the technique to recover the number density of the particles through the decays extracted from the SPLI-2P technique. It can be noticed that the resulting number density appears to be closer to the theoretical one through LIF process rather than through Mie scattering. As introduced earlier, correcting the anisotropy of the scattered intensity all around the droplet surface is complex because it depends upon several parameters that cannot be controlled in some situations. Even if the optical system has been setup in order to reduce the multiple scattering effect to the limit, its influence still affects the recorded signal. On the other hand, the LIF signal does not present anisotropy of the radiation emission and therefore presents clear advantage to perform quantitative measurements in polydisperse particle/droplet distributions.

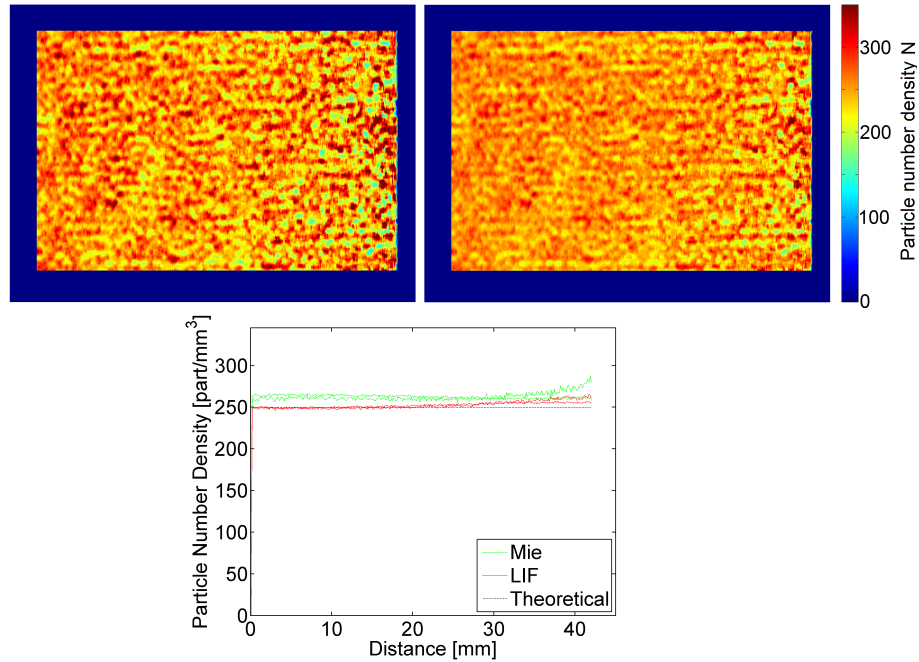


Figure 4.17: 2-D number density maps for Mie (left) and LIF (right) at 22 mm from front wall. Number density profiles along laser path (bottom), theoretical has been calculated by actual optical depth. ($15 \mu\text{m}$, $\tau = 4$).

From the particle diameter and the number density, the particle concentration or volume-mass fraction can be calculated. This methodology is the object of the next-coming section, in which SPLI-2P is applied to a DI Diesel spray with the aim of measuring the fuel mass fraction on the illumination plane.

4.4 Application to sprays

The Structured Planar Laser Imaging technique has shown its efficiency in controlled test situations with relatively high optical depth alike conditions found in a modern DI Diesel spray. This methodology will therefore be applied to measure the fuel mass fraction of a non-evaporative Diesel spray. The differences with the medium simulated by the particles are various:

- The diameter of the droplet is not known and not uniform within the sample. As addressed by the theory of the technique, the droplet diame-

ter must be known to calculate the number density and the concentration correctly. However, the tests demonstrated that the results extracted from LIF/Mie ratio were still valid with polydisperse particles.

- The number density also changes according to the position in the spray, for example, considering the results found in the literature, the concentration of droplets on the center-line of the spray is higher. There is a dramatically high gradient of number density in a spray making the dynamic response of the system a real issue.
- If the number density is dependent upon the distance from the center-line for example or upon the distance from the orifice, a methodology is required to estimate the extinction of light from the illumination plane to the optical system.

As outlined here, a complete calibration of the system is required, after a brief presentation of the equipment and setup used for this work, the basic parameters of the fluorescent emission, e.g. absorption and emission spectra, lifetime, quantum yield, will be investigated. To finish, an evaluation of the parameters driving successful Planar Droplet Sizing measurements will be carried out. These parameters, d-cube dependency for example, are also paramount for fuel mass measurements.

4.4.1 Experimental setup

The experiments concerning the visualization of the spray have all been performed in the cold spray test rig presented in section 3.4.1. The spray has been generated by a purposely-designed injection system described in section 3.2 capable of keeping the pressure constant with control and accuracy. An additional equipment has been designed to control the temperature of the injector as this may affect the fluid and the hydraulic properties of the injector itself, this would therefore have an impact on the behavior of the injection process and on the structure of the spray.

Light source and laser-sheet generation

To illuminate the spray with accuracy and precision, a pulsed Nd:YAG laser (*Continuum - Surelite II*) has been used. This type of laser is called solid-state, it is represented by a crystal of YAG (Yttrium Aluminum Garnet) doped with triply ionized Nd (Neodymium) as used in numerous lasers all over the world.

The flash lamp network is a Xenon-based one with a flash duration of about 200 μs . The control system of the laser, called Q-switching, is able to restrain the laser radiation propagation inside the optical resonator until it reaches its maximum intensity (reached at 198 μs). It is composed of a Pockels effect cell, a quarter-wave plate and a linear polarizer (reflecting the light at 99.9% for a 90° polarized radiation and 99.9% transparent for a 180° polarized radiation). To avoid the laser radiation, it is just necessary to electrically deactivate the Pockels cell, so that the radiation pass through the quarter-wave plate twice, letting it 90° polarized, thus the polarizer only reflects it. Thanks to this mechanism, it becomes possible to get pulses by triggering the activation of the Pockels cell.

After these elements, a relatively short pulse has been generated at a wavelength of 1064 nm. As all the previous tests have been done using 532 nm wavelength, the same frequency has been used to light the spray, for this, the second harmonic generator has been utilized. The frequency doubler is a crystal network (*KDP* and *KH₂PO₄*) which acts like a nonlinear material making the input electromagnetic radiation to double its energy and frequency thus reducing its wavelength by a factor of two [44]. After this element, the beam is composed by both the fundamental, i.e. 1064 nm, and the harmonic generated by the frequency doubler, in other words, the wavelength of interest: 532 nm. The fundamental is then removed by placing dichroic mirrors on the path of the beam toward the exit, figure 4.18 is a scheme of the optical layout of the laser source used in this work. In this study, the pulse duration has been measured via an ultra-fast photodiode and revealed to be as short as 5ns.

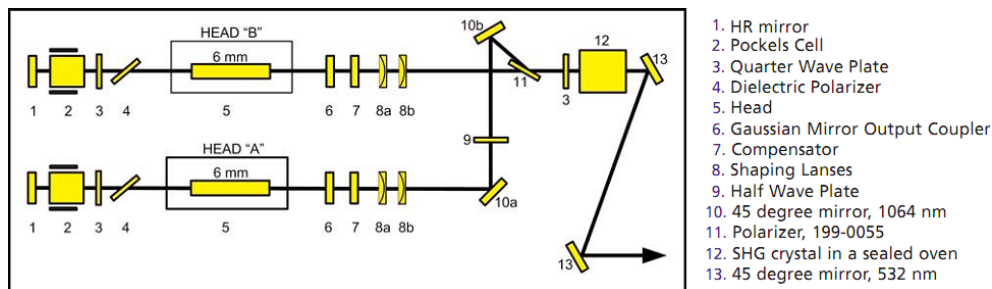


Figure 4.18: Schematic of the optical layout of the Nd:YAG laser source. (Source : Continuum)

After exiting the laser, the beam has been steered toward the measurement section with three high-efficient (99.5 % at 532 nm) laser-line mirrors. The laser-sheet used to cut sections of the spray has been generated by three

cylindrical BK7 lenses. The first lens ($FL = 500$ mm) compresses the beam on the vertical dimension and is responsible of the thickness of the laser-sheet, the second one ($FL = -10$ mm) opens the beam on the horizontal direction to create a sheet. The third lens ($FL = 100$ mm) purpose is to concentrate the laser-sheet again and achieve parallel rays. The last element on the laser-sheet path is a sine-pattern filter that gives the illumination plane its structural behavior. The laser-sheet goes through this pattern and the spray is then illuminated by a spatial sinusoidal modulation with a period of 2 mm.

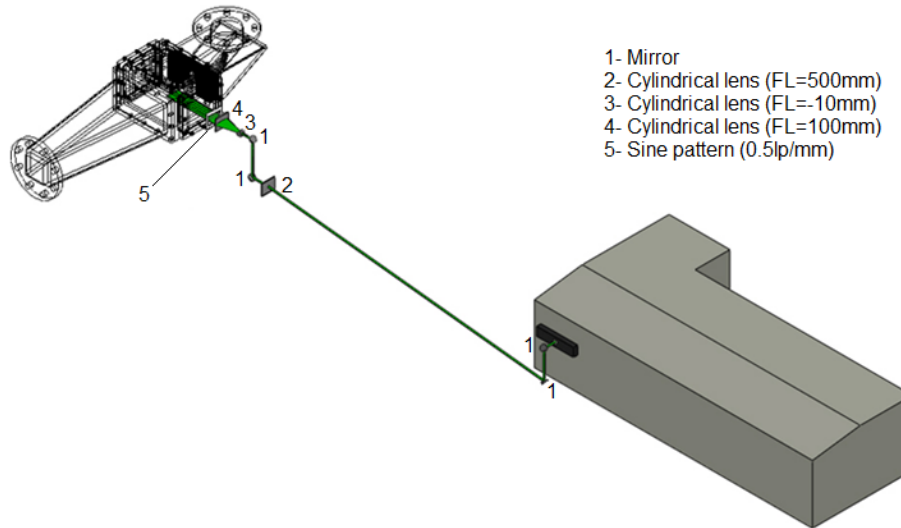


Figure 4.19: Illustration of the optical setup used in this study. The Nd:YAG laser is on the right (gray) and the testing section on the left (drawing lines).

Figure 4.19 presents an illustration of the optical arrangement used in this study. The characteristics of the illumination plane have been carefully specified as the objective was to get a laser-sheet thinner than the orifice of the injector, this in order to light all the spray on the central plane. The laser-sheet used in this study was 48 mm wide and $82\ \mu\text{m}$ thick at the spray axis location, as a reminder, the diameter of the nozzle's orifice is $90\ \mu\text{m}$. The thickness has been measured by the knife method [45] with an accuracy of about $2\ \mu\text{m}$. The intensity profile along the axis of the spray has also been recorded in order to make further corrections if needed.

Imaging system

The main organ of the acquisition system is a 12-bit CCD camera (*PCO - Sensicam*), the sensor has a resolution of 1376×1040 to ensure a relatively high pixel to millimeter ratio. The CCD chip is kept at a temperature of -11°C thanks to a Peltier cell to reduce thermal noise. The images are saved individually in 16-bit tiff format not to lose information. The exposure time of the camera has been set to $1\ \mu\text{s}$ keeping the flare of the external environment as low as possible. Note that the laser power being relatively high compared to the ambient luminosity, the final gate of the image would be the laser pulse duration (about 5 ns).

The camera is equipped with a 60 mm focal length objective (Nikkor Lens). To make the spray experiment alike the simulation done with the particles, the collection angle has been set really low to reduce the effect of the multiple light scattering on the results. For this purpose, the diaphragm of the objective has been shut down to $f/\# = 8$, being the final collection angle of the acquisition system as low as 23 mrad.

The same filters have been used to separate the two scattering processes: Mie (532 nm interference filter) and LIF (570 cut-off long-pass filter). The dynamic range of the acquisition system has been adjusted by the addition of neutral density filters to better use the capabilities of the camera. For each phase, an amount of 100 images have been acquired to get statistically repetitive images, the images are acquired individually and the process of averaging is realized during the SPLI-2P image treatment.

The last element of the experimental apparatus set up to record the images of the spray via Structured Planar Laser Imaging is the electronic synchronization system. This equipment is necessary due to the really short time of the event, some milliseconds for the injection, some nanoseconds for the laser pulse. This purposely designed control system is based on a 16-bit micro-controller which communicates with a PC and generates the Transistor-transistor logic (TTL) signals to trigger the injection, the flash-lamp and Q-switch of the laser, and the camera.

Choice of fluorescent dye

The fuel used in this study being a pure alkane (n-dodecane), it does not absorb light and therefore, does not emit any fluorescent signal. A dye must be added to the fuel to record the corresponding fluorescent signal; Sulfo-rhodamine B

has been chosen to dope the pure fuel because as many other dyes, it absorbs light at 532 nm. A dye absorbing light at 532 nm was the main parameter for the choice of the fluorescent dopant as all the previous experiments and calibrations have been carried out at this wavelength. In addition, as 532 nm is within the visible range, the alignment procedure becomes easier and as a result, the quality of the illumination plane is better.

Sulfo-rhodamine B has a high fluorescence efficiency which means that only a small quantity would be necessary to collect enough fluorescent signal when excited by a pulsed Nd:YAG laser. Experiments to check both the fluorescent emission intensity and the non-existence of Morphology Dependent Resonance (MDR) have been carried out. The probability of MDR mainly depends upon the concentration of dye as long as droplet size and laser wavelength are input parameters of the system. If the absorption of the dye within the droplet is too low, resonance may occur; it has been observed however that for such a concentration of dye, the existence of MDR was very limited [46,47]. When MDR exist, the droplets act like a resonating optical cavity and the result is an amplification of the emitted fluorescent signal, intensity peaks are present on the recorded image. Therefore, the dye content must not be either too low (MDR appearance) or too high (high absorption and d^3 dependency not respected). Finally, the experiments revealed that the optimum quantity of Sulfo-Rhodamine B to be added to the fuel was 12 mg/L, which is in agreement with quantities used for LIF experiments found in the literature [17,20,36,38,48].

On the other hand, Sulfo-rhodamine B is not directly miscible with fuel and to achieve a complete and stable dilution of the dye, it has been dissolved into ethanol (1 % in volume) and the mixture has been incorporate to the n-dodecane. The mechanical fluid characteristics (e.g. density, viscosity and surface tension) of the fuel have been measured and showed that the doped fuel obtained presents the same properties as pure n-dodecane (see tab. 3.1 for more information).

4.4.2 Fluorescence properties of the dyed fuel

The characteristics of the fluorescent signal are determinant for the calibration of the system. Sulfo-rhodamine B is a kind of Xanthene dye, its properties in terms of fluorescent emission mainly rely on solvent polarity, dye concentration and pH value of the mixture [49]. Table 4.5 shows the chemical structure of the Sulfo-rhodamine B together with the main parameters of interest in this study.

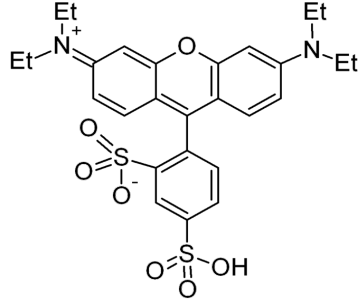
	Chemical formula	
	Properties	
	Molecular formula	$C_{27}H_{30}N_2O_7S_2$
	Molar mass	558.666 g/mol
	Absorption (max. in ethanol)	556 nm
	Fluorescence (max. in ethanol)	575 nm
Molar absorptivity	11.1 m ² /mol	

Table 4.5: Chemical structure and general characteristics of the Sulfo-rhodamine B molecule.

The fluorescence properties are investigated here through measurements of absorption and emission spectra, quantum yield and lifetime to better understand the process of fluorescence of such a dye in n-dodecane. The absorption coefficient will be calculated from the results as well and the linearity of the fluorescent signal intensity will be checked as the methodology relies on non-saturated fluorescent emission.

Absorption and emission spectra

The spectra for absorption of light and fluorescent emission have been determined with a photon-counting spectro-fluorometer (*Photon Technology International - QuantaMaster 40*). The wavelength to excite the Sulfo-rhodamine B in n-dodecane has been set to 532 nm as the experiments will be performed at this frequency with the Nd:YAG laser used in this work. Figure 4.20 presents the fluorescent emission signal as a function of wavelength together with the molar absorption coefficient.

The spectra of the filters used to collect the fluorescence and Mie scattering signals are displayed and show that there is no overlapping of the signals. As seen on the graph, the maximum absorption of the dye in n-dodecane occurs at 556 nm, which agrees with the literature [50] for Sulfo-rhodamine B dissolved in ethanol, remind that the dopant has been dissolved in ethanol prior to addition to the fuel. Concerning the fluorescent emission, when excited at 532 nm, the Sulfo-rhodamine emits radiation with a peak at 577 nm, which is slightly higher than the cut-off transition wavelength of the filter used (570 nm long-pass).

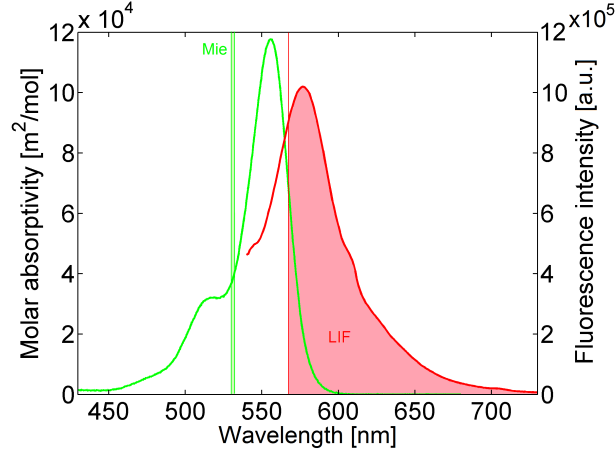


Figure 4.20: Molar Absorptivity and fluorescence emission spectra of the Sulfo-rhodamine B. Note that the signals are presented on distinct intensity scales.

Fluorescence quantum yield and absorption coefficient

As quickly expounded in the theoretical section 4.2.1, the fluorescence quantum yield Φ is given as the ratio of the number of photons emitted to the number of photons absorbed by the sample and is conceptually represented in expression 4.22.

$$\Phi = \frac{\#Photons_{em}}{\#Photons_{abs}} \quad (4.22)$$

It can also be described as the relative rates of the radiative R_r over the radiative and non-radiative R_{nr} processes. The radiative process is responsible of radiation emission via fluorescence whereas the non-radiative ones deactivate the excited state of the molecule.

$$\Phi = \frac{R_r}{R_r + \sum R_{nr}} \quad (4.23)$$

$\sum R_{nr}$ describes the sum of the rate for the various processes that compete with the emission process. These processes, reducing the fluorescent emission efficiency include photochemical, dissociative processes and others less well characterized that result in a return to the ground state with simultaneous dissipation of the energy of the excited state into heat instead of visible radiation.

The quantum yield is therefore strongly dependent upon the medium in which the dye has been dissolved and it must be measured specifically. A widely used solution to determine the quantum yield of a fluorophore is to compare the fluorescent signal intensity to a standard or reference with known quantum yield. As Sulfo-rhodamine B is frequently used as a laser dye for pulsed and continuous wave (CW) operations, its properties (generally dissolved into water) have been investigated [51]. In that way, Sulfo-rhodamine B dissolved into water has been chosen as our reference to determine the quantum yield of the Sulfo-rhodamine B mixed with n-dodecane. When a reference quantum yield is known, the quantum yield of the sample under study can be calculated via equation 4.24 [52].

$$\Phi = \Phi_{ref} \frac{I_0}{I_{ref}} \frac{\tau_{ref}}{\tau} \frac{n^2}{n_{ref}^2}, \quad (4.24)$$

where I_0 is the intensity of the incident radiation, τ the optical depth as expounded in equation 4.13 and n the refractive index of the fluid. The subscript "ref" refers to the reference, i.e. the Sulfo-rhodamine B dissolved into water. The values of the refractive indices measured and used for the calculation were: $n_{ref} = 1.335$ for water with Sulfo-rhodamine B at 532 nm and $n = 1.422$ for n-dodecane doped with Sulfo-rhodamine B at the same wavelength. The optical depths have been measured by placing the two solutions into optical cuvettes, the intensity signals have been recorded by a high-power photo-diode. The light source was the pulsed Nd:YAG laser already described earlier in section 4.4.1 and the same interference filter (532 nm) has been used to be consistent with the imaging process. Note that the measurements done to characterize the fluorescence quantum yield of the n-dodecane plus Sulfo-rhodamine B have been performed at ambient condition (1 atm and 293 K).

The quantum yield of the reference sample is $\Phi = 0.31$ [53–55] and thanks to equation 4.24 and the optical depth measurements done, the quantum yield of the Sulfo-rhodamine B into n-dodecane is $\Phi = 0.68$. As the dye has been dissolved into ethanol, a high quantum yield had to be expected. On the other hand, the quantum yield of the fluorescence emitted by the Sulfo-rhodamine B is higher in n-dodecane than in water; higher quenching in water might explain this aspect. This fact that the water acts as a fluorescent quencher has been highlighted by several researchers [56–58], they basically observed that the quantum yield was decreasing with the water content.

From the measurements of optical depth, the molar absorptivity of the fluid can be extracted as described in equation 4.10. In order not to change the

concentration of dye, to avoid potential changes in photochemical processes at lower Sulfo-rhodamine quantity, cuvettes of different optical paths have been used to obtain the optical depth and therefore extract the absorption coefficient. When excited at 532 nm, the solution of n-dodecane with 0.012 g/L (2.07×10^{-5} mol/L) of Sulfo-rhodamine B has a molar absorption coefficient of $\epsilon = 4.16 \times 10^4$ m²/mol. This value of the molar absorption coefficient agrees with the results provided by the photon-counting spectro-fluorometer and according to the literature [46, 47], it should avoid Morphology Dependent Resonance (MDR) phenomenon.

Fluorescence lifetime

The average time within which the molecule stays at its excited state and therefore emits red-shifted electromagnetic radiation is called the fluorescence lifetime. As briefly introduced previously, a fluorophore excited by a photon will drop to the ground state with a certain probability based on the decay rates through a number of different (radiative and/or non-radiative) decay pathways.

The lifetime is independent upon the initial intensity of the emitted light and has been measured by an L-format cuvette-based lifetime spectrofluorometer (*PTI, TimeMaster LED TM-20*) capable of making fluorescence lifetime measurements with a temporal resolution of 100 picoseconds. In the following expression, Γ is the decay rate which is the inverse of the fluorescence lifetime, and I_f is the intensity of the fluorescence signal with respect to the time t_t :

$$I_f(t) = I_f(t = 0) \exp(-\Gamma t) . \quad (4.25)$$

The initial time ($t = 0$) is the time of the excitation pulse, the lifetime can also be calculated by the subtraction of the excitation time length to the fluorescence lifetime of the sample under study. The lifetime has been measured at the wavelength of the maximum fluorescent emission, which means at $\lambda = 577$ nm (see fig. 4.20).

The measured decay of the fluorescent emission signal with respect to time at 293 K provided a fluorescence lifetime of 3.6 ns when Sulfo-rhodamine B is added to n-dodecane. As a comparison, the fluorescence lifetime of Sulfo-rhodamine B dissolved into water has been measured to be 1.8 ns, which is consistent to what can be found in the literature for such a dye [51, 59].

4.4.3 Theoretical evaluation of the PDS parameters

The Planar Droplet Sizing relies on collecting the scattered light and the fluorescent emission of an ensemble of droplets to make the ratio of both intensities to provide a 2-D map of Sauter Mean Diameter. This technique therefore assumes that the collected intensity of the scattered light is proportional to the total surface of a droplet and that of the fluorescence proportional to the droplet volume.

Serious works have been already carried out to evaluate the veracity of these two assumptions [15, 36], but the d^2 and d^3 dependencies are strongly affected by the dye content and careful analysis is required prior to Planar Droplet Sizing experiments. This section presents the evaluation of these two main parameters that govern the PDS technique through theoretical calculation based upon experimental results.

Scattered light vs. droplet surface

As shown in equation 4.6, the intensity of the light scattered by a droplet much bigger than the wavelength is proportional to the square of its diameter in theory and follows the expression drawn here:

$$I_s = k_{Mie} d^2, \quad (4.26)$$

where I_s is the intensity of the scattered light, k_{Mie} a constant mainly depending on the incident light intensity and the collection efficiency of the system, finally, d is the droplet diameter. The intensity of the light scattered by a droplet illuminated by a single beam of parallel rays has been studied by many authors and generally showed good agreement [15, 20, 36]. However, due to the presence of a dye in the fluid, the molecular absorption affects the intensity of the light traveling inside the droplet and thus the global scattered intensity.

The Mie scattering theory published by Bohren and Huffman [30] has been used to compute the dependency of the scattered intensity with droplet surface (square diameter). The optical setup of the experimental installation presented in section 4.4.1 has been reproduced to simulate the signals with consistency. The acquisition system is then placed at 90° with respect to the incident illumination, this angle being optimum for sizing measurements [21]. The collection angle, for integration of the signal over the area of acquisition, has been set to 23 mrad ($f/\# = 8$) as in the experiments. The wavelength of the light source was 532 nm and the refractive index measured earlier ($n = 1.422$)

as well as the molar absorptivity ($\varepsilon = 4.16 \times 10^4 \text{ m}^2/\text{mol}$) have been used as inputs to the simulation.

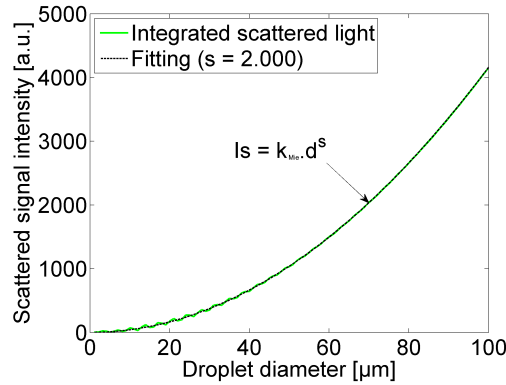


Figure 4.21: Scattered light intensity as a function of droplet diameter for *n*-dodecane doped with Sulfo-rhodamine B. The curve has been fitted to measure the exponent on the droplet diameter.

The intensity of the scattered light as a function of droplet diameter is plotted in figure 4.21 together with the best fit in order to extract the exponent over the droplet diameter. As shown on the figure, the simulated scattered light and the fitting match all along the range of droplet diameters used (from 1 to 100 μm). The best match between scattered light and fitting has returned an exponent coefficient of 2.000 which means that absolutely no deviation from the d-square law is observed.

Fluorescent emission vs. droplet volume

The fuel mass fraction of a liquid spray can be assumed and acquired only when the intensity of the fluorescence signal is linearly dependent to the cube of the droplet diameter as expounded in equation 4.9. This dependency has been deeply studied by Domann and Hardalupas [36,38] and their findings showed that the exponent on the diameter of the droplets depends on the concentration of fluorescent dye present in the liquid. If the absorption coefficient of the fuel is too high (for high dye concentration), the laser irradiance that reaches the other side of the droplet will be too low and thus will affect the intensity of the signal emitted. Consequently, the measurements done will underestimate the actual mass of fluorophore present in the droplet and thus the d-cube

dependency presented in equation 4.27 is not respected.

$$I_f = k_{LIF} d^3 \quad (4.27)$$

In this equation I_f is the intensity of the fluorescent signal emitted and k_{LIF} a constant mainly depending on the incident light intensity, quantum efficiency and collection efficiency of the acquisition system.

The d-cube law has been computed taking into account the absorption of light over the 1st, 2nd and 3rd paths within a droplet, although it has been observed that the contribution of 2nd and 3rd orders of internal scattering was nearly negligible [37]. The method used to compute the intensity emitted through scattering by a single droplet has been used together with the Beer-Lambert law of extinction. The parameters of the section concerning the scattered light dependency with diameter have been used for this simulation as well. Figure 4.22 shows the results of the calculation of the fluorescence intensity vs. droplet diameter; the best fitting has been used to evaluate the exponent on the diameter to follow the calculation as done for the scattered light.

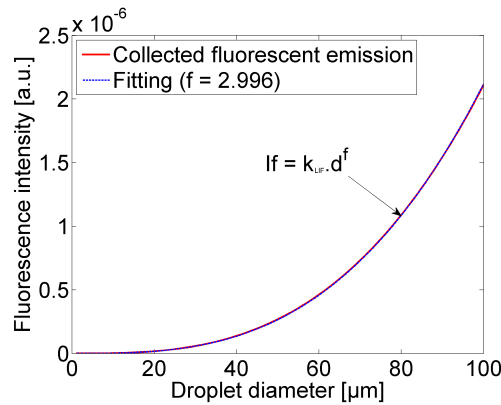


Figure 4.22: Fluorescence intensity as a function of droplet diameter for n-dodecane doped with Sulfo-rhodamine B. The curve has been fitted to measure the exponent on the droplet diameter.

The exponent obtained by the best match between simulation and fitting for the n-dodecane doped with Sulfo-rhodamine B is 2.996, which is really close to 3 and would allow qualitative and quantitative measurements. With such an exponent, the maximum error on the measured volume must be below

3 % and such a value only concerns the largest droplets considered by the simulation (100 μm).

4.5 Quantitative measurements in a spray

In this section, the Structured Planar Laser Imaging technique is employed to quantitatively measure the fuel mass fraction (or mixture fraction) distribution in a modern Diesel spray. The methodology described in the previous section of this chapter has been applied to a non-uniform, polydisperse and optically dense spray.

The SPLI-2P technique has been applied first to measure the droplet diameter using the Planar Droplet Sizing technique has demonstrated in section 4.3.3. Then, a methodology to estimate the extinction of light between the laser-sheet and the acquisition system is presented. Finally, the intensity radiated by the laser-sheet toward the camera has been used to recover the mixture fraction via the Beer-Lambert law using the 2-D droplet diameter distribution previously obtained.

Figure 4.23 is a sample image of the spatial modulation illuminating a spray on its axis. This example presents a Mie scatter imaged by the acquisition system, it is an average over 100 images for one phase of the SPLI-2P. By shifting the sine pattern by a millimeter horizontally, corresponding to half a period, the phase of the modulation is changed and the second image can be acquired.

From the two phases, the envelope of the signal can be extracted as described in section 4.3. The signal of the SPLI-2P technique is the intensity of the radiation emitted or scattered by the illumination plane as seen by the acquisition system. These raw signals already contain interesting information, as a first utilization, the LIF/Mie ratio can be done as it does not require further correction or light extinction compensation.

4.5.1 Spray sizing via Structured Planar Laser Imaging

The methodology described in section 4.3.3 is used to extract the Mie and LIF signals via SPLI-2P to apply the Planar Droplet Sizing technique in order to obtain the droplet size distribution in an isothermal spray. Figure 4.24 presents Mie and LIF signals (false color) processed using the SPLI-2P technique at an

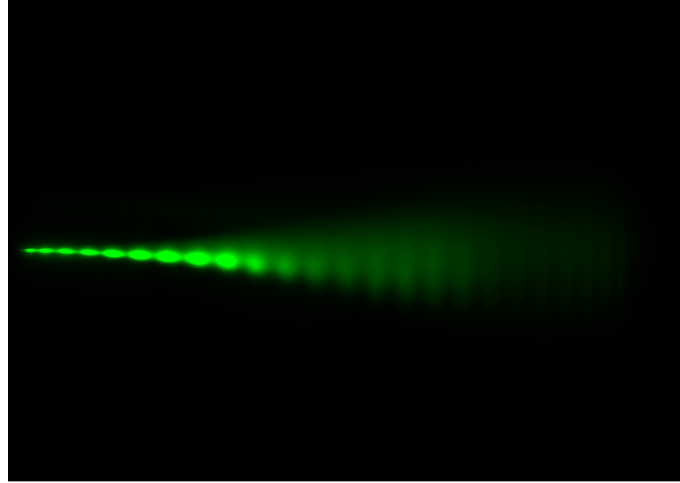


Figure 4.23: Example of a spray image illuminated by a sinusoidal modulation (false color). This is an average over 100 images of the Mie scattering process. The spray is illuminated from the bottom.

injection pressure of 150 MPa and a discharge density of 22.8 kg/m^3 , the laser-sheet crosses the spray on its axis.

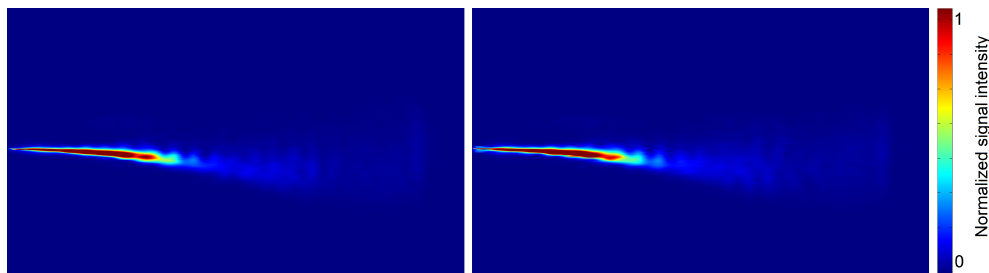


Figure 4.24: Mie (left) and LIF (right) signals extracted via SPLI-2P in a real Diesel spray. Incident illumination comes from the bottom of the image.

A decrease in terms of signal intensity can be noticed as we move downstream from the tip. As these two images present the intensity radiated by the laser-sheet and acquired by the camera, the decays of light along the illumination plane can also be noticed. The name "intensity profiles" rather than "decays" is more correct as the intensity radiated by the laser-sheet is a combination of mainly the number density, droplet size and light intensity as suggested by the Beer-Lambert law (eq. 4.10). These profiles will be used later

with the law of light extinction in a medium containing scatterers to extract quantitative information of the mixture fraction in a spray.

The radial profiles of the Mie and LIF signals are plotted in figure 4.25 together with the axis of the spray. The axis of a spray is always hard to define with accuracy and is strongly dependent on the method employed. In this work, it has been evaluated through macro-visualization with a two-side illumination to get the boundary of the liquid spray. The acquisition system used for the visualization is composed by the CCD camera and the objective presented in section 4.4.1 to record the SPLI-2P signals. The spray is illuminated on both sides through optic fibers connected to Xenon flash lamps in the aim of getting homogeneous lighting on the edges. The accuracy regarding the position of the spray axis is estimated to be within 3 pixels error, which means less than 0.14 mm deviation at maximum penetration length. A mis-positioning should not affect the results as the error engendered is generally below 1 % of the spray width.

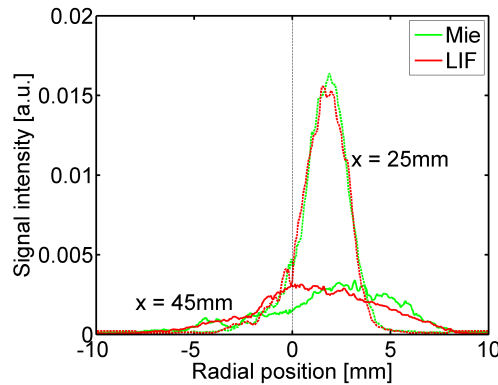


Figure 4.25: Radial profiles of SPLI-2P resulting signals for Mie and LIF at 25 and 45 mm downstream. Illumination source is on the right side.

These two profiles show what has been quickly expounded earlier that the intensity radiated by the laser-sheet along the direction of the illumination is increasing first and decreasing then. The intensity radiated by the laser can also be expressed as the incident intensity minus the transmitted intensity. Considering an integration area of the size of a pixel for example, the intensity of the incident illumination would be the intensity exiting the previous one in the same direction. Therefore, the intensity exiting the considered pixel would be the intensity entering the pixel minus the radiated intensity acquired by the acquisition system, taking into account the global efficiency of the collection

system.

From a theoretical approach, an electromagnetic radiation traveling into a turbid media can be evaluated by the Beer-Lambert law as described in section 4.2.2. From equations 4.10 and 4.12, the transmitted light intensity is proportional to the droplet number density, to the extinction cross-section (eq. 4.5) and to the size of the volume of consideration. The droplet diameter does not vary so much radially in a Diesel spray [20, 48], on the contrary of the number density, which changes of several order of magnitude from the edge to the centerline as described in section 2.5. As a simplification, a single droplet diameter is considered at radial position far enough to assume complete atomization, low number density on the edge should provide low radiated intensity. On the other hand, while moving along the illumination direction (from spray boundary to spray axis), the droplet number density increases until it reaches its maximum at the center of the spray (see sec. 2.5.3). Another parameter must be considered, the intensity of the illumination is decreasing as it travels into the spray, this explains why the maximum intensity is not on the centerline.

The extinction of the laser-sheet along the radial position in the spray has a strong impact on the measurement as the SNR decreases with the intensity of the illumination until zero when the signal gets too low. The light extinction is therefore one of the principal limitations of the Structured Planar Laser Imaging technique as explained in section 4.3.4. For high values of the optical depth, the modulation of the light is low and the processed signal can go down to zero. This phenomenon can be observed on the intensity profiles presented in figure 4.25, the obtained signals are already really low after the axis of the spray due to a high extinction of the incident illumination. This means that the data extracted from these signals on the other side of the spray axis have a low SNR and the results would not be accurate.

For this reason and with the sole intention of presenting accurate results, only half of the spray has been considered in this study. The axi-symmetrical aspect of modern Diesel sprays is a widespread concept [60–63], so as long as the axis of the spray is accurately determined, presenting half a spray seems to be the best alternative solution. The ratio of the Mie and LIF signals as described by the theory of PDS is presented in figure 4.26. Note that no corrections like extinction compensation or scattering phase function have been applied on this picture as their influence on the ratio of both signals are limited. The LIF/Mie ratio has become quantitative through calibrated measurements thanks to a PDPA instrument (see sec. 3.4.3) and performed at 45 mm downstream on the edges of the spray where the extinction is relatively

low and allows accurate measurements. The total number of droplets measured for the calibration was over 5000 to ensure accuracy and statistic robustness of the results. To extract the mixture fraction, the mean volume diameter is required. Therefore, the SMD map provided by the LIF/Mie ratio has been adjusted with the mean volume diameter measured by the PDPA instrument. Additional details are given later in section 4.5.3 and an analysis of the error induced by assuming similar two-dimensional SMD and volume mean diameter distributions is given in appendix A. The results of additional measurements performed with the PDPA instrument are also presented in figure 4.26 to compare the radial evolution of the volume mean diameter in the spray.

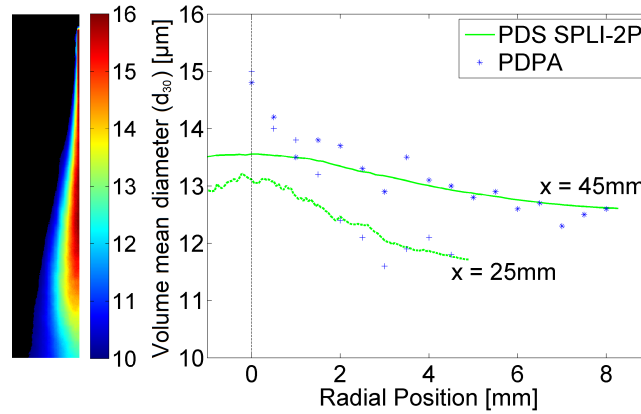


Figure 4.26: 2-D map of LIF/Mie ratio (SMD) in a Diesel spray calibrated through PDPA measurements of the volume mean diameter d_{30} (left). Radial profiles of volume mean diameter via PDS when applying SPLI-2P method and PDPA at 25 and 45 mm (right).

The evolution of the droplet size with respect to axial and radial position for the LIF/Mie ratio, when Structured Planar Laser imaging is applied, agrees well with the results obtained through phase Doppler interferometry (PDPA) measurements. In addition to that, the results found throughout the literature [23, 48, 64, 65] support the droplet size distribution presented in figure 4.26. It has to be noted that the droplets near the axis of the spray provided by the LIF/Mie ratio are smaller than the those measured by the PDPA instrument. The spray is known to be denser at this location and the large number density may affect the accuracy of the phase Doppler interferometer as described by several authors [20, 66, 67].

The droplet diameter distribution is now known for half the spray (considered axi-symmetrical), an additional step is nevertheless required before

utilizing the intensity profiles to recover the mixture fraction. The SPLI-2P signals obtained do not account for the extinction of light between the illumination plane and the acquisition system. And, if this is not important for sizing as it is self-corrected by considering the ratio of Mie and LIF signals, it becomes crucial when a single signal is used.

4.5.2 Light extinction between illumination and acquisition

The light scattered by the laser-sheet toward the acquisition system has to travel through the spray and is therefore extinguished, mainly via scattering. Depending on the wavelength of the collected signal (Mie or LIF), the absorption can also play a role in the extinction of light through the spray. Figure 4.27 is an illustration of the extinction of the radiation propagating through the spray toward the imaging system.

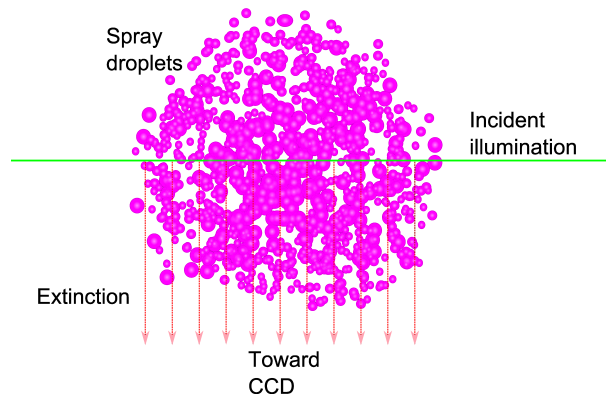


Figure 4.27: Scheme of the extinction process between the illumination plane and the acquisition system in a spray.

To get the proper signal emitted by the laser-sheet in the spray, the extinction of light must be known to correct the SPLI-2P signal. The next two sections present experimental methods to measure the extinction of light in the spray and therefore build a strategy to correct the signal provided by the Structured planar Laser imaging technique.

Estimation of the optical depth of a Diesel spray

The optical depth of a spray has been evaluated through line-of-sight extinction measurements as presented in [68]. The experimental setup is composed by

a 25 mW continuous wave He-ne laser, which wavelength is $\lambda = 632.8$ nm to ensure no absorption by the fuel used, i.e. n-dodecane + Sulfo-rhodamine B (see fig. 4.20). The transmitted light intensity has been recorded by a planar silicon PN photo-diode, an interference filter centered on 632.8 nm (FWHM = 2 nm) has been placed as close as possible to the photo-sensor in order to remove undesired light. The scattered light in the forward direction only has been acquired by placing a diaphragm to obtain a collection angle as low as 0.25 mrad. The complete system has been placed on a 3-D computer controlled traverse to move the measuring section with an accuracy of about 5 μm .

The transmitted signal recorded has a length of 10 ms and an acquisition rate of 100 KHz, note that the rise-time of the photo-diode is at least three times faster than the step resolution. Only the steady period of the injection has been used to extract the value of the extinction and the processed signal is an average over 100 injection events. Three axial distances from the injector tip have been tested: 20, 30 and 40 mm, at each distance, the system has been moved radially every 500 μm to recover the whole spray.

The optical depth is the natural logarithm of the ratio of the intensities before and after the spray as shown in equation 4.13.

Considering that the spray is axi-symmetrical, a deconvolution can be done to extract the optical depth anywhere in the spray. The technique is however limited by the high optical depth of the spray which induces the signal to go to zero as the laser beam is moved closer to the center of the spray. To extend the results to the complete spray, the measurements have been fitted with a Gaussian-like function as suggested in [68]. Figure 4.28 shows the radial profiles of the measured optical depth at two locations from the outlet (25 and 45 mm); the fitting used here is the distribution function proposed by Abramovich [69].

As depicted on figure 4.28, the optical depth in such situation can go up to $\tau = 10$. This value agrees with some other sources concerning sprays [70, 71] and place the light scattering in such conditions within the multiple scattering regime. As the conclusion drawn earlier in section 4.3.3, an optical depth of $\tau \approx 6$ maybe the limit of the Structured Planar Laser Imaging technique applied in such conditions. This reinforces the use of half the spray in this study as the extinction of light in half the spray would be $\tau \approx 5$ as suggested by the optical depth measurements.

With this methodology it is then possible to correct the signal extracted from the SPLI-2P image in order to obtain the real intensity radiated by the laser-sheet in the spray. Nevertheless due to the high extinction, this solution

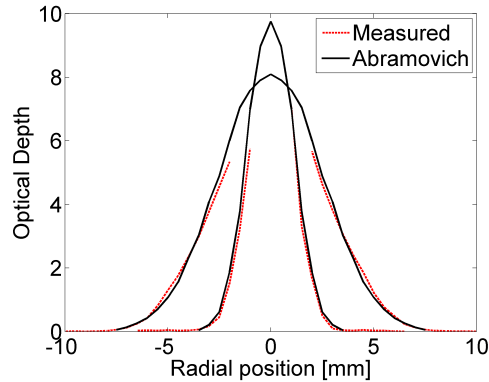


Figure 4.28: Measured and calculated radial profiles of the optical depth at 25 and 45 mm from the injector tip.

extends the results via a fitting, which could bring uncertainty on the actual optical depth value. In addition, this line-of-sight technique is time consuming and an alternative providing 2-D maps must be considered.

3-D correction for light extinction in a spray

The solution developed to correct the Structured Planar Laser Imaging signal from extinction consists in mapping the spray in three dimensions by imaging successive planes from the outside to inside of the spray until the illumination plane reaches the axis of the spray. This technique called discrete tomography [72] has been applied recently to evaluate the extinction coefficient in relatively dense sprays [43]. The procedure relies on the fact that the extinction between the illumination plane and the acquisition system follows the Beer-Lambert law. This assumption has been verified earlier in section 4.3.3 as the extinction of light or optical depth has been demonstrated to behave similarly along the laser path and from the illumination to the imaging system.

In this experiment, the plane of illumination is shifted by a step size of a millimeter until it exits the spray; as addressed by figure 4.27, the laser-sheet is moved in the Z-direction toward the CCD. The procedure to mathematically account for light extinction is conceptually described in figure 4.29. A spray image represents a 2-D coordinate system (X, Y), as the illumination is moved along the Z-direction, the SPLI-2P technique only keeps the modulated signal and a 3-D matrix of the spray is built.

The experimental setup has been described earlier (see sec. 4.4.1) and as

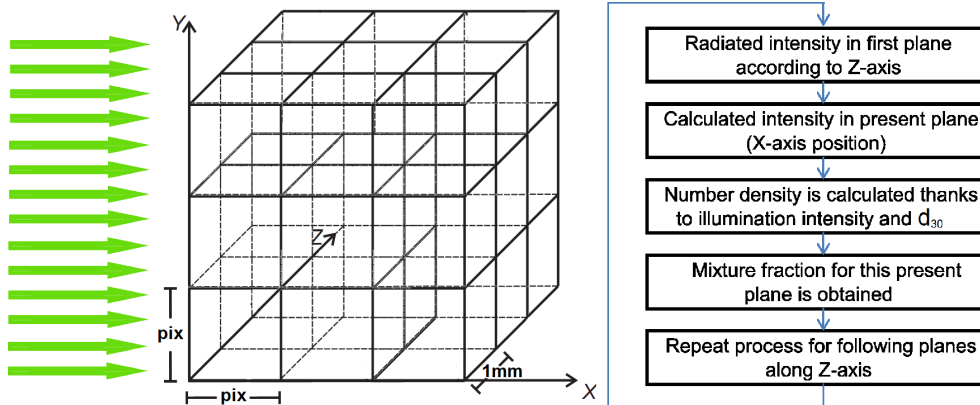


Figure 4.29: Concept of the 3-D methodology to correct the SPLI-2P signal from extinction between illumination plane and imaging system.

explained, the collection angle is small enough (23 mrad) to consider the light traveling in the Z-direction only. The first image is taken at the outer boundary of the spray; in the second one, the number density is relatively low and thus the extinction toward the camera can be considered as negligible. Hence, the intensity radiated by the laser-sheet toward the camera is the signal processed by the Structured Planar Laser Imaging technique multiplied by the global efficiency of the system. Since this first plane, the laser-sheet intensity and the optical depth can be calculated for every integration area, i.e, a pixel. Then, by mapping the spray in the Z-direction, the optical depth is known for every location and the original radiated signal extracted from the SPLI-2P image can be corrected.

4.5.3 Mixture fraction

The equivalence ratio is one of the most used parameters to consider in a combusting spray as it provides the boundary where the stoichiometric ratio is obtained. When the system is inert, like a spray injected in N_2 or SF_6 for example, the fuel mass fraction Y_f or mixture fraction Z is then utilized.

The mixture fraction Z measures the fuel/gas ratio and is therefore a combination of the droplet diameter and number density. A mixture fraction of $Z = 1$ means that at this location, there is only fuel, $Z = 0$ means that there is only gas, in other words outside the stream.

Resulting mixture fraction in a spray

The mathematical procedure described in section 4.3.4 provides the number density N at any location if the SPLI-2P signal has been corrected from light extinction. This means that equation 4.21 can be applied with the solution presented earlier aiming at estimating the optical depth of a spray to calculate the number density.

The solution employed to account for light extinction between the laser-sheet and the receiving system has been setup in order to compute the number density at the same time. From the intensity of the signal originally scattered by the laser-sheet calculated by the 3-D correction strategy, the number density of droplets in the spray can be obtained by applying equation 4.21 for all recorded planes. The various elements of both the images of droplet size and number density are processed in a discrete control volume (corresponding to a pixel of the images) to compute the fuel mass fraction according to the following expression:

$$Y_f = Z = \frac{\rho_f}{\rho_f + \rho_g \left(\frac{6}{N \pi d_{30}^3} - 1 \right)}, \quad (4.28)$$

The fuel mass fraction or mixture fraction is then a function of the droplet diameter, the number density N , the densities of the fuel ρ_f and the surrounding gas ρ_g . As it has been introduced earlier, an approximation has been made as the droplet diameter used in this equation is the volume mean diameter d_{30} extracted through LIF/Mie ratio, which theoretically provides the SMD (d_{32}). This approximation is based on the assumption of a constant relationship between volume mean diameter and Sauter Mean Diameter. The analysis of this approximation (see appendix A) confirmed that for the reference Diesel spray droplet diameter distribution, the maximum error made was as low as 1.5 % throughout the measured part of the spray.

Figure 4.30 presents the procedure developed in this study to obtain the fuel mass fraction from the original SPLI-2P images of Mie and LIF.

By applying the methodology presented above on the LIF signal, preferred to the Mie signal because it does not present anisotropy, a 2-D map of the mixture fraction of the spray is obtained. The illumination plane for the sample image presented in figure 4.31 crosses the spray on its axis, the injection pressure for this example is 150 MPa and the discharge density is 22.8 kg/m³.

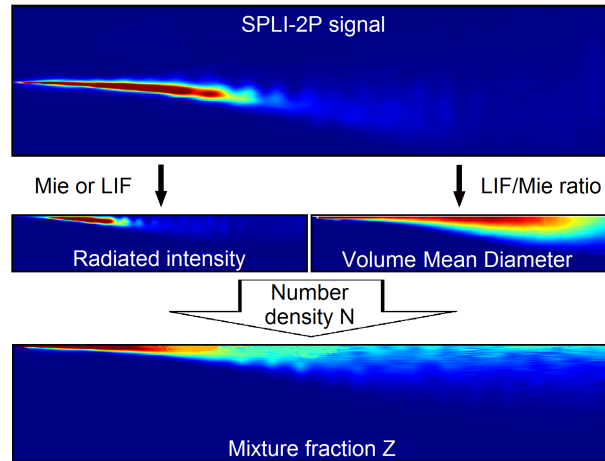


Figure 4.30: Illustration of the procedure to extract the mixture fraction from the Mie and LIF Structured Planar Laser Images. The images have been replicated by symmetry according to the axis of the spray.

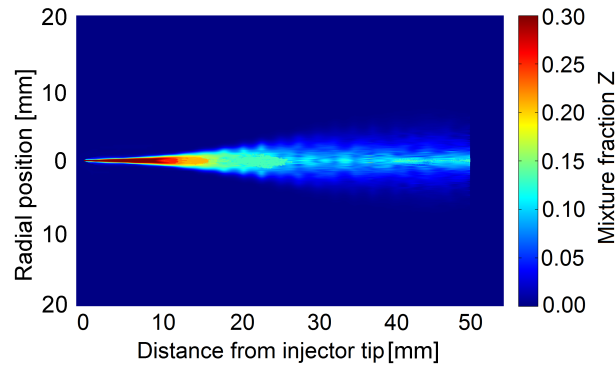


Figure 4.31: Resulting 2-D map of the mixture fraction with symmetry according to spray axis for the LIF signal. ($p_{inj} = 150 \text{ MPa}$ and $\rho_g = 22.8 \text{ kg.m}^{-3}$).

Validation of the results with a mixing model

A simple mixing model has been used to verify the validity of the data extracted from the SPLI-2P technique concerning the mixture fraction. Naber and Siebers [73] developed an analytical model describing penetration behavior of the jet based on the conservation of mass and momentum for a steady injection rate. In order to be simple, the model assumes a Schmidt number equal to the unity ($Sc = 1$), which means that velocity and mass distribution profiles are assumed to be the same at any axial distance from the injector outlet. They found that a constant accounting for this simplification of similar velocity and mass distributions was necessary for the model to fit the penetration rate and spreading angle data correctly.

More recently, the model has been extended by Musculus [74] by incorporating multiple control volumes and a realistic radial distribution of fuel mass as proposed by Abramovich [69] and described in equation 2.38. Figure 4.32 presents a schematic of the model with the control volumes used for the calculation as well as the radial distribution profile of the momentum according to Abramovich [69]. The radial distribution coefficient C_{R2} presented in section 2.5.4 gives the radial profile its shape. In this model, it starts from the infinity at $x = 0$ and decreases to reach a steady value of 1.5 after a short distance, resulting in a Gaussian-like profile.

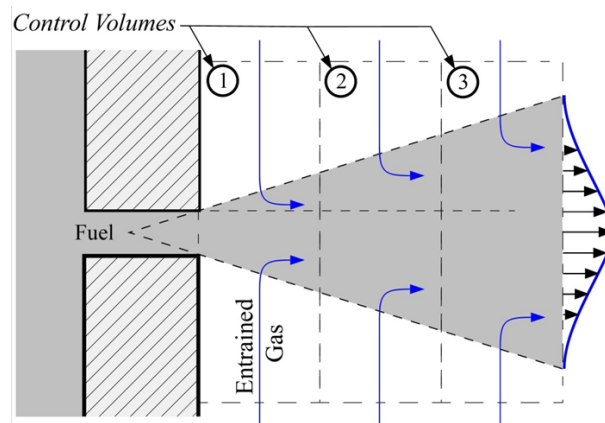


Figure 4.32: Schematic of the one-dimensional discrete control volume for transient jet model (Musculus [74]).

The use of multiple control volumes makes the model to predict penetration and mixing process for variable injection rates and after the end of injection [74, 75]. Spreading angles are still required as input to the model

to predict penetration and mixing distribution with accuracy. Since the fuel liquid volume fraction $\bar{\chi}_f$ is known at any location in the jet, the local fuel/ambient mass ratio m_f/m_g can therefore be calculated such as:

$$\frac{m_f}{m_g} = \frac{\rho_f \bar{\chi}_f}{\rho_g (1 - \bar{\chi}_f)}. \quad (4.29)$$

As the two densities of the fuel and ambient gases are characteristics of the experiments, the mixture fraction is obtained thanks to the fuel to ambient mass ratio as presented in equation 4.30.

$$Z = Y_f = \frac{\frac{m_f}{m_g}}{\frac{m_f}{m_g} + 1} \quad (4.30)$$

The local mixture fraction or fuel mass fraction is then obtained for any location within the jet as long as the spreading angle θ , the fuel and ambient densities ρ_f and ρ_g respectively are known, and a radial profile is assumed. In addition, as the rate of injection is an input to the model, the hydraulic parameters of the injector used such as area (C_a) and discharge (C_d) coefficients must be specified. These coefficients are generally measured experimentally and the results of the hydraulic characterization will be presented in chapter 6.

Several models of this kind have been developed throughout the years of Diesel spray studies, among them, the model proposed by Desantes et al. [76] and further improved by Pastor et al. [77] must be mentioned. This model is also based on the gas-jet theory and considers complete mixing of fuel and ambient in 1-D along the axis of the jet. When assuming a mixing distribution such as the exponential one recommended by the authors, a value of the Schmidt number can be given as an input. The Musculus model has been chosen because it has been quantitatively compared to two-dimensional mixing results of evaporative jets as a validation [78]; however, the Desantes-Pastor model should provide similar mixing predictions as they both rely on the same approach and similarity with gas-jets.

As a first comparison, the values of the input parameters have been obtained either experimentally or from the specifications provided by the suppliers of the equipment used. The spreading angle of the spray has been measured through high-speed imaging to visualize the spray macroscopically and the value obtained is $\theta = 17.3^\circ$. As a first approximation, the hydraulic parameters of the nozzle given by the manufacturer are used to adjust the model. The value of the discharge coefficient given by Bosch is $C_d = 0.86$; as

no value was available for the area coefficient C_a , the value has been set to the unity. This value of 1 is reasonable though, the nozzle has been shaped through hydro-grounding and the area contraction should therefore be very limited. The hydraulic characterization of the injector is presented further in the comparative chapter in section 6.2.

Figure 4.33 presents the axial profile of the mixture fraction of a spray of n-dodecane at 150 MPa injected into SF_6 at a density of 22.8 kg/m^3 obtained with the SPLI-2P technique and confronted to the Musculus model.

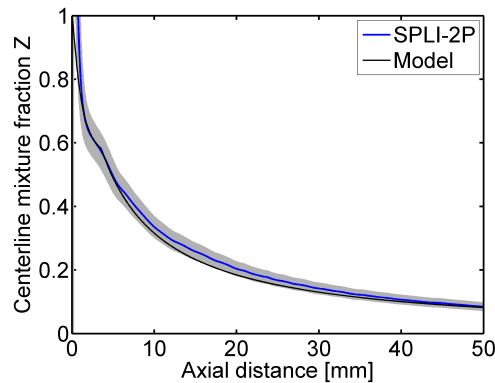


Figure 4.33: Experimental and computed mixture fraction on the spray centerline. ($p_{inj} = 150 \text{ MPa}$ and $\rho_g = 22.8 \text{ kg.m}^{-3}$).

The evolutions of the profiles along the axis of the spray are quite similar, they both follow the same trend. However, it can be noticed that the experimental plot seems to be slightly higher than the computed one, which still remains within the experimental uncertainties (gray filled area). The uncertainties represented here are based on the resulting standard deviation of the experiments made on the fluorescent microspheres (see sec. 4.3) plus the error made on droplet diameter (see appendix A).

The radial profile at two distances from the tip are represented in figure 4.34, the solution provided by the model assuming a radial distribution is also presented.

The radial profiles of the mixture fraction obtained by applying the Structured Planar Laser Imaging technique look narrower than that computed by the jet model. The assumptions of the model such as the radial distribution or the total momentum and mass transfer to be equivalent may not be appropriate for liquid sprays. As the model is based on the gas-jet theory, results

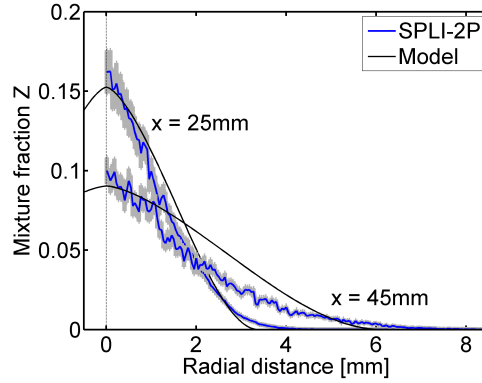


Figure 4.34: Experimental and computed radial profiles of the mixture fraction at 25 and 45 mm from the tip. ($p_{inj} = 150$ MPa and $\rho_g = 22.8$ kg.m⁻³).

of evaporating sprays may present more similarities, this is the object of the next-coming chapter implementing Rayleigh scattering in the vapor-phase of a Diesel spray (Chapter 6).

As the fuel mass must be conserved along the spray axis, the mean mixture fraction has been plotted in figure 4.35 versus the axial distance in the spray.

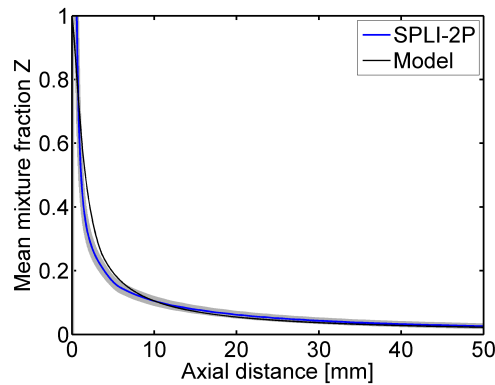


Figure 4.35: Comparison of the experimental and computed mean mixture fraction along the axis of the spray. ($p_{inj} = 150$ MPa and $\rho_g = 22.8$ kg.m⁻³).

The comparison of the two axial profiles of the mean mixture fraction validates the experimental solution setup in this study to evaluate the mixture fraction at any location in the spray. It shows that the increase observed on the centerline is actually balanced by the reduction on the side of the

Gaussian-like radial profile and produces a mean mixture fraction to be within the uncertainty of the experimental results.

Chapter 6 presents further discussions over the results under evaporative conditions or not as well as an evaluation of the different parameters influencing the spray development and mixing process. It also provides additional information concerning the utilization of experimental data together with a simple model to predict spray characteristics such as penetration rate, spreading angle and global mixing process.

4.6 Conclusions

The technique developed in this chapter is based on the scattering of light described by Mie applied to a medium containing droplets such as optically dense Diesel sprays. This diagnostic relies on multiple scattering removal thanks to the use of a spatially modulated planar illumination, its aim is to measure the mixture fraction at any location in a spray injected into discharge gases at ambient temperature (293 K).

By introducing the Mie scattering theory for droplets bigger than the wavelength, like it is mainly the case in such direct-injected Diesel sprays, the inhomogeneity of the scattered signal intensity has been shown. On the other hand, the advantage presented by the fluorescence (LIF) regarding the isotropy of the emitted signal demonstrated that this scattering process was an interesting alternative. However, due to the propagation of light in a medium containing scatterers such as liquid droplets and the fluorescent emission being dependent upon the Mie scattered light within the medium, the anisotropy of the elastically scattered light strongly affects the resulting LIF signal. At the same time, the possibility to extract the fuel volume fraction through extinction measurements has been described, this solution requires the droplet diameter though.

An alternative to the Structured Laser Illumination Planar Imaging technique has been developed by using only two phases (instead of three) to remove the multiply scattered photons thanks to adequate post-processing of the images. This diagnostic called Structured Planar Laser Imaging is capable of providing quantitative two-dimensional map of the particles number density. Specially-designed for particle sizing, polystyrene fluorescent microspheres have been put into solution with distilled water to simulate the propagation of light in an optically dense medium in a matter of validating the

SPLI-2P diagnostic. The experiments showed that the LIF/Mie ratio of the two signals aiming at providing SMD maps were consistent within the sample while they were not for conventional Planar Droplet Sizing (PDS - unstructured illumination).

The application to isothermal Diesel sprays required some preliminary studies aiming at characterizing the fluorescent emission (LIF). The fuel (n-dodecane) has been doped with a powerful fluorescent dye: the sulforhodamine B to ensure high quantum efficiency of the fluorescence signal. The absorption and emission spectra, as well as the fluorescence lifetime and quantum yield have been measured to adjust the experimental setup to the best possible conditions. Then, an analysis of the main parameters for successful PDS measurements has been done through the evaluation of the square and cubic dependencies of the scattered and fluorescent signal intensities, respectively.

The preliminary results showed that the sprays injected in this study presented such a high optical depth τ that only half the spray could be evaluated quantitatively. The first step of the process is to obtain two-dimensional droplet size distribution thanks to the LIF/Mie ratio as the droplet diameter (d_{30}) must be known to further calculate the fuel mass fraction through extinction measurements. Secondly, the extinction between the illumination plane and the acquisition system has been evaluated thanks to a 3-D correction process computing the extinction within the spray from the outside to the center. In the meantime, the number density of the droplets in the control volume used for the calculation, finally, the mixture fraction can be extracted by merging the both droplet size and number density maps. To assess the quantitative aspect of the SPLI-2P technique in sprays, the results have been confronted to a 2-D mixing model. The experimental-simulation confrontation showed great potential; despite the experiments provided higher mixture fraction on the centerline, the narrower shape of the spray appeared to be balanced as supported by the mean mixture fraction along the axis of the spray.

Bibliography

- [1] L. Lorenz. Uber die refractionsconstante. *Annalen Der Physik und Chemie*, 11:70–103, 1880.

-
- [2] G. Mie. Beitrage zur Optik truber Medien, speziell kolloidaler Metallösungen. *Annalen der Physik*, 330(3):377–445, 1908.
- [3] H.C. Van De Hulst. Light scattering by small particles. *Dover Publications, Inc., New-York*, 1981.
- [4] M. Kerker. The scattering of light and other electromagnetic radiation. *Academic Press, London*, 1969.
- [5] A. D’alessio. Laser light scattering and fluorescence diagnostics of rich flames produced by gaseous and liquid fuels. *Particulate Carbon: Formation During Combustion*, pages 207–259, 1981.
- [6] F. Beretta, A. Cavaliere, and D. D’alessio. Drop size and concentration in a spray by sideward laser light scattering measurements. *Combustion Science and Technology*, 36(1):19–37, 1984.
- [7] N. Chigier. Combustion measurements. *Hemisphere Publishing Corporation*, 1991.
- [8] A.C. Eckbreth. Laser diagnostics for combustion species and temperature. *Abacus, Cambridge, Mass*, pages 249–252, 1988.
- [9] P. Andresen, G. Meijer, H. Schluter, H. Voges, A. Koch, W. Hentschel, W. Oppermann, and E. Rothe. Fluorescence imaging inside an internal combustion engine using tunable excimer lasers. *Applied Optics*, 29(16):2392–2404, 1990.
- [10] A. Arnold, F. Dinkelacker, T. Heitzmann, P. Monkhouse, M. Schafer, V. Sick, J. Wolfrum, W. Hentschel, and K.P. Schindler. DI Diesel engine combustion visualized by combined laser techniques. *Symposium (International) on Combustion*, 24(1):1605–1612, 1992.
- [11] J.M. Seitzman and R.K. Hanson. Planar fluorescence imaging in gases. *Instrumentation for flows with combustion*, 1993.
- [12] M. Berckmuller, N.P. Tait, D. Lockett, D.A. Greenhalgh, K. Ishii, Y. Urata, H. Umiyama, and K. Yoshida. In-cylinder crank-angle-resolved imaging of fuel concentration in a firing spark-ignition engine using planar laser-induced fluorescence. *Symposium (International) on Combustion*, 25(1):151–156, 1994.

- [13] C.N. Yeh, H. Kosaka, and T. Kamimoto. A fluorescence/scattering imaging technique for instantaneous 2-D measurement of particle size distribution in a transient spray. *3rd International Congress on Optical Particle Sizing, Yokohama, Japan*, pages 355–361, 1993.
- [14] C.N. Yeh, H. Kosaka, and T. Kamimoto. Measurement of drop sizes in unsteady dense sprays. *Recent advances in spray combustion: Spray atomization and drop burning phenomena.*, 1:297–308, 1996.
- [15] P. Le Gal, N. Farrugia, and D.A. Greenhalgh. Development of laser sheet drop sizing (lsd) for spray characterization. *IMEchE conference transactions*, pages 113–120, 1998.
- [16] R.D. Lockett, J. Richter, and D.A. Greenhalgh. The characterisation of a diesel spray using combined laser induced fluorescence and laser sheet dropsizing. *Conference on Lasers and Electro-Optics Europe, 1998*, 1998.
- [17] D.A. Greenhalgh. Planar measurements of fuel vapour, liquid fuel, liquid droplet size and soot. *Planar Optical Measurement Methods for Gas Turbine Components*, pages 1–7, 1999.
- [18] S.V. Sankar, K.E. Maher, D.M. Robart, and W.D. Bachalo. Spray characterization using a planar droplet sizing technique. *International journal of fluid mechanics research*, 24:578–589, 1997.
- [19] P. Le Gal, N. Farrugia, and D.A. Greenhalgh. Laser sheet dropsizing of dense sprays. *Optics and Laser Technology*, 31(1):75–83, 1999.
- [20] M.C. Jermy and D.A. Greenhalgh. Planar dropsizing by elastic and fluorescence scattering in sprays too dense for phase doppler measurement. *Applied Physics B: Lasers and Optics*, 71(5):703–710, 2000.
- [21] R. Domann and Y. Hardalupas. A study of parameters that influence the accuracy of the planar droplet sizing (PDS) technique. *Particle & Particle Systems Characterization*, 18(1):3–11, 2001.
- [22] R. Domann and Y. Hardalupas. Quantitative measurement of planar droplet sauter mean diameter in sprays using planar droplet sizing. *Particle & Particle Systems Characterization*, 20(3):209–218, 2003.
- [23] J.V. Pastor, J.J. Lopez, J.E. Juliá, and J.V. Benajes. Planar laser-induced fluorescence fuel concentration measurements in isothermal diesel sprays. *Optics Express*, 10(7):309–323, 2002.

-
- [24] M.B. van der Mark, M.P. van Albada, and A. Lagendijk. Light scattering in strongly scattering media: multiple scattering and weak localization. *Physical Review B*, 37(7):3575–3592, 1988.
- [25] S.A. Ahmed, Z.W. Zang, K.M. Yoo, M.A. Ali, and R.R. Alfano. Effect of multiple light scattering and self-absorption on the fluorescence and excitation spectra of dyes in random media. *Applied Optics*, 33(13):2746–2750, 1994.
- [26] L. Araneo and R. Payri. Experimental quantification of the planar droplet sizing technique error for micro-metric mono-dispersed spherical particles. *ILASS Conference, Como lake, Italy*, 2008.
- [27] J.V. Pastor, R. Payri, L. Araneo, and J. Manin. Correction method for droplet sizing by laser-induced fluorescence in a controlled test situation. *Optical Engineering*, 48:013601, 2009.
- [28] L. Lorenz. Lysbevaegelser i og uden for en af plane lysbolger belyst kugle. *Det kongelig danske Videnskabernes Selskabs Skrifter*, 6:1–62, 1890.
- [29] P. Debye. Der lichtdruck auf kugeln von beliebigem material. *Annalen der physik*, 335(11):57–136, 1909.
- [30] C.F. Bohren and D.R. Huffman. Absorption and scattering of light by small particles. *Wiley-Interscience, New York*, 1983.
- [31] G. Gouesbet and G. Grehan. Sur la generalisation de la theorie de lorenz-mie. *Journal of Optics (Paris)*, 13(2):97–103, 1982.
- [32] A. Jablonski. Efficiency of anti-stokes fluorescence in dyes. *Nature*, 131(3319):839–840, 1933.
- [33] J.R. Lakowicz and B.R. Masters. Principles of fluorescence spectroscopy. *Journal of Biomedical Optics*, 13, 2008.
- [34] A. Beer. Bestimmung der absorption des rothen lichts in farbigen flussigkeiten. *Annalen der Physik und Chemie*, 86(2), 1852.
- [35] J.D. Ingle and S.R. Crouch. Spectrochemical analysis. *Englewood Cliffs, NJ*, 1988.
- [36] R. Domann and Y. Hardalupas. Evaluation of the planar droplet sizing (PDS) technique. *ICLASS 2000, Pasadena, CA*, pages 131–138, 2000.

- [37] R. Domann and Y. Hardalupas. Spatial distribution of fluorescence intensity within large droplets and its dependence on dye concentration. *Applied Optics*, 40(21):3586–3597, 2001.
- [38] R. Domann, Y. Hardalupas, and A.R. Jones. A study of the influence of absorption on the spatial distribution of fluorescence intensity within large droplets using mie theory, geometrical optics and imaging experiments. *Measurement Science and Technology*, 13:280, 2002.
- [39] M.C. Jermy and A. Allen. Simulating the effects of multiple scattering on images of dense sprays and particle fields. *Applied optics*, 41(20):4188–4196, 2002.
- [40] M.A.A. Neil, R. Juskaitis, and T. Wilson. Method of obtaining optical sectioning by using structured light in a conventional microscope. *Optics Letters*, 22(24):1905–1907, 1997.
- [41] T. Breuninger, K. Greger, and E.H.K. Stelzer. Lateral modulation boosts image quality in single plane illumination fluorescence microscopy. *Optics letters*, 32(13):1938–1940, 2007.
- [42] E. Berrocal, I. Meglinski, and M. Jermy. New model for light propagation in highly inhomogeneous polydisperse turbid media with applications in spray diagnostics. *Optics Express*, 13:9181–9195, 2005.
- [43] A. Berrocal, R. Wellander, and E. Kristensson. Accounting for multiple scattering signal attenuation and laser extinction using structured laser illumination planar imaging. *ILASS Conference, Brno, Czech Republic*, 2010.
- [44] P.A. Franken, A.E. Hill, C.W. Peters, and G. Weinreich. Generation of optical harmonics. *Physical Review Letters*, 7(4):118–119, 1961.
- [45] M.M. El-Wakil, P.S. Myers, and O.A. Uyehara. Fuel vaporization and ignition lag in Diesel combustion. *SAE Transactions*, 64:712, 1956.
- [46] M.D. Barnes, W.B. Whitten, and J.M. Ramsey. Enhanced fluorescence yields through cavity quantum-electrodynamic effects in microdroplets. *Journal of the Optical Society of America B*, 11(7):1297–1304, 1994.
- [47] G. Chen, M. Mazumder, R.K. Chang, J.C. Swindal, and W.P. Acker. Laser diagnostics for droplet characterization: application of morphology dependent resonances. *Progress in Energy and Combustion Science*, 22(2):163–188, 1996.

- [48] D.A. Greenhalgh and M. Jermy. Laser diagnostics for droplet measurements for the study of fuel injection and mixing in gas turbines and ic engines. *Applied combustion diagnostics*, pages 408–438, 2002.
- [49] F.H. Ko, L.Y. Weng, C.J. Ko, and T.C. Chu. Characterization of imprinting polymeric temperature variation with fluorescent rhodamine B molecule. *Microelectronic Engineering*, 83(4-9):864–868, 2006.
- [50] U. Brackmann. Lambdachrome laser dyes - 3rd edition. *LambdaPhysik*, 2000.
- [51] D. Magde, G.E. Rojas, and P.G. Seybold. Solvent dependence of the fluorescence lifetimes of xanthene dyes. *Photochemistry and Photobiology*, 70(5):737–744, 1999.
- [52] A.T.R. Williams, S.A. Winfield, and J.N. Miller. Relative fluorescence quantum yields using a computer-controlled luminescence spectrometer. *Analyst*, 108(1290):1067–1071, 1983.
- [53] P.R. Hammond. Laser dye dcm, its spectral properties, synthesis and comparison with other dyes in the red. *Optics Communications*, 29(3):331–333, 1979.
- [54] V.S. Antonov and K.L. Hohla. Dye stability under excimer-laser pumping. *Applied Physics B: Lasers and Optics*, 30(3):109–116, 1983.
- [55] M. Broyer, J. Chevaleyre, G. Delacretaz, and L. Woste. CVL-pumped dye laser for spectroscopic application. *Applied Physics B: Lasers and Optics*, 35(1):31–36, 1984.
- [56] W.M. Vaughn and G. Weber. Oxygen quenching of pyrenebutyric acid fluorescence in water. dynamic probe of the microenvironment. *Biochemistry*, 9(3):464–473, 1970.
- [57] M.R. Eftink and C.A. Ghiron. Fluorescence quenching of indole and model micelle systems. *The Journal of Physical Chemistry*, 80(5):486–493, 1976.
- [58] A. Calatayud, V.I. Deltoro, E. Barreno, and S. Valle-Tascon. Changes in in vivo chlorophyll fluorescence quenching in lichen thalli as a function of water content and suggestion of zeaxanthin-associated photoprotection. *Physiologia Plantarum*, 101(1):93–102, 1997.

- [59] A.J.W.G. Visser, K. Vos, A. Van Hoek, and J.S. Santema. Time-resolved fluorescence depolarization of rhodamine B and (octadecyl) rhodamine B in triton X-100 micelles and aerosol OT reversed micelles. *The Journal of Physical Chemistry*, 92(3):759–765, 1988.
- [60] D.B. Spalding. Combustion and mass transfer. *Pergamon international library of science, technology, engineering, and social studies*, 1979.
- [61] F. Payri, J. M. Desantes, and J. Arrègle. Characterization of DI diesel sprays in high density conditions. *SAE Paper 960774*, 1996.
- [62] D.L. Siebers. Scaling liquid-phase fuel penetration in diesel sprays based on mixing-limited vaporization. *SAE Paper 1999-01-0528*, 1999.
- [63] J. Arrègle, J.V. Pastor, and S. Ruiz. Influence of the injection parameters on Diesel spray characteristics. *SAE Paper 1999-01-0200*, 1999.
- [64] T. Kamimoto, H. Yokota, and H. Kobayashi. A new technique for the measurement of sauter mean diameter of droplets in unsteady dense sprays. *SAE Paper 890240*, 27, 1989.
- [65] C. Tropea. Laser doppler anemometry: recent developments and future challenges. *Measurement Science and Technology*, 6(6):605–619, 1995.
- [66] L. Araneo, V. Soare, R. Payri, and J. Shakal. Setting up a PDPA system for measurements in a Diesel spray. *Journal of Physics: Conference Series*, 45:85, 2006.
- [67] Vlad Soare. *Phase doppler measurement in diesel dense sprays: optimization of measurements and study of the orifice geometry influence over the spray at microscopic level*. PhD thesis, E.T.S. Ingenieros Industriales. Universidad Politècnica de Valencia, Valencia, 2007.
- [68] R. Payri, F.J. Salvador, J. Gimeno, and G. Bracho. The effect of temperature and pressure on thermodynamic properties of Diesel and biodiesel fuels. *Fuel*, 2010.
- [69] G.N. Abramovich. The theory of turbulent jets. *MIT Press, Cambridge, Massachusetts*, 1963.
- [70] C. Roze, T. Girasole, L. Mevc, G. Grehan, L. Hespel, and A. Delfour. Interaction between ultra short pulses and a dense scattering medium by monte carlo simulation: consideration of particle size effect. *Optics Communications*, 220(4-6):237–245, 2003.

-
- [71] E. Berrocal, D.L. Sedarsky, M.E. Paciaroni, I.V. Meglinski, and M.A. Linne. Laser light scattering in turbid media part II: Spatial and temporal analysis of individual scattering orders via monte carlo simulation. *Optics Express*, 17(16):13792–13809, 2009.
- [72] G.T. Herman and A. Kuba. Discrete tomography: Foundations, algorithms, and applications. *Birkhauser*, 1999.
- [73] J. Naber and D. Siebers. Effects of gas density and vaporization on penetration and dispersion of diesel sprays. *SAE Paper 960034*, 1996.
- [74] M.P.B. Musculus. Entrainment waves in decelerating transient turbulent jets. *Journal of Fluid Mechanics*, 638:117–140, 2009.
- [75] S. Kook, L.M. Pickett, and M.P.B. Musculus. Influence of diesel injection parameters on end-of-injection liquid length recession. *SAE International Journal of Engines*, 2(1):1194, 2009.
- [76] J.M. Desantes, J.J. Lopez, J.M. Garcia, and J.M. Pastor. Evaporative Diesel spray modeling. *Atomization and Sprays*, 17(3):193–232, 2007.
- [77] J.V. Pastor, J.J. Lopez, J.M. Garcia, and J.M. Pastor. A 1D model for the description of mixing-controlled inert diesel sprays. *Fuel*, 87(13-14):2871–2885, 2008.
- [78] L. Pickett, J. Manin, C.L. Genzale, D.L. Siebers, M.P.M. Musculus, and Idicheria C.A. Relationship between diesel fuel spray vapor penetration/dispersion and local fuel mixture fraction. *SAE Paper 2011-01-0686*, SAE International Journal of Engines, 2011.

Chapter 5

Rayleigh scattering measurements in vapor phase

Contents

5.1	Introduction	180
5.2	Rayleigh scattering theory	183
5.2.1	General formulation	184
5.2.2	Rayleigh cross-section	186
5.2.3	Rayleigh scattering in jets	189
5.3	Calibration of the experiments	190
5.3.1	Specific optical arrangement	190
5.3.2	Estimation of the cross-sections	192
5.3.3	General diagnostic protocol	195
5.4	Data processing and corrections	198
5.4.1	Image post-processing	199
5.4.2	Further corrections and improvements	201
5.4.3	Uncertainty analysis	202
5.5	Mixture fraction and temperature distributions	204
5.5.1	Single jet analysis	205
5.5.2	Mixture fraction in vaporized jets	206
5.5.3	2-D temperature distribution	211
5.6	Conclusions	212
	Bibliography	213

5.1 Introduction

A good mixture between fuel and air is one of the preponderant steps to get the most efficient combustion possible leading to lowering pollutant emissions. As most fuels are stored and transported as the liquid state, it must be evaporated prior to burning to ensure a complete combustion. The previous chapter concerning the atomization and mixing process pointed out the relatively narrow spreading angle of the spray under non-evaporative conditions (see sec. 4.5.3). We will see if these conclusions are still true when a Diesel spray is being evaporated or if the mixing process considering state change from liquid to gas makes the distribution to be more similar to that of the gas-jet theory.

The discussion drawn in chapter 4 to choose which technique would apply the best to our experimental configuration must be repeated here concerning the methods available to study the vapor phase of the jet. It is clear that the laser-based techniques present a considerable advantage when testing in the vapor phase, mainly because of they are non-intrusive and because the small cross-section of the molecules makes the measurements easier and the results more reliable. The fact that laser-based diagnostics are non-intrusive is also true when the liquid phase is studied, nevertheless, the size of the particles or scatterers affects the measurements in such ways that specific corrections have to be applied as described all along chapter 4.

There are many ways to study a gas stream with lasers and imaging technologies, depending on the objective of the experiments, a review of the different methods has been published by Zhao and Ladommatos [1]. A brief introduction of these different techniques is outlined in the forthcoming paragraphs, highlighting the advantages and drawbacks of each of them. Some methods are punctual, others mono-dimensional, and some directly provide 2-D maps, a critical comparison is driven here to make select the best technique to apply for the study of an evaporative Diesel jet.

The Laser Mie Scattering is more likely to be applied to study the liquid phase as demonstrated in the previous chapter. It has been seen previously that due to high extinction and multiple scattering effects, the signal recorded was not quantitative. A solution is possible though, the addition of silicone oil with a high boiling point can make the Mie scattering technique quantitative to study an evaporative jet. Thanks to a separate calibration procedure where an identified amount of fuel is sprayed and knowing the conditions of injection, fuel mass fraction distribution can be extracted. The Laser Mie Scattering can be performed in one or two dimensions depending on the optical setup,

this versatility makes the technique a promising alternative for complete spray mapping.

The Spontaneous Raman Scattering (SRS) is used for quantitative measurements of the different species present in the environment under study. It has been introduced by Johnston [2] almost 30 years ago and allows detecting many different molecules such as H₂O, CO₂, N₂, O₂, fuel. The air/fuel ratio can then be directly obtained by ratioing the quantities of two of the major species present in the fuel and the ambient gases. The principle is that when a photon collides with a molecule, the molecule exchanges some energy with the scattered photon due to a change of its energy state (both rotational and vibrational). This change in terms of energy level results in a Stoke shift of the wavelength which is species specific, making the measurement really accurate. However, the weakness of the signal and the poor spatial resolution which is generally single point or 1-D make this experimental technique inconvenient for jet characterization.

A fluorescence-based technique is always useful to perform measurements in an engine due to the inelastic property of the radiation acquired. The Planar Laser-Induced Fluorescence is of that kind, it has been widely used in combustion machines over the last decades as it allows to observe both vapor and liquid phases. The principle of this diagnostic relies on the ability of a tracer, mixed in the fuel, to emit photons when excited at a particular wavelength. As the signal emitted has experienced a Stoke shift, the SNR is relatively high as a large part of the background noise has been removed by filtering. Therefore, the high sensitivity of the technique permits detection of species at sub-ppm level but care must be taken concerning the measurements because of the various corrections applied to account for radiative decay rates and non-radiative losses such as quenching, pre-dissociation and photo-ionization [3]. The Planar Laser-Induced Fluorescence methodology offers the advantage of being two dimensional as it has been described in detail in section 4.2 when applied to isothermal liquid sprays.

An alternative to the Laser-Induced Fluorescence has been developed to experimentally dissociate the fluorescent signals emitted by the liquid droplets and by the vaporized region. The Planar laser-Induced Exciplex Fluorescence (PLIEF) technique proposed by Melton in the early 1980's [4], consists in separating spectrally (via filtering) the fluorescent emissions of the vapor and liquid phases. This is achieved by adding to the fuel two tracer species which act like a monomer (M)-Quencher(G) pair that easily form together a loosely bound excited complex called exciplex (E*). The method seems very promising as it

allows quantitative measurements of liquid and vapor fuel mass fraction in an evaporative Diesel jet at the same time. Nonetheless, the stability of the Excimer compound strongly depends on temperature and largely affects the signal strength [1] and therefore requires specific and complex calibration. Moreover, differences between fuel and tracer evaporation point could make the calibration more difficult and therefore, the results have to be analyzed with regard to the accuracy of the calibration [5]. Although the PLIEF technique clearly presents an advantage to reach the objectives of this thesis, the complexity of the calibration under non-isothermal environment cannot make it as the best choice for quantitative 2-D imaging of the mixture fraction in a spray.

The Planar Laser Rayleigh Scattering (PLRS) is capable of providing good results in 2-D imaging setups with fairly good resolution thanks to high SNR [6]. It mainly relies on the scattering theory for particles smaller than the wavelength published by Lord Rayleigh at the end of the XIXth Century [7–9]. The main advantage is that it does not require specific calibration and any information can be extracted almost directly from the theory and species calibration. As the Rayleigh scattering is an elastic process, the signal acquired may suffer from Mie scattering interferences and other scattering from the elements due to reflections that could affect the results. Hence, the difficulty lies in finding a way to avoid as much as possible the unwanted scatter and reflection effects from various sources other than the species under study. Examples of optical noise sources can be particles in the fuel or in the ambient, fuel droplets not evaporated yet, and flare coming from the windows and laser-sheet delivery optics. The spatial coexistence of both liquid droplets and vaporized fuel is certainly the main limitation of the utilization of PLRS inside the engine. The fuel-air mixing entrains liquid droplets and vaporized fuel in the same stream and results in the incapacity of measuring the vapor-phase quantitatively due to strong scatterers (fuel droplets).

To combat these inherent problems from external sources of elastic scattered radiation, the Filtered Rayleigh Scattering (FRS) outlined by Miles et al. [10] could be an attractive alternative. The principle is based on the Laser Rayleigh Scattering theory by additionally taking into account the Doppler shifting of the scattered signal by the particle movements, thus making the wavelength range wider. Then a narrow filter is used to remove the first order of scattering coming from any immobile sources, and a cleaner signal can be acquired. Because of this filtering, removing most information from the initial scattered light, the signal strength gets too low and must be intensified before acquisition, thus decreasing the global SNR of the system. This represents the main downside of the method, because lowering the SNR, which is the advan-

tage of the Laser Rayleigh Scattering, makes that the accuracy of the results is finally dependent upon the quality of the imaging system (Intensifier + camera) and the calibration of the spectral filtering. The Planar Laser Rayleigh Scattering has been selected over the filtered solution because the combustion vessel used for this work (see sec. 3.5.1) is wide enough so that the scattered light coming from other sources does not represent a major issue.

The objective of this work is to characterize a vaporized Diesel jet from a quantitative point of view, from the last paragraphs, it appears that PLIF and PLRS presents the most advantage in this aim. Due to the fact that PLIF needs specifically designed correction strategy considering radiation losses and hazards in both emitted and received signal, the PLRS has been chosen because it provides more accurate results relying on only simple calibration. In addition, Laser Rayleigh Scattering does not require any additive and therefore the integrity of the fuel is conserved thus respecting the evaporation behavior of the n-dodecane.

The present chapter aims at carrying out quantitative measurements in an evaporative jet thanks to the PLRS technique within the vapor phase only. The theory of the scattering of light by particles smaller than the wavelength as described by Rayleigh is presented in the next-coming section. The calibration of the technique together with the experimental setup form the third part of this chapter. The processing strategy is described next, showing the improvements on the image contrast through mathematical solutions. The quantitative results together with a comparison to the Musculus' mixing model employed earlier are presented before the conclusions over the mixture fraction measurements under evaporative conditions.

5.2 Rayleigh scattering theory

The Rayleigh scattering (named after John William Strutt widely known as Lord Rayleigh) is the phenomenon occurring between an incident ray of light and a particle smaller than the wavelength, generally atoms or molecules [7]. As described in the introduction, the Rayleigh scattering is an elastic process, which means that the incident signal and the scattered one are of the same electromagnetic wave frequency. This formulation of the scattering of light by particles is not an extension of the Mie theory briefly described in section 4.2, but it can be assimilated as a simplification.

As the Rayleigh scattered light intensity is dependent upon the polarizability of the particle, it is proportional to the wavelength (λ^4 dependency) and the intensity of the incident radiation, the size of the molecule, and many other parameters that are described in the following sections. An adiabatic mixing has been assumed to evaluate both the vaporized fuel mass fraction and the temperature distributions in the jet as proposed by Espey et al. [11].

5.2.1 General formulation

Lord Rayleigh undertook a campaign of works on the propagation of electromagnetic waves in different media, the transmission of light by small particles published in 1871 [7] provides a mechanical theory based on the propagation of transverse waves within an elastic medium (ether). The mathematical expressions developed by Rayleigh were in line with the contemporary theory in place at that time to explain light propagation in vacuum.

A few years earlier, Maxwell [12] described the light as transverse electric and magnetic fields oscillating perpendicularly to one another. After some communications with Maxwell (in which the consistency of the two models is addressed [9]), Rayleigh decided to translate his mechanical approximation into electromagnetic descriptions of the light scattered by small particles by an incident wave.

This task led to the expression of the Rayleigh signal intensity scattered by a dipole included in a sphere [9]:

$$I_{Ray} = \frac{\pi^2 \alpha^2}{\varepsilon_0^2 \lambda^4 R_{dipole}^2} I_0 \sin^2 \varphi . \quad (5.1)$$

In this formulation of the scattered intensity I_S observed at an angle φ and excited by an incident wave of intensity I_0 of wavelength λ , α is the polarizability of the molecule, ε_0 the vacuum permittivity and R_{dipole} the radius of the sphere including the dipole.

By integration of the scattered intensity presented in equation 5.1 over a the surface of a large sphere of radius R_{dipole} , the total power W_T scattered by the dipole can be calculated as expounded in the following equation:

$$W_T = \int_{\beta=0}^{2\pi} \int_{\varphi=0}^{\pi} \frac{\pi^2 \alpha^2}{\varepsilon_0^2 \lambda^4 r^2} I_0 \sin^2(\varphi) R_{dipole} \sin(\varphi) d\varphi R_{dipole} d\beta . \quad (5.2)$$

Where φ and β are the two dimensions of the integration to collect the energy scattered all over the surface of the sphere. After integration, the solution of the total power scattered by a dipole small compared to the wavelength can be simply expressed as [10]:

$$W_T = \frac{\pi^2 \alpha^2}{\varepsilon_0^2 \lambda^4 R_{dipole}^2} I_0 . \quad (5.3)$$

Most of the theoretical solutions to express the Rayleigh scattered signal intensity use a differential cross-section [1,6,10] although it is not necessary as the total scattered power can also be expressed as a function of the Rayleigh cross-section of the dipole and the incident intensity. The basic idea of the cross-section has been described in chapter 4 concerning the propagation of light in a medium containing scatterers (sec. 4.2). The principle is that any particle or droplet has a cross-section (area), which basically represents how much light will be removed from the incident intensity. Therefore, the Rayleigh cross-section σ_R , which is an area, can be expressed as the ratio of the total scattered power and the incident intensity [10].

$$\sigma_R = \frac{W_T}{I_0} \quad (5.4)$$

By the same token, the total power scattered by a cloud of small particles is the sum of the power emitted by any single scatterer. To simplify, if the particles are considered of the same kind, like a mono-component gas for example, a constant Rayleigh cross-section can be assumed and the total scattered power becomes:

$$W_T = \sum_{i=1}^{\varpi V} I_0 \sigma_R, \quad (5.5)$$

with ϖV the number of particles ϖ within the considered volume V . This means that the total power emitted by an ensemble of gases molecules can be expressed as:

$$W_T = \varpi V I_0 \sigma_R . \quad (5.6)$$

From this simple expression, the scattered power recorded by an acquisition system placed orthogonally to the illumination plane can be calculated by introducing the collection angle Ω and the global efficiency of the system η_{opt} .

The power of the signal W_R recorded by the imaging system can then be expressed as:

$$W_R = \varpi V I_0 \Omega \eta_{opt} \sigma_R . \quad (5.7)$$

Then, the area probed has to be considered to obtain the intensity of the signal scattered by the molecules. Thanks to the normalization of the number of particles as a number density N and by the introduction of the length scale L_{opt} of the probed volume, equation 5.8 gives the intensity scattered by Rayleigh scattering for a gas of known cross-section and density.

$$I_R = N L_{opt} I_0 \Omega \eta_{opt} \sigma_R \quad (5.8)$$

Equation 5.8 is certainly the most widely used for Rayleigh scattering measurements as it directly relates the number density to the recorded intensity as long as the system has been previously calibrated and properties of the species under study are known.

5.2.2 Rayleigh cross-section

As described by equation 5.8, the Rayleigh cross-section must be known to draw the mathematical relationship between the intensity of the signal acquired and the number density of the gases molecules, in other words, the concentration. Knowing the Rayleigh cross-section with accuracy is paramount for quantitative measurements. The cross-section of the molecule in the Rayleigh regime (particle much smaller than the wavelength) is dependent upon polarizability and not directly upon size, as it is for particle in the Mie regime (see eq. 4.5). By combining equations 5.3 and 5.4, the Rayleigh cross-section can therefore be expressed as:

$$\sigma_R = \frac{\pi^2 \alpha^2}{\varepsilon_0^2 \lambda^4 R_{dipole}^2} . \quad (5.9)$$

The polarizability α is coefficient of proportionality which relates the electric field \vec{E} to the induced moment of the dipole \vec{p} such as: $\vec{p} = \alpha \vec{E}$. If the approximation of the symmetrically spherical dipole is made, as α is a scalar, the moment of the dipole is induced in the same direction as the incident electro-

magnetic radiation [1,10]. The Lorenz-Lorentz equation presents another way to express the polarizability of the molecules such as [13,14]:

$$\alpha = \frac{3 \varepsilon_0 n^2 - 1}{N_0 n^2 + 2}, \quad (5.10)$$

in which N_0 is the standard number density (Number density at STP: Standard Temperature and Pressure) also called the Loschmidt constant and n is the refractive index of the medium (gas). By replacing the polarization as described by Lorenz and Lorentz in equation 5.10 into the general formulation of the Rayleigh cross-section (eq. 5.9), the following expression is obtained [10,15,16]:

$$\sigma_R = \frac{24 \pi^3}{N_0^2 \lambda^4} \left(\frac{n^2 - 1}{n^2 + 2} \right)^2. \quad (5.11)$$

According to the last equation, the Rayleigh cross-section is finally expressed as a function of the Loschmidt constant N_0 , the wavelength of the incident radiation λ and the refractive index of the gases n . Therefore, the refractive index has to be estimated with accuracy to get a correct value for the cross-section as the other parameters are experimental input (λ) or constant (N_0).

Refractive index of gases

The measurement of the refractive index of gases is not as straightforward as for liquid for example. The refractive index of n-dodecane at the gaseous state has not been a subject of investigation and its value is still unknown with accuracy. It is possible to experimentally measure the refractive index of gases thanks to a laser interferometer as presented by Schellekens et al. [17] but the equipment is still expensive.

Another accurate method to estimate the refractive index of gases is to use the molar refractivity A as they are related by the Lorenz-Lorentz equation [14] as shown in equation 5.12.

$$A = \frac{n^2 - 1}{n^2 + 2} \frac{N_A}{N_0} \quad (5.12)$$

The refractive index n is then a function of the Avogadro and Loschmidt constants, respectively N_A and N_0 , and the molar refractivity A . The ratio

of the Avogadro and Loschmidt constants is actually equivalent to the molar volume V_M . By rearranging equation 5.12, the expression of the refractive index of the gas is obtained as a function of the molar volume and the molar refractivity:

$$n = \sqrt{\frac{V_M + 2 A}{V_M - A}} . \quad (5.13)$$

Note that the refractive index is a function of the wavelength and its value is generally given either at 587.49 nm or at 589.29 nm corresponding to the Helium or Sodium D lines respectively because these wavelengths are close to the center of the visible spectrum. The empirical relationship proposed by Sellmeier [18] is often used as a correction to estimate the refractive index at the working wavelength.

King correction factor

The simplification made for spherical particles is valid in most cases; however, the specificity of the light scattered by small particles with non-spherical shapes can be addressed in terms of molecular polarizability. This polarizability can be expressed as a three-dimensional tensor which takes into account symmetric and anti-symmetric components. It has been observed that the anisotropy of the non-spherical molecules affects the cross-section and the distribution of the scattered light. This effect has been introduced by Strutt (Lord Rayleigh's son) and is commonly named the depolarization ratio, which basically represents the incomplete polarization of the light scattered perpendicularly [19].

No more than five years later, King proposed a correction factor now known as the King correction factor, which compensate the anisotropy of the molecule polarizability when the cross-section is calculated [20]. This correction factor, generally added at the end of the cross-section formula is computed differently depending on the characteristics of the incident illumination (Unpolarized or polarized). Equation 5.14 presents the formulation of the King correction factor for an incident polarized electromagnetic wave.

$$F_K = \frac{3 + 6 \varrho_p(\lambda)}{3 - 4 \rho_p(\lambda)}, \quad (5.14)$$

where ϱ_p is the depolarization ratio of the molecule for a polarized illumination; note that the depolarization ratio is wavelength dependent. The depolariza-

tion ratio can be calculated thanks to the Böttcher's formula [21] adapted to polarized light as available in the literature [16,22,23], such that:

$$\rho_p = \frac{3 \Psi^2}{45 \bar{\alpha}^2 + 7 \Psi^2} - 1, \quad (5.15)$$

with Ψ the anisotropy of the polarizability and $\bar{\alpha}$ the trace of the polarizability tensor of the molecule. Calculation of the King correction factor with additional information will be done in the calibration section 5.3.2.

5.2.3 Rayleigh scattering in jets

The intensity emitted by the scattered light within the Rayleigh regime has been given in equation 5.8. In order to simplify this expression and to adapt it to experimental measurements, the collection angle, the scale of the probed volume and the global efficiency of the system have been replaced by a dimensional efficiency factor η_T . As the aim of applying Rayleigh scattering in mixing jets is to measure the mixture fraction, the cross-section can be defined as the weighted sum of the cross-sections of the different species and the expression becomes:

$$I_{Ray} = N_T I_0 \eta_T \sum X_i \sigma_{Ri}, \quad (5.16)$$

with X_i and σ_{Ri} the molar fraction and cross-section of specie i , respectively. N_T represents the total number density within the probed volume. Considering that the mixture is composed by ambient gases and evaporated fuel, the global cross-section denoted σ_{mix} is the result of the following expression:

$$\sigma_{mix} = X_{fuel} \sigma_{fuel} + X_{amb} \sigma_{amb} . \quad (5.17)$$

The subscripts "fuel" and "amb" refer to the injected fuel (n-dodecane) and the ambient gases present in the chamber at the time of injection. Taking into account that the chamber only contains ambient gases and injected fuel at any time as there is no reaction: $X_{fuel} + X_{amb} = 1$ and thus σ_{mix} can be calculated. Then, according to equation 5.16, the total number density can be calculated at any location as I_0 and η_T are calibration constants (see sec. 5.3.3).

5.3 Calibration of the experiments

The system used to generate the sprays under evaporative conditions differs slightly from a regular common-rail injection system as described in section 2.2. The difference only resides in the high-pressure pump, which is an axial hydraulic type, electrically powered, instead of being a the rotative type entrained by an electric motor. This kind of pump has been preferred because of the low frequency of the experiments (about one every 4 minutes) due to the pre-burn process used to reach the desired thermodynamic conditions. Nevertheless, this does not affect the injected spray if the pressure is well regulated and controlled from event to event.

Proper calibration of the optics is necessary to perform quantitative measurements with the Planar Laser Rayleigh Scattering technique. The arrangement of the illumination and the acquisition is closely related to the reduction of the background noise, which has a direct impact on the SNR.

5.3.1 Specific optical arrangement

The sprays are injected in a specific constant-volume combustion chamber as described in section 3.5.1 equipped with three orthogonally disposed optical accesses allowing laser entrance and exit, and image collection at 90° .

The illumination source is a solid-state Nd:YAG laser (*Spectra Physics - Quanta-Ray Lab 190*). This laser is of the same type as the one used for measurements in non-evaporative liquid sprays and a description of the working principle is available in section 4.4.1. The wavelength of the experiments has been chosen to be the second harmonic of the laser fundamental radiation frequency, i.e. 532 nm producing an energy of 150 mJ and a pulse duration of about 7 μ s (FWHM). A discussion has been carried out by Idicheria and Pickett [24] because the intensity of the signal is wavelength dependent (λ^{-4} as suggested by eq. 5.1). They concluded that exciting at 532 nm was a better solution than in the UV ($\lambda = 355$ nm) for several reasons such as a lower energy pulse of the laser due to losses in the third harmonic generator (THG) or a lower quantum efficiency of the CCD camera employed. Therefore, the decrease observed in terms of SNR could go from 5 % in the ambient up to almost 40 % in the fuel-rich regions.

The laser-sheet to cross the jet has been generated by three cylindrical quartz lenses. The first lens (FL = 750 mm) optically compresses the laser beam on the vertical plane in order to create a thin beam on the axis of the

jet, the second one is negative (FL = -25mm) and opens the beam onto the horizontal direction. The third lens (FL = 100 mm) purpose is to make the rays parallel again in order to get the same mean spatial intensity on both sides of the jet. For this study, the sheet width was about 40mm and the thickness on the axis of the jet was 300 μm (FWHM) experimentally measured thanks to the knife method (same methodology as in sec. 4.4.1). A beam-blocker has been placed at a reasonable distance after the exit window on the laser path in order to avoid back scattering from the illumination.

Concerning the acquisition side, the signals have been imaged by a back-illuminated 16-bit CCD camera (*PIXIS - 1024B*). The resolution of the camera is 1024×1024 with a pixel area of 13 μm^2 allowing high quantum efficiency of more than 90 % at 532 nm. The CCD chip was maintained at a constant temperature of -70°C by thermo-electrical cooling thanks to a Peltier cell to keep the dark current as low as possible (0.03e-/pixel). In order to minimize the readout noise (3.6e- RMS), the output operating gain has been set to 1 e-/count and the readout rate to 100 kHz; which is not restrictive as the combustion chamber only allows performing a test every 4 minutes.

The camera has been equipped with a 105 mm objective (Nikkor Lens - 105 mm f/1.8D) with a close-up lens providing a pixel to millimeter ratio slightly higher than 14. An interference filter centered on 532 nm (band width = 10 nm FWHM) has been placed in front of the close-up lens (500 D lens) to remove the undesired light from the exterior.

Due to the critical aspect of the elastic scattering interferences produced by sources others than fuel and ambient gases, several improvements have been done to make the experimental setup better. In this aim, special fused-silica windows have been designed (see fig. 5.1) to reduce birefringence effect observed on larger sapphire windows normally installed in the vessel, scattering and reflection is also reduced due to the lower refractive index of the fused-silica (1.46 versus 1.77 at 532 nm). The fused-silica rectangular slits are mounted in a circular metal geometry to be fitted into the regular port of the combustion chamber. The metallic part of the window has been coated with absorptive carbon black on the internal side to reduce reflection. On the external side of the window, beam-blocks have been attached to act like knife edges in order to cut the unwanted light coming from aberrations of the transmitting optics.

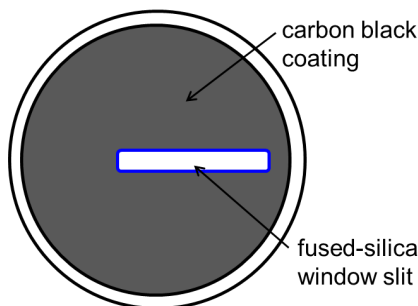


Figure 5.1: Metal port with fused-silica window insert ($7 \times 58\text{mm}$) for laser-sheet transmission.

5.3.2 Estimation of the cross-sections

As a conclusion to the theory of the Rayleigh scattering described earlier in this chapter (sec. 5.2), the cross-section of the substance under study must be carefully calculated. The technique used to evaluate the cross-section uses the refractive index computed thanks to the molar refractivity of the fluid. It is therefore necessary to estimate the refractive index of the evaporated n-dodecane with accuracy. Then, the anisotropy of the molecule polarizability is corrected via the King correction factor described earlier in section 5.2.2.

Molar refractivity and refractive index

The refractive index of a substance is dependent upon the molar refractivity as described by the Lorenz-Lorentz formula in equation 5.10. The molar refractivity is a measure of the total polarizability of the molecule and it can be calculated from the chemical bonds between the different atoms forming the molecule. Each bond has its own refraction and as the n-dodecane is an alkane (linear chain), the total molar refractivity is the summation of the refractions of all the bonds such as:

$$[A_{C_k H_{2k+2}}] = (k - 1)[A_{C-C}] + (2k + 2)[A_{C-H}] . \quad (5.18)$$

The refractions of bonds $C-C$ and $C-H$ being respectively A_{C-C} and A_{C-H} , the molar refractivity of the n-dodecane is then computed as $k = 12$. The solving gives a molar refractivity for the n-dodecane of $A_{C_{12}H_{26}} = 57.64 \text{ cm}^3$, this is in agreement with the experimental values found in the literature [25,26] for the Sodium D line.

Then, by introducing the molar refractivity into equation 5.13, the refractive index of the n-dodecane at the gaseous state can be calculated as the Avogadro and Loschmidt constants are known. The refractive index of the vaporized n-dodecane at a wavelength corresponding to the Sodium D line is $n_D = 1.003860$.

The refractive index is affected by the wavelength and can be adjusted thanks to the Sellmeier dispersion formula [18] as introduced earlier. The Sellmeier coefficients are available for the commonly used glasses, but much more difficult to find for gases as these are empirically estimated and the effect of the wavelength on gases is quite low. An example of this effect on the refractive index of the methane gas (CH_4) is available in reference [27] and the result is a decrease lower than 4×10^{-4} % when the wavelength goes from 589.29 nm to 532 nm. As a conclusion of the estimation of the refractive index, the wavelength dependency has been neglected as it would affect the sixth decimal of the value only, which roughly corresponds to the uncertainty of calculation.

Influence of the King correction factor

Due to the anisotropy of the polarizability of an alkane linear chain, the Rayleigh cross-section of the fuel used in this study (n-dodecane) might be affected. To potentially correct this phenomenon, the King correction factor has been introduced, and to do so, the depolarization ratio ρ_p of the molecule is required as suggested by equation 5.15.

The depolarization ratio can be computed thanks to the tensor of the polarizability as a function of the trace and the anisotropy of the polarizability. The trace $\bar{\alpha}$ corresponds the mean of the sum of the items on the diagonal of the polarizability tensor its value can be found in the literature [28] such that $\bar{\alpha} = 22.75 \times 10^{-24} \text{ cm}^3$. This value is somewhat really close to the mean polarizability as expressed in the following equation [25]:

$$\alpha = \frac{3 A}{4 \pi N_A}, \quad (5.19)$$

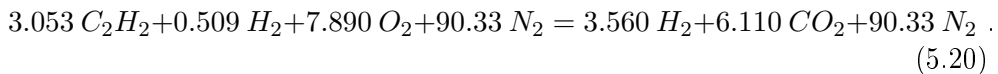
giving $\alpha = 22.85 \times 10^{-24} \text{ cm}^3$, meaning that the polar moment of the n-dodecane is mainly on the diagonal. The anisotropy of the polarizability Ψ has also been experimentally measured [23,29] and its value is $\Psi^2 = 15.29 \times 10^{-48} \text{ cm}^6$. Therefore, the depolarization ratio of the fuel molecule for a polarized illumination is estimated to be $\rho_p = 1.36 \times 10^{-3}$.

By introducing the depolarization ratio into equation 5.14, the King correction factor can be calculated, the value obtained is $F_K - 1 = 1.302 \times 10^{-2}$. Note that under high temperature conditions (in the range of 1000 K), some authors [22] measured the depolarization ratio for alkanes at different temperatures and found that it was generally decreasing as the temperature increases. By extrapolation of the results published by Smith [22], the value of the King correction factor obtained is slightly lower than that computed at STP, it means $F_K - 1 = 0.865 \times 10^{-2}$.

Cross-sections of the different species

Equation 5.11 provides the formula used to estimate the Rayleigh cross-section of the fuel injected in the ambient. Therefore, thanks to the refractive index and the King correction factor, the Rayleigh cross-section of the n-dodecane at 532 nm is $\sigma_{fuel} = 858.4 \times 10^{-27} \text{ cm}^2$.

Concerning the Rayleigh cross-sections of the ambient gases present in the chamber at the time of injection, as these species have been already studied, the cross-section of the mixture is a combination of the different mass fraction of the species (see eq. 5.17). The ambient is composed of N_2 , H_2 , C_2H_2 , and O_2 before the pre-combustion and the products after pre-combustion would be N_2 , CO_2 and H_2O considering a complete reaction and thus, the equation of the reaction is:



This equation allows the molar fractions of the different species after pre-combustion to be evaluated. The Rayleigh cross-section of the ambient is then calculated and the value obtained is $\sigma_{amb} = 5.609 \times 10^{-27} \text{ cm}^2$; the Rayleigh cross-sections are organized in table 5.1 along with the particular molar fractions.

The Rayleigh cross-section is not constant and changes with temperature as well. This temperature dependency causes a slight increase of molecule volume because of the augmentation of the energetic rotational and vibrational states [1,25]. There is no work specifically focusing on the n-dodecane at high temperature (gaseous state) and the evolution of the Rayleigh cross-section to present an accurate estimation of this growth. Consequently, this topic is being treated in section 5.4.3 concerning the uncertainty of the diagnostic.

Components	Molar fractions X_i [%]	Rayleigh Cross-sections σ_i [$\times 10^{-27}$ cm ²]
Nitrogen [N ₂]	89.71	5.23
Carbon Dioxide [CO ₂]	6.52	12.02
Water [H ₂ O]	3.77	3.66
N-Dodecane [C ₁₂ H ₂₆]	X_f	858.4

Table 5.1: Molar fractions and Rayleigh cross-sections of the species in the combustion chamber at the time of injection.

5.3.3 General diagnostic protocol

The strategy applied in this work to build a relationship between the intensity of the signal recorded by the acquisition system and the number density of fuel within the jet is an auto-calibration using the intensity of the signal in the ambient. Thanks to equations 5.16 and 5.17, the number density of both the ambient and the vaporized jet can be predicted from the intensity of the signals. The two following equations give the relationship between recorded intensity and number density for the ambient: I_{amb} and N_{amb} respectively; and the jet, being a mix of ambient and fuel denoted as I_{mix} and N_{mix} :

$$I_{amb} = N_{amb} I_0 \eta_T \sigma_{amb} \text{ and } I_{mix} = N_{mix} I_0 \eta_T \sigma_{mix} . \quad (5.21)$$

As σ_{mix} is dependent upon the mixture fraction, the ratio of both equations can reduce the problem to a single equation. Therefore, knowing that $X_{fuel} + X_{amb} = 1$ and applying the ideal gas law, such that $N_{mix}/N_{amb} = T_g/T_{mix}$; the following expression (eq. 5.22) is obtained. T_g and T_{mix} represent the temperatures of the ambient gases and within the air - fuel mixture, respectively.

$$\frac{I_{mix}}{I_{amb}} = \frac{\frac{\sigma_{fuel}}{\sigma_{amb}} + \frac{N_{amb}}{N_{fuel}}}{\frac{N_{amb}}{N_{fuel}} + 1} \frac{T_g}{T_{mix}} \quad (5.22)$$

From the last equation, T_{mix} is still needed to extract the fuel to ambient ratio of number densities. One solution is to consider the spray injected into isothermal conditions, meaning that the fuel molecules are already at the ambient

temperature. This hypothesis is the same as assuming $T_{mix} = T_g$ and leads to the following relation:

$$\frac{N_{fuel}}{N_{amb}} = \left(\frac{I_{mix}}{I_{amb}} - 1 \right) \frac{\sigma_{fuel}}{\sigma_{amb}}. \quad (5.23)$$

This simple expression provides the ratio of the number densities of fuel over ambient under isothermal conditions, it is generally employed to investigate flows of gases. The isothermal might not be suitable for this work because of the high temperature difference between the injected fuel (about 363 K) and the ambient gases (at least 900 K). For this reason, a more realistic and accurate way which relies on adiabatic mixing of the fuel and the ambient has been used to compute the mixture fraction. As the time-scale is very short (a few milliseconds), this assumption seems correct and should lead to accurate results, and the fuel to ambient ratio therefore becomes:

$$\frac{N_{fuel}}{N_{amb}} = \left(\frac{I_{mix}}{I_{amb}} - \frac{T_g}{T_{mix}} \right) \frac{\sigma_{fuel}}{\sigma_{amb}}. \quad (5.24)$$

The temperature of the mixture can then be calculated thanks to the equation of the conservation of energy. Knowing the thermodynamical properties of the fuel and the ambient gases, a relationship can be built between the number density ratio of the species N_{fuel}/N_{amb} and the corresponding adiabatic mixing temperature T_{mix} . Equation 5.25 represents the mathematical expression of the conservation of energy according to El-Wakil [30].

$$\int_{T_{mix}}^{T_g} C_{p,amb} dT = \frac{m_f}{m_g} \left(\int_{T_{fuel}}^{T_{vap}} C_{p,fuel} dT + H_{vap,T_{vap}} + \int_{T_{vap}}^{T_{mix}} C_{p,fuel} dT \right). \quad (5.25)$$

The left side of equation 5.25 represents the total thermal energy loss of the ambient from the initial temperature to the actual temperature after mixing with the jet. The mass ratio of fuel over ambient m_f/m_g is found on the right side, multiplied by the thermal increase of energy of the fuel in liquid phase, until evaporation $\int_{T_{fuel}}^{T_{vap}} C_{p,fuel} dT$, the enthalpy of vaporization at boiling temperature $H_{vap,T_{boil}}$ and finally, the energy to reach the mixing temperature $\int_{T_{vap}}^{T_{mix}} C_{p,fuel} dT$, corresponding to a certain fuel to ambient ratio.

The thermodynamical properties of the species present in the chamber are obtained by looking into thermodynamic databases (Look-up tables). From

these data, equation 5.25 on the conservation of energy can be solved for different mass ratios of fuel over ambient. Finally, a linear interpolation is done between the data points to get a continuous relationship of the adiabatic mixing temperature as a function of the fuel to ambient ratio (number density) as plotted in figure 5.2.

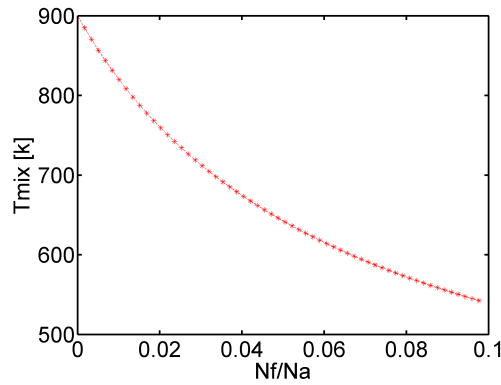


Figure 5.2: Calibration curve of the adiabatic mixing temperature as a function of the number density ratio N_{fuel}/N_{amb} .

As T_{mix} is now known, equation 5.24 can be solved and a relationship between the ratio of the intensities of both signals in the jet and in the ambient and the can be drawn. Figure 5.3 represents the calibration curve of this relationship.

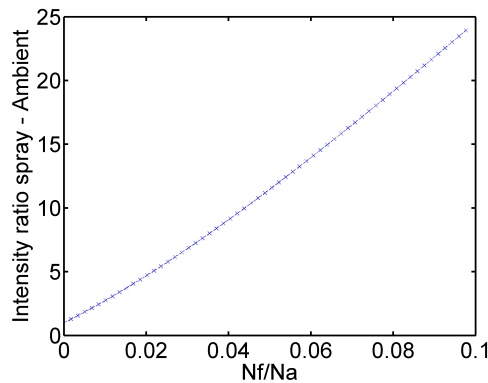


Figure 5.3: Calibration curve of the recorded intensities ratio (I_{mix}/I_{amb}) as a function of the number density ratio (N_{fuel}/N_{amb}).

A 2-D map of fuel to ambient ratio (N_{fuel}/N_{amb}) is finally obtained by applying this procedure to every location (pixel) in the recorded image. Note that during this process, the adiabatic mixing temperature is also calculated and a 2-D map can be extracted the same way.

5.4 Data processing and corrections

As shown in equation 5.24, the signals coming from the ambient and the jet must be accurately estimated for quantitative measurements as the number densities associated are directly dependent to the ratio of the intensities. Therefore, the background and flare present on the image have to be removed because they would change the ratio of the two intensities, hence affecting the results. Different sources have been identified to potentially affect the background signal: The camera dark-current, the thermal emission and the flare of the laser scattered by the windows and optics and reflecting in the chamber. The last one has been reduced as much as possible thanks to a special design of the windows and laser path (see sec. 5.3.1).

The dark-current corresponds to the noise emitted by the current passing through the pixels of the CCD array when not exposed to light radiation (no photon reception); it can be minimized by lowering the temperature of the CCD chip as described in section 5.3.1. The digital level of the image does not represent the signal of the radiation emitted through Rayleigh scattering and can be evaluated by acquiring an image, named I_{DC} , by covering the CCD sensor and at ambient conditions (no thermal radiation).

The thermal radiation mainly emitted by the walls of the vessel, but also by the hot gases also increases the digital level of the image as the camera gate is opened for a relatively long time (20 ms). Therefore, a background image is acquired to correct the original signal from thermal radiation and background non-uniformity. This image is taken regularly before and after a set of injections to control the evolution of the back-walls emission at the same time. The polarization of the laser is changed in order not to collect any data from the ambient but the laser flare and reflections; the test is realized with an empty vessel (atmospheric pressure) and no injection. From this image, the dark-current is subtracted and then, the intensity level is adjusted according to an interrogation area outside the jet to give I_{BG} .

The corrected 2-D Rayleigh signal can be expressed by the following mathematical relation: $I_{corr} = I_{raw} - I_{DC} - I_{BG}$, where I_{raw} is the digitalized image acquired by the camera and I_{corr} the corrected image as shown in figure 5.4.

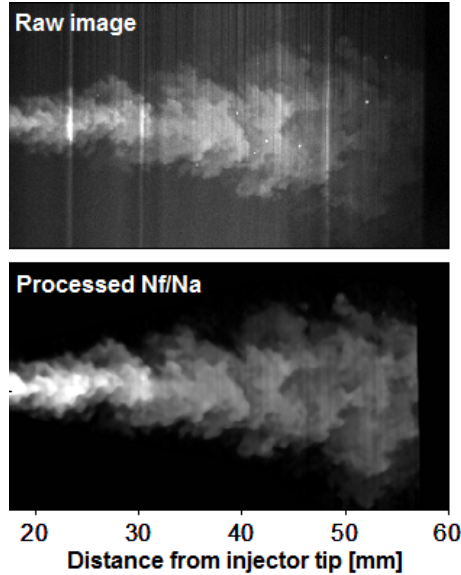


Figure 5.4: Sample images of the raw signal acquired by the acquisition system and the N_{fuel}/N_{amb} map obtained after correction procedure.

5.4.1 Image post-processing

The post-processing of the image starts once the corrected image of the Rayleigh signal is obtained. The process to obtain quantitative two-dimensional maps of the number density ratio of fuel and ambient is composed of three different steps.

First, the user selects the outer boundary of the vaporized jet, as close to the jet as possible in order to get the correct intensity level scattered by the ambient gases on both sides. This intensity is directly related to the laser-sheet spatial intensity and the mean levels before and after the jet are evaluated to check if the present experiment is correct. Due to the really small cross-section of the gas molecules, the extinction of the laser radiation crossing the evaporated jet is barely measurable; the average intensity before and after informs the user about some eventual problems.

High density gradients produce the laser-sheet to suffer from beam steering as it crosses the region close to the entrance window where a layer of high temperature difference is formed. Beam steering is an optical phenomenon induced by a change of the refractive index of the medium in which the light is transmitting through. Temperature fluctuations at the wall interfaces result

in different refractive index values, thus changing the direction of the incident light. These variations are unpredictable and lead to error on the measurements as the proportionality between intensity and number density is no longer correct. The technique used in this study to correct this effect has been described by Gronki et al. [31] and utilizes the spatial intensity in the ambient before and after the jet. As Rayleigh scattering is able to measure the signal of the ambient, the intensity profiles on both sides of the jet are extracted on individual images. Then, a linear interpolation is done between the both intensity profiles to generate the illumination plane "without" the jet. This process produces the Rayleigh signal emitted by the ambient gases only but accounting for the beam steering "fingerprint" of this specific experiment.

Note that such a correction can only be applied to Rayleigh scattering diagnostic as the ambient signal is recorded, on the contrary to high temperature LIF for example, which also suffers from beam steering. This methodology presents another advantage as it takes into account the laser intensity fluctuations from shot-to-shot, which is not necessarily possible with other techniques.

The last part of the post-processing is to divide the two Rayleigh images generated earlier. The first one being the corrected Rayleigh signal from the jet and the ambient and the second one, the Rayleigh image recreated during step two, containing the ambient only. The ratio of the two images is then placed into equation 5.24 and a 2-D map of number density ratio N_{fuel}/N_{amb} is obtained (see sec. 5.3.3 for more information). Figure 5.5 represents a composite image of the light emitted by the liquid phase through Mie scattering and the number density ratio measured via Rayleigh scattering.

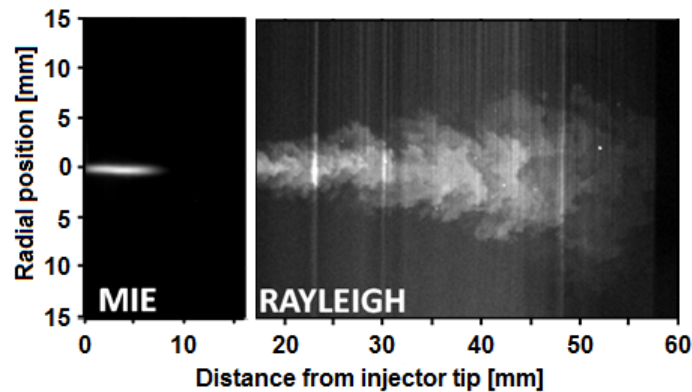


Figure 5.5: Composite image of Mie (left) and Rayleigh (right) scattered signals. This images show that the signal of the ambient gases is recorded through Rayleigh scattering and not with Mie.

Figure 5.5 represents a composite image of the light emitted by the liquid phase through Mie scattering and the number density ratio measured via Rayleigh scattering.

5.4.2 Further corrections and improvements

The methodology applied in this work to correct the results from beam steering has been explained earlier and forms part of the global data post-processing. The particles present in the fuel stream represent another matter as they severely interfere with the signal emitted through Rayleigh scattering. Most of the work to combat this problem has been done in the experimental hardware via filters mounted on the feeding line (30 nm filtering) or the use of n-dodecane fuel with a high level of purity. Nevertheless, two corrections routines have been applied during post-processing of the image depending on the content and size of the particles in the image.

Particle inpainting

An improvement on the image quality has been made by introducing a function to remove relatively big particles (bigger than the fuel molecules) that scattered light toward the acquisition system: the inpainting. This technique based on texture replacement is generally used in image editing and showed great results to replace a region from its neighborhood [32]. The scattering of aforementioned particles harms the analysis of the proper Rayleigh signal causing over-evaluation of the laser intensity and therefore mistaking the number density. The inpainting process acts in the way of rebuilding the image through interpolation of the particles surroundings where the intensity is assumed to be that of the real Rayleigh signal from this specific region of the jet.

The threshold used in the inpainting function to detect pixels as outliers has been defined after statistical and judicious analysis. This limit never interferes with real data coming from the ambient gases or the jet, where the intensity is higher. The intensity level of particles in the fuel stream can be of order of magnitude two times higher than the actual signal from the jet and the detection is not a problem in this way. As this threshold level has been selected to be conservative and not to veer the results due to a bias applied during the image processing, some small particles are still present on individual images.

Median filtering

To clean the images from smaller scatterers (which intensities were below the inpainting threshold), a 2-D median filter has been applied to the single shots. This process operates comparing the intensity levels of the pixels in the neighborhood and then smooths the difference between one and another [33]. The area of the median filtering process applied in this work is square and has been set as small as possible (6×6 pixels corresponding to less than a fifth of square millimeter) not to affect much the results from a quantitative point of view.

The effect of median filtering to smooth the image from small scatterers has been investigated in by Idicheria et al. [24]; they found that a bias error of approximately 1 % may remain after filtering. Thanks to the inpainting function, the size of the area used to apply the median filter is about four times smaller than in this work (real dimension), which means that the effect of the filter on the digital level of the image is expected to be smaller.

Figure 5.6 is an example of the image correction procedure with a confrontation of a raw image processed to obtain the mixture fraction and the same image corrected with particle inpainting and median filtering.

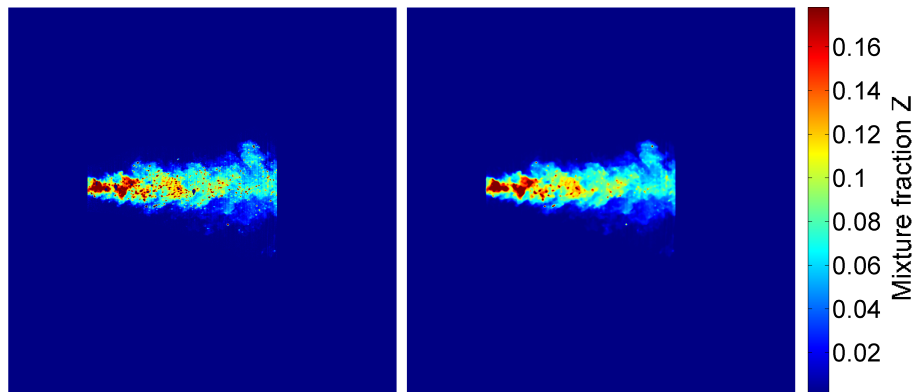


Figure 5.6: Example of the image correction procedure influence on the original image (left). The corrected image (right) is obtained after particle inpainting and median filtering (6×6 pixels).

5.4.3 Uncertainty analysis

The first purpose of the present chapter is to evaluate the mixture fraction of an evaporated jet through Rayleigh scattering measurements. The results

presented are composed of ensemble-average of multiple injection events to get statistically consistent data. Therefore, the uncertainty of the results is a combination of the deviation from shot-to-shot during the experiments and additional bias errors that have not been corrected. This method of uncertainty analysis has been proposed by Moffat [34], in which the shot-to-shot uncertainty is expressed within a 95 % confidence interval.

Error on the estimation of σ

The bias error is mainly represented by the uncertainty on the calculation of the Rayleigh cross-section, obtained through estimation of the refractive index of the molecule. The refractive index of the fuel molecule at the gaseous state has been calculated by using the molar refractivities of the chemical bonds. Denbigh [25] stated that the error made on the experimental estimation of the total molar refractivity of the n-dodecane was 0.0 %, as the value has been confirmed by other sources [26,35], the molar refractivity is no longer considered as a source of error. A similar conclusion has been reached concerning the effect of the wavelength on the refractive index as explained in section 5.3.2.

The temperature also affects the refractive index, a decrease of 0.05 %, resulting in a 0.1 % loss on the cross-section, seems reasonable for gases within a temperature range of 273 K to 900 K according to literature [36].

The temperature has an opposite effect on the Rayleigh cross-section due to different energy states. The effective volume of the molecule generally increases with temperature as the excitation state of the atoms increases leading to higher levels of rotational and vibrational forces. These forces tend to stretch the chemical bonds resulting in a larger volume of the molecule than that observed at the ground state (lower temperature conditions). As an example for the molecule of methane (CH_4), which presents the same bonds, The volume augmentation for a temperature range of 273 K to 900 K is expected to induce an increase of the Rayleigh cross-section of about 1.2 % [6].

The pressure has an opposite effect on the molecular volume augmentation as described by Naus et al. [15], but no real studies are available to quantify the reduction of size of the molecules due to surface forces.

The analysis of the systematic bias error for the Rayleigh cross-section showed that a global augmentation of 1.1 % can be expected, which can mainly be attributed to temperature variation. This estimation of the potential error is integrated in the global uncertainty (coupled with the standard deviation) presented together with the results.

Local density variation and shot-to-shot deviation

The ambient density in the core region of the vessel where the jet is injected and evaporated affects the Rayleigh scattering measurement quantitatively through variation in the molecular number density. This random error has been analyzed over the set of images taken to study an averaged behavior of the jet. This error is merged into the variation expressed in terms of mass distribution from shot-to-shot during the different injection events recorded.

This, together with the turbulent behavior of the jet, represent the major source of uncertainty as the number of Rayleigh images acquired at a particular condition is limited. The amount of data-shots used to realize an ensemble-average of the Rayleigh scattering mixture fraction varies from 20 to 40 events; reminding that the lower the number of images, the higher the uncertainty. This limitation is due to the low repetition rate of the hot spray test-rig coupled with the fact that some images have not been processed because of severe particle contamination, which would affect the results quantitatively even with the correction procedure developed.

The estimation of the global uncertainty has been included in the results presented in the following section to carefully show the possible deviation of the data with respect to the model.

5.5 Mixture fraction and temperature distributions

The results extracted from the Planar Laser Rayleigh Scattering technique applied to a jet injected under evaporative conditions are presented here. The conditions used as a reference, it means an injection pressure of 150 MPa and a discharge density of 22.8 kg/m^3 , have been recreated at a temperature of 900 K. This would then allow the comparison of the development and mixing of the spray depending if it is isothermal or evaporative (see chapter 6).

The Rayleigh signal being really sensitive, even at location close to the jet boundary due to a relatively high SNR, the spreading angle has been extracted from these data. As averaging the injection events generally provides apparently wider jets, because the axis of the jet is randomly moving around the mean position [37], individual Rayleigh images (number density of mixture fraction) have been used to evaluate the spreading angle of the jet.

The ensemble-average 2-D map of the mixture fraction in the vaporized region of the jet is then presented. The axial and radial profiles of the results

are compared to the mixing model proposed by Musculus [38] and used to compare the mixture fraction of an isothermal spray in the previous chapter (sec. 4.5).

The 2-D map of the resulting temperature in the jet assuming adiabatic mixing is presented at the end of this section together with plots of the axial and radial profiles of the temperature evolution as additional information.

5.5.1 Single jet analysis

The analysis of the individual images of the vaporized region of the jet processed thanks to the Rayleigh diagnostic described in this chapter is interesting as it points out the turbulent behavior of the jet. Two maps of the number density ratio of fuel over ambient are displayed in figure 5.7 as an example.

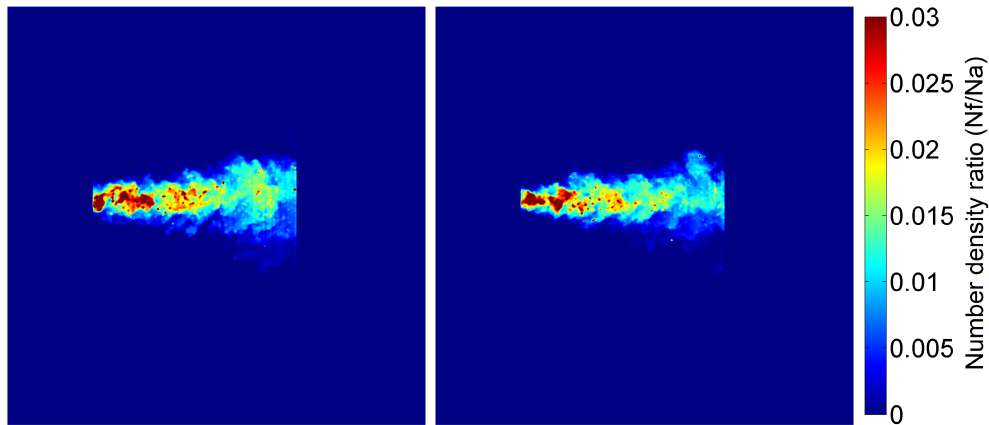


Figure 5.7: Sample two-dimensional signals of the fuel over ambient ratio in terms of number density. The two maps are different events of the same testing condition dataset.

Even if the two sample images show the different structures on the edges of the jet due to the interaction with the ambient gases, the high number density of fuel molecules on the axis is pointed out. Both the maps show that the central region of the jet presents higher fuel to ambient ratio than when moving radially to the boundaries of the jet, well defined on these maps.

It appears clearly on both samples that the area closer to the injector tip (after complete evaporation, represented by the position of the laser-sheet) presents higher local fuel over ambient ratio. As long as we move downstream, the number density of fuel molecules is decreasing, due to the spreading angle

of the jet and therefore the entrainment of the ambient gases, thus lowering N_{fuel}/N_{amb} .

In addition to similarities observed on the local fuel distribution, the sample images present the same macro-structure as well, both jets seem to be inscribed into a cone. This corresponds to the widely known theory of the Diesel spray, which has been inspired by the gas-jet theory [39]. This cone centered on the jet axis virtually contains the development and mixing of a 3-D jet and thus an important parameter known as the spreading angle can be defined. The spreading angle is the solid angle of the cone and basically represents how much the jet opens as theoretically described in section 2.5.2. In 2-D, this solid angle becomes a regular angle and can potentially be measured by direct visualization of the jet; considering the jet axis-symmetrical its value and meaning remain [40].

Nevertheless, it is always complicated to determine the spreading angle experimentally in evaporative jets and visualization techniques such as Schlieren or shadowgraphy generally fail to provide this parameter with accuracy and precision. On the other hand, thanks to the SNR level offered by the Rayleigh scattering diagnostic applied in this study, allowing accurate measurements on the edges of the jet, the spreading angle of the vapor phase can be determined.

To experimentally estimate the spreading angle, individual maps of number density ratio have been utilized. The data available within the vapor region have been used to determine the position of the jet boundary corresponding to 1 % of the centerline value. Then, both sides of the vapor region of the jet have been linearly fitted with the following condition that the lines cross at the position of the injector's outlet. An example of an individual image is shown on figure 5.8 together with the computer-processed jet axis and linear fits.

This methodology has been done for all the individual images of Rayleigh scattering taken and successfully processed and the final result is an average of the individual values such that the spreading angle is $\theta = 21.9^\circ$. The standard deviation of the spreading angle has been calculated to be about 1.1° , which represents a deviation within 5 % around the mean value.

5.5.2 Mixture fraction in vaporized jets

As introduced in the results section of the chapter concerning non-evaporative conditions (sec. 4.5), the mixture fraction is always useful to evaluate the fuel distribution at a particular location within the jet. For this same reason

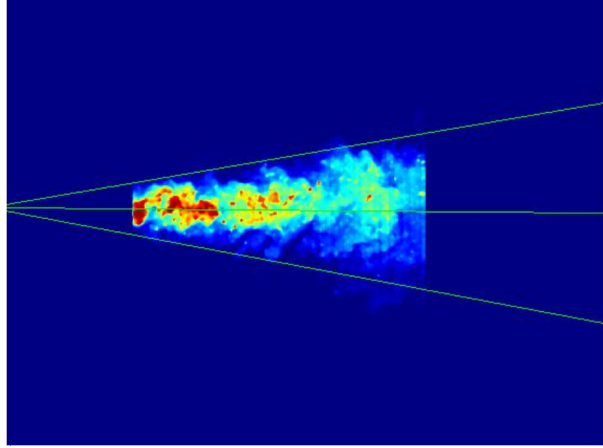


Figure 5.8: Spreading angle and jet axis experimentally evaluated on a single-shot image. The outlet of the injector is not imaged by the acquisition system.

and in order to further compare the mixture fraction distribution between sprays injected under non-evaporative and evaporative conditions, the results are presented in terms of mixture fraction.

2-D maps in terms of mixture fraction

Some differences concerning the first resulting data when compared to the measurements performed into the liquid spray have to be noted. First, the intensity loss between the laser-sheet and the acquisition system can be neglected due to the really low extinction for the same reasons explained in section 5.4.1. Another distinction has to be made when analyzing the results extracted from both techniques, the Rayleigh diagnostic provides a map of number density ratio of fuel over ambient whereas the Structured Planar Laser Imaging gives the droplet number density. This difference modifies the way to obtain the mixture fraction from the first resulting image, the description of the mathematical procedure follows.

First, the ratio of fuel over ambient in terms of mass m_f/m_g is calculated by the product of the number density ratio and the molar masses of the species in presence, such that:

$$\frac{m_f}{m_g} = \frac{N_{fuel}}{N_{amb}} \frac{M_{fuel}}{M_{amb}}. \quad (5.26)$$

M_{fuel}/M_{amb} represents the ratio of the molar masses of the n-dodecane ($M_{fuel} = 170.34$ g/mol) and the ambient gases present in the chamber ($M_{amb} = 28.679$ g/mol). The ratio of the mass of fuel over ambient is also useful and widely used for chemical reactions such as combustion in the case of an engine.

The second and last step is to replace the fuel to ambient ratio by mass in equation 4.30 presented in section 4.5 to get the mixture fraction Z at any location in the imaged jet.

The mixing measurements obtained through Planar Laser Rayleigh Scattering have been performed for the reference condition: $p_{inj} = 150$ MPa and $\rho_g = 22.8$ kg/m³. To get stabilized jets, long injection timing have been used as the particle matter has been observed to be less severe after long delay after the start of injection (Time ASOI). The jet eventually impinges against the back wall, but it forms into a radial wall jet that does not wrap around to the measurement location at the time of acquisition. As a result, the ambient gases remain undisturbed within the laser-sheet region (up to 50 mm from the tip).

Figure 5.9 shows a 2-D map of the mixture fraction in the vapor region of the jet injected according to the reference testing conditions. This resulting image has been obtained by averaging several injection events (35 in this case) in order to present a statistically repetitive jet.

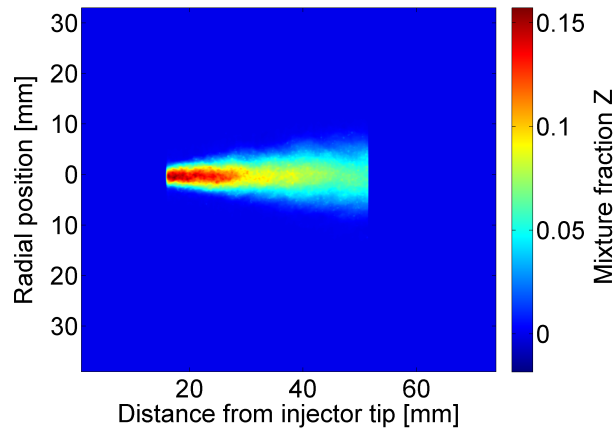


Figure 5.9: Two-dimensional distribution of the quantitative mixture fraction on the jet axis plane.

The general characteristics pointed out with the individual jets concerning

the number density distribution are also observed on the mean jet mixture fraction. On the image presented in figure 5.9, the vapor region of the jet illuminated by the laser-sheet seems to have a trapezoidal shape, which is a truncated cone by extension (revolution around jet axis). In addition, the central region of the jet, on the centerline neighborhood, presents a higher mixture fraction than the edges, with a maximum reached at the closest distance from the injector's outlet.

It has to be noted, however, that the structures corresponding to the turbulent behavior born from the jet-stream - ambient gases interactions have been predominantly toned down by the averaging. These structures are specificities of an individual injection event and are largely random, making them to be different from shot-to-shot and hence to be almost erased when averaging enough injected jets.

Comparison to the jet model

The results of mixture fraction are compared to the Naber and Siebers model [41] improved by Musculus [38] to show how well the measurements done under evaporative conditions follow a validated model [42]. To make this comparison in a quantitative and comprehensive way, both the experimental axial and radial mixing profiles at different location from the tip are displayed together with the uncertainty. The model predictions are presented on the same plots for a direct comparison. The uncertainty of the experimental mixture fraction is represented as a gray fill and corresponds to a 95 % confidence interval as described in section 5.4.3. Therefore, if the results computed by the Musculus model pass within the gray fill region, it can be assumed that the mixture fraction has been accurately measured by the diagnostic applied.

As explained in the previous chapter (sec. 4.5), the jet model input parameters are required, the discharge $C_d = 0.86$ and area contraction $C_a = 1$ coefficients remain the same as they are hydraulic aspects of the injector. The other input parameter is the spreading angle, its value has been extracted earlier from the individual images to be $\theta = 21.9^\circ$. This makes a difference with the liquid spray (sec. 4.5) as the spreading angle was only $\theta = 17.3^\circ$, which indicates that the development of the jet is different under evaporative conditions or not as described by Garcia [43].

The axial profiles for both experimental and computed results obtained on the jet center-line for the reference condition are represented in figure 5.10. Recall that the value of the spreading angle is affecting the quantitative mix-

ture fraction on the centerline and the capability of the Rayleigh technique to provide an accurate value for this parameter represents a great improvement when compared to the non-evaporative measurements.

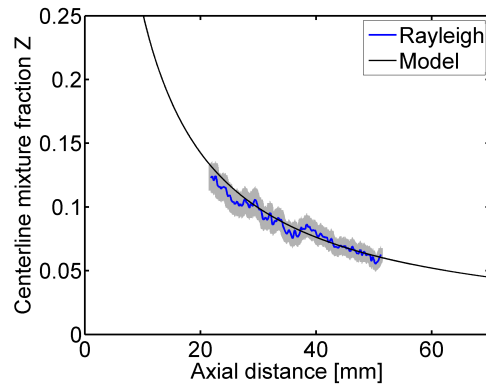


Figure 5.10: Experimental and computed mixture fraction on the jet centerline.

The plots show that the model predictions for mixture fraction fall within the experimental uncertainty along the axis of the jet where the measurements have been done. The decay $1/x$ employed in the model and based on the gas-jet theory seems to be a valid assumption also for evaporative liquid fuel sprays as demonstrated by the confrontation to the model.

Figure 5.11 presents the radial profile at two distances from the tip. The results of the model have been computed using the radial profile described by Abramovich [44] like for the non-evaporative experiments.

A similar observation can be done concerning the radial profiles as the experimental mixture fraction follows the computed one on both sides of the jet axis. On the contrary to the measurements performed in the isothermal spray, the radial profile appears justified here based on the closeness of the results obtained via experiments and modeling.

To ensure that those preliminary conclusions drawn from the observations made on one testing condition are valid in a more general way, other conditions varying ambient density and injection pressure are presented and confronted altogether in the next-coming chapter (chapter 6).

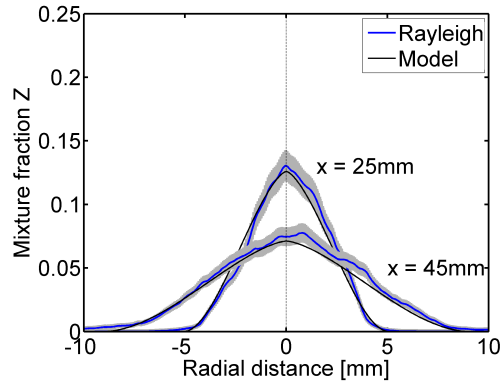


Figure 5.11: Experimental and computed radial profiles of the mixture fraction at 25 and 45 mm from the tip of the injector.

5.5.3 2-D temperature distribution

The injection of liquid fuel into a high temperature vessel produces a change of the local temperature as fuel is vaporizing and therefore absorbing temperature from the ambient gases. From the model used in this study, the adiabatic mixing temperature can be extracted. Figure 5.12 shows a 2-D map of the temperature distribution in the jet assuming adiabatic mixing.

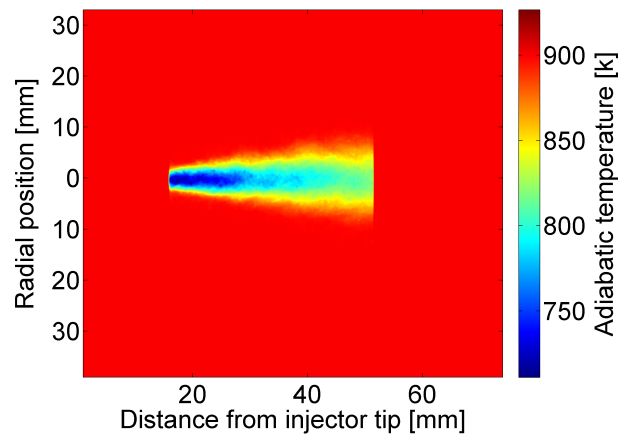


Figure 5.12: Ensemble-average of 2-D map of adiabatic mixing temperature of a liquid fuel jet injected into hot gases.

It appears clearly that the temperature distribution presented on this figure is really similar to the mixture fraction distribution presented before. The mass

of fuel being cold, assuming an adiabatic mixing means that the amount or mass of cold fuel over hot gases entrained within a constant volume determines the temperature at this particular location. Taking into account the energy or enthalpy of vaporization, the richer in fuel the region is, the colder it would get; this confirms the results shown on the temperature map and its similarity with the mixture fraction image.

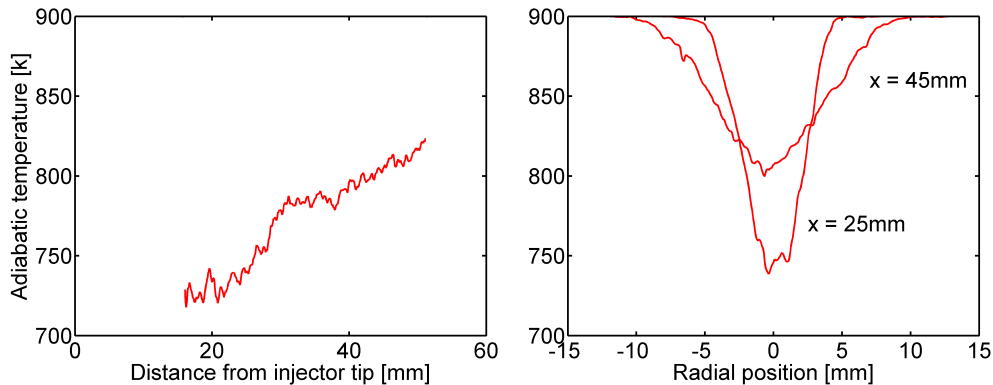


Figure 5.13: Axial and radial profiles of the adiabatic mixing temperature of the jet. The axial profile is recorded on the center-line and the radial distributions are extracted at 25 and 45 mm.

Figure 5.13 represents the axial and radial profiles of the adiabatic mixing temperature. The results seem to be the negatives of the profiles extracted from the mixture fraction distribution; the radial profiles also present a characteristic Gaussian-like distribution. As expected, the lowest temperature (around 730 K in this case) is found at the shortest distance to the tip, on the jet center-line, where the mixture fraction is maximum.

5.6 Conclusions

The PLRS technique has been preferred to existing alternatives because of its capability of providing two-dimensional quantitative mixing results while not requiring complex calibration or corrections. This scattering process being elastic, the main limitations come from the external noise potentially detected by the acquisition system as well, thus affecting the results quantitatively. However, the geometrical dimensions of the high temperature facility reduce extensively the noise coming from the background reflections making the PLRS an attractive solution for quantitative mixing measurements.

The theory proposed by Lord Rayleigh to electromagnetically describe the scattering of light by particles much smaller than the incident wavelength has been presented in this chapter. The widely used expression proposed to carry out Rayleigh scattering measurements directly relate the particle number density to the scattered intensity for a calibrated system. The most important step to previously calibrate such system is the calculation of the Rayleigh cross-section of the different species under study, particularly the fuel molecules. A methodology to calculate the cross-section of the n-dodecane is to obtain the refractive index of the vaporized fuel from the molar refractivity of the molecule.

Two-dimensional maps of the molecules number density have been obtained through auto-calibration by using the Rayleigh signal emitted by the ambient gases surrounding the vaporized jet. As part of the calculation, the temperature has been evaluated assuming adiabatic mixing of the injected fuel and the ambient. Several steps have been done to increase the quality of the results such as specific window slits as part of the optical improvements to reduce background noise or post-processing image correction like inpainting or median filtering. An estimation of the uncertainty of the results showed that the main limiting factor was actually the number of images used to provide ensemble-average mixing distribution maps rather than bias error.

The analysis of the individual images demonstrated the possibility to extract accurate information on macroscopic parameters such as boundary or spreading angle of the vapor region of the jet. With correct spreading angle input, the predictions of the mixing model fall within the uncertainty of the experimental results for both axial and radial distribution profiles. These observations reinforce the quantitative aspect of the Planar Laser Rayleigh Scattering diagnostic applied in this work. At the same time, these results represent good justification to the utilization of the Abramovich distribution for vaporized fuel jets. Finally, the assumption concerning temperature made during image processing also permits obtaining two-dimensional maps of adiabatic mixing temperature distribution in the jet.

Bibliography

- [1] H. Zhao and N. Ladommatos. Optical diagnostics for in-cylinder mixture formation measurements in ic engines. *Progress in Energy and Combustion Science*, 24(4):297–336, 1998.

- [2] S.C. Johnston. Precombustion fuel/air distribution in a stratified charge engine using laser raman spectroscopy. *SAE Paper 790433*, 1979.
- [3] Q.V. Nguyen and P.H. Paul. KrF laser-induced photobleaching effects in O₂ planar laser-induced fluorescence signals: experiment and model. *Applied optics*, 36(12):2675–2683, 1997.
- [4] L.A. Melton. Spectrally separated fluorescence emissions for diesel fuel droplets and vapor. *Applied optics*, 22(14):2224–2226, 1983.
- [5] J.M. Desantes, J.V. Pastor, J.M. Pastor, and J.E. Julia. Limitations on the use of the planar laser induced exciplex fluorescence technique in Diesel sprays. *Fuel*, 84(18):2301–2315, 2005.
- [6] F.Q. Zhao and H. Hiroyasu. The applications of laser rayleigh scattering to combustion diagnostics. *Progress in Energy and Combustion Science*, 19(6):447–485, 1993.
- [7] J.W. Strutt Rayleigh. On the light from the sky, its polarization and colour. *Philosophical Magazine Series 4*, 41(271):107–120, 1871.
- [8] J.W. Strutt Rayleigh. On the electromagnetic theory of light. *Philos. Mag*, 12:81–101, 1881.
- [9] J.W. Strutt Rayleigh. On the transmission of light through an atmosphere containing small particles in suspension, and on the origin of the blue of the sky. *Philos. Mag*, 47(375):132, 1899.
- [10] R.B. Miles, W.R. Lempert, and J.N. Forkey. Laser rayleigh scattering. *Measurement Science and Technology*, 12:R33–R51, 2001.
- [11] C. Espey, J.E. Dec, T.A. Litzinger, and D.A. Santavicca. Planar laser rayleigh scattering for quantitative vapor-fuel imaging in a Diesel jet. *Combustion and Flame*, 109(1-2):65–78, 1997.
- [12] J.C. Maxwell. A dynamical theory of the electromagnetic field. *Philosophical Transactions of the Royal Society of London*, 155:459–512, 1865.
- [13] L. Lorenz. Uber die refractionsconstante. *Annalen Der Physik und Chemie*, 11:70–103, 1880.
- [14] M. Born and E. Wolf. Principles of optics. *Pergamon press, Oxford*, 1975.
- [15] H. Naus and W. Ubachs. Experimental verification of rayleigh scattering cross sections. *Optics Letters*, 25(5):347–349, 2000.

-
- [16] M. Snee and W. Ubachs. Direct measurement of the rayleigh scattering cross section in various gases. *Journal of Quantitative Spectroscopy and Radiative Transfer*, 92(3):293–310, 2005.
- [17] P. Schellekens, G. Wilkening, F. Reinboth, M.J. Downs, K.P. Birch, and J. Spronck. Measurements of the refractive index of air using interference refractometers. *Metrologia*, 22:279, 1986.
- [18] W. Sellmeier. Zur erklärang der abnormen farbenfolge im spectrum einiger substanzen. *Annalen der Physik und Chemie*, 219:272–282, 1871.
- [19] R.J. Strutt. The light scattered by gases: its polarisation and intensity. *Proceedings of the Royal Society of London. Series A, Containing Papers of a Mathematical and Physical Character*, 95(667):155–176, 1918.
- [20] L.V. King. On the complex anisotropic molecule in relation to the dispersion and scattering of light. *Proceedings of the Royal Society of London. Series A, Containing Papers of a Mathematical and Physical Character*, 104(726):333–357, 1923.
- [21] C.J.F. Bottcher, O.C. Van Belle, P. Bordewijk, A. Rip, and D.D. Yue. Theory of electric polarization. *Journal of The Electrochemical Society*, 121:211C, 1974.
- [22] R.P. Smith and E.M. Mortensen. Calculation of depolarization ratios, anisotropies, and average dimensions of n-alkanes. *The Journal of Chemical Physics*, 35:714, 1961.
- [23] R.L. Jernigan and P.J. Flory. Optical anisotropy of chain molecules. theory of depolarization of scattered light with application to n-alkanes. *The Journal of Chemical Physics*, 47:1999, 1967.
- [24] C.A. Idicheria and L. Pickett. Quantitative mixing measurements in a vaporizing Diesel spray by rayleigh imaging. *SAE Paper 2007-01-0647*, 2007.
- [25] K.G. Denbigh. The polarisabilities of bonds - I. *Transactions of the Faraday Society*, 36:936–948, 1940.
- [26] A.I. Vogel. Physical properties and chemical constitution of aliphatic hydrocarbons. *J. Chem. Soc*, 9:133–142, 1946.
- [27] M.J. Weber. Handbook of optical materials. *CRC Press*, 2003.

- [28] K.T. No, K.H. Cho, M.S. Jhon, and H.A. Scheraga. An empirical method to calculate average molecular polarizabilities from the dependence of effective atomic polarizabilities on net atomic charge. *Journal of the American Chemical Society*, 115(5):2005–2014, 1993.
- [29] C. Clement and P. Bothorel. Etude de l’anisotropie optique moleculaire d’alcanes normaux, ramifies et halogenes. effet de solvant. *Journal de chimie physique et de physico-chimie biologique*, page 878, 1964.
- [30] M.M. El-Wakil, P.S. Myers, and O.A. Uyehara. Fuel vaporization and ignition lag in Diesel combustion. *SAE Transactions*, 64:712, 1956.
- [31] J. Gronki, C. Schulz, and H. Scharr. Correction of beam steering effects in 2d-laser-diagnostic measurements in combustion engines by image post-processing. *Eurotherm Seminar 2002, Visualisation, Imaging and Data Analysis in Convective Heat and Mass Transfer*, pages 301–306, 2002.
- [32] D.J. Heeger and J.R. Bergen. Pyramid-based texture analysis/synthesis. pages 229–238, 1995.
- [33] J.W. Tukey. The future of data analysis: Chap. 1. exploratory data analysis. *Addison-Wesley, Reading, MA*, 1977.
- [34] R.J. Moffat. Describing the uncertainties in experimental results. *Experimental thermal and fluid science*, 1(1):3–17, 1988.
- [35] J. Ortega and J.S. Matos. Estimation of the isobaric expansivities from several equations of molar refraction for some pure organic compounds. *Materials Chemistry and Physics*, 15(5):415–425, 1986.
- [36] J.C. Owens. Optical refractive index of air: dependence on pressure, temperature and composition. *Applied Optics*, 6(1):51–59, 1967.
- [37] S. Kampmann, B. Dittus, P. Mattes, and M. Kirner. The influence of hydro grinding at VCO nozzles on the mixture preparation in a DI diesel engine. *SAE Transactions*, 105(3):1329–1339, 1996.
- [38] M.P.B. Musculus. Entrainment waves in decelerating transient turbulent jets. *Journal of Fluid Mechanics*, 638:117–140, 2009.
- [39] D.B. Spalding. Combustion and mass transfer. *Pergamon international library of science, technology, engineering, and social studies*, 1979.

-
- [40] J. Arrègle, J.V. Pastor, and S. Ruiz. Influence of the injection parameters on Diesel spray characteristics. *SAE Paper 1999-01-0200*, 1999.
- [41] J. Naber and D. Siebers. Effects of gas density and vaporization on penetration and dispersion of diesel sprays. *SAE Paper 960034*, 1996.
- [42] L. Pickett, J. Manin, C.L. Genzale, D.L. Siebers, M.P.M. Musculus, and Idicheria C.A. Relationship between diesel fuel spray vapor penetration/dispersion and local fuel mixture fraction. *SAE Paper 2011-01-0686*, SAE International Journal of Engines, 2011.
- [43] Jose Maria Garcia. *Aportaciones al estudio del proceso de combustion turbulenta de chorros en motores Diesel de inyección directa*. PhD thesis, E.T.S. Ingenieros Industriales. Universidad Politécnica de Valencia, Valencia, 2004.
- [44] G.N. Abramovich. The theory of turbulent jets. *MIT Press, Cambridge, Massachusetts*, 1963.

Chapter 6

Results and experimental conditions influence

Contents

6.1	Introduction	220
6.2	Hydraulic characterization of the injector	221
6.2.1	Internal geometry of the nozzle tip	221
6.2.2	Rate of injection	223
6.2.3	Momentum flux of the spray	226
6.2.4	Additional characteristic parameters	228
6.2.5	Summary table of the hydraulic parameters	231
6.3	Mixing evolution in isothermal sprays	232
6.3.1	Macroscopic parameters of the liquid spray	233
6.3.2	Discussion on radial distribution profile	236
6.3.3	Influence of experimental conditions on mixing	240
6.4	Mixing evolution of vaporized jets	245
6.4.1	Vapor jet boundary	247
6.4.2	Mixing measurements and parameters influence	249
6.5	Comparative study of isothermal and evaporative sprays	255
6.5.1	Spray tip penetration	256
6.5.2	Spray opening	258
6.5.3	Mixing of isothermal and evaporative sprays	260
6.6	Conclusions	264
	Bibliography	266

6.1 Introduction

As it has been highlighted all along this dissertation, the mixing process between fuel and oxidizer is one of the main parameters for the quality of combustion [1]. The spray behavior and structure are influenced by several parameters related to the environment in which the spray is injected and other parameters inherent to the injection system [2]. In the theoretical background concerning spray development and behavior (chap. 2), it has been seen that the atomization and mixing of a spray were influenced by hydraulic characteristics of the specific testing conditions.

The techniques developed and applied in this work offer the possibility to measure the mixing process of sprays injected under evaporative conditions or not in a quantitative way. Modern Diesel engines but also those working with gasoline are working with the fuel injected directly in the cylinder. Therefore, the injection process offers the engineers and developers more versatility to build new combustion strategies in order to reduce emissions and increase efficiency. This has a direct consequence on the process of injection as the fuel must be injected in really changing environments, depending on the combustion strategy used (LTC, MK, HCCI, etc.), the load or even the temperature of the engine (cold-start).

In the same way, the ambient density and injection pressure are known to be the two main parameters that influence the spray development and mixing as described in chapter 2. These entities affect the injection process from the internal flow, within the nozzle of the injector, until the atomization and/or evaporation process, depending on the temperature of the ambient gases.

In addition to this, there are still a lot of discrepancies concerning the experimental results published addressing spray tip penetration or spreading angle for either the liquid or vapor phases. For example, it has been seen in the last two chapters (chap. 4 and 5) that the spreading angle of the same spray was notably different at high or low temperature. This may lead to error when using simple jet models as the one used earlier to predict the amount of ambient gases entrained into the flow as they depend upon spreading angle.

Because of the reasons listed above, this chapter presents an evaluation of the impact of the discharge density and the injection pressure on the global mixing process of sprays injected under cold and hot environments. First of all, an analysis of the hydraulic properties of the injection system used provides

fundamental information concerning the flow at the outlet and thus crucial data for predictions. Then, the development and mixing of the isothermal spray as a function of injection pressure and density are discussed and the influence of experimental parameters are investigated. A similar analysis is carried out in the following section focusing on the jets injected under evaporative and oxygen free (non-reacting) conditions. Finally, the development and mixing processes of non-evaporative and evaporative jets are confronted to make the light on the differences between atomizing and evaporating liquid spray behavior.

6.2 Hydraulic characterization of the injector

The hydraulic characterization of the injector, which is the main organ of the complete injection system concerning flow characteristics, is an important step prior to analyze the spray and its atomization. The results of the different experimental techniques described in section 3.3 are presented in the following paragraphs. The mass flow rate and spray momentum, together with the internal geometry of the nozzle tip are used to describe the flow at the orifice exit as developed in section 2.3.

Knowing the dimensionless parameters concerning the internal flow such as discharge, momentum, velocity and area coefficients is of great help to understand and explain the behavior of the developing spray. The intensity of the turbulence or the apparition of cavitation is directly reflected in those parameters and their evaluation represents additional and solid scientific information.

6.2.1 Internal geometry of the nozzle tip

The parameters defining the relationship between the different geometrical aspects of the internal shape of the nozzle tip, mainly the orifice and its connection to the needle seat have been measured thanks to silicone molding as described in section 3.3.1 or in reference [3].

The nozzle of the injector used is of the mini-sac type with a single orifice placed axi-symmetrically, it means on the same axis as the injector's body. As commented previously, the orifice is conical (k -factor = 1.5, see eq. 2.1) and the desired flow has been reached thanks to hydro-erosion, which also increases the entrance radius of the orifice, thus making the boundary layer to thicken the wall. Both characteristics should avoid the apparition of cavitation and in the same way, area contraction can be expected to be minimal, resulting in

relatively high discharge coefficient. Some sample pictures of the silicone molds acquired by the Scanning Electron Microscope (SEM) are shown in figure 6.1.

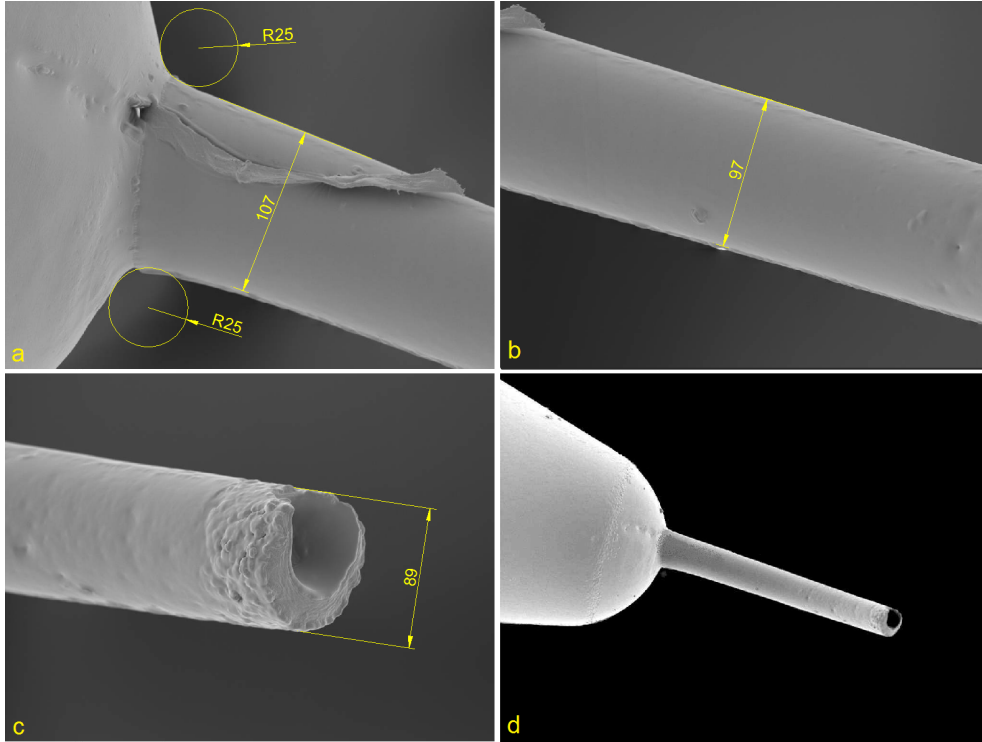


Figure 6.1: Sample SEM images of the silicone mold with computer-processed measurements of the single-hole nozzle used in this study: (a) inlet diameter and entrance radii, (b) half-distance diameter, (c) outlet diameter and (d) general view.

The results of the internal geometry of the injector measured by the silicone technique are presented in table 6.1 together with the dimensionless parameters described in section 3.3.1. The length of the orifice is provided by the manufacturer to be 1 mm, the dimension has been verified through X-Ray tomography to be $L = 1.005$ mm; this minor deviation would not affect the general tendency of the results anyway. The results of the X-Ray tomography have also been used in order to validate the results obtained with the silicone mold and the discrepancies between both techniques were within the experimental uncertainty (see sec. 3.3.1).

The results show that the orifice shape is more conical than specified by the manufacturer (k -factor = 1.8 instead of 1.5). In addition to that, the rel-

Internal geometry					
r_e [μm]	D_i [μm]	D_m [μm]	D_o [μm]	k -factor	AR [%]
25	107	97	89	1.8	16.8
Dimensionless parameters					
L/D_o		r_e/D_i		D_i/D_o	
11.3		0.23		1.20	

Table 6.1: Internal geometry and dimensionless parameters extracted from silicone molding of the nozzle.

atively large entrance radius (25 μm) would make the flow motion to thicken the walls and very limited area contraction can be expected from the results of the internal geometry. It has to be noticed however that the outlet diameter is really close to that provided by the manufacturer's technical drawing (89 μm instead of 90 μm , fig. 3.2); note that this difference is within the measurement uncertainty. The value of the k -factor is affected by the inlet and outlet diameter and care must be taken when measuring these dimensions as one micrometer difference represents a tenth of the value of k -factor.

These values are typical for such nozzle type, the position of the orifice (axi-symmetrical) and the internal geometrical specificities of the nozzle should mean that the flow does not present cavitation phenomenon. The next-coming section makes the light on these assumptions through hydraulic characterization of the injector.

6.2.2 Rate of injection

To study the flow at the orifice outlet, different injection pressures have been selected to match the running points of modern Diesel injection systems: 50, 100, 150 and 200 MPa; as well as two discharge densities or back pressures: 2.0 and 6.0 MPa. Two injection durations have been chosen, the first corresponds to an injection of $t_{inj} = 1500 \mu\text{s}$ long, which has been achieved by tuning the energizing timing of the solenoid excitation. This in order to get a constant actual injection duration for all testing pressures. The second one however has been set by controlling the electronic signal only with a constant duration of $ET = 2500 \mu\text{s}$; this induces that the actual injection length may vary depending on the injection and discharge pressures. This second timing has been selected in the aim of getting a longer stabilized part of the injected flow corresponding to the maximum needle lift. For the analysis, only the steady

period of the signal only has been considered to get mean values of both the rate of injection for each testing condition. Note that this testing plan has been applied for the momentum flux measurements as both results are utilized later to extract the hydraulic parameters.

Figure 6.2 presents the two processed signals of the mass flow rate for the reference condition changing the injection duration. It appears clearly that both signals are superimposed until the mass flow rate of the shorter injection starts to decrease, meaning that the needle is closing the injector.

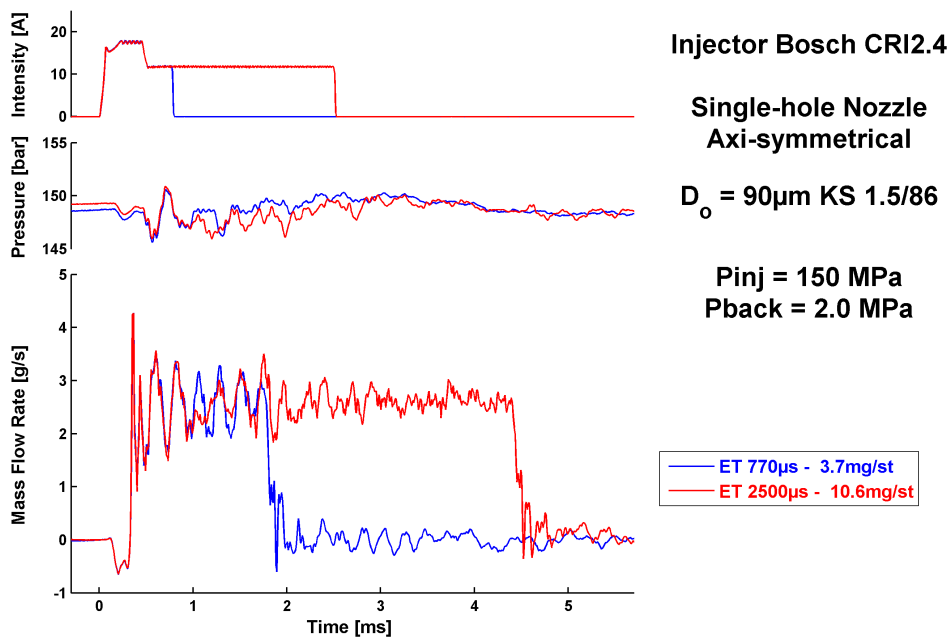


Figure 6.2: Temporal evolution of the rate of injection recorded by the flow rate meter. The electronic signal is plotted at the top and the pressure signal measured at 70 mm from the injector is represented in the middle.

This signal presents the mass flow rate recorded by the experimental equipment available, the initial ramp of the injection corresponds to the needle opening and the final decay, before the mass flow rate drops down to zero is the closing of the needle. Although these two periods are really important for the development of the spray and air entrainment, they cannot be used to extract the hydraulic coefficients in a quantitative way. For these reasons, figure 6.3 presents the mean value of the mass flow rate as a function of the square root of the pressure drop ΔP with $\Delta p = p_{inj} - p_b$, which should be linear theoretically as described by equations 2.11 and 2.12.

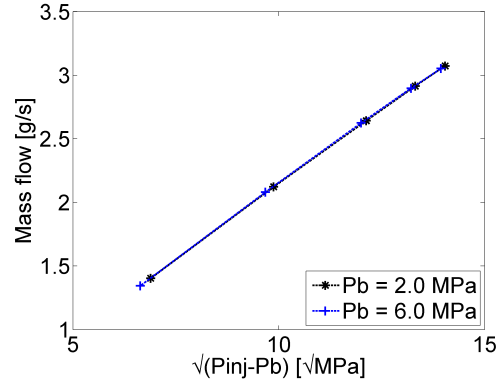


Figure 6.3: Steady mass flow rate as a function of the square root of the pressure difference.

As the mass flow rate follows a linear tendency, it can be concluded that the flow at the outlet is not restricted, this means that no cavitation phenomenon is observed for this injector for all conditions tested. The discharge coefficient is another way to represent the mass flow rate, this well-known dimensionless parameter is represented in figure 6.4 as a function of the theoretical Reynolds number [4].

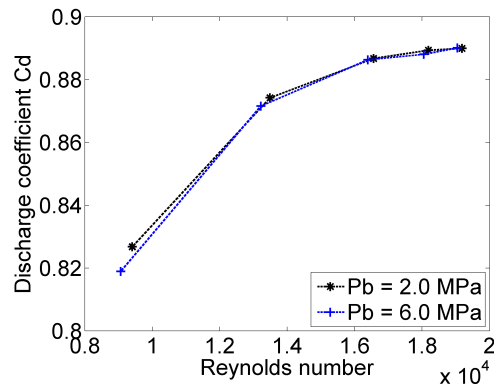


Figure 6.4: Discharge coefficient C_d as a function of the Reynolds number. Reynolds number has been calculated thanks to the theoretical velocity of Bernoulli (eq. 2.11).

This last plot clearly indicated the evolution of the discharge coefficient with respect to the Reynolds number mainly controlled by the injection pressure. The value of the discharge coefficient presents a first ramp for relatively

lower Reynolds number and then, the evolution seems to be more controlled with a slightly increasing linear tendency. This behavior has been observed by other researchers [5–7] who attributed those two distinct tendencies in the evolution of the C_d to the fact that the flow goes from laminar (or within the transition zone) to turbulent while Re increases.

It appears that the measured discharge coefficient is actually higher than the value specified by the manufacturer, it is however in agreement with the values found for such nozzles of slightly larger diameters [8].

6.2.3 Momentum flux of the spray

As commented in the previous section, the same test matrix has been used to perform momentum flux measurements. The equipment and procedures employed in this study have been detailed earlier (sec. 3.3.3) and more information is available in reference [8]. Sample signals of the momentum flux at the orifice outlet with respect to time are shown in figure 6.5 for two injection durations.

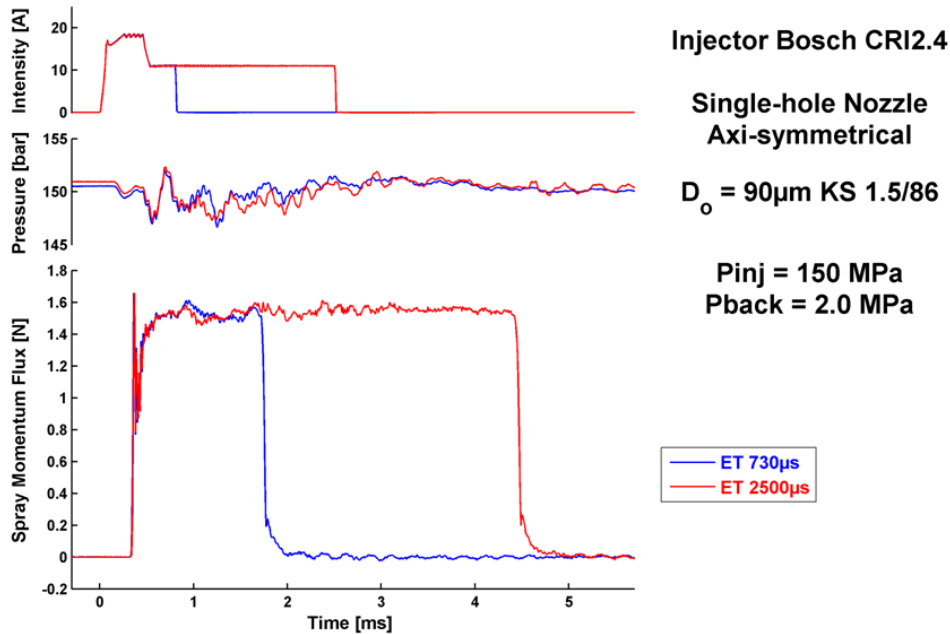


Figure 6.5: Momentum flux of the spray measured as a function of time.

The observations made on the rate of injection signals can be repeated

concerning the spray momentum. The signal is also composed of three phases or periods, the needle opening, triggering the start of injection, then, the steady period, when the needle lift is maximum and finally, the closing of the injector, when the needle is going back to its initial position. As introduced earlier, the opening and closing stages are transient periods and therefore, depending on the equipment and the methodology of the experimental technique, they may provide different results. As the purpose of this study is to evaluate the mixing process in steady conditions, the dynamic behavior of the spray in the transient regions is not part of the work.

Nevertheless, a remark has to be made concerning the steady period of the injection: the oscillations observed on the mass flow rate (fig. 6.2) are still present in the momentum flux, but their amplitude is several times smaller. The larger oscillations observed on the recorded signals of the temporal evolution of the mass flow rate are inherent to the technology employed, it means the long tube or Bosch method. The fuel being injected into an incompressible fluid (the same fuel actually), the energy released is not damped out as it is when injecting into gases, like it is the case for spray momentum measurements. A fluid-hammer is generated as both the fuel to be injected and the fuel remaining in the testing section of the rate meter are traveling in opposite directions to fill the gap opened by the needle as it moves backwards. Thus, the particular hydraulic aspect of the mass flow rate is produced by the experimental technology which enhances the amplitude of the vibro-acoustic modes of the injector principally. This is an additional reason to support the fact that only the mean value of the steady period is used for the analysis.

The mean value of the momentum flux of the spray is represented in figure 6.6 as a function of the pressure drop. As expected, the momentum flux is linear with the pressure drop as theoretically described by equation 3.9 and applying the theoretical velocity of Bernoulli as presented in equation 2.11.

The momentum flux can also be represented as a dimensionless parameter as described by equation 3.15 and shown as a function of the Reynolds number in figure 6.7.

The behavior of this parameter called the momentum coefficient is similar to that of the discharge coefficient with a softer transition between flow regimes. The tendencies of these two coefficients may differ if the apparition of cavitation inside the orifice causes a restriction of the flow, which is apparently not the case for this injector.

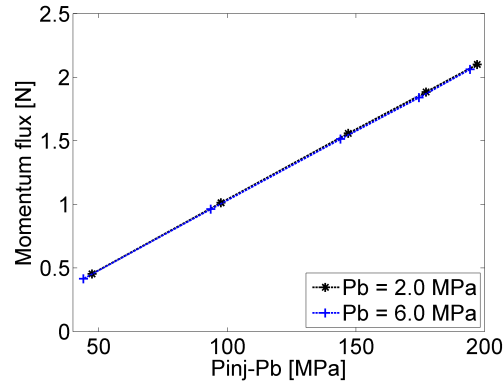


Figure 6.6: Mean value of the momentum flux in the steady period as a function of the pressure difference.

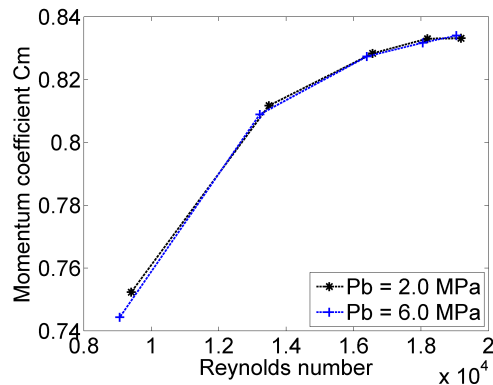


Figure 6.7: Momentum coefficient C_m as a function of the Reynolds number.

6.2.4 Additional characteristic parameters

Section 3.3.3 describes the hydraulic characteristics that can be extracted from merging the results of the mass flow rate and momentum flux from the same injected spray together. The resulting parameters such as effective velocity and diameter present a real advantage as they actually permit to get an estimation of the momentum flux (as well as the mass flow rate), which commonly used to predict spray penetration for example (see sec. 2.5.1).

Effective outlet velocity

The effective velocity of the fuel stream can be calculated thanks to the mean value of the mass flow rate and momentum flux under steady conditions as described by equation 3.10. Figure 6.8 represents the effective velocity at the outlet as a function of the square root of the pressure drop.

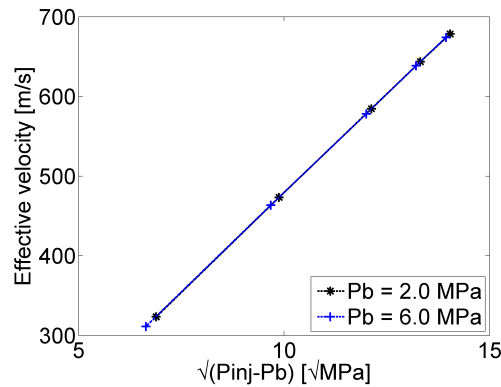


Figure 6.8: Effective velocity of the flow at the orifice exit as a function of the square root of the pressure difference.

As expected for non-cavitating nozzles, the velocity of the spray is linear with the square root of the pressure difference, as suggested by the theoretical velocity proposed by Bernoulli (eq. 2.11). From the effective velocity, the velocity coefficient can be extracted according to equation 3.12. This other dimensionless parameter basically represents the difference between the actual velocity of the stream with the theoretical velocity and its evolution with the Reynolds number is depicted on figure 6.9.

The behavior of the resulting velocity coefficient differs from the previous coefficients calculated in the fact that the transition from lower to higher Reynolds number is not clear anymore. Nevertheless, this trend is in agreement with previous results from similar geometries [8], which showed asymptotic tendency as the Reynolds number increases.

Effective area of the orifice

Another important parameter provided by the experimental techniques employed here is the effective area; in other words, the effective diameter of the

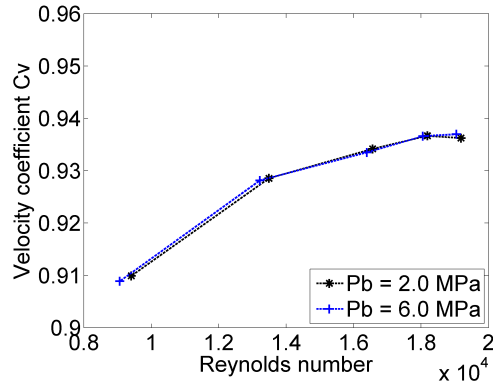


Figure 6.9: Velocity coefficient C_v as a function of the Reynolds number.

orifice. Figure 6.10 shows the effective diameter of the orifice used in this work as a function of Reynolds number.

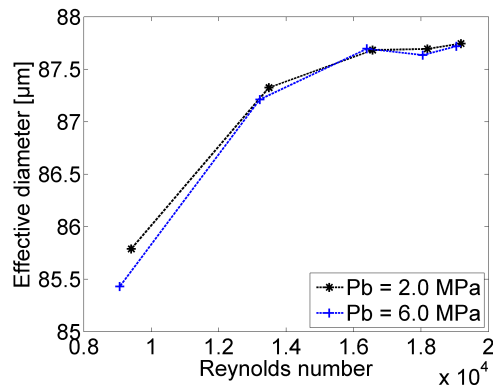


Figure 6.10: Effective diameter of the orifice as a function of the Reynolds number.

The resulting effective diameter (or area) increases with Reynolds number until it stabilizes to remain constant, for the range of testing conditions chosen for this study. The effective diameter actually depends on the Reynolds number and therefore on the regime of the flow as observed on the plots of the other dimensionless coefficients, which present similar behaviors. On the other hand, this contrasts with the velocity coefficient in which there was no real change of the general behavior according to Reynolds number.

The area coefficient represents the ratio of the effective area and the geo-

metrical one, provided by the manufacturer of the injector or any other experimental solution to extract the actual geometrical shape of the orifice (Silicone mold, X-Ray tomography, etc.). From the mathematical expression of the area coefficient (eq. 3.13), its behavior must be similar to that of the effective diameter presented in figure 6.10.

The evolution of the effective diameter with the Reynolds number can be explained by the fact that when the regime of the flow is within the transition phase between laminar and turbulent, the boundary layer still affects the flow in the orifice. The transition phase of the flow regime means that the flow is intermittent, or in other words, sometime laminar and sometime turbulent. Obviously, for lower Reynolds number in this region, the flow is more laminar and on the contrary, more turbulent for higher Reynolds number [9]. This evolution of the flow regime within the transition phase can explain the behavior of the effective diameter and area coefficient.

6.2.5 Summary table of the hydraulic parameters

The following table presents a summary of the various parameters obtained through the hydraulic characterization driven for the injector used in this study.

Data recompilation	Values	Units
Injected mass	3.72	mg/st
Steady mass flow	2.63	g/s
Steady momentum flux	1.56	N
Effective diameter	87.7	μm
Effective velocity	580	m/s
Discharge coefficient C_d	0.88	[-]
Area coefficient C_a	0.95	[-]
Velocity coefficient C_v	0.93	[-]
Momentum coefficient C_m	0.83	[-]

Table 6.2: Summary of the measured hydraulic parameters for the reference conditions ($p_{inj} = 150 \text{ MPa}$) as well as flow coefficients to be used to potentially adjust model predictions.

The different characteristics of the injection system are always useful to better understand and explain the behavior of the injected spray when inter-

acting with the ambient gases.

The effective diameter is lower than that specified by the manufacturer, but the value reported here gets actually closer to the measurements obtained through silicone molding. Concerning the hydraulic coefficients, everything has been already said above; the discharge coefficient seems to be slightly higher than the value specified by the manufacturer (0.88 vs. 0.86).

6.3 Mixing evolution in isothermal sprays

The results of the experiments performed in the aim of studying the evolution and global mixing process of modern Diesel sprays injected under non-evaporative conditions are presented in this section. An analysis of the results provided by the different experimental diagnostics is carried out as well as a comparison with the Musculus jet model used earlier [10] as it can provide additional information about the results from a critical point of view.

As it has been described in the chapter concerning the experimental techniques (chap. 3), the isothermal sprays have been studied through macro-visualization to get the boundary and thus extract tip penetration and spreading angle. The laser diagnostic developed and extensively described in chapter 4 provides the results of mixing in terms of two-dimensional maps of mixture fraction. A discussion about the results from a comparative point of view is proposed to see if the assumption generally done that considers an isothermal spray mixing field similar to that of a gas-jet is valid or not. These diagnostics have also been applied to different experimental conditions in order to evaluate the influence of parameters such as injection pressure or ambient density on the development of sprays and global mixing process.

The testing conditions chosen to study the evolution of isothermal sprays have been thought with the similar philosophy as that used to hydraulically characterize the injection system. This means that the objective was to match the possible conditions in terms of injection pressure and ambient density of a modern Direct-Injection Diesel engine. For this purpose, the same injection pressures have been selected: 50, 100, 150 and 200 MPa. Concerning the ambient density, the condition: $p_{inj} = 150$ MPa, $\rho_g = 22.8$ kg/m³ is the reference as it represents an intermediate running point in modern injection process in Diesel engines. From this reference, two additional conditions have been chosen to get the influence of the density of the ambient gases on mixing, leading to a total of three discharge densities: 7.6, 22.8 and 45.6 kg/m³. Note that the testing conditions referring to ambient density during hydraulic characterization is

expressed in terms of discharge pressure as pressure drop is the main parameter to study internal flow. On the other hand, when studying spray development and mixing in the relatively far-field, the ambient density is the parameter of control. The injector energizing time has been set to $ET = 2800 \mu\text{s}$ as this time was long enough for the steady region of the spray to reach the end of the visualization window at all testing conditions.

6.3.1 Macroscopic parameters of the liquid spray

The global penetration rates for non-evaporative sprays as a function of time are presented in figure 6.11 for the four ambient densities at an injection pressure of 150 MPa (a) and for the four injection pressures under an ambient density of 22.8 kg/m^3 (b). The time after start of energizing (ASOE) refers to the time from the electronic command of the solenoid, it does not take into account the hydraulic delay of the injector.

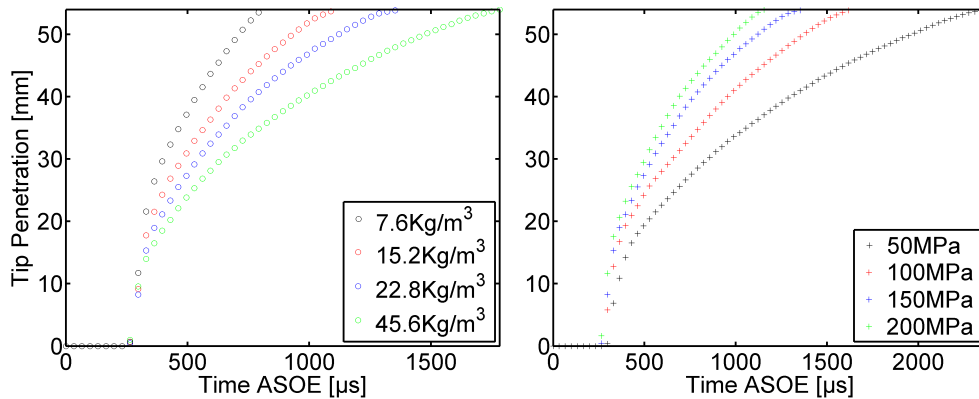


Figure 6.11: Temporal evolution of the tip penetration for non-vaporizing sprays. The plots represent the influence of ambient density (left) and injection pressure (right).

The plots show that for an increase of the ambient density, the penetration rate decreases, and inversely, it increases with a increment of the injection pressure. These observations are in agreement with both the theory presented in section 2.5.1 and the experimental results found in the literature [11–13]. As it can be noticed, both the injection pressure and ambient density have important impact on spray tip penetration. The correlations available to predict the penetration rate of injected sprays require the spreading angle, for

that reason, this macroscopic parameter has been measured according to the methodology described in section 3.4.2.

Figure 6.12 shows the resulting spreading angle as a function of time for all ambient densities at constant injection pressure (150 MPa) (a) and for the different injection pressures under constant ambient density (22.8 kg/m^3) (b).

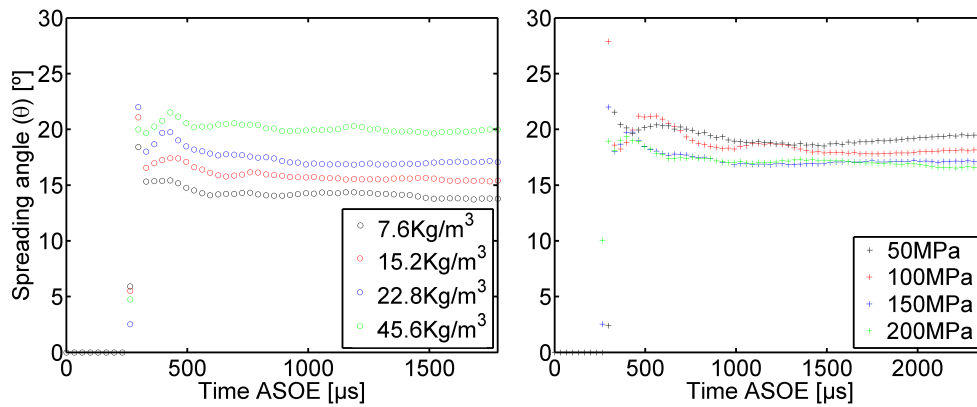


Figure 6.12: Spreading angle as a function of time for non-vaporizing sprays. The influence of ambient density is plotted on the left and injection pressure on the right side.

On these two graphs, the first observation can be that the spreading angle does not seem to be affected after a certain time, which corresponds to the break-up time proposed by Hiroyasu et al. [14]. Another comment is also that the effect of the discharge density on the spreading angle appears to be higher than the effect of the injection pressure whereas this difference does not appear clearly on the penetration rate. It has to be said that the conclusion drawn here concerning the influence of the ambient density on spreading angle has been already formulated by other researchers [12, 14], the observations made on the effect of the injection pressure is still the subject of controversy.

Care must be taken when analyzing results of spreading angle with conventional optical techniques like macro-visualization of the spray because the parameters used during image processing affect the resulting spreading angle widely. For instance, the total standard deviation on the spreading angle for the reference testing conditions ($p_{inj} = 150 \text{ MPa}$, $\rho_g = 22.8 \text{ kg/m}^3$) is higher than 4° , which represents about 25 % of the measured spreading angle: $\theta = 17.3^\circ$.

Figure 6.13 represents a confrontation of the penetration rate measured for the reference condition and that predicted by the Musculus model [10] for

the spreading angle measured through macro-visualization. In addition, this plot shows the predicted spray tip penetration by tuning the spreading angle in order to match the measured penetration rate. The input parameters of the model predictions concerning the hydraulic characteristics of the injection system are presented in table 6.2. The resulting spreading angle to achieve the better fitting between measured and predicted appears to be smaller than that extracted from the images.

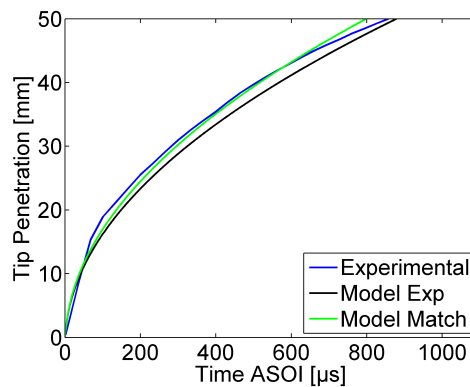


Figure 6.13: Comparison of the measured and modeled spray tip penetration rates for the reference condition. The dashed line is the predicted penetration for the measured spreading angle and the dot line the prediction obtained by tuning the spreading angle to match penetration rate.

The comparison between experimental and predicted penetration shows that they both present slightly different behaviors. It appears that the spray penetrates faster in the chamber during the first instants than the prediction and then, the velocity penetration rate decreases to follow the predicted one better. This can be explained by the limited momentum transfer between the liquid droplets and the ambient gases at the beginning of the injection. This causes a velocity slip between both media and therefore, the spray droplets travel at higher speed making the spray tip to penetrate faster. Then, the air entrained within the spray stream increases and the momentum transfer is more complete, making the penetration to resemble the predicted one.

Therefore, the difference in terms of spray width can be explained from two points of view. A first hypothesis is that the measured spray is too wide; this explanation could be valid as long as the standard deviation of the measured spreading angle is relatively high, even in the steady period of the spray. The difficulty to measure the spreading angle has been observed and supported by

measurements published by other researchers [13]. The second explanation might be a difference in terms of development between the isothermal liquid spray and the predictions based on the gas-jet theory as introduced in the previous paragraph. This is supported by the results of section 4.5.3 with figures 4.33 and 4.34, in which the mixture fraction distribution within such a two-phase flow does not match the mixing distribution of the model.

Despite this and in a matter of comparing quantitative results of mixture fraction distribution with a validated model for vaporized Diesel jets [10], the spreading angle is obtained through model-measurement penetration rate matching. Table 6.3 presents both the measured and modeled spreading angles for the different experimental conditions.

Spreading Angle Exp / Model		Injection Pressure [MPa]			
		50	100	150	200
Ambient density [kg/m ³]	7.6	16.0 / 14.5	15.7 / 14.0	14.3 / 13.5	14.5 / 13.5
	15.2	17.8 / 16.5	17.5 / 16.0	16.0 / 14.5	15.9 / 14.5
	22.8	19.2 / 17.0	18.8 / 16.5	17.3 / 15.5	17.4 / 15.5
	45.6	21.8 / 19.5	21.2 / 19.5	20.0 / 18.5	19.7 / 18.0

Table 6.3: Summary of the resulting spreading angles from experiments and through fitting of the measured penetration rate.

6.3.2 Discussion on radial distribution profile

The development of isothermal sprays is not exactly predicted by the model proposed by Musculus [10]. The modeled penetration rate does not adjust the experiments all along the development of the spray and therefore, this has an influence on the comparison of the mixing field. Figure 4.33 and 4.34 presented in chapter 4 already introduced this particularity of liquid Diesel sprays by the fact that the experimental distribution does not match the predictions.

First, the spreading angle can be implicated to explain the difference between model and experiments. It has been observed in the previous section that the resulting spreading angle was different to match penetration rate better. Based on the spreading angle to fit spray development, a plot of the resulting mixture fraction along the centerline of the spray is presented in figures 6.14 along with the radial profiles of the mixture fraction at two distances from the orifice exit. These profiles concern the reference condition ($p_{inj} = 150$ MPa, $\rho_g = 22.8$ kg/m³) and have already been presented in chapter 4 but in these

two graphs, the model predictions have been adjusted with the methodology described above.

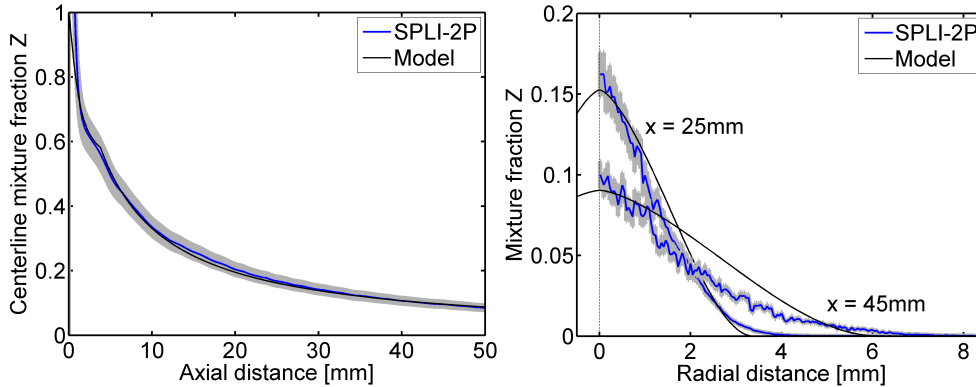


Figure 6.14: Measured mixture fraction and model predictions of the isothermal spray on centerline and for radial profiles at two axial distances for the reference condition: $p_{inj} = 150 \text{ MPa}$, $\rho_g = 22.8 \text{ kg.m}^{-3}$.

The experimental results presented here have been extracted by applying the SPLI-2P technique performed over an average of two times a hundred images (100 per phase) to reduce the uncertainty of the measurements due to spray dispersion. A different spreading angle as input to the model seems to make the predictions to get closer to the measurements when compared to the results presented in figures 4.33 and 4.34, particularly concerning the mixture fraction on the centerline. On the radial profiles, the predictions appear to match the very edge of the mixture fraction correctly, showing the capability of the SPLI-2P technique to record the mixture fraction even for low values. On the other hand, the experimental radial profiles look narrower than the predictions for both distances from the orifice outlet.

This corroborates the observations made earlier on the experimental results concerning the mixture fraction distribution in an isothermal spray (sec. 4.5.3) in figures 4.33 and 4.34. These results make the mean mixture fraction along the axial direction to match better between the model and the experiments as the spreading angle is now larger, thus reducing the mean mixture fraction in the spray axially as depicted in figure 6.15. Good agreement with the mean mixture fraction demonstrates that the experimental technique performs quantitatively in liquid Diesel sprays and that the methodology developed to obtain spreading angle is valid.

It has to be noted also that the model radial distribution is not exactly

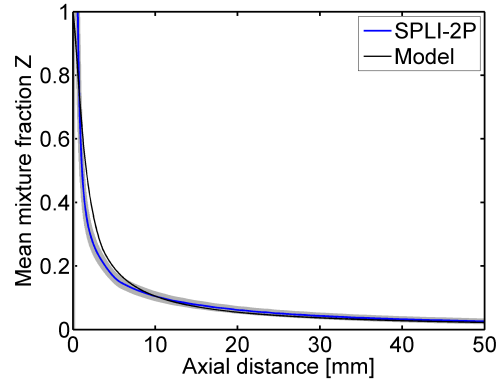


Figure 6.15: Experimental and computed mean mixture fraction for the reference condition along with the axis of the spray. Spreading angle has been adjusted by matching penetration rate.

a Gaussian error function as the mixture fraction on the edge of the jet according to the model-based prediction is equal to zero. Whereas it would be approximately 3 % with a realistic Gaussian-like profile [10]. Due to the low mixture fraction on the spray boundaries, the SNR of the measurements is also low and the absolute value concerning mixture fraction in these regions is not warranted.

The model proposed by Musculus calculates the mean volume fraction (transformed into mass or mixture fraction via eq. 4.29 and 4.30) in the spray axially as in the initial version of the model presented by Naber and Siebers [12]. Then, the model uses the radial distribution proposed by Abramovich [15] to rebuild both the axial distribution on the centerline and the radial one.

Several definitions of the radial distributions can be found throughout the literature [15–19] all based upon experimental results and empirically adjusted to fit them. In the last decade of liquid spray analysis, the distribution profile initially proposed by Hinze [16] and later adjusted by Correas [19] for isothermal liquid sprays has been found to be the best fit for numerous works [20–23].

The next figure (fig. 6.16) shows the axial and radial profiles of the mixture fraction for the reference condition compared to the predictions assuming the Abramovich profile suggested by Musculus [10] and the exponential shape of the radial distribution proposed by Correas [19]. The radial distribution experimentally adjusted by Correas has been presented in the theoretical section (sec. 2.5.4) and is mathematically described in equations 2.37.

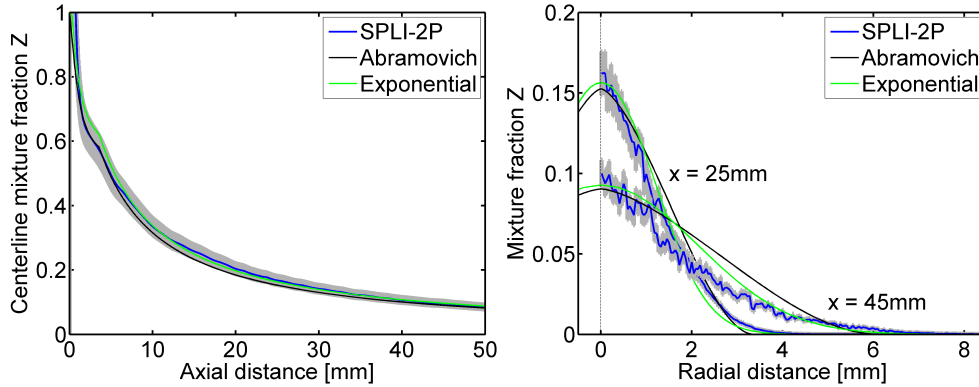


Figure 6.16: Comparison of the measured mixture fraction with model predictions assuming two distinct distribution profiles: Abramovich [15] and exponential [19]. This sample corresponds to the reference condition. Centerline is plotted on the left side of the figure and radial profiles on the right.

The exponential profile distribution seems to make the model to follow the experiments better for both the centerline and the radial profiles. There are almost no difference between modeled and experimented mixture fraction on the centerline except for short distances to the injector tip. Radially, the base of the Gaussian-like profiles (exponential) close to the spray boundaries coincide well with the experiments, confirming once again the value of the spreading angle. Following the profile, based on its narrower shape, the exponential radial profile gets closer to the experiments and both lines are almost matching each other until the centerline for the 25 mm location downstream.

Another argument can be advanced to explain the difference of shape between predictions and experiments: the different distributions between mass and momentum. This physical aspect can be interpreted as the different distribution of mass and velocity within the spray. Depending on the kinematic fluid viscosity and mass diffusivity, this phenomenon is described by the Schmidt number presented in section 2.5.4 through equation 2.34. The formulation of the exponential distribution presented by Correias (eq. 2.37 [19]) includes the Schmidt number. However, to apply this formulation, the radius or spreading angle of the spray from a point of view of the velocity distribution is required.

Nevertheless, several works intended to adjust the value of the Schmidt number for the model to predict fuel concentration in isothermal liquid sprays and generally found values below the unity. The study driven by Prasad and Kar [24] provided values of the Schmidt number in the range of 0.7-0.8 for low

injection pressures (about 20 MPa) and relatively large nozzle orifices (minimum diameter: $D = 0.4$ mm). More recently, Desantes et al. [22] developed a model to predict fuel distribution in liquid sprays and their results showed good agreement for values the Schmidt number around $Sc = 0.8$. Last year, the same group compared the results obtained via a technique using two-dimensional X-Ray radiography developed at Argonne National Laboratories to their model and found lower Schmidt number ($Sc = 0.5$) for good agreement within the near-nozzle field [25].

This represents the last study based on robust X-Ray dataset published up to now, this confirms that the Schmidt number for isothermal liquid sprays, on the contrary to gas-jets, can be assumed to be below the unity. This assumption goes in the same direction as the mixture fraction measured through Structured Planar Laser Imaging as it means higher mass distribution on the centerline and thus narrower radial distribution, assuming a constant spreading angle.

6.3.3 Influence of experimental conditions on mixing

The Structured Planar Laser Imaging technique developed in chapter 4 has been applied to the test matrix presented earlier to study the global air-fuel mixing over a wide range of experimental conditions. As explained in the corresponding chapter, the images have been acquired after relatively long time after the start of injection (time ASOI) in order to ensure that the laser-sheet illuminated the steady period of the development of the spray. These timings have been known thanks to the high-speed imaging recording the spray tip penetration within the chamber.

In order to draw conclusions over a wider range of experimental conditions, figures 6.17 and 6.18 presents axial and radial profiles of the mixture fraction for the two other ambient densities: $\rho_g = 7.6$ and 45.6 kg/m³. The results of the model correspond to the axial and radial profiles (Abramovich and exponential distributions) adjusted according to the discussion carried out in the section above. Note that the two additional conditions concerning ambient density represent a third (7.6 kg/m³) and twice (45.6 kg/m³) the value of the reference density condition. These two points represent a full range of ambient conditions for sprays in modern Diesel engines with the last injection strategies (multiple injections for example) and technologies (e.g. turbochargers) implemented.

The density of the ambient gases affects the behavior of the spray in terms

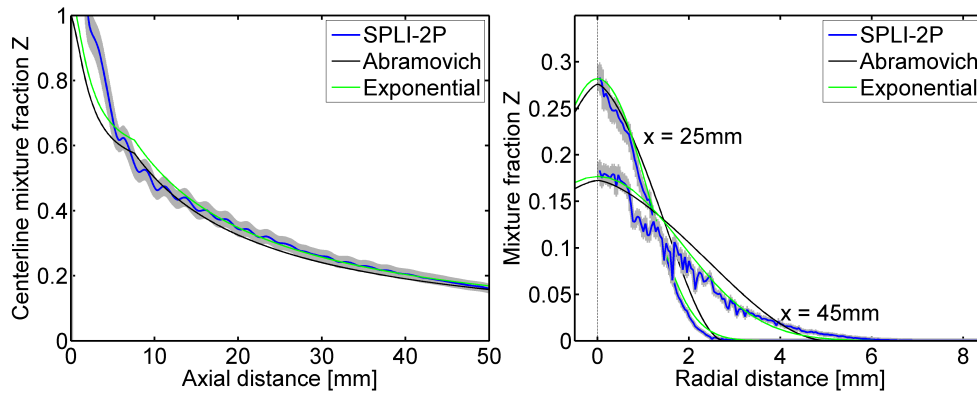


Figure 6.17: Measured mixture fraction and model predictions of the isothermal spray on centerline and for radial profiles at two axial distances. Experimental conditions: $p_{inj} = 150$ MPa, $\rho_g = 7.6$ kg.m⁻³.

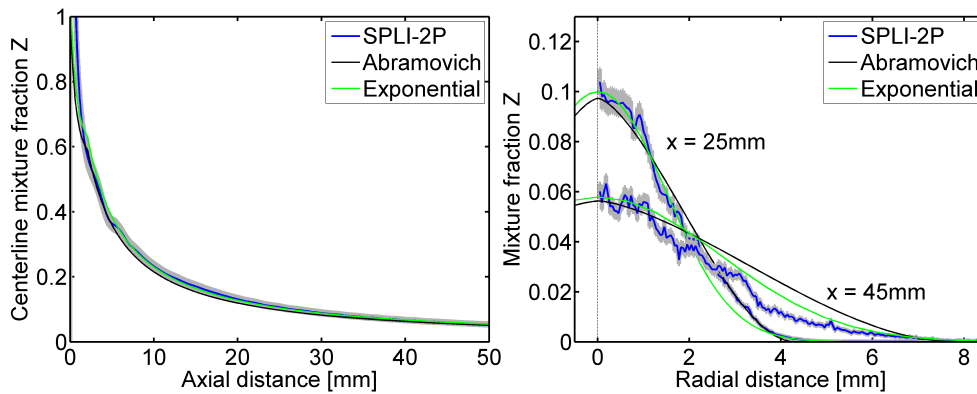


Figure 6.18: Measured mixture fraction and model predictions of the isothermal spray on centerline and for radial profiles at two axial distances. Experimental conditions: $p_{inj} = 150$ MPa, $\rho_g = 45.6$ kg.m⁻³.

of penetration rate, as it has been already said, but also in terms of global mixing as both are ultimately related. This dataset however shows the consistency of the experiments as the same observations can be made concerning the evolution of the mixture fraction either axially or radially.

Lower discharge density makes the spray to penetrate faster, but also to be narrower and therefore, to entrain less ambient gases in the stream. The impact on the mixture fraction distribution is that it is narrower and has a higher maximum on the centerline. Under higher ambient density conditions, the contrary is observed, the spreading angle of the spray is larger, thus entraining the ambient gases at a higher rate. As a result, the mixture fraction on the centerline is lower and the Gaussian-like radial profile wider. This difference in terms of mixing distribution is represented in figure 6.19 in which the resulting axial and radial profiles of the mixture fraction are plotted together.

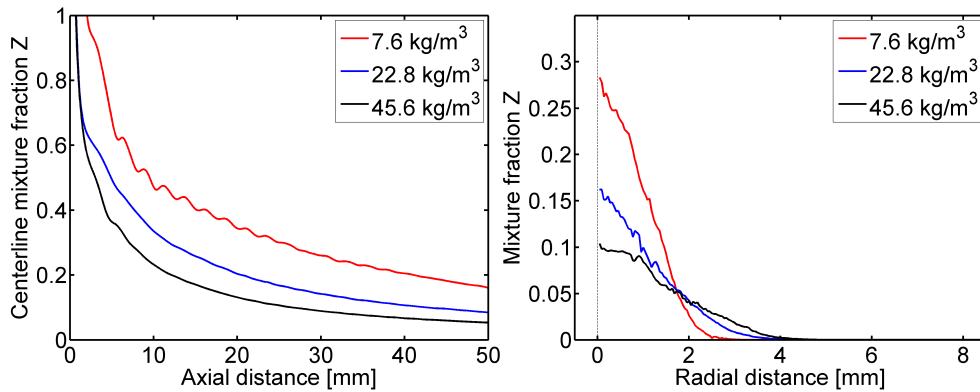


Figure 6.19: Measured mixture fraction of the isothermal spray on the centerline (left) and radially at 25 mm downstream. This graph shows the influence of ambient density on fuel-ambient mixing at constant injection pressure: $p_{inj} = 150 \text{ MPa}$.

This has an influence on the global mixing and further processes as the boundary for stoichiometric fuel-air ratio is observed to be at different locations depending on the discharge density. Taking into account that this parameter is changing with time, it is understandable that the injection strategy is a key in the global internal combustion process of modern Direct-Injection engines.

The injection pressure is another important parameter concerning spray development as depicted on figure 6.11 as the injected mass flow rate is a function of this. On the other hand, it has been observed that the spreading angle was only slightly affected by the injection pressure as shown on figure 6.12(b).

The results recompiled in table 6.3 confirms this influence and shows that the isothermal spray gets narrower when injection pressure increases. Note that this effect is lower for low discharge densities, in other words, almost no difference is observed for the lowest ambient density applied in this study. The next figure (fig. 6.20) presents a confrontation of the resulting mixture fraction measured by the SPLI-2P technique when the injection pressure is varied.

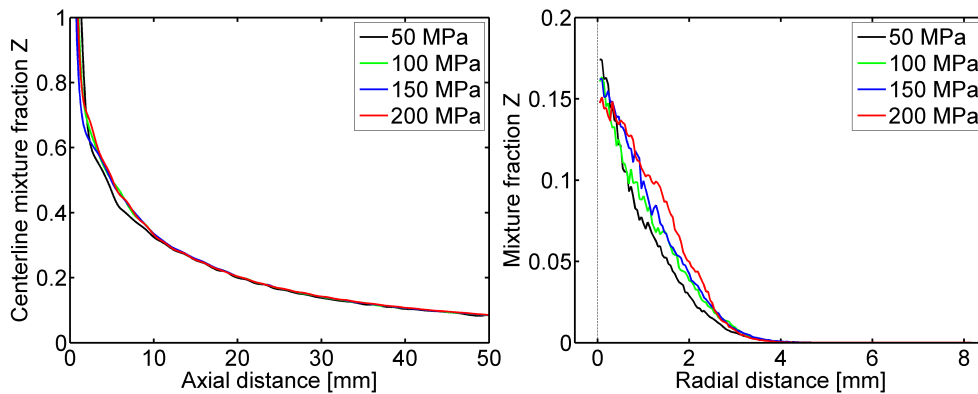


Figure 6.20: Measured mixture fraction on the centerline (left) and at 25 mm downstream (right) for different injection pressures. These results corresponds to the reference ambient density condition: $\rho_g = 22.8 \text{ kg.m}^{-3}$.

The graph shows only slight differences between the mixture fraction distribution of the spray for injection pressures from 50 to 200 MPa under a typical ambient density of 22.8 kg/m^3 . Therefore, it is hard to make a conclusion on whether an increment of the injection pressure is helpful for the mixing or prejudicial. According to the results, the simple explanation is that even if the fuel is supplied at a higher mass flow, the entrainment rate of the ambient gases is balanced and hence, the mixture fraction remains similar.

In order to present the results concerning the mixture fraction distribution of an isothermal spray from a global point of view, the mixture fractions on the centerline at an axial distance of 25 mm have been graphically represented in figure 6.21. This figure is a compilation of the 12 different experimental conditions tested in this work.

The impact of the experimental conditions on global mixing of liquid sprays appears clearly in this figure. The effect of the ambient density has already been observed directly on the mixing distribution on the centerline and more particularly on the radial profiles. As commented before, the ambient density affects the development of the spray, by increasing ambient density, the

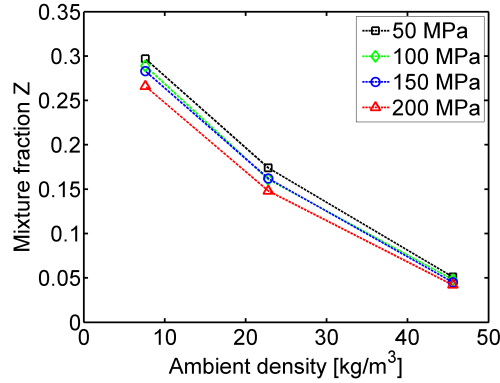


Figure 6.21: Graphical representation of the mixture fraction evolution as a function of ambient density for all injection pressures tested. The values are taken on the centerline at 25 mm from the tip.

momentum flux of the stream "fights" against higher forces to penetrate in the gases and this increases the ratio between axial and radial diffusion components. Hence, the global mixing field of the spray is extended radially, or in other words, the spray opens more, thus entraining the ambient gases at a higher rate. The logical conclusion is that the local mixture fraction gets lower when the entrainment rate of the ambient gases surrounding the spray increases. This effect can be summarized as a balance between spray momentum and ambient density as supported by the numerous works [26,27] and models [12,20,21] available to predict penetration or global mixing distribution of sprays as described earlier in the theoretical background (sec. 2.5).

The relationship between global mixing within the spray and spray tip penetration has been pointed out as both are closely related to momentum flux. The consequence of increasing injection pressure while holding ambient density makes the spray to penetrate faster in the chamber. On the other hand, it has been observed that the injection pressure does not have a large influence on spray opening or spreading angle, thus meaning that the gas entrainment is balanced with spray development. This makes the fuel concentration or mixture fraction to remain sensibly the same no matter the injection pressure, for those particular experimental conditions as shown on figure 6.21. However, one collateral phenomenon of an increment of the injection pressure is the cavitation [28–30]. The spray injected by a nozzle under cavitating conditions has been seen to have different development behavior such as slower penetration and wider spreading angle than under non-cavitating conditions [31]. The phe-

nomenon of cavitation has been described in the theoretical part of this thesis in chapter 2, relating the influence of cavitation to disintegration rate.

6.4 Mixing evolution of vaporized jets

In modern Direct-Injection engines, the sprays are directly injected into the combustion chamber, which is at different ambient conditions depending on the running point and injection strategy. From a practical point of view, the ambient conditions change according to the position or time in the engine cycle as described in section 2.2. The injection of fuel generally starts during the compression phase, as the piston compresses the gases present in the already closed combustion chamber, their pressure (density) and temperature increase until top dead center (TDC). At the same time, depending on the technology of the engine, the ambient conditions at TDC change and for this reason, it becomes interesting to study the evolution of development and mixing of evaporative jets for a range of internal conditions.

For this purpose, the sprays have been injected in a specific facility capable of simulating conditions in terms of temperature and pressure found at TDC in modern Diesel engines as described in section 3.5.1. Macro-visualization and Planar Laser Rayleigh Scattering diagnostics have been applied to study the evaporative jets generated by the same injection system used all along this study. The results are confronted to the mixing model proposed by Musculus [10] as the previous results showed good agreement between experiments and predictions. An analysis of the influence of the experimental parameters on development and global mixing of vaporized jets is also drawn as for non-evaporative sprays.

To study the influence of the parameters from both the injection and the ambient gases sides, the injection pressure and the ambient density of the gases in the chamber have been varied in a similar range to that used for hydraulic characterization and non-vaporizing sprays. The test matrix applied to these tests differs a little from the one built for isothermal sprays mainly due to limitations of the diagnostics or equipments. Concerning the ambient density, it has been observed that beam steering at the highest case ($\rho_g = 45.6 \text{ kg/m}^3$) was too severe thus being prejudicial for quantitative measurements as the correction strategy implemented to compensate this phenomenon was not performing correctly. For this reason, the highest ambient density case has been removed, leading to the following density conditions: 7.6 and 22.8 kg/m^3 . Because of the limitations of the injection system, the highest injection pressure condition has

not been tested in the evaporative jet facility, meaning that the three pressure conditions were: 50, 100, and 150 MPa. In a matter of presenting mixing evolution with experimental parameters, an additional density condition has been simulated, it corresponds to two thirds of the reference density and has only been tested with the reference injection pressure (150 MPa). Due to the internal dimensions of the vessel (100 mm long), the injection electronic timings have been varied from 2.5 to ≈ 8.5 ms depending on testing condition in order to always get the steady period of the jet at the time of laser radiation for Rayleigh scattering measurements. The image timings have been obtained thanks to Schlieren imaging of the vaporized jet penetration and were in the range of 3.5 ms to 9.0 ms after start of electronic command of the injector (time ASOE).

To perform Rayleigh scattering in evaporative jets, one preliminary objective is to prevent liquid droplets from reaching the illumination plane that would strongly interfere with the measurements as introduced earlier. The reference condition imposes the most relevant parameters such as ambient density, injection pressure and temperature to be $\rho_g = 22.8 \text{ kg/m}^3$, $p_{inj} = 150 \text{ MPa}$ and $T_g = 900 \text{ K}$, respectively. At this condition, the length of the liquid region measured through Mie scattering revealed to be around 11 mm, thus providing complete vaporization of the fuel before the laser-sheet placed at 17 mm. Nevertheless, the liquid length changes with operating conditions, for example, decreasing ambient density from 22.8 to 7.6 kg/m^3 extends liquid length from 11 to more than 19 mm according to the scaling law proposed by Siebers [32]. Note that a liquid length of 11 mm does not mean that there is absolutely no liquid droplets after this distance but some may penetrate further; that is why the laser-sheet is placed several millimeters downstream.

Therefore, one solution could be to move the laser-sheet forward far enough to avoid interferences from liquid droplets for lower discharge densities. As the objective of the study is also to confront the resulting mixing fields against each other, this solution has not been ruled out. The approach used here has been to raise the temperature of the ambient gases up when decreasing ambient density to reduce the liquid length. The temperatures of the ambient gases to obtain approximately constant liquid length have been predicted by the liquid scaling law proposed by Siebers [32]. This model considers perfect mix between injected fuel and ambient to assume complete momentum transfer, which does no longer depend upon ambient temperature but ambient density only. The resulting temperatures to get constant liquid length prediction when applying Siebers model are 1100 K at 15.2 kg/m^3 and 1400 K at 7.6 kg/m^3 , in addition to the 900 K of the reference condition (22.8 kg/m^3).

6.4.1 Vapor jet boundary

Schlieren imaging has been used to obtain the vapor boundary of the developing jets under evaporative conditions and to extract penetration rate and spreading angle. Figure 6.22 shows a sample Schlieren image of a vaporizing jet together with the boundary of the vapor region processed through the methodology described in section 3.5.2.

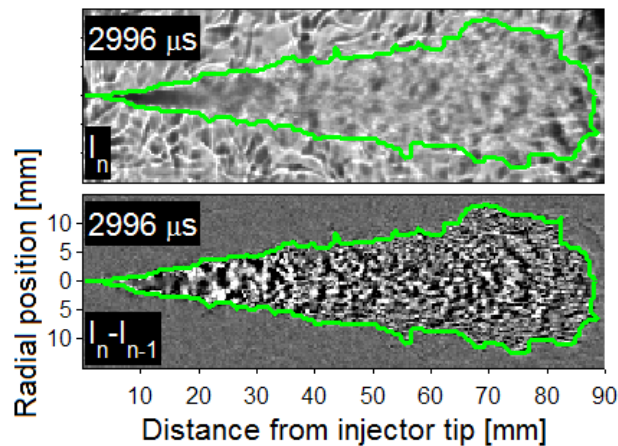


Figure 6.22: Sample image extracted from high-speed Schlieren for the reference condition with computed vapor boundary plotted in green. Raw image (top) and corrected image (bottom) are shown according to image processing (sec. 3.5.2).

The background of the raw image shows disturbances due to temperature (density) gradient that causes beam steering. In addition, these disturbances may affect the processing as the background is not flat and therefore, the real boundary of the jet can be mis-detected. Pickett et al. [33] observed that for different Schlieren sensitivity setups, the disturbances in the background were changing thus influencing the detection of the boundary, leading to different macroscopic parameters, particularly concerning the spreading angle.

The spreading angle of the evaporative jet is required as an input to the model in order to compare the experimental results to the predictions. Figure 6.23 is a plot of the temporal evolution of the spreading angle for the three ambient densities. Note that the injection pressure has not been varied for vapor penetration measurements as the first objective is to extract spreading angle. Variations on spreading angle while changing injection pressure have been observed to be very limited [13, 14]. Therefore, because of the lack of

accuracy of the boundary detection through Schlieren imaging, the small differences induced by injection pressure variation could barely be measured.

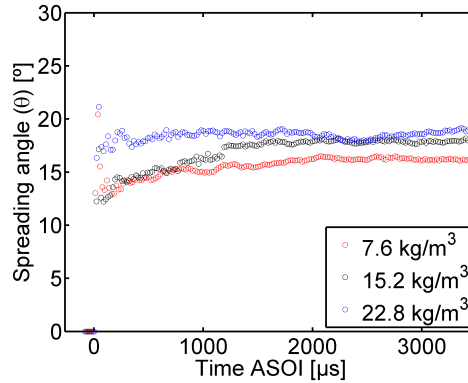


Figure 6.23: Spreading angle of the vapor region of the jet as a function of time for different ambient densities.

The results of the spreading angles measured on Schlieren imaging are in agreement with the expectations, it means narrower jets at lower ambient density. On the other hand, thanks to the accuracy of the Rayleigh scattering diagnostic developed in this work, the spreading angle can also be evaluated from the quantitative mixing results directly as presented in section 5.5.1. It is interesting nevertheless to compare the results of the spreading angles extracted through Schlieren to the values provided by Rayleigh scattering measurements. Table 6.4 presents the average spreading angle for the steady period of the developing jets extracted from Schlieren images and compared to the average of the resulting angle measured on of the single-shot mixing maps.

Spreading Angle Schlieren / Rayleigh		Injection Pressure [MPa]		
		50	100	150
Ambient density [kg/m ³]	7.6	- / 15.6	- / 17.0	14.3 / 17.9
	15.2	- / -	- / -	16.0 / 21.0
	22.8	- / 21.4	- / 21.7	18.7 / 21.9

Table 6.4: Summary of the spreading angles obtained through Schlieren experiments and thanks to an evaluation of the jet opening on two-dimensional individual mixing fields.

The values of the spreading angles summarized in this table show that the results extracted from the jet boundary detected on Schlieren images always

provide several degrees lower spreading angles (narrower jets). This has been observed by Pickett et al. [33] and they explained this aspect by a lower sensitivity of the Schlieren optical setup, hence influencing the detection threshold. For this reason, the spreading angles extracted from averaging the single-shot values on Rayleigh scattering signals have been used as input to the Musculus jet model [10] for comparison.

Figure 6.24 represents the vapor phase penetration as a function of time for the different ambient densities. On this same graph, the penetration rate predicted by the model when the spreading angles from Rayleigh scattering shown in table 6.4 are used as input.

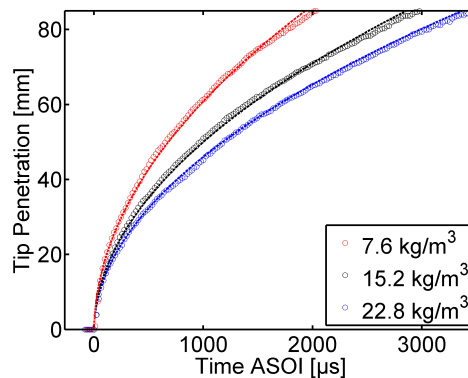


Figure 6.24: Temporal evolution of the vapor-phase penetration measured through Schlieren imaging. The predicted penetration rates are also represented (dashed lines).

The penetration rates for the different ambient density conditions are matching each other, although it has been noticed that the vapor boundary obtained from Schlieren imaging provided smaller spreading angles. This observation is important as it proved the accuracy of Schlieren diagnostic to record tip penetration, this aspect has also been studied by Pickett et al. [33]. From another point of view, such good agreement for penetration rate between experiments and predictions could confirm the validity of the spreading angles extracted from Rayleigh scattering signals.

6.4.2 Mixing measurements and parameters influence

Two-dimensional mixing maps of jets injected under evaporative conditions have been obtained thanks to the Planar Laser Rayleigh Scattering technique

developed in chapter 5. The long timing after start of injection have been used to ensure the acquisition of steady jets, in addition to reduce the particle contamination as explained earlier. The resulting two-dimensional map and profiles of mixture fraction of the vapor region of the jet for the reference condition ($p_{inj} = 150$ MPa, $\rho_g = 22.8 \text{ kg.m}^{-3}$ and $T_g = 900$ K) have been presented in section 5.5.2. The results showed good agreement with the predictions of the model proposed by Musculus [10] as the predictions were within the uncertainties of the measurements all along the axial and radial profiles. The mixture fraction for the two lower density conditions are presented in figures 6.25 ($\rho_g = 15.2 \text{ kg/m}^3$) and 6.26 ($\rho_g = 7.6 \text{ kg/m}^3$) on the centerline and along the radial profile at two distances from the tip. The results come along with a gray fill representing a 95 % confidence interval corresponding to the uncertainty of the measurements developed in section 5.4.3. The spreading angles of the developing jets used for to compute the predictions of the Musculus model have been measured on the single-shot Rayleigh signals as described previously in section 5.5.1. The values of the input spreading angles are given in table 6.4. We remind that the temperature of the ambient gases have been raised up in order to keep the liquid length approximately constant for all testing conditions.

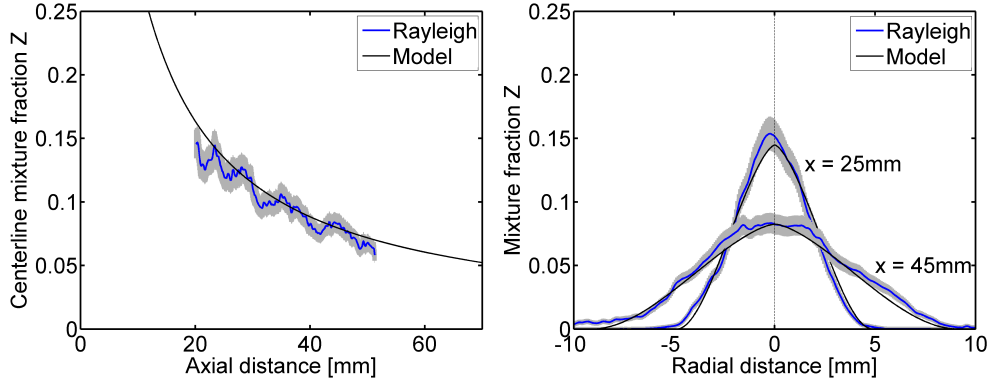


Figure 6.25: Measured mixture fraction and model predictions of the vapor region of the jet on centerline and for radial profiles at two axial distances. Experimental conditions: $p_{inj} = 150$ MPa, $\rho_g = 15.2 \text{ kg.m}^{-3}$ and $T_g = 1100$ K.

The predictions for the intermediate density ($\rho_g = 15.2 \text{ kg/m}^3$, fig. 6.25) fall within the uncertainty of the experiments when the radial profile proposed by Abramovich [15] is used. As commented in the previous chapter (sec.5.5.2), this profile appears appropriate as suggested by the closeness of the model

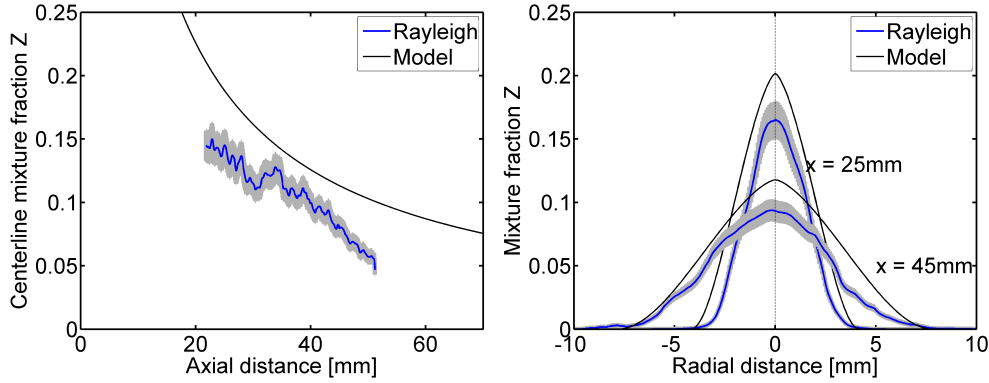


Figure 6.26: Measured mixture fraction and model predictions of the isothermal spray on centerline and for radial profiles at two axial distances. Experimental conditions: $p_{inj} = 150$ MPa, $\rho_g = 7.6$ kg.m⁻³ and $T_g = 1400$ K.

predictions with the experimental resulting mixture fraction. A divergence is observed however on the edges of the radial distributions where the mixture fraction goes down near zero. In fact, the spreading angle used to adjust the modeled radial distribution is for a mixture fraction of zero, whereas the angle of the jet measured on the experimental data has been set for a value of 1 % of the centerline. Nevertheless, the mixture fraction measured through Rayleigh scattering globally follows the predictions when the spreading angle of the model is correctly adjusted.

This is not the case concerning the lower density case ($\rho_g = 7.6$ kg/m³, fig. 6.26) in which the predictions are between 30 and 50 % higher than the experimental mixture fraction. For this specific density, the temperature has been set to $T_g = 1400$ K to avoid liquid droplet interference and seems to cause the fuel to decompose. Fuel decomposition may occur even if the ambient gases are inert, like in these tests, due to high temperature. This phenomenon affects the intensity of the signal emitted through Rayleigh scattering as the fuel molecules break down and hence, their cross-sections are not conserved. This effect has been observed by Schulz and Sick [34] applying Laser-Induced Fluorescence (LIF) in high temperature conditions or flames. They observed a reduction in signal intensity at elevated temperature and attributed this to molecular decomposition of the LIF tracer.

To illustrate numerically the potential influence of fuel decomposition on Rayleigh signal intensity, table 6.5 presents the cross-sections of several hydro-

carbon fuels and mixtures.

Hydrocarbons	σ_i [$\times 10^{-27} \text{ cm}^2$]	Z_{st} [$\times 10^{-2}$]	σ_{eq} [$\times 10^{-27} \text{ cm}^2$]
Methane [CH ₄]	11.4	5.50	5.99
Propane [C ₃ H ₈]	67.2	6.02	7.91
Heptane [C ₇ H ₁₆]	309.8	6.21	11.12
Dodecane [C ₁₂ H ₂₆]	858.4	6.27	14.92

Table 6.5: Rayleigh cross-sections for different linear alkanes together with stoichiometric mixtures. The equivalent cross-sections for stoichiometric mixture fraction are also presented.

It can be appreciated that the Rayleigh cross-sections decrease significantly as the molecules contain less carbon atoms, which seems reasonable as pointed out by Adam et al. [35]. In addition to that, a break down of the initial molecule affects the Rayleigh signal in larger scale as the cross-section is not linear with the number of carbons as shown in table 6.5. This must be processed together with the stoichiometric mixture fraction of the lower alkane chains with respect to the initial fuel molecule. By combining those two properties, the apparent Rayleigh cross-section of the different molecules under stoichiometric ratio is obtained and given in the fourth column of table 6.5. Considering that all the n-dodecane fuel (C₁₂H₂₆) have experienced molecular break down into heptane (C₇H₁₆) for example, the resulting signal would be about 25 % lower and this intensity loss would almost be twice as much if all n-dodecane broke down into propane (C₃H₈).

In order to evaluate whether or not the fuel decomposition process occurs under the operating conditions studied in this work, a simplified form of a two-stage Lagrangian (TSL) reacting jet model [36,37] has been used. The model takes into account the mixing process of two reactants, in this case, the vaporized fuel and the ambient gases. Then, thanks to the laws of chemical kinetics, the quantity of injected fuel to break down is evaluated as the temperature of the core increases with entrainment of the ambient gases. The conclusions are that minimal fuel decomposition can be expected for temperature conditions below $T_g = 1100 \text{ K}$, whereas over this limit, concretely at 1400 K , molecular decomposition is very likely. It has to be said nonetheless that the decomposition of alkanes chains does not break the molecules down to single carbon molecules but to higher carbon atoms [38]. This limits somehow the reduction in terms of signal intensity as the n-dodecane for example

can be expected to break down into two hexanes (C_6H_{14}) and not into twelve molecules of methane (CH_4).

Due to fuel decomposition, the lower density case cannot be considered as valid concerning the mixture fraction quantitatively. However, the spreading angle extracted from Rayleigh scattering measurements showed good agreement with the model prediction concerning tip penetration and still represents valuable data.

Figure 6.27 shows the mixture fraction along the axis of the jet and the radial profiles at 25 mm from the nozzle exit for the two density conditions considered as quantitatively valid. The predicted mixture fractions on the jet centerline is also plotted as references for the measurements.

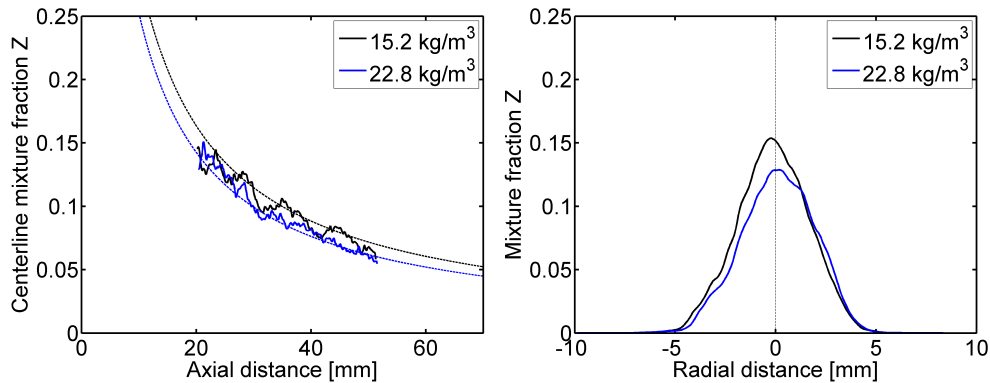


Figure 6.27: Measured mixture fraction of the isothermal jet on the centerline (left) and radially at 25 mm downstream (right). The predictions are also plotted as references along the centerline (dashed lines). The injection pressure is the reference one ($p_{inj} = 150$ MPa).

According to the plots shown on figure 6.27, the influence of the ambient density on mixing appears clearly. As expected, the centerline mixture fraction is higher, simultaneously reducing the width of the jet for the lower discharge density. This confirms the spreading angles measured on the two-dimensional maps obtained through Rayleigh scattering as the jet opens less at low density.

On the other hand, if the same approach is conducted, the influence of injection pressure would be limited as suggested by the spreading angle measurements presented in table 6.4. Figure 6.28 confronts the different injection pressures of the test matrix built to evaluate mixing under evaporative condition. Both the profiles, axial and radial are almost superimposed for all in-

jection pressure conditions. Therefore, it can be concluded that the injection pressure is not a parameter influencing fuel-air mixing process. The preliminary comments concerning the relationship between jet mixing and spreading angle seems justified as for similar spreading angle, the local mixture fraction remains constant no matter the injection pressure.

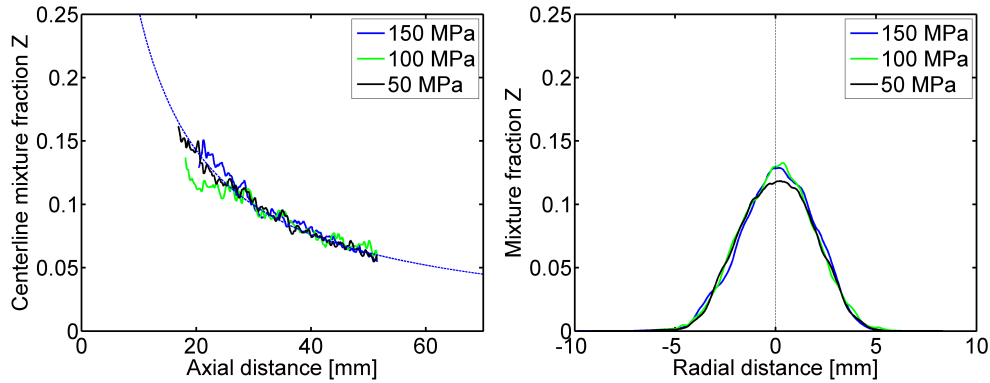


Figure 6.28: Measured mixture fraction on the centerline (left) (with model predictions) and at 25 mm downstream (right) for different injection pressures. This sample corresponds to the reference ambient density condition: $\rho_g = 22.8 \text{ kg.m}^{-3}$.

The lack of dependence upon injection pressure for global mixing of steady-state evaporative jets is supported by numerous works carried out in this field showing that the spreading angle is almost not affected [12, 39]. In addition to this, some studies focusing on the liquid-phase penetration length showed that this parameter is generally not affected by injection pressure [40]. Other studies available in the literature can support this through modeling of liquid vaporization [32] or combustion experiments concerning flame length of reacting Diesel sprays [41].

The graph presented in figure 6.29 illustrates the evolution of mixture fraction as a function of ambient density and injection pressure for the experimental results finally considered as quantitative.

By grouping the mixing results on a single graph, the influence of ambient density appears clearly, at the same time, the impact of injection pressure on global mixing does not appear as negligible as commented previously. On this graph, the resulting mixture fraction at 25 mm downstream on the centerline seems to increase for lower injection pressures. This difference might be compared to that induced by a change of ambient density as the values are

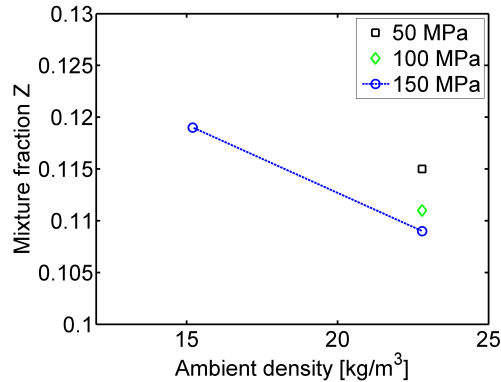


Figure 6.29: Graphical representation of the mixture fraction evolution as a function of ambient density for all injection pressures tested. The values are taken on the centerline at 25 mm from the tip.

somewhat similar. On the other hand, the injection pressure has been changed from 50 to 150 MPa, being a three times variation, while the ambient density has been varied from 15.2 to 22.8 kg/m³, which represents a 50 % increment only. Due to the limited amount of data for evaporative jets, the conclusion is that mixing is dependent upon spray momentum and spreading angle, closely related to ambient density [12]. This is also supported by experiments concerning mixing distribution in gas-jets [42–44] and has already been observed and described for non-vaporizing jets in section 6.3.3. In other words, the entrainment rate of ambient gases plays a major role in the global mixing behavior of sprays, either liquid or gaseous.

6.5 Comparative study of isothermal and evaporative sprays

Due to the physical confines of a real engine, specific facilities have to be built to study the different parameters separately without interferences. This leads to sprays injected in a chamber at room temperature and sometimes even at atmospheric pressure. Under these conditions, a liquid fuel spray is more likely to be non-evaporative and therefore, experimental problems arise when attempting to measure fuel mass fraction for example due to the optical density of the medium (high number density of polydisperse droplets) as seen in chapter 4. In addition, mixing behavior may be different between

a room temperature liquid spray and the same spray injected in high-pressure high-temperature gases. After some distance, the fuel evaporates and the momentum transfer is expected to be different as the densities of the flows are now closer than in a two-phase liquid-gas flow.

At the same time, because of the difficulties encountered when measuring internal features of isothermal liquid sprays, the models are crucial tools to improve the general understandings of sprays. One common hypothesis when building models aiming at predicting development and mixing of sprays/jets is to assume the similarity with gas-jets [20,21,45], although the fuel is injected under non-evaporative conditions. The validity of this assumption is supported by several studies which generally conclude that the theory based upon gas-jet must be adjusted to fit experiments in liquid-phase developing sprays [20,21,46,47]. These corrections are generally empirical and their scientific meaning is sometime unclear and even worse, their value change depending on which physical aspect the study was focusing on.

The last two sections presented the results of development and mixing for sprays injected in cold and inert gases (typically about 293 K), thus avoiding evaporation and, into hot gases (from 900 to 1400 K) to obtain complete vaporization of the spray in about 11 mm. The resulting mixture fraction distributions have been confronted to the predictions of the model proposed by Musculus [10] and demonstrated to provide quantitative data for vaporizing jets. The results of the comparison with the same model concerning liquid isothermal spray measurements did not show similar tendency and the discussion on the radial distribution concluded that Abramovich distribution [15] might not be the most appropriate for liquid sprays. In addition, the mass distribution of liquid sprays showed that values of the Schmidt number below the unity should be used to calibrate the predictions to fit the measurements better as observed by other researchers [24,25].

6.5.1 Spray tip penetration

The macroscopic parameters of sprays represent a starting point to compare the development of evaporative jets and isothermal sprays. The spreading angle of the spray is always hard to define and comparison of tip penetration with empirical expressions showed that the measured opening angle might not be accurate. Even if it has been seen that this parameter was accurately measured by quantitative Rayleigh scattering measurements, this kind of diagnostics is not likely to be used to record spreading angle. On the other hand, com-

mon visualization techniques such as diffused back-illumination or Schlieren demonstrated their lack of accuracy to measure spreading angle. One parameter from a macroscopic point of view appears to be consistent however: spray tip penetration. According to Pickett et al. [33], penetration rate is almost not affected by illumination variation or global sensitivity of the optical system.

A comparison of the spray tip penetration as a function of time for the three ambient density conditions applied to evaporative jets are shown in figure 6.30. Note that the intermediate density case, for $\rho_g = 15.2 \text{ kg/m}^3$, has been added to the test matrix of the isothermal experiments as well. The penetration rate presented here corresponds to a constant injection pressure of 150 MPa, the only variables being ambient density and temperature.

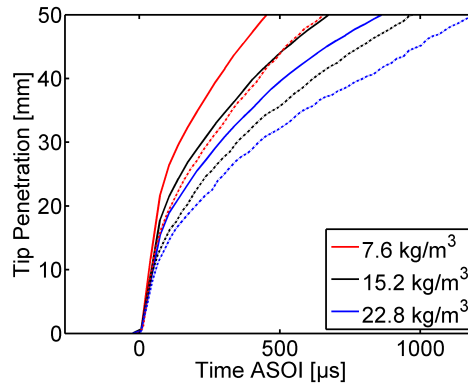


Figure 6.30: Spray tip penetration vs. time at different ambient densities for vaporizing (dashed) and non-vaporizing (solid) sprays. The injection pressure is set to $p_{inj} = 150 \text{ MPa}$.

The evolution in terms of penetration rate whilst changing ambient density has been described earlier and showed to be influenced the same way for both temperature conditions. The important observation concerning these plots resides in the fact that two identical sprays penetrate differently depending on the temperature of the ambient gases in the discharge chamber. The hydraulic of the flow at the outlet is assumed to be really similar as the injection system, i.e. the injector is the same. This means that the momentum flux as well as the mass flow rate exiting the orifice of the single-hole nozzle used in this study should be the same no matter the temperature condition tested. Despite this fact, the penetration rates of liquid sprays are significantly faster than that of vaporizing jets injected into hot gases; although the discharge density, other main parameter for spray development (sec. 2.5.1), remains the same.

It has been presented that the temporal evolution of the penetration distance can be summarized as a function of spray momentum and ambient density (see sec. 2.5.1). Since the momentum flux at the outlet can be assumed to be the same and ambient density is a parameter of the experiments, it can be concluded that the state of the fluid (liquid or gas) influences spray development. Under evaporative conditions, the fuel is already evaporated after approximately 11 mm, corresponding to the liquid length held during these experiments (imposed by Rayleigh measurements). For that reason, the spray can be considered as a gas-jet after complete vaporization and its development would no longer be that of a two-phase flow. The results seem to go in that direction as the penetration rates are close until approximately 10 mm and then the liquid sprays penetrate at higher speed than already evaporated jets.

Further downstream, it looks like the slopes of both penetration rates become more similar, meaning that the behavior of the two different phases gets closer. Therefore, it seems that the developments of the sprays are similar in a first region, when both are liquid (within the liquid length). Then, the isothermal spray penetrates faster in the chamber, even at equivalent ambient density in both testing sections. Finally, both developments appear to become more similar as the liquid tip penetration slows down slightly to apparently match that of the respective evaporative jet. This observation might suggest a difference in terms of momentum transfer between liquid-gas and gas-gas flows; this concept can be developed further thanks to mixing measurements.

6.5.2 Spray opening

The opening of the spray or spreading angle is the other main macroscopic parameter of the spray, on the contrary to penetration which is always dependent upon time, the spreading angle remains quite stable after the constant breakup length of the injected spray [12, 40]. In fact, the spray penetrates in the discharge chamber thanks to the initial momentum flux until the end of injection, after what the inertial forces drag the stream further. This implies that a stabilized spray would keep penetrating in the ambient gases while the spreading angle would be constant. The penetration rate and spreading angle are closely related to air entrainment and thus mixing as it has been observed earlier in this chapter. At the same time, for different injection pressures, penetration rate changes while spreading angle remains quite similar [12, 32, 40] and it has been concluded that the spreading angle was one of the main parameters to control fuel-air mixing distribution.

On the other side, the measure of the spreading angle with regular visualization techniques is not accurate enough to characterize spray opening as it has been repeated several times along this thesis. Penetration rate matching between experiment and predictions may present a great advantage because of its robustness. This methodology demonstrated to provide consistent spreading angles values particularly for evaporative jets; although some reservations have been expressed about isothermal sprays. The resulting spreading angles for steady-state sprays at different ambient densities and injection pressures are provided in figure 6.31, the graph aims at comparing hot and cold conditions.

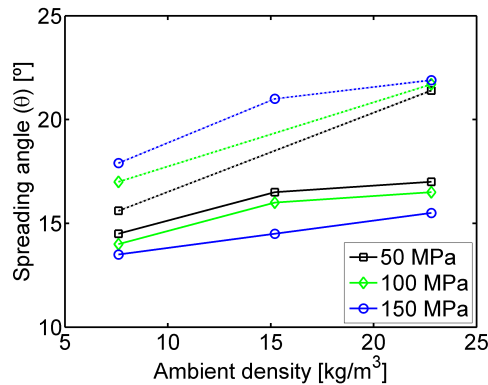


Figure 6.31: Stabilized spreading angle for ambient density from 7.6 to 22.8 $\text{kg}\cdot\text{m}^{-3}$ as a function of injection pressure for vaporizing and non-vaporizing sprays.

The influence of ambient density has already been observed clearly on figures 6.12(a) and 6.23, which means smaller spreading angles at lower ambient density conditions for both evaporative conditions and isothermal. The main difference shown by figure 6.31 is the behavior of the spreading angle with respect to injection pressure. For isothermal sprays, an increase of injection pressure results in narrower sprays (smaller spreading angles). On the contrary, when the fuel is injected under evaporative conditions, the tendency is inverted and jets get wider when injection pressure increases, particularly at low ambient density. It has to be noted that at relatively high ambient density condition (22.8 kg/m^3), the difference on spreading angle are almost not appreciable, even with the sensitivity offered by the Rayleigh scattering diagnostic.

The momentum transfer between liquid droplets and gases may not be considered as complete as when vaporized fuel penetrates into gases as commented

earlier. The density of the liquid droplets is at least 15 times higher than the gas density when the spray is injected under isothermal conditions. This density ratio affects the transfer of the momentum carried by the liquid droplets of the injected stream to the ambient gases in the discharge chamber. The logical conclusion is that the kinetic energy of the droplets is not immediately transferred to the gases surrounding the spray and therefore, the entrainment rate is lower compared to a complete momentum transfer. The consequence is that the penetration of liquid droplets in gases is faster than a gas-gas flow and thus, the spray opens less, leading to smaller steady spreading angles.

A similar explanation can be used to describe that injection pressure produces narrower liquid sprays, while slightly wider under evaporative conditions. In fact, at higher injection pressure, the momentum is higher and the velocity gradient between liquid fuel and ambient gases is higher. As the kinetic energy is not completely transferred, higher gradient may indicate relatively higher momentum in the axial direction, thus resulting in narrower developing sprays.

The incomplete momentum transfer for isothermal sprays can be considered as the main explanation concerning spray opening and development. In such sprays, the fuel stream initially travels inside the chamber in a direction collinear to the orifice of the nozzle. Due to the density of the liquid much higher than that of the ambient gases, less air is entrained. The axial component of the momentum flux is then higher than the radial one and the global mixing must be affected and leads to narrower sprays from a macroscopic point of view.

On the other hand, when the jet is vaporized, the density ratio of the evaporative fuel stream and the ambient gases is close to the unity. This means that the flow can be considered as the mixing of gas into gas and the development of the jets is then more similar to that described by the gas-jet theory.

6.5.3 Mixing of isothermal and evaporative sprays

The differences observed in terms of spreading angle and tip penetration must have a direct impact on global mixing of the sprays whether they are injected under vaporizing conditions or not. With respect to ambient density, both isothermal and evaporative sprays showed that mixture fraction increases with a decrease in discharge density. This has been attributed to spray opening as the momentum and mass flow rate being kept approximately constant. There-

fore, less ambient gas is entrained in the stream, making the mixture more fuel rich as shown in figures 6.19 and 6.27. It has to be noted that considering the macroscopic parameters as a possible explanation of this trend, the air-fuel mixing for the lower density condition ($\rho_g = 7.6 \text{ kg/m}^3$) should go in this direction as well.

Figure 6.32 presents a confrontation of the mixture fraction along the axis of the spray and radially at 25 and 45 mm from the tip for both evaporative and isothermal conditions. The lower density case being considered invalid, only the intermediate ($\rho_g = 15.2 \text{ kg/m}^3$) and the reference ambient densities (22.8 kg/m^3) are presented in this graph. The predictions provided by the model are also plotted (dashed lines) as a reference for the evaporative conditions.

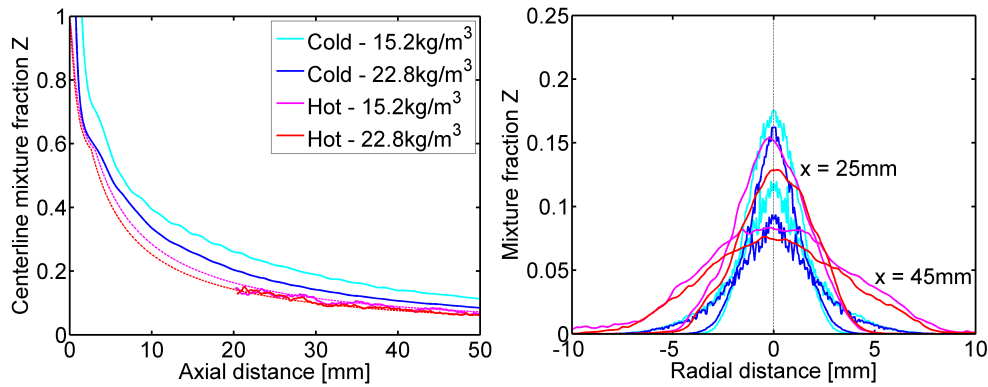


Figure 6.32: Comparison of the mixture fraction on the centerline (left) and radial distribution at 25 and 45 mm from the tip (right) for different ambient densities ($\rho_g = 15.2$ and 22.8 kg.m^{-3} , $p_{inj} = 150 \text{ MPa}$).

All the profiles of the mixture fraction plotted in this figure follow the same trend, however, the difference between vaporizing and non-vaporizing sprays is quite impressive. Sprays injected into relatively cold environment present a more fuel rich mixture on the centerline meaning that a higher mass of fuel is concentrated in the center of the spray. At the same time, the sprays are narrower as suggested by the results concerning spreading angle presented earlier. The penetration rates analyzed previously already showed notable difference between the two ambient conditions and these last results confirm the precedent findings.

Such results support the hypothesis formulated earlier based upon momentum transfer being different for liquid sprays injected into hot conditions compared to isothermal injected sprays. The radial distribution profiles shown in

figure 6.32 support the fact that non-evaporative sprays appear to carry more fuel in the region close to the axis of the spray. This makes sense as the fuel stream exiting the orifice initially goes in the spray axis direction, generally guided by the nozzle hole. This means that the radial component of the momentum flux of the flow should almost be negligible directly at the outlet. Then, as the density ratio between liquid fuel and ambient gases is relatively high, the momentum transfer is not complete and still a large amount of fuel droplets are traveling in the axial direction. This has an obvious impact on the fuel mass fraction which increases in the region close to the spray centerline.

Looking even closer to the results, it appears that the mixing distributions for isothermal and evaporative conditions become more similar at longer distance from the orifice. For example, the relative difference between evaporative and isothermal mixture fraction on the centerline at 45 mm is smaller than that at 25 mm from the tip. It is still quite difficult to appreciate this tendency on the radial profiles as the isothermal sprays are effectively narrower. Going back to the results for isothermal sprays, when special attention is paid on the centerline mixture fraction, it seems that the measured and modeled profiles get closer with the distance (see figures. 6.14, 6.17 and 6.18). One simple and logical explanation for this observation is that the momentum is more completely transferred after a certain distance and the consequence is that both spray developments, evaporative and isothermal, are more similar.

This phenomenon can be explained by the drag efficiency of the droplets traveling in the ambient gases. When a fluid at the liquid state is injected in a chamber containing gases, the liquid core disintegrates or breaks up into liquid ligaments or structures. This first stage called the first breakup has been extensively described in section 2.4.2 as well as the second breakup process representing the small and round droplets generation. Within the first stage of the disintegration process, the liquid structures are traveling at relatively high speed, thus entraining less ambient. During and after the second breakup process, the entrainment rate increases and depending on the conditions, the momentum transfer between liquid droplets and ambient gases may be complete. If this hypothesis is correct, the spray should be narrower at short distance from the orifice, meaning that the spray entrains less ambient gases during the breakup process and as a result, the spreading angle has to be smaller.

Some studies focused on the near-nozzle region to analyze spray breakup process and development mainly in non-evaporative sprays. Most of these works found that the spreading angle in the dense region of the spray (close to

the outlet) was actually smaller than the macroscopic angle corresponding to a fully atomized spray [48–50]. This would mean that the momentum transfer of the liquid spray with the ambient is gradual and can be estimated to be complete only after a certain distance from the nozzle depending upon the operating conditions.

Such tendency has also been observed by Pickett et al. [33] in the case of evaporative jets. In this work, they measured and compared the Full Width Half Maximum (FWHM) rather than spreading angle of the vaporized region of the jet. They observed that the FWHM in the vapor region was fairly linear with respect to distance from the tip. In addition to that, a linear fitting of the experimental FWHM provided a virtual origin of the jet at positive axial distances from the injector. This confirms that the spreading angle must be different near the nozzle, starting with smaller spreading angle that transitions to larger values further downstream.

It has to be added that when comparing the results published on evaporative jets to the non-vaporizing ones, this change in spreading angle is relatively small and may also be the result of the initial breakup of the liquid region not yet vaporized. Rapid calculation returns a change in spreading angle lower than 10 % in all cases for evaporative jets while this value goes up to more than 30 % for some operating conditions in isothermal sprays.

The previous section concerning spreading angle of isothermal and evaporative sprays pointed out the fact that the injection pressure has different effect on spray opening depending on the temperature of the ambient gases (evaporative condition or not). At the same time, the impact of injection pressure on mixing is hard to appreciate as noticed several times earlier in this study. Figure 6.33 compares the mixture fraction axially and radially for 50 and 150 MPa injection pressure at the reference ambient density ($\rho_g = 22.8 \text{ kg/m}^3$).

The predictions of the model are plotted in this graph for the centerline as well (dashed line); as explained earlier, the results from the model are not dependent upon injection pressure because of the closeness of the spreading angle values. According to this graph, the same comments can be made concerning mixing distribution for evaporative jets or not as those already exposed in the respective sections. The very limited influence of injection pressure on mixing is nothing new and has been treated earlier in this chapter for either evaporative or isothermal sprays as well. One important thing must be said nonetheless, the tendency observed on spreading angle cannot be confirmed as the resulting profiles presented in these two plots are too close.

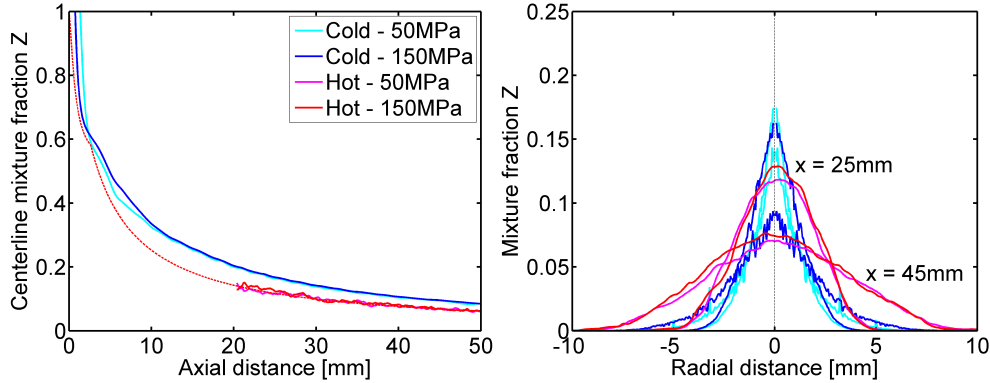


Figure 6.33: Comparison of the mixture fraction on the centerline (left) and radial distribution at 25 and 45 mm from the tip (right) for different injection pressures ($p_{inj} = 50$ and 150 MPa, $\rho_g = 22.8 \text{ kg.m}^{-3}$).

The lack of accuracy of standard visualization techniques like the diffuse back-illumination used to record tip penetration and spreading angle has been repeated all along this study. In addition, the penetration rate matching method used to extract the spreading angle has been proven to be limited in isothermal sprays as the predictions fit the experiments only over a relatively small region. Therefore, care must be taken when looking at spreading angle results for non-evaporative sprays as this value may be valid for a narrow range of spray development. The discussion on the incomplete momentum transfer of the liquid spray with the ambient gases presented earlier confirms that the spray opens differently according to the phase of the breakup process. Following in the same direction, a higher injection pressure induces a higher breakup intensity, which means that the spray is fully atomized at shorter distances from the injector. Consequently, the momentum transfer should be considered as complete within shorter distances as well, thus contradicting the experimental results concerning spreading angle in isothermal sprays.

6.6 Conclusions

The main organ of the injection system, i.e. the injector, has been hydraulically characterized. The internal shape of the nozzle extracted thanks to silicone molding showed that such features should ensure high discharge efficiency due to relatively large entrance radius and orifice convergence. Measurement of the steady mass flow rate confirmed the results concerning internal geometry as

the resulting discharge coefficient is close to 0.9, this value being higher than the manufacturer's specifications. Mass flow rate coupled with momentum flux measurements demonstrated that the nozzle used in this study does not cavitate under the operating conditions applied. These two measurements also provide additional characteristics such as effective velocity of the flow at the outlet as well as effective area or diameter of the orifice.

Direct visualization of the back-illuminated sprays injected under isothermal conditions showed the influence of ambient density on development rather than the effect of injection pressure. Thanks to the model, the spreading angle of the sprays have been adjusted through penetration matching due to the lack of accuracy of boundary detection on the edges. Nevertheless, the predicted penetration behaves somewhat differently with a slower penetration rate at the beginning and then a faster one, meaning that the development of isothermal sprays is not correctly predicted by the simulation. This led to discuss the distribution profile of such sprays because of a mismatch between gas-jet model predictions and experiments. It has been showed that the distribution profile proposed by Abramovich and successful in vaporized jets did not fit non-evaporative distribution profiles. In addition, the momentum transfer between liquid droplets and ambient gases may not be complete, thus conducting to values of the Schmidt number below the unity. As expected, the impact of ambient density on 2-D mixing results has been observed to be quite important; whereas, it is not the case concerning injection pressure.

Spray tip penetration of vaporizing jets has been recorded through high-speed Schlieren imaging. The results concerning spreading angle showed large deviation when compared to the values measured Rayleigh scattering maps, meaning that boundary detection can be an issue when applying Schlieren technique in evaporative jets. However, good agreement on spreading angle has been found when penetration rate was matched by the predictions of the model. When confronted to the model, both the axial and radial distribution profiles presented high level of similarity except for the lower density case. Fuel decomposition due to high temperature must explain lower mixture fraction; as a matter of fact, fuel break down makes the equivalent Rayleigh cross-section of the lower alkanes to be smaller, hence reducing scattered intensity. The effect of ambient density on mixing of evaporative jets has been pointed out, along with almost no influence of injection pressure.

The comparison of sprays injected in ambient and hot temperature conditions showed significant difference on development, as highlighted by the

respective penetration rates. The general behavior is that isothermal sprays penetrate faster than vaporizing jets. Looking closer, the development of sprays for both conditions get closer after some time, once momentum transfer between droplet and ambient is assumed to be more complete. As regards spreading angle, similar physical process may explain the differences observed as the momentum transfer is not complete until some distances far away from the outlet. Non-evaporative sprays are narrower than vaporizing jets; this is balanced by faster penetration as suggested by same momentum flux. Sprays injected into isothermal environment are more fuel rich due to incomplete momentum transfer inducing lower entrainment rate of the ambient gases. The similarity of isothermal and evaporative sprays at longer distances from the tip also appears on global mixing fields as supported by spreading angle evolution with axial distance.

Bibliography

- [1] E.N. Balles and J.B. Heywood. Fuel-air mixing and Diesel combustion in a rapid compression machine. *Society of Automotive Engineers international congress and exposition, Detroit, MI, USA*, 1988.
- [2] R. Payri, J.M. Garcia, F.J. Salvador, and J. Gimeno. Using spray momentum flux measurements to understand the influence of diesel nozzle geometry on spray characteristics. *Fuel*, 84(5):551–561, 2005.
- [3] V. Macián, V. Bermudez, R. Payri, and J. Gimeno. New technique for determination of internal geometry of a diesel nozzle with the use of silicone methodology. *Experimental Techniques*, 27(2):39–43, 2003.
- [4] O. Reynolds. An experimental investigation of the circumstances which determine whether the motion of water shall be direct or sinuous, and of the law of resistance in parallel channels. *Philosophical Transactions of the Royal Society of London*, 174:935–982, 1883.
- [5] A. K. Lichtarowicz, R. K. Duggins, and E. Markland. Discharge coefficients for incompressible non-cavitating flow through long orifices. *Journal of Mechanical Engineering and Science*, 7(2):210–219, 1965.
- [6] T.A. Fox and J. Stark. Discharge coefficients for miniature fuel injectors. *Proc. Inst. Mech Engrs*, 203:75–78, 1989.

-
- [7] C. von Kuensberg Sarre, S.C. Kong, and R. Reitz. Modeling the effects of injector nozzle geometry on diesel sprays. *SAE Paper 1999-01-0912*, 1999.
- [8] Jaime Gimeno. *Desarrollo y aplicacion de la medida del flujo de cantidad de movimiento de un chorro Diesel*. PhD thesis, E.T.S. Ingenieros Industriales. Universidad Politécnica de Valencia, 2008.
- [9] J. Rotta. Experimenteller beitrag zur entstehung turbulenter strömung im rohr. *Ingenieur-Archiv*, 24(4):258–281, 1956.
- [10] M.P.B. Musculus. Entrainment waves in decelerating transient turbulent jets. *Journal of Fluid Mechanics*, 638:117–140, 2009.
- [11] H. Hiroyasu, M. Arai, and M. Shimizu. Break-up length of a liquid jet and internal flow in a nozzle. *ICLASS 1991, Gaithersburg, Maryland*, 1991.
- [12] J. Naber and D. Siebers. Effects of gas density and vaporization on penetration and dispersion of diesel sprays. *SAE Paper 960034*, 1996.
- [13] R. Payri, F.J. Salvador, J. Gimeno, and V. Soare. Determination of diesel sprays characteristics in real engine in-cylinder air density and pressure conditions. *Journal Of Mechanical Science And Technology*, 19(11):2040–2052, 2005.
- [14] H. Hiroyasu and M. Arai. Structures of fuel spray in Diesel engines. *SAE Paper 900475*, 1990.
- [15] G.N. Abramovich. The theory of turbulent jets. *MIT Press, Cambridge, Massachusetts*, 1963.
- [16] J.O. Hinze. Turbulence: an introduction to its mechanism and theory. *McGraw-Hill, New York*, 162, 1959.
- [17] D.B. Spalding. Combustion and mass transfer. *Pergamon international library of science, technology, engineering, and social studies*, 1979.
- [18] H. Schlichting. Boundary layer theory. *McGraw-Hill, Series in Mechanical Engineering*, 1979.
- [19] David Correas. *Estudio teórico-experimental del chorro libre Diesel isoterma*. PhD thesis, E.T.S. Ingenieros Industriales. Universidad Politécnica de Valencia, Valencia, 1998.

- [20] J.M. Desantes, R. Payri, F.J. Salvador, and A. Gil. Development and validation of a theoretical model for diesel spray penetration. *Fuel*, 85(7-8):910–917, 2005.
- [21] J.M. Desantes, R. Payri, F.J. Salvador, and A. Gil. Deduction and validation of a theoretical model for a free Diesel spray. *Fuel*, 85:910–917, 2006.
- [22] J.M. Desantes, R. Payri, J.M. Garcia, and F.J. Salvador. A contribution to the understanding of isothermal Diesel spray dynamics. *Fuel*, 86(7-8):1093–1101, 2007.
- [23] R. Payri, B. Tormos, F.J. Salvador, and L. Araneo. Spray droplet velocity characterization for convergent nozzles with three different diameters. *Fuel*, 87(15-16):3176–3182, 2008.
- [24] C.M.V. Prasad and S. Kar. An investigation on the diffusion of momentum and mass of fuel in a diesel fuel spray. *ASME J. Eng. Power*, pages 1–11, 1976.
- [25] J.M. Desantes, F.J. Salvador, J.J. Lopez, and J. De la Morena. Study of mass and momentum transfer in Diesel sprays based on X-ray mass distribution measurements and on a theoretical derivation. *Experiments in Fluids*, pages 1–14, 2010.
- [26] P. Hay and P.L. Jones. Comparison of the various correlations for spray penetration. *SAE Paper 720776*, 1972.
- [27] J.C. Dent. A basis for comparison of various experimental methods for studying spray penetration. *SAE Paper 710571*, 1971.
- [28] W. Bergwerk. Flow pattern in Diesel nozzle spray holes. *Proc. Inst. Mech. Engrs*, 173, n. 25., 1959.
- [29] W. H. Nurick. Orifice cavitation and its effects on spray mixing. *Journal of fluids engineering*, 98:681–687, 1976.
- [30] A. Barrero and M. Perez-Saborid. Fundamentos y aplicaciones de la mecanica de fluidos. *McGraw-Hill Interamericana de España*, 2005.
- [31] Sjoerd Hermens. *Influence of Diesel injector nozzle geometry on the injection and combustion process*. PhD thesis, E.T.S. Ingenieros Industriales. Universidad Politécnica de Valencia, Valencia, 2007.

-
- [32] D.L. Siebers. Scaling liquid-phase fuel penetration in diesel sprays based on mixing-limited vaporization. *SAE Paper 1999-01-0528*, 1999.
- [33] L. Pickett, J. Manin, C.L. Genzale, D.L. Siebers, M.P.M. Musculus, and Idicheria C.A. Relationship between diesel fuel spray vapor penetration/dispersion and local fuel mixture fraction. *SAE Paper 2011-01-0686*, SAE International Journal of Engines, 2011.
- [34] C. Schulz and V. Sick. Tracer-LIF diagnostics: quantitative measurement of fuel concentration, temperature and fuel/air ratio in practical combustion systems. *Progress in Energy and Combustion Science*, 31(1):75–121, 2005.
- [35] A. Adam, P. Leick, G. Bittlinger, and C. Schulz. Visualization of the evaporation of a Diesel spray using combined mie and rayleigh scattering techniques. *Experiments in fluids*, 47(3):439–449, 2009.
- [36] J.E. Broadwell and A.E. Lutz. A turbulent jet chemical reaction model: Nox production in jet flames. *Combustion and Flame*, 114(3-4):319–335, 1998.
- [37] L.M. Pickett, J.A. Caton, M.P.B. Musculus, and A.E. Lutz. Evaluation of the equivalence ratio-temperature region of diesel soot precursor formation using a two-stage lagrangian model. *International Journal of Engine Research*, 7(5):349–370, 2006.
- [38] C.S. McEnally, D.M. Ciuparu, and L.D. Pfefferle. Experimental study of fuel decomposition and hydrocarbon growth processes for practical fuel components: heptanes. *Combustion and Flame*, 134(4):339–353, 2003.
- [39] J. Arrègle, J.V. Pastor, and S. Ruiz. Influence of the injection parameters on Diesel spray characteristics. *SAE Paper 1999-01-0200*, 1999.
- [40] D.L. Siebers. Liquid-phase fuel penetration in diesel sprays. *SAE Transaction*, 107:1205–1227, 1998.
- [41] L.M. Pickett and D.L. Siebers. Soot in diesel fuel jets: effects of ambient temperature, ambient density, and injection pressure. *Combustion and Flame*, 138(1-2):114–135, 2004.
- [42] H.A. Becker, H.C. Hottel, and G.C. Williams. The nozzle-fluid concentration field of the round, turbulent, free jet. *Journal of Fluid Mechanics*, 30(02):285–303, 1967.

- [43] A.D. Birch, D.R. Brown, M.G. Dodson, and J.R. Thomas. The turbulent concentration field of a methane jet. *Journal of Fluid Mechanics*, 88(03):431–449, 1978.
- [44] A.D. Birch, D.R. Brown, M.G. Dodson, and F. Swaffield. The structure and concentration decay of high pressure jets of natural gas. *Combustion Science and technology*, 36(5):249–261, 1984.
- [45] J.M. Desantes, J. Arrègle, and P.J. Rodríguez. Computational model for simulation of Diesel injection systems. *SAE Paper 1999-01-0915*, 1999.
- [46] J.V. Pastor, J.J. Lopez, J.E. Juliá, and J.V. Benajes. Planar laser-induced fluorescence fuel concentration measurements in isothermal diesel sprays. *Optics Express*, 10(7):309–323, 2002.
- [47] J.V. Pastor, R. Payri, L. Araneo, and J. Manin. Correction method for droplet sizing by laser-induced fluorescence in a controlled test situation. *Optical Engineering*, 48:013601, 2009.
- [48] R. Reitz and F. Bracco. On the dependence of spray angle and other spray parameters on nozzle design and operating conditions. *SAE Paper 790494*, 1979.
- [49] C. Heimgartner. Investigation of the primary spray breakup close to the nozzle of a common-rail high-pressure Diesel injection system. 2000.
- [50] A.L. Kastengren, C.F. Powell, Y. Wang, K.S. Im, and J. Wang. X-ray radiography measurements of diesel spray structure at engine-like ambient density. *Atomization and Sprays*, 19(11):1031–1044, 2009.

Chapter 7

Conclusions and further developments

Contents

7.1	Conclusions	272
7.2	Suggestions for future works	276

This chapter aims at drawing the main conclusions with respect to the work carried out along this thesis. Individual conclusions have been redacted at the end of every chapters, from the development of sprays to the comparison of the global mixing process in both evaporative and isothermal sprays. The following conclusion addresses the objective of this work, which is to study and analyze the air-fuel mixing as well as the influence of experimental parameters, from a general point of view.

The last section of this document proposes a summary of the potential developments in order to improve the quality of the results obtained and presented in this thesis. The limitations concerning measurements of isothermal sprays from a quantitative point of view are treated first leading to the possibility of introducing other diagnostic techniques. Finally, different ways to help modelers to possibly improve their codes are presented as CFD has become a major part of the works applied to study injection and combustion process.

7.1 Conclusions

Along this work, it has been observed that a large amount of equipments and technical solutions must be used to achieve a complete and robust study. The field approached in this thesis, i.e. the injection and mixing processes of liquid sprays in cold and hot environments have been studied for decades and improving the knowledge requires conscientious work and specific installations. The different diagnostics applied provided important information, from the commonly used rate of injection measurement to the state-of-the-art planar structured illumination. All these experimental techniques allowed performing solid studies concerning such a fast and complex process as spray disintegration and vaporization. It has to be added also that the setup and calibration of these equipments are the result of years of development in experimental diagnostics and every contribution represents great support to the general scientific knowledge.

The numerous stages necessary to achieve the present work provided support to the scientific community either from a technical point of view, through the implementation of a new measurement technique and the improvement of the another; or from a scientific approach with the face-to-face comparison between global mixing behavior of liquid and vaporized sprays. A summary of the general results obtained along this work is presented in this section together with the main contributions to science.

A complete hydraulic characterization has been performed to better understand the flow at the outlet as its properties mainly drive the disintegration process and spray development when injected in a constant discharge environment. Rate of injection together with spray momentum provided information concerning the behavior of the flow as well as the hydraulic parameters of the global injection system; mainly represented by the injector or even the nozzle itself. These measurements showed that the flow was not cavitating under all the experimental conditions and that the hydraulic characteristics were in agreement with the internal geometry measurements performed.

The study of the propagation of light in a controlled environment designed in order to simulate the radiation of light within an optically dense medium showed that the conventional planar laser imaging techniques were very limited for measurements in isothermal Diesel sprays. The anisotropy of the light scattered by such small liquid droplets led to results of the qualitative kind

only when coupled to the high number density of such medium. This dense droplet population encountered in the center of a Diesel spray produces high extinction of light that strongly affects the acquired signals. By applying the Planar Droplet Sizing technique to this testing situation, it has been observed that the propagation of light through Mie scattering and fluorescence was not similar enough to overcome multiple scattering and light extinction issues.

At the same time, a technique based on spatially modulated incident light and inspired by the recently developed Structured Laser Illumination Planar Imaging (SLIPI) has been developed to remove the multiply scattered light. By assuming that the photons that have experienced several scattering events loses the incident modulation of light, the structural information recorded by the acquisition system therefore only presents the singly scattered signal. The envelope of the resulting signal re-built through computer-assisted post-processing represents the signal scattered or emitted (depending on the scattering process: Mie or LIF) by the illuminated plane only. Finally, a three-dimensional extinction evaluation of the spray permits to evaluate the optical depth between the acquisition system and any plane within the spray in two dimensions.

This experimental solution demonstrated its capability to provide quantitative results when applying the Planar Droplet Sizing technique by making the ratio of the LIF and Mie scatter signals extracted from SPLI-2P experiments. The consistency of the signals recorded at different positions within the medium showed relatively high accuracy and precision for both Mie and LIF scattering processes. From the intensity signals along the laser path, the number density has been extracted through the Beer-Lambert law of extinction. The results showed to be more convincing when using the fluorescent emission as it does not suffer from anisotropy of the output radiation like Mie scattering.

The preliminary studies concerning the fluorescent dye to be mixed with the n-dodecane fuel used in this work led to select the Sulfo-rhodamine B. This choice has been partly driven by the equipment available in the laboratory such as light source (Nd:YAG laser) and absorption spectrum matching, but also because of the characteristics of this fluorescent dopant. An analysis of the fluorescent properties has been carried out to understand how to better use the Sulfo-rhodamine B. The measurements showed high quantum yield when dissolved into n-dodecane; in addition, the absorption and emission spectra helped to arrange the optical equipment through correct spectral filtering.

An evaluation of the parameters influencing the accuracy of the results

obtained through Planar Droplet Sizing has been done. The square and cubic dependencies with droplet diameter of the scattered light and fluorescent emission intensities, respectively, affect the resulting two-dimensional Sauter Mean Diameter maps quantitatively. With an appropriate choice of dye quantity added to the fuel, these two parameters showed good agreement with the theoretical values, thus providing valid experimental results thanks to the SPLI-2P technique.

A criterion concerning the accuracy and precision of the results limited the two-dimensional measurements under non-evaporative conditions to half a spray. The high extinction of light from side-to-side ($\tau \approx 10$) made the acquired signal to be dramatically weak quickly after the axis of the spray. This is consistent with the results provided by the fluorescent particle measurements as the results started to decrease significantly for optical depth values in the range $4 \leq \tau \leq 6$.

The confrontation of the two-dimensional 2-D droplet size distribution obtained through LIF/Mie ratio of the SPLI-2P signals with spray mapping via a phase Doppler instrument demonstrated the consistency of the results. The ratio of both the elastic scattered light and the fluorescent emission provided lower droplet diameter than that provided by the PDPA instrument for locations closer to the center of the spray. Known for being optically denser, the capability of the phase Doppler technique in this region has been pointed out to be limited.

The extinction of light between the illumination plane and the acquisition system being sparse, a mapping of the spray in the laser-sheet - CCD direction has been performed to evaluate this parameter. From this, the two maps of number density and droplet diameter have been grouped to extract two-dimensional results of mixing distributions. When compared to a validated mixing model, the results showed good agreement, particularly concerning the mean mixture fraction along spray axis.

The results provided by the Structured Planar Laser Imaging technique demonstrated that the isothermal sprays presents a higher fuel concentration in the center than the predictions of the model when applying widely used distribution profiles. The explanation is that the momentum transfer between liquid droplets and ambient gases is not complete, thus making the axial forces higher than the radial ones, leading to a narrower fuel distribution profile. This means that the distribution of liquid penetrating sprays presents values of the Schmidt number below the unity as suggested by other experimental observations.

Concerning quantitative measurements within the vapor-phase region of the jet, the Planar Laser Rayleigh Scattering technique has been implemented to obtain two-dimensional results to compare the global mixing of evaporative jets to those injected in relatively cold ambient gases. A methodology to calculate the Rayleigh cross-section has been developed. This parameter, which strongly affects the accuracy of the measurements, has been computed through the molar refractivity of the fuel molecule to extract the refractive index. Due to the anisotropy of the linear alkane chain of the n-dodecane, the King correction factor F_K has also been calculated. This deep evaluation of the parameters influencing the Rayleigh cross-section led to obtain a highly accurate value.

The calibration of the Rayleigh scattered signal with the intensity of the ambient gases permits direct relationship and high SNR of the fuel concentration measurements. Together with the correct Rayleigh cross-section, the assumption of adiabatic mixing represents the best possible condition to perform accurate quantitative measurements.

Adequate post-processing of the images, specific hardware design as well as the implementation of image editing algorithm such as inpainting or 2-D median filtering considerably improved the quality of the measurements.

The two-dimensional maps of mixture fraction extracted from the PLRS technique showed to provide accurate measurements of the macroscopic parameters due to the high sensitivity on the edges. Spreading angle has been extracted from the individual 2-D mixing maps and the confrontation of the adjusted model predictions demonstrated the accuracy and precision of the diagnostic for vapor-phase measurements. A map of global adiabatic mixing temperature has also been extracted from the results of the Rayleigh scattering technique and presents additional useful information concerning air-fuel mixing.

Some limitations have been pointed out during the experiments: beam steering issues at elevated density and break down of the fuel molecule at high temperature. The first one limited the range of experimental conditions to evaluate their influence on mixing; while the second one discarded the measurements performed at lower ambient density as it has been chosen to keep the liquid length constant.

The application of the numerous experimental techniques described in this document or developed in this work provided useful information concerning the mixing process of sprays. The influence of ambient density has been evaluated

for both temperature conditions: evaporative and isothermal. The conclusion is that the discharge density qualitatively affects spray development and mixing in the same way no matter the state of the fluid to be mixed. Higher ambient densities make the spray to open more as a result of slower penetration, therefore bettering air entrainment and reducing global mixture fraction.

On the other hand, even if the influence of injection pressure on global mixing has been observed to be quite limited, the following comment has to be made, that the spreading angle of isothermal sprays presents an opposite tendency to that of vaporizing ones. This is explained by the fact that the droplets travel faster at higher injection pressure, inducing higher momentum in the axial direction due to incomplete kinetic energy transfer and thus producing narrower sprays.

The comparison of sprays injected under evaporative and non-evaporative conditions showed significant differences in terms of development and mixing. The faster penetration rate of isothermal sprays demonstrated to provide narrower global distributions with a higher fuel concentration near the central axis. This is a direct consequence of incomplete momentum transfer between traveling liquid droplets and steady ambient gases on the contrary to vapor-phase penetrating jets.

As the momentum flux at the outlet is assumed to be the same, these observations are in line with the physics of spray development and mixing. The consequence is that the application of models based upon the gas-jet theory and assuming complete momentum transfer simply fail at predicting global mixing of isothermal liquid sprays, whereas successful model-experiments confrontation has been observed for evaporative jets.

7.2 Suggestions for future works

The mechanisms that influence mixing of injected sprays with the surrounding environment are complex and so far not fully identified or understood. The main objective of the present work was to evaluate and analyze the behavior of sprays that mix with ambient gases at hot or cold temperature conditions. Due to the complexity of the mixing process and the limitations of the experimental techniques, there still remain much scope for research in completing the description of global mixing process in the field of Diesel sprays.

From an experimental approach, the technique developed in this work to evaluate the mixture fraction of isothermal sprays can be improved:

- It has been seen that the solution proposed here which only uses two phases instead of three was less sensitive to mis-shifting of the signals. On the other hand, the reconstruction of the envelope of the signal requires longer computer time than the original Structured Laser Illumination Planar Imaging (SLIPI) technique.
- Another fluorescent dye may be used to dope the fuel as the Sulforhodamine B added to the n-dodecane did required the addition of other components, thus increasing difficulty and instability of the mix. Pyrromethene seems to present great potential to be mixed with hydrocarbons such as Diesel fuels for its capability to be dissolved directly in them.
- A step forward would be to apply the SPLI-2P technique to the liquid region of evaporating sprays. As this technique relies on light extinction along the laser path of both Mie scattering and fluorescent emission, the elastically scattered light can be used to extract approximated results. The issues arising from temperature dependency of the fluorescent signal may be higher than the error induced by the anisotropy of the Mie scattered light.
- Another technological solution to analyze the liquid region could improve the general knowledge in this field. One that particularly proved to perform well in liquid sprays is the X-Ray tomography. A similar study with such an impressive and rare facility to evaluate the robustness of the SPLI-2P technique or just to provide quantitative results would represent useful information to the scientific community.

Some improvements can also be done concerning the measurements of evaporative jets, such as:

- The limitations of the high pressure, high temperature facility used in this work mainly concern the frequency of the experiments due to the pre-burn process to reach the desired environmental conditions at the time of injection. A solution to reduce spatial beam steering would also make the quality of the results higher, for example with a double glazing windows to decrease local temperature gradients.
- To increase the level of accuracy of the diagnostic, the Rayleigh cross-section of the fuel molecule could be directly measured thanks to the technique of the cavity ring-down spectroscopy (CRDS) commonly used for this kind of measurements.

From a general point of view, using different geometry of injector (nozzle) could also present great support to Science. This enters in the scope of changing the parameters to obtain a range of conditions in order to evaluate their influence. All this work is of major interest for modelers as they generally have to empirically adjust their code to fit the experiments. A larger amount of experimental conditions, as long as the results are consistent between each other would carry more information to modelers and by such, a potential improvement of the predictions.

Following the same philosophy, the results presented in this thesis clearly demonstrated the present models to fail at predicting liquid development and mixing processes. Therefore, a study of the momentum transfer between liquid droplets and ambient gases also presents a huge interest to improve model predictions for liquid penetrating sprays.

Bibliography

- [1] G.N. Abramovich. The theory of turbulent jets. *MIT Press, Cambridge, Massachusetts*, 1963.
- [2] A. Adam, P. Leick, G. Bittlinger, and C. Schulz. Visualization of the evaporation of a Diesel spray using combined mie and rayleigh scattering techniques. *Experiments in fluids*, 47(3):439–449, 2009.
- [3] S.A. Ahmed, Z.W. Zang, K.M. Yoo, M.A. Ali, and R.R. Alfano. Effect of multiple light scattering and self-absorption on the fluorescence and excitation spectra of dyes in random media. *Applied Optics*, 33(13):2746–2750, 1994.
- [4] P. Andresen, G. Meijer, H. Schluter, H. Voges, A. Koch, W. Hentschel, W. Oppermann, and E. Rothe. Fluorescence imaging inside an internal combustion engine using tunable excimer lasers. *Applied Optics*, 29(16):2392–2404, 1990.
- [5] V.S. Antonov and K.L. Hohla. Dye stability under excimer-laser pumping. *Applied Physics B: Lasers and Optics*, 30(3):109–116, 1983.
- [6] M. Arai, M. Shimizu, and H. Hiroyasu. Similarity between the breakup lengths of a high speed liquid jet in atmospheric and pressurized conditions. *ICLASS 1991, Gaithersburg, Maryland*, 1991.
- [7] M. Arai, M. Tabata, and M. Shimizu. Disintegrating process and spray characterization of fuel jet injected by a Diesel nozzle. *SAE Paper 840275*, 1984.
- [8] L. Araneo and R. Payri. Experimental quantification of the planar droplet sizing technique error for micro-metric mono-dispersed spherical particles. *ILASS Conference, Como lake, Italy*, 2008.

-
- [9] L. Araneo, V. Soare, R. Payri, and J. Shakal. Setting up a PDPA system for measurements in a Diesel spray. *Journal of Physics: Conference Series*, 45:85, 2006.
- [10] C. Arcoumanis, M. Badami, H. Flora, and M. Gavaises. Cavitation in real-size multi-hole Diesel injector nozzles. *SAE Paper 2000-01-1249*, 2000.
- [11] C. Arcoumanis, H. Flora, M. Gavaises, N. Kampanis, and R. Horrocks. Investigation of cavitation in a vertical multi-hole Diesel injector. *SAE Paper 1999-01-0524*, 1999.
- [12] A. Arnold, F. Dinkelacker, T. Heitzmann, P. Monkhouse, M. Schafer, V. Sick, J. Wolfrum, W. Hentschel, and K.P. Schindler. DI Diesel engine combustion visualized by combined laser techniques. *Symposium (International) on Combustion*, 24(1):1605–1612, 1992.
- [13] J. Arrègle, J.V. Pastor, and S. Ruiz. Influence of the injection parameters on Diesel spray characteristics. *SAE Paper 1999-01-0200*, 1999.
- [14] W.D. Bachalo and M.J. Houser. Development of the phase/doppler spray analyzer for liquid drop size and velocity characterizations. *AIAA, SAE, and ASME, Joint Propulsion Conference, Cincinnati, OH*, 1984.
- [15] C. Badock, R. Wirth, A. Fath, and A. Leipertz. Investigation of cavitation in real size Diesel injection nozzles. *International Journal of Heat and Fluid Flow*, 20(5):538–544, 1999.
- [16] E.N. Balles and J.B. Heywood. Fuel-air mixing and Diesel combustion in a rapid compression machine. *Society of Automotive Engineers international congress and exposition, Detroit, MI, USA*, 1988.
- [17] M.D. Barnes, W.B. Whitten, and J.M. Ramsey. Enhanced fluorescence yields through cavity quantum-electrodynamic effects in microdroplets. *Journal of the Optical Society of America B*, 11(7):1297–1304, 1994.
- [18] A. Barrero and M. Perez-Saborid. Fundamentos y aplicaciones de la mecanica de fluidos. *McGraw-Hill Interamericana de España*, 2005.
- [19] H.A. Becker, H.C. Hottel, and G.C. Williams. The nozzle-fluid concentration field of the round, turbulent, free jet. *Journal of Fluid Mechanics*, 30(02):285–303, 1967.

- [20] A. Beer. Bestimmung der absorption des rothen lichts in farbigen flüssigkeiten. *Annalen der Physik und Chemie*, 86(2), 1852.
- [21] M. Berckmuller, N.P. Tait, D. Lockett, D.A. Greenhalgh, K. Ishii, Y. Urata, H. Umiyama, and K. Yoshida. In-cylinder crank-angle-resolved imaging of fuel concentration in a firing spark-ignition engine using planar laser-induced fluorescence. *Symposium (International) on Combustion*, 25(1):151–156, 1994.
- [22] F. Beretta, A. Cavaliere, and A. D'alessio. Ensemble laser light scattering diagnostics for the study of fuel sprays in isothermal and burning conditions. *Symposium (International) on Combustion*, 20(1):1249–1258, 1985.
- [23] F. Beretta, A. Cavaliere, and D. D'alessio. Drop size and concentration in a spray by sideward laser light scattering measurements. *Combustion Science and Technology*, 36(1):19–37, 1984.
- [24] W. Bergwerk. Flow pattern in Diesel nozzle spray holes. *Proc. Inst. Mech. Engrs*, 173, n. 25., 1959.
- [25] A. Berrocal, R. Wellander, and E. Kristensson. Accounting for multiple scattering signal attenuation and laser extinction using structured laser illumination planar imaging. *ILASS Conference, Brno, Czech Republic*, 2010.
- [26] E. Berrocal, E. Kristensson, M. Richter, M. Linne, and M. Aldèn. Application of structured illumination for multiple scattering suppression in planar laser imaging of dense sprays. *Optics Express*, 16:17870–17881, 2008.
- [27] E. Berrocal, E. Kristensson, D. Sedarsky, and M. Linne. Analysis of the slipi technique for multiple scattering suppression in planar imaging of fuel sprays. *ICLASS 2009, Vail, Colorado, USA*, 2009.
- [28] E. Berrocal, I. Meglinski, and M. Jermy. New model for light propagation in highly inhomogeneous polydisperse turbid media with applications in spray diagnostics. *Optics Express*, 13:9181–9195, 2005.
- [29] E. Berrocal, D.L. Sedarsky, M.E. Paciaroni, I.V. Meglinski, and M.A. Linne. Laser light scattering in turbid media part II: Spatial and temporal analysis of individual scattering orders via monte carlo simulation. *Optics Express*, 17(16):13792–13809, 2009.

-
- [30] A.D. Birch, D.R. Brown, M.G. Dodson, and F. Swaffield. The structure and concentration decay of high pressure jets of natural gas. *Combustion Science and technology*, 36(5):249–261, 1984.
- [31] A.D. Birch, D.R. Brown, M.G. Dodson, and J.R. Thomas. The turbulent concentration field of a methane jet. *Journal of Fluid Mechanics*, 88(03):431–449, 1978.
- [32] M. Blessing, G. König, C. Krüger, U. Michels, and V. Schwarz. Analysis of flow and cavitation phenomena in Diesel injection nozzles and its effects on spray and mixture formation. *SAE Paper 2003-01-1358*, 2003.
- [33] J. Bode, H. Chaves, W. Hentschel, A. Kubitzek, F. Obermeier, K. Schindler, and T. Schneider. Fuel spray in Diesel engines. part I: Spray formation. *ATA 92A065*, 1992.
- [34] DC Bogue. Entrance effects and prediction of turbulence in non-newtonian flow. *Industrial & Engineering Chemistry*, 51(7):874–878, 1959.
- [35] C.F. Bohren and D.R. Huffman. Absorption and scattering of light by small particles. *Wiley-Interscience, New York*, 1983.
- [36] M. Born and E. Wolf. Principles of optics. *Pergamon press, Oxford*, 1975.
- [37] W. Bosch. Fuel rate indicator is a new measuring instrument for display of the characteristics of individual injection. *SAE Paper 660749*, 1966.
- [38] C.J.F. Bottcher, O.C. Van Belle, P. Bordewijk, A. Rip, and D.D. Yue. Theory of electric polarization. *Journal of The Electrochemical Society*, 121:211C, 1974.
- [39] U. Brackmann. Lambdachrome laser dyes - 3rd edition. *LambdaPhysik*, 2000.
- [40] T. Breuninger, K. Greger, and E.H.K. Stelzer. Lateral modulation boosts image quality in single plane illumination fluorescence microscopy. *Optics letters*, 32(13):1938–1940, 2007.
- [41] J.E. Broadwell and A.E. Lutz. A turbulent jet chemical reaction model: Nox production in jet flames. *Combustion and Flame*, 114(3-4):319–335, 1998.

- [42] M. Broyer, J. Chevalleyre, G. Delacretaz, and L. Woste. CVL-pumped dye laser for spectroscopic application. *Applied Physics B: Lasers and Optics*, 35(1):31–36, 1984.
- [43] E. Buckingham. Model experiments and the form of empirical equations. *Trans. ASME*, 37:263, 1915.
- [44] A. Calatayud, V.I. Deltoro, E. Barreno, and S. Valle-Tascon. Changes in in vivo chlorophyll fluorescence quenching in lichen thalli as a function of water content and suggestion of zeaxanthin-associated photoprotection. *Physiologia Plantarum*, 101(1):93–102, 1997.
- [45] J.M. Char, K.K. Kuo, and K.C. Hsieh. Observations of breakup processes of liquid jets using real-time X-ray radiography. *Journal of Propulsion and Power*, 6:544–551, 1990.
- [46] H. Chaves, C. Kirmse, and F. Obermeier. Velocity measurements of dense Diesel fuel sprays in dense air. *Atomization and sprays*, 14(6):589–609, 2004.
- [47] H. Chaves, M. Knapp, A. Kubitzek, and F. Obermeier. Experimental study of cavitation in the nozzle hole of Diesel injectors using transparent nozzles. *SAE Paper 950290*, 1995.
- [48] G. Chen, M. Mazumder, R.K. Chang, J.C. Swindal, and W.P. Acker. Laser diagnostics for droplet characterization: application of morphology dependent resonances. *Progress in Energy and Combustion Science*, 22(2):163–188, 1996.
- [49] N. Chigier. Combustion measurements. *Hemisphere Publishing Corporation*, 1991.
- [50] N. Chinzei, G. Masuya, T. Komuro, A. Murakami, and K. Kudou. Spreading of two-stream supersonic turbulent mixing layers. *Physics of Fluids*, 29:1345, 1986.
- [51] W.H. Chou, L.P. Hsiang, and G.M. Faeth. Temporal properties of drop breakup in the shear breakup regime. *International Journal of Multiphase Flow*, 23(4):651–669, 1997.
- [52] C. Clement and P. Bothorel. Etude de l’anisotropie optique moléculaire d’alcanes normaux, ramifiés et halogènes. effet de solvant. *Journal de chimie physique et de physico-chimie biologique*, page 878, 1964.

-
- [53] C.F. Colebrook. Turbulent flow in pipes, with particular reference to the transition region between the smooth and rough pipe laws. *Journal of the ICE*, 11(4):133–156, 1939.
- [54] S.H. Collicott and H. Li. True-scale, true-pressure internal flow visualization for Diesel injectors. *SAE Paper 2006-01-0890*, 2006.
- [55] David Correas. *Estudio teórico-experimental del chorro libre Diesel isotermo*. PhD thesis, E.T.S. Ingenieros Industriales. Universidad Politécnica de Valencia, Valencia, 1998.
- [56] Z. Dai and G.M. Faeth. Temporal properties of secondary drop breakup in the multimode breakup regime. *International Journal of Multiphase Flow*, 27(2):217–236, 2001.
- [57] A. D’alessio. Laser light scattering and fluorescence diagnostics of rich flames produced by gaseous and liquid fuels. *Particulate Carbon: Formation During Combustion*, pages 207–259, 1981.
- [58] T. Dan, T. Yamamoto, J. Senda, and H. Fujimoto. Effect of nozzle configurations for characteristics of non-reacting Diesel fuel spray. *SAE Paper 970355*, 1997.
- [59] K. Date, H. Nobechi, H. Kano, M. Kato, and T. Oya. Experimental analysis of fuel flow characteristics in the nozzle for direct injection engines. *SAE Paper 931002*, 1993.
- [60] P. Debye. Der lichtdruck auf kugeln von beliebigem material. *Annalen der physik*, 335(11):57–136, 1909.
- [61] K.G. Denbigh. The polarisabilities of bonds - I. *Transactions of the Faraday Society*, 36:936–948, 1940.
- [62] J.C. Dent. A basis for comparison of various experimental methods for studying spray penetration. *SAE Paper 710571*, 1971.
- [63] J. M. Desantes, R. Payri, J. M. Pastor, and J. Gimeno. Experimental characterization of internal nozzle flow and Diesel spray behavior. part I: Nonevaporative conditions. *Atomization And Sprays*, 15(5):489–516, September 2005.
- [64] J. M. Desantes, R. Payri, F. J. Salvador, and J. Gimeno. Measurements of spray momentum for the study of cavitation in Diesel injection nozzles. *SAE Paper 2003-01-0703*, 2003.

-
- [65] J.M. Desantes, J. Arrègle, and P.J. Rodríguez. Computational model for simulation of Diesel injection systems. *SAE Paper 1999-01-0915*, 1999.
- [66] J.M. Desantes, J.J. Lopez, J.M. Garcia, and J.M. Pastor. Evaporative Diesel spray modeling. *Atomization and Sprays*, 17(3):193–232, 2007.
- [67] J.M. Desantes, J.V. Pastor, J.M. Pastor, and J.E. Julia. Limitations on the use of the planar laser induced exciplex fluorescence technique in Diesel sprays. *Fuel*, 84(18):2301–2315, 2005.
- [68] J.M. Desantes, J.V. Pastor, R. Payri, and J.M. Pastor. Experimental characterization of internal nozzle flow and Diesel spray behavior. part II: Evaporative conditions. *Atomization And Sprays*, 15(5):517–543, 2005.
- [69] J.M. Desantes, R. Payri, A. Garcia, and J. Manin. Experimental study of biodiesel blends' effects on Diesel injection processes. *Energy & Fuels*, 23:3227–3235, 2009.
- [70] J.M. Desantes, R. Payri, J.M. Garcia, and F.J. Salvador. A contribution to the understanding of isothermal Diesel spray dynamics. *Fuel*, 86(7-8):1093–1101, 2007.
- [71] J.M. Desantes, R. Payri, F.J. Salvador, and J. De la Morena. Cavitation effects on spray characteristics in the near-nozzle field. *SAE Paper 2009-24-0037*, 2009.
- [72] J.M. Desantes, R. Payri, F.J. Salvador, and A. Gil. Development and validation of a theoretical model for diesel spray penetration. *Fuel*, 85(7-8):910–917, 2005.
- [73] J.M. Desantes, R. Payri, F.J. Salvador, and A. Gil. Deduction and validation of a theoretical model for a free Diesel spray. *Fuel*, 85:910–917, 2006.
- [74] J.M. Desantes, F.J. Salvador, J.J. Lopez, and J. De la Morena. Study of mass and momentum transfer in Diesel sprays based on X-ray mass distribution measurements and on a theoretical derivation. *Experiments in Fluids*, pages 1–14, 2010.
- [75] F. Di Giorgio, D. Laforgia, and V. Damiani. Investigation of drop size distribution in the spray of a five-hole, vco nozzle at high feeding pressure. *SAE Paper 950087*, 1995.

- [76] C. Diver, J. Atkinson, B. Befrui, H. J. Helml, and L. Li. Improving the geometry and quality of a micro-hole fuel injection nozzle by means of hydroerosive grinding. *Proceedings of the Institution of Mechanical Engineers - Part B - Engineering Manufacture*, 221(1):1–9, 2007.
- [77] R. Domann and Y. Hardalupas. Evaluation of the planar droplet sizing (PDS) technique. *ICLASS 2000, Pasadena, CA*, pages 131–138, 2000.
- [78] R. Domann and Y. Hardalupas. Spatial distribution of fluorescence intensity within large droplets and its dependence on dye concentration. *Applied Optics*, 40(21):3586–3597, 2001.
- [79] R. Domann and Y. Hardalupas. A study of parameters that influence the accuracy of the planar droplet sizing (PDS) technique. *Particle & Particle Systems Characterization*, 18(1):3–11, 2001.
- [80] R. Domann and Y. Hardalupas. Quantitative measurement of planar droplet sauter mean diameter in sprays using planar droplet sizing. *Particle & Particle Systems Characterization*, 20(3):209–218, 2003.
- [81] R. Domann, Y. Hardalupas, and A.R. Jones. A study of the influence of absorption on the spatial distribution of fluorescence intensity within large droplets using mie theory, geometrical optics and imaging experiments. *Measurement Science and Technology*, 13:280, 2002.
- [82] F. Durst and M. Zare. Laser doppler measurements in two-phase flows. *Proceedings LDA-Symposium, Copenhagen*, pages 403–429, 1976.
- [83] A.C. Eckbreth. Laser diagnostics for combustion species and temperature. *Abacus, Cambridge, Mass*, pages 249–252, 1988.
- [84] M.R. Eftink and C.A. Ghiron. Fluorescence quenching of indole and model micelle systems. *The Journal of Physical Chemistry*, 80(5):486–493, 1976.
- [85] M.M. El-Wakil, P.S. Myers, and O.A. Uyehara. Fuel vaporization and ignition lag in Diesel combustion. *SAE Transactions*, 64:712, 1956.
- [86] C. Espey, J.E. Dec, T.A. Litzinger, and D.A. Santavicca. Planar laser rayleigh scattering for quantitative vapor-fuel imaging in a Diesel jet. *Combustion and Flame*, 109(1-2):65–78, 1997.
- [87] G.M. Faeth, L.P. Hsiang, and P.K. Wu. Structure and breakup properties of sprays. *International Journal of Multiphase Flow*, 21:99–127, 1995.

-
- [88] T.A. Fox and J. Stark. Characteristics of miniature short-tube orifice flows. *Proc. Inst. Mech Engrs*, 203:351–357, 1989.
- [89] T.A. Fox and J. Stark. Discharge coefficients for miniature fuel injectors. *Proc. Inst. Mech Engrs*, 203:75–78, 1989.
- [90] P.A. Franken, A.E. Hill, C.W. Peters, and G. Weinreich. Generation of optical harmonics. *Physical Review Letters*, 7(4):118–119, 1961.
- [91] P.A. Galland, X. Liang, L. Wang, K. Breisacher, L. Liou, P.P. Ho, and R.R. Alfano. Time-resolved optical imaging of jet sprays and droplets in highly scattering medium. *ASME - HTD*, 321:585–588, 1995.
- [92] Jose Maria Garcia. *Aportaciones al estudio del proceso de combustion turbulenta de chorros en motores Diesel de inyección directa*. PhD thesis, E.T.S. Ingenieros Industriales. Universidad Politécnica de Valencia, Valencia, 2004.
- [93] Jaime Gimeno. *Desarrollo y aplicacion de la medida del flujo de cantidad de movimiento de un chorro Diesel*. PhD thesis, E.T.S. Ingenieros Industriales. Universidad Politécnica de Valencia, 2008.
- [94] A.R. Glover, S.M. Skippon, and R.D. Boyle. Interferometric laser imaging for droplet sizing: a method for droplet-size measurement in sparse spray systems. *Applied Optics*, 34(36):8409–8421, 1995.
- [95] G. Gouesbet and G. Grehan. Sur la generalisation de la theorie de lorenz-mie. *Journal of Optics (Paris)*, 13(2):97–103, 1982.
- [96] P. Gravesen, J. Branebjerg, and O.S. Jensen. Microfluidics - A review. *Journal of Micromechanics and Microengineering*, 3:168, 1993.
- [97] D.A. Greenhalgh. Planar measurements of fuel vapour, liquid fuel, liquid droplet size and soot. *Planar Optical Measurement Methods for Gas Turbine Components*, pages 1–7, 1999.
- [98] D.A. Greenhalgh and M. Jermy. Laser diagnostics for droplet measurements for the study of fuel injection and mixing in gas turbines and ic engines. *Applied combustion diagnostics*, pages 408–438, 2002.
- [99] J. Gronki, C. Schulz, and H. Scharr. Correction of beam steering effects in 2d-laser-diagnostic measurements in combustion engines by image postprocessing. *Eurotherm Seminar 2002, Visualisation, Imaging*

- and Data Analysis in Convective Heat and Mass Transfer*, pages 301–306, 2002.
- [100] P.R. Hammond. Laser dye dcm, its spectral properties, synthesis and comparison with other dyes in the red. *Optics Communications*, 29(3):331–333, 1979.
- [101] P. Hay and P.L. Jones. Comparaison of the various correlations for spray penetration. *SAE Paper 720776*, 1972.
- [102] J.C. Hebden, R.A. Kruger, and K.S. Wong. Time resolved imaging through a highly scattering medium. *Applied optics*, 30(7):788–794, 1991.
- [103] D.J. Heeger and J.R. Bergen. Pyramid-based texture analysis/synthesis. pages 229–238, 1995.
- [104] C. Heimgartner. Investigation of the primary spray breakup close to the nozzle of a common- rail high-pressure Diesel injection system. 2000.
- [105] G.T. Herman and A. Kuba. Discrete tomography: Foundations, algorithms, and applications. *Birkhauser*, 1999.
- [106] Sjoerd Hermens. *Influence of Diesel injector nozzle geometry on the injection and combustion process*. PhD thesis, E.T.S. Ingenieros Industriales. Universidad Politécnic de Valencia, Valencia, 2007.
- [107] J.O. Hinze. Turbulence: an introduction to its mechanism and theory. *McGraw-Hill, New York*, 162, 1959.
- [108] H. Hiroyasu and M. Arai. Structures of fuel spray in Diesel engines. *SAE Paper 900475*, 1990.
- [109] H. Hiroyasu, M. Arai, and M. Shimizu. Break-up length of a liquid jet and internal flow in a nozzle. *ICLASS 1991, Gaithersburg, Maryland*, 1991.
- [110] H. Hiroyasu, M. Arai, and M. Tabata. Empirical equations for the sauter mean diameter of Diesel spray. *SAE Paper 890464*, 1989.
- [111] H. Hiroyasu, M. Shimizu, and M. Arai. The breakup of high speed jet in a high pressure gaseous atmosphere. *ICLASS 1982*, pages 69–74, 1982.
- [112] L.P. Hsiang and G.M. Faeth. Near-limit drop deformation and secondary breakup. *International Journal of Multiphase Flow*, 18(5):635–652, 1992.

- [113] C.A. Idicheria and L. Pickett. Quantitative mixing measurements in a vaporizing Diesel spray by rayleigh imaging. *SAE Paper 2007-01-0647*, 2007.
- [114] J.D. Ingle and S.R. Crouch. Spectrochemical analysis. *Englewood Cliffs, NJ*, 1988.
- [115] A. Jablonski. Efficiency of anti-stokes fluorescence in dyes. *Nature*, 131(3319):839–840, 1933.
- [116] M.C. Jermy and A. Allen. Simulating the effects of multiple scattering on images of dense sprays and particle fields. *Applied optics*, 41(20):4188–4196, 2002.
- [117] M.C. Jermy and D.A. Greenhalgh. Planar dropsizing by elastic and fluorescence scattering in sprays too dense for phase doppler measurement. *Applied Physics B: Lasers and Optics*, 71(5):703–710, 2000.
- [118] R.L. Jernigan and P.J. Flory. Optical anisotropy of chain molecules. theory of depolarization of scattered light with application to n-alkanes. *The Journal of Chemical Physics*, 47:1999, 1967.
- [119] S.C. Johnston. Precombustion fuel/air distribution in a stratified charge engine using laser raman spectroscopy. *SAE Paper 790433*, 1979.
- [120] Jose Enrique Julia. *Medida de concentraciones de combustible en chorros Diesel mediante tecnicas de fluorescencia inducida por laser*. PhD thesis, E.T.S. Ingenieros Industriales. Universidad Politécnic de Valencia, 2003.
- [121] T. Kamimoto, H. Yokota, and H. Kobayashi. A new technique for the measurement of sauter mean diameter of droplets in unsteady dense sprays. *SAE Paper 890240*, 27, 1989.
- [122] S. Kampmann, B. Dittus, P. Mattes, and M. Kirner. The influence of hydro grinding at VCO nozzles on the mixture preparation in a DI diesel engine. *SAE Transactions*, 105(3):1329–1339, 1996.
- [123] A.L. Kastengren, C.F. Powell, Y. Wang, K.S. Im, and J. Wang. X-ray radiography measurements of diesel spray structure at engine-like ambient density. *Atomization and Sprays*, 19(11):1031–1044, 2009.
- [124] M. Kato, H. Kano, K. Date, T. Oya, and K. Niizuma. Flow analysis in nozzle hole in consideration of cavitation. *SAE Paper 970052*, 1997.

-
- [125] M. Kerker. The scattering of light and other electromagnetic radiation. *Academic Press, London*, 1969.
- [126] L.V. King. On the complex anisotropic molecule in relation to the dispersion and scattering of light. *Proceedings of the Royal Society of London. Series A, Containing Papers of a Mathematical and Physical Character*, 104(726):333–357, 1923.
- [127] R.T Knapp, J.W. Daily, and F.G. Hammitt. Cavitation. *McGraw-Hill, New York*, 1970.
- [128] F.H. Ko, L.Y. Weng, C.J. Ko, and T.C. Chu. Characterization of imprinting polymeric temperature variation with fluorescent rhodamine B molecule. *Microelectronic Engineering*, 83(4-9):864–868, 2006.
- [129] S. Kook, L.M. Pickett, and M.P.B. Musculus. Influence of diesel injection parameters on end-of-injection liquid length recession. *SAE International Journal of Engines*, 2(1):1194, 2009.
- [130] E. Kristensson, E. Berrocal, M. Richter, S.G. Pettersson, and M. Aldèn. High-speed structured planar laser illumination for contrast improvement of two-phase flow images. *Optics letters*, 33(23):2752–2754, 2008.
- [131] J.R. Lakowicz and B.R. Masters. Principles of fluorescence spectroscopy. *Journal of Biomedical Optics*, 13, 2008.
- [132] J.C. Lasheras and E.J. Hopfinger. Liquid jet instability and atomization in a coaxial gas stream. *Annual Review of Fluid Mechanics*, 32(1):275–308, 2000.
- [133] P. Lauvin, A. Löffler, A. Schmitt, W. Zimmermann, and W. Fuchs. Electronically controlled high pressure unit injector system for diesel engines. *SAE Paper 911819*, 1991.
- [134] P. Le Gal, N. Farrugia, and D.A. Greenhalgh. Development of laser sheet drop sizing (lsd) for spray characterization. *IMEchE conference transactions*, pages 113–120, 1998.
- [135] P. Le Gal, N. Farrugia, and D.A. Greenhalgh. Laser sheet dropsizing of dense sprays. *Optics and Laser Technology*, 31(1):75–83, 1999.
- [136] C.S. Lee and R.D. Reitz. Effect of liquid properties on the breakup mechanism of high-speed liquid drops. *Atomization and Sprays*, 11(1):1–20, 2001.

-
- [137] N. Levy, S. Amara, and J.C. Champoussin. Simulation of a diesel jet assumed fully atomized at the nozzle exit. *SAE Paper 981067*, 1998.
- [138] H. Li and S.H. Collicott. Visualization of cavitation in high-pressure diesel fuel injector orifices. *Atomization and Sprays*, 16(8):875–886, 2006.
- [139] A. K. Lichtarowicz, R. K. Duggins, and E. Markland. Discharge coefficients for incompressible non-cavitating flow through long orifices. *Journal of Mechanical Engineering and Science*, 7(2):210–219, 1965.
- [140] M. Linne, M. Paciaroni, T. Hall, and T. Parker. Ballistic imaging of the near field in a diesel spray. *Experiments in Fluids*, 40(6):836–846, 2006.
- [141] R.D. Lockett, J. Richter, and D.A. Greenhalgh. The characterisation of a diesel spray using combined laser induced fluorescence and laser sheet dropsizing. *Conference on Lasers and Electro-Optics Europe, 1998*, 1998.
- [142] L. Lorenz. Über die refractionsconstante. *Annalen Der Physik und Chemie*, 11:70–103, 1880.
- [143] L. Lorenz. Lysbevaegelser i og uden for en af plane lysbolger belyst kugle. *Det kongelig danske Videnskabernes Selskabs Skrifter*, 6:1–62, 1890.
- [144] V. Macián, V. Bermudez, R. Payri, and J. Gimeno. New technique for determination of internal geometry of a diesel nozzle with the use of silicone methodology. *Experimental Techniques*, 27(2):39–43, 2003.
- [145] V. Macián, R. Payri, X. Margot, and F. J. Salvador. A CFD analysis of the influence of diesel nozzle geometry on the inception of cavitation. *Atomization and Sprays*, 13:579–604, 2003.
- [146] A.G. MacPhee, M.W. Tate, C.F. Powell, Y. Yue, M.J. Renzi, A. Ercan, S. Narayanan, E. Fontes, J. Walther, J. Schaller, et al. X-ray imaging of shock waves generated by high-pressure fuel sprays. *Science*, 295(5558):1261–1263, 2002.
- [147] M. Maeda, T. Kawaguchi, and K. Hishida. Novel interferometric measurement of size and velocity distributions of spherical particles. *Measurement Science and Technology*, 11:L13–L18, 2000.
- [148] D. Magde, G.E. Rojas, and P.G. Seybold. Solvent dependence of the fluorescence lifetimes of xanthene dyes. *Photochemistry and Photobiology*, 70(5):737–744, 1999.

- [149] J.C. Maxwell. A dynamical theory of the electromagnetic field. *Philosophical Transactions of the Royal Society of London*, 155:459–512, 1865.
- [150] C.S. McEnally, D.M. Ciuparu, and L.D. Pfefferle. Experimental study of fuel decomposition and hydrocarbon growth processes for practical fuel components: heptanes. *Combustion and Flame*, 134(4):339–353, 2003.
- [151] L.A. Melton. Spectrally separated fluorescence emissions for diesel fuel droplets and vapor. *Applied optics*, 22(14):2224–2226, 1983.
- [152] G. Mie. Beitrage zur Optik truber Medien, speziell kolloidaler Metallosungen. *Annalen der Physik*, 330(3):377–445, 1908.
- [153] R.B. Miles, W.R. Lempert, and J.N. Forkey. Laser rayleigh scattering. *Measurement Science and Technology*, 12:R33–R51, 2001.
- [154] R.J. Moffat. Describing the uncertainties in experimental results. *Experimental thermal and fluid science*, 1(1):3–17, 1988.
- [155] R. Morgan, J. Wray, D.A. Kennaird, C. Crua, and M.R. Heikal. The influence of injector parameters on the formation and break-up of a diesel spray. *SAE Transactions*, 110(3):389–399, 2001.
- [156] R.A. Mugele and H.D. Evans. Droplet size distribution in sprays. *Industrial & Engineering Chemistry*, 43(6):1317–1324, 1951.
- [157] M.P.B. Musculus. Entrainment waves in decelerating transient turbulent jets. *Journal of Fluid Mechanics*, 638:117–140, 2009.
- [158] J. Naber and D. Siebers. Effects of gas density and vaporization on penetration and dispersion of diesel sprays. *SAE Paper 960034*, 1996.
- [159] H. Naus and W. Ubachs. Experimental verification of rayleigh scattering cross sections. *Optics Letters*, 25(5):347–349, 2000.
- [160] M.A.A. Neil, R. Juskaitis, and T. Wilson. Method of obtaining optical sectioning by using structured light in a conventional microscope. *Optics Letters*, 22(24):1905–1907, 1997.
- [161] Q.V. Nguyen and P.H. Paul. KrF laser-induced photobleaching effects in O₂ planar laser-induced fluorescence signals: experiment and model. *Applied optics*, 36(12):2675–2683, 1997.

- [162] K.T. No, K.H. Cho, M.S. Jhon, and H.A. Scheraga. An empirical method to calculate average molecular polarizabilities from the dependence of effective atomic polarizabilities on net atomic charge. *Journal of the American Chemical Society*, 115(5):2005–2014, 1993.
- [163] W. H. Nurick. Orifice cavitation and its effects on spray mixing. *Journal of fluids engineering*, 98:681–687, 1976.
- [164] R. Ochoterena, M. Larsson, S. Andersson, and I.G. Denbratt. Optical studies of spray development and combustion characterisation of oxygenated and fischer-tropsch fuels. *SAE Paper 2008-01-1393*, 2008.
- [165] W. Ohnesorge. Formation of drops by nozzles and the breakup of liquid jets. *eitschrift für Angewandte Mathematik und Mechanik (ZAMM)*, 16(4):355–358, 1936.
- [166] J. Ortega and J.S. Matos. Estimation of the isobaric expansivities from several equations of molar refraction for some pure organic compounds. *Materials Chemistry and Physics*, 15(5):415–425, 1986.
- [167] J.C. Owens. Optical refractive index of air: dependence on pressure, temperature and composition. *Applied Optics*, 6(1):51–59, 1967.
- [168] M. Paciaroni and M. Linne. Single-shot, two-dimensional ballistic imaging through scattering media. *Applied optics*, 43(26):5100–5109, 2004.
- [169] D. Papamoschou and A. Roshko. Observations of supersonic free shear layers. *Sadhana*, 12(1):1–14, 1988.
- [170] T.E. Parker, L.R. Rainaldi, and W.T. Rawlins. A comparative study of room-temperature and combusting fuel sprays near the injector tip using infrared laser diagnostics. *Atomization and Sprays*, 8(5):565–600, 1998.
- [171] J.V. Pastor, J. Arrègle, and A. Palomares. Diesel spray images segmentation using a likelihood ratio test. *Applied Optics*, 40(17):2876–2885, 2001.
- [172] J.V. Pastor, J.J. Lopez, J.M. Garcia, and J.M. Pastor. A 1D model for the description of mixing-controlled inert diesel sprays. *Fuel*, 87(13-14):2871–2885, 2008.
- [173] J.V. Pastor, J.J. Lopez, J.E. Juliá, and J.V. Benajes. Planar laser-induced fluorescence fuel concentration measurements in isothermal diesel sprays. *Optics Express*, 10(7):309–323, 2002.

- [174] J.V. Pastor, R. Payri, L. Araneo, and J. Manin. Correction method for droplet sizing by laser-induced fluorescence in a controlled test situation. *Optical Engineering*, 48:013601, 2009.
- [175] F. Payri, V. Bermúdez, R. Payri, and F.J. Salvador. The influence of cavitation on the internal flow and the spray characteristics in diesel injection nozzles. *Fuel*, 83:419–431, 2004.
- [176] F. Payri, J. M. Desantes, and J. Arrègle. Characterization of DI diesel sprays in high density conditions. *SAE Paper 960774*, 1996.
- [177] F. Payri, J.V. Pastor, R. Payri, and J. Manin. Determination of the optical depth of a di diesel spray. *Journal of Mechanical Science and Technology*, 114, 2010.
- [178] R. Payri, J.M. Garcia, F.J. Salvador, and J. Gimeno. Using spray momentum flux measurements to understand the influence of diesel nozzle geometry on spray characteristics. *Fuel*, 84(5):551–561, 2005.
- [179] R. Payri, C. Guardiola, F. J. Salvador, and J. Gimeno. Critical cavitation number determination in diesel injection nozzles. *Experimental Techniques*, 28(3):49–52, 2004.
- [180] R. Payri, X. Margot, and F.J. Salvador. A numerical study of the influence of diesel nozzle geometry on the inner cavitating flow. *SAE Paper 2002-01-0215*, 2002.
- [181] R. Payri, S. Ruiz, F.J. Salvador, and J. Gimeno. On the dependence of spray momentum flux in spray penetration. *Journal of Mechanical Science and Technology*, 21(7):1100–1111, 2007.
- [182] R. Payri, FJ Salvador, J. Gimeno, and G. Bracho. A new methodology for correcting the signal cumulative phenomenon on injection rate measurements. *Experimental Techniques*, 32(1):46–49, 2008.
- [183] R. Payri, F.J. Salvador, J. Gimeno, and G. Bracho. The effect of temperature and pressure on thermodynamic properties of Diesel and biodiesel fuels. *Fuel*, 2010.
- [184] R. Payri, F.J. Salvador, J. Gimeno, and J. de la Morena. Study of cavitation phenomena based on a technique for visualizing bubbles in a liquid pressurized chamber. *International Journal of Heat and Fluid Flow*, 30:768–777, 2009.

- [185] R. Payri, F.J. Salvador, J. Gimeno, and V. Soare. Determination of diesel sprays characteristics in real engine in-cylinder air density and pressure conditions. *Journal Of Mechanical Science And Technology*, 19(11):2040–2052, 2005.
- [186] R. Payri, F.J. Salvador, J. Gimeno, and L.D. Zapata. Diesel nozzle geometry influence on spray liquid-phase fuel penetration in evaporative conditions. *Fuel*, 87(7):1165–1176, 2008.
- [187] R. Payri, B. Tormos, F.J. Salvador, and L. Araneo. Spray droplet velocity characterization for convergent nozzles with three different diameters. *Fuel*, 87(15-16):3176–3182, 2008.
- [188] L. Pickett, J. Manin, C.L. Genzale, D.L. Siebers, M.P.M. Musculus, and Idicheria C.A. Relationship between diesel fuel spray vapor penetration/dispersion and local fuel mixture fraction. *SAE Paper 2011-01-0686*, SAE International Journal of Engines, 2011.
- [189] L.M. Pickett, J.A. Caton, M.P.B. Musculus, and A.E. Lutz. Evaluation of the equivalence ratio-temperature region of diesel soot precursor formation using a two-stage lagrangian model. *International Journal of Engine Research*, 7(5):349–370, 2006.
- [190] L.M. Pickett, S. Kook, and T.C. Williams. Visualization of diesel spray penetration, cool-flame, ignition, high-temperature combustion, and soot formation using high-speed imaging. *SAE Paper 2009-01-0658*, 2(1):439, 2009.
- [191] L.M. Pickett and D.L. Siebers. Soot in diesel fuel jets: effects of ambient temperature, ambient density, and injection pressure. *Combustion and Flame*, 138(1-2):114–135, 2004.
- [192] M. Pilch and C.A. Erdman. Use of breakup time data and velocity history data to predict the maximum size of stable fragments for acceleration-induced breakup of a liquid drop. *International journal of multiphase flow*, 13(6):741–757, 1987.
- [193] Alejandro Hernán Plazas. *Modelado unidimensional de inyectores common-rail Diesel*. PhD thesis, E.T.S. Ingenieros Industriales. Universidad Politécnica de Valencia, Valencia (Spain), 2005.
- [194] D. Potz, W. Chirst, and B. Dittus. Diesel nozzle: The determining interface between injection system and combustion chamber. *THIESEL 2000*

- Conference on Thermo and Fluid-dynamic Processes in Diesel Engines, Valencia, Spain, 2000.*
- [195] C. Powell, S. Ciatti, S.K. Cheong, J. Liu, and J. Wang. X-ray characterization of diesel sprays and effects of nozzle geometry. *Proceedings of the Diesel Engine Emission Reduction Conference, 2004.*
- [196] C.F. Powell, Y. Yue, R. Poola, and J. Wang. Time-resolved measurements of supersonic fuel sprays using synchrotron x-rays. *Journal of synchrotron radiation*, 7(6):356–360, 2000.
- [197] C.M.V. Prasad and S. Kar. An investigation on the diffusion of momentum and mass of fuel in a diesel fuel spray. *ASME J. Eng. Power*, pages 1–11, 1976.
- [198] R. Ragucci, A. Cavaliere, and P. Massoli. Drop sizing by laser light scattering exploiting intensity angular oscillation in the mie regime. *Particle & Particle Systems Characterization*, 7(1-4):221–225, 1990.
- [199] K. Ramamurthi and K. Nandakumar. Characteristics of flow through small sharp-edged cylindrical orifices. *Flow Measurement and Instrumentation*, 10(3):133–143, 1999.
- [200] A.A. Ranger and J.A. Nicholls. Aerodynamic shattering of liquid drops. *AIAA Journal*, 7(2):285–290, 1969.
- [201] J.W. Strutt Rayleigh. On the light from the sky, its polarization and colour. *Philosophical Magazine Series 4*, 41(271):107–120, 1871.
- [202] J.W. Strutt Rayleigh. On the electromagnetic theory of light. *Philos. Mag*, 12:81–101, 1881.
- [203] J.W. Strutt Rayleigh. On the transmission of light through an atmosphere containing small particles in suspension, and on the origin of the blue of the sky. *Philos. Mag*, 47(375):132, 1899.
- [204] R. Reitz and F. Bracco. On the dependence of spray angle and other spray parameters on nozzle design and operating conditions. *SAE Paper 790494*, 1979.
- [205] R. Reitz and F. Bracco. Mechanism of atomization of a liquid jet. *Physics of Fluids*, 25(10):1730–1742, 1982.

- [206] R. Reitz and F. Bracco. Mechanism of breakup of round liquid jets. *Encyclopedia of Fluids Mechanics, Gulf publishing*, 3, 1994.
- [207] R. Reitz and R. Diwakar. Effect of drop breakup on fuel sprays. *SAE Paper 860469*, 1986.
- [208] R. Reitz and R. Diwakar. Structure of high-pressure fuel sprays. *SAE Paper 870598*, 1987.
- [209] Rolf Reitz. *Atomization and other breakup regimes of a liquid jet*. PhD thesis, Princeton University, 1978.
- [210] O. Reynolds. An experimental investigation of the circumstances which determine whether the motion of water shall be direct or sinuous, and of the law of resistance in parallel channels. *Philosophical Transactions of the Royal Society of London*, 174:935–982, 1883.
- [211] Nader Rizk. *Studies on liquid sheet disintegration in airblast atomizers*. PhD thesis, Cranfield University, Cranfield, UK, 1976.
- [212] J. Rotta. Experimenteller beitrag zur entstehung turbulenter strömung im rohr. *Ingenieur-Archiv*, 24(4):258–281, 1956.
- [213] C. Roze, T. Girasole, L. Mevcs, G. Grehan, L. Hespel, and A. Delfour. Interaction between ultra short pulses and a dense scattering medium by monte carlo simulation: consideration of particle size effect. *Optics Communications*, 220(4-6):237–245, 2003.
- [214] F. Ruiz. A few useful relations for cavitating orifices. *ICLASS 1991, Gaithersburg, Maryland*, pages 595–602, 1991.
- [215] F. Ruiz. Turbulence inside a cavitating injector orifice: a different animal. *ILASS-Americas*, pages 133–137, 1998.
- [216] S.V. Sankar and W.D. Bachalo. Response characteristics of the phase doppler particle analyzer for sizing spherical particles larger than the light wavelength. *Applied optics*, 30(12):1487–1496, 1991.
- [217] S.V. Sankar, K.E. Maher, D.M. Robart, and W.D. Bachalo. Spray characterization using a planar droplet sizing technique. *International journal of fluid mechanics research*, 24:578–589, 1997.
- [218] P. Schellekens, G. Wilkening, F. Reinboth, M.J. Downs, K.P. Birch, and J. Spronck. Measurements of the refractive index of air using interference refractometers. *Metrologia*, 22:279, 1986.

- [219] H. Schlichting. Boundary layer theory. *McGraw-Hill, Series in Mechanical Engineering*, 1979.
- [220] D.P. Schmidt and M.L. Corradini. The internal flow of diesel fuel injector nozzles: a review. *ImechE, Int. J. Eng. Res.*, 2(6), 2001.
- [221] C. Schulz and V. Sick. Tracer-LIF diagnostics: quantitative measurement of fuel concentration, temperature and fuel/air ratio in practical combustion systems. *Progress in Energy and Combustion Science*, 31(1):75–121, 2005.
- [222] D. Sedarsky, E. Berrocal, and M. Linne. Ballistic imaging for measurement of flow structures in dense multiphase media. *14th International Symposium on Applications of Laser Techniques to Fluid Mechanics, Lisbon*, pages 7–10, 2008.
- [223] D.L. Sedarsky, M.E. Paciaroni, M.A. Linne, J.R. Gord, and T.R. Meyer. Velocity imaging for the liquid-gas interface in the near field of an atomizing spray: proof of concept. *Optics letters*, 31(7):906–908, 2006.
- [224] J.M. Seitzman and R.K. Hanson. Planar fluorescence imaging in gases. *Instrumentation for flows with combustion*, 1993.
- [225] W. Sellmeier. Zur erklärang der abnormen farbenfolge im spectrum einiger substanzen. *Annalen der Physik und Chemie*, 219:272–282, 1871.
- [226] G.S. Settles. Flow visualization techniques for practical aerodynamic testing. *Flow Visualization III*, pages 306–315, 1985.
- [227] G.S. Settles. Schlieren and shadowgraph techniques: visualizing phenomena in transparent media. *Springer, Berlin, Heidelberg, New-York*, 2001.
- [228] D.L. Siebers. Liquid-phase fuel penetration in diesel sprays. *SAE Transaction*, 107:1205–1227, 1998.
- [229] D.L. Siebers. Scaling liquid-phase fuel penetration in diesel sprays based on mixing-limited vaporization. *SAE Paper 1999-01-0528*, 1999.
- [230] R.P. Smith and E.M. Mortensen. Calculation of depolarization ratios, anisotropies, and average dimensions of n-alkanes. *The Journal of Chemical Physics*, 35:714, 1961.

- [231] M. Snee and W. Ubachs. Direct measurement of the rayleigh scattering cross section in various gases. *Journal of Quantitative Spectroscopy and Radiative Transfer*, 92(3):293–310, 2005.
- [232] Vlad Soare. *Phase doppler measurement in diesel dense sprays: optimisation of measurements and study of the orifice geometry influence over the spray at microscopic level*. PhD thesis, E.T.S. Ingenieros Industriales. Universidad Politécnic de Valencia, Valencia, 2007.
- [233] C. Soteriou, R. Andrews, and M. Smith. Direct injection diesel sprays and the effect of cavitation and hydraulic flip on atomization. *SAE Paper 950080*, 1995.
- [234] C. Soteriou, S. Zuelch, M. Lambert, and D. Passerel. The flow characteristics of high efficiency diesel nozzles with enhanced geometry holes. *THIESEL 2006 Conference on Thermo and Fluid-dynamic Processes in Diesel Engines, Valencia, Spain*, 2006.
- [235] A. Sou, A. Tomiyama, S. Hosokawa, S. Nigorikawa, and T. Maeda. Cavitation in a two-dimensional nozzle and liquid jet atomization. *JSME, International Journal Series B*, 49(4):1253–1259, 2006.
- [236] A. Sou, A. Tomiyama, S. Hosokawa, S. Nigorikawa, and Y. Matsumoto. Visualization of cavitation in a two-dimensional nozzle and liquid jet. *Proc. 5th International Conference on Multiphase Flow*, 2004.
- [237] D.B. Spalding. Combustion and mass transfer. *Pergamon international library of science, technology, engineering, and social studies*, 1979.
- [238] G.G. Stokes. On the effect of the internal friction of fluids on the motion of pendulums. *Trans. Cambridge Philos. Soc*, 9(8), 1851.
- [239] R.J. Strutt. The light scattered by gases: its polarisation and intensity. *Proceedings of the Royal Society of London. Series A, Containing Papers of a Mathematical and Physical Character*, 95(667):155–176, 1918.
- [240] G. Stumpp and M. Ricco. Common rail - an attractive fuel injection system for passenger car DI diesel engines. *SAE Paper 960870*, 1996.
- [241] J. Swithenbank, J.M. Beer, D.S. Taylor, D. Abbot, and G.C. McCreath. A laser diagnostic technique for the measurement of droplet and particle size distribution. *AIAA, Aerospace Sciences Meeting*, 1976.

- [242] C. Tropea. Laser doppler anemometry: recent developments and future challenges. *Measurement Science and Technology*, 6(6):605–619, 1995.
- [243] J.W. Tukey. The future of data analysis: Chap. 1. exploratory data analysis. *Addison-Wesley, Reading, MA*, 1977.
- [244] H.C. Van De Hulst. Light scattering by small particles. *Dover Publications, Inc., New-York*, 1981.
- [245] M.B. van der Mark, M.P. van Albada, and A. Lagendijk. Light scattering in strongly scattering media: multiple scattering and weak localization. *Physical Review B*, 37(7):3575–3592, 1988.
- [246] W.M. Vaughn and G. Weber. Oxygen quenching of pyrenebutyric acid fluorescence in water. dynamic probe of the microenvironment. *Biochemistry*, 9(3):464–473, 1970.
- [247] A.J.W.G. Visser, K. Vos, A. Van Hoek, and J.S. Santema. Time-resolved fluorescence depolarization of rhodamine B and (octadecyl) rhodamine B in triton X-100 micelles and aerosol OT reversed micelles. *The Journal of Physical Chemistry*, 92(3):759–765, 1988.
- [248] A.I. Vogel. Physical properties and chemical constitution of aliphatic hydrocarbons. *J. Chem. Soc*, 9:133–142, 1946.
- [249] C. von Kuensberg Sarre, S.C. Kong, and R. Reitz. Modeling the effects of injector nozzle geometry on diesel sprays. *SAE Paper 1999-01-0912*, 1999.
- [250] Y. Wakuri, M. Fujii, T. Amitani, and R. Tsumeya. Studies of the penetration of a fuel spray in a diesel engine. *JSME*, 3(9):123–130, 1960.
- [251] J. Walther, J.K. Schaller, R. Wirth, and C. Tropea. Characterization of cavitating flow fields in transparent diesel injection nozzles using fluorescent particle image velocimetry (FPIV). *ILASS-Europe*, 2000.
- [252] J. Wang, Y. Wang, K.S. Im, K. fezzaa, and W. Lee. X-ray vision of an air-assisted sprays: from radiography to quantitative phase-contrast imaging. *ICLASS 2006*, 2006.
- [253] M.J. Weber. Handbook of optical materials. *CRC Press*, 2003.
- [254] F.M. White. Fluid mechanics. *McGraw-Hill Science/Engineering/Math*, 5th edition, 2004.

-
- [255] A.T.R. Williams, S.A. Winfield, and J.N. Miller. Relative fluorescence quantum yields using a computer-controlled luminescence spectrometer. *Analyst*, 108(1290):1067–1071, 1983.
- [256] C.N. Yeh, H. Kosaka, and T. Kamimoto. A fluorescence/scattering imaging technique for instantaneous 2-D measurement of particle size distribution in a transient spray. *3rd International Congress on Optical Particle Sizing, Yokohama, Japan*, pages 355–361, 1993.
- [257] C.N. Yeh, H. Kosaka, and T. Kamimoto. Measurement of drop sizes in unsteady dense sprays. *Recent advances in spray combustion: Spray atomization and drop burning phenomena.*, 1:297–308, 1996.
- [258] Y. Yeh and H.Z. Cummins. Localized fluid flow measurements with an he-ne laser spectrometer. *Applied Physics Letters*, 4:176, 1964.
- [259] F.Q. Zhao and H. Hiroyasu. The applications of laser rayleigh scattering to combustion diagnostics. *Progress in Energy and Combustion Science*, 19(6):447–485, 1993.
- [260] H. Zhao and N. Ladommatos. Optical diagnostics for in-cylinder mixture formation measurements in ic engines. *Progress in Energy and Combustion Science*, 24(4):297–336, 1998.

Appendices

Appendix A

Estimation of the error made on droplet sizing

As commented in section 4.5.1 and 4.5.3, the volume mean diameter obtained via PDPA measurements has been used to adjust the droplet size distribution extracted from LIF/Mie ratio. The ratio of LIF and Mie signals theoretically provides the Sauter Mean Diameter (d_{32}) which, for an ensemble of polydisperse droplets, may deviate from the volume mean diameter (d_{30}).

Table A.1 presents the results of the different mean diameters defined in table 2.3 measured by the PDPA instrument. It can be observed that the average diameter is different depending on which definition is used.

Radial distance [mm]	d_{10}	d_{20}	d_{30}	SMD - d_{32}
0 (spray axis)	13,8	14,5	15,2	16,6
1	13,0	13,8	14,5	16,1
2	12,7	13,5	14,1	15,6
3	12,6	13,3	14,0	15,5
4	12,4	13,1	13,8	15,4
5	12,1	12,8	13,5	14,9
6	11,8	12,5	13,1	14,4
7	11,4	12,1	12,7	14,0
8	11,5	12,1	12,8	14,2

Table A.1: Mean diameter using different definitions: d_{10} , d_{20} , d_{30} and d_{32} or SMD. The droplets have been measured with the PDPA instrument (TSI) at 45 mm downstream and are given in micrometer.

These results are consistent with previous measurements carried out with this instrument and show that the weighted diameters: d_{20} , d_{30} and d_{32} present higher mean diameters than the geometrical one (d_{10}). This therefore demonstrates that the different definitions of mean diameters do not provide similar results when considering a real Diesel spray which presents a polydisperse distribution. In addition to that, different droplet size distributions (Probability Density Function, see sec. 2.5.3) generally provide different relationship between mean diameter definitions (e.g. d_{30} and d_{32}). However, assuming that the relative difference between those definitions is held within the entire spray, it makes possible to relate LIF/Mie ratio to volume mean diameter.

The next table (tab. A.2) provides the error made on the mean volume diameters obtained through adjustment of the Sauter Mean Diameter on the furthest location from the axis of the spray (8 mm at 45 mm downstream). The volume mean diameter is obtained from the SMD (d_{32}) considering that the relative difference between both definitions is constant throughout the spray.

Radial distance [mm]	d_{30}	SMD - d_{32}	Adjusted SMD	Difference [%]
0 (spray axis)	15,2	16,6	15,0	1,5
1	14,5	16,1	14,4	0,6
2	14,1	15,6	14,0	0,9
3	14,0	15,5	13,9	0,6
4	13,8	15,4	13,8	0,0
5	13,5	14,9	13,4	0,6
6	13,1	14,4	13,0	0,9
7	12,7	14,0	12,6	0,6
8	12,8	14,2	12,8	0,0

Table A.2: Estimation of the error induced by adjusting the volume mean diameter with to Sauter Mean Diameter (d_{32}). Measurements provided in table A.2.

These results showed that a maximum error of 1.5 % can be induced by the approximation made to extract volume mean diameter from LIF/Mie ratio.

The next plot (fig. A.1) shows the difference between original SMD and volume mean diameter as well as the adjusted volume mean diameter.

This last plot demonstrates the validity of the assumption made concerning mean droplet diameters as the original volume mean diameter and the adjusted one obtained through SMD present similar results.

This slight deviation also affects the mixture fraction because it is function

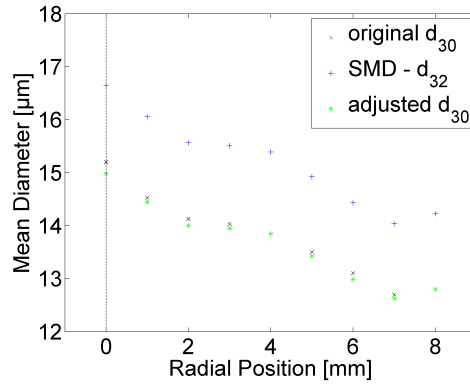


Figure A.1: Radial profiles of the different definitions concerning droplet mean diameter. Adjusted d_{30} has been extracted from LIF/Mie ratio adjusted with PDPA volume mean diameter assuming constant relative difference between Sauter and volume mean diameter definitions.

of the droplet diameter (d_{30}) as presented in equation 4.28. The maximum error made on the mixture fraction due to a deviation of the droplet diameter can go up to 4.5 %. This error has been taken into account in the global uncertainty of the technique together with the uncertainties concerning sizing in the solution of monodisperse fluorescent particles.

Appendix B

Structured Planar Laser Imaging (SPLI-2P) function

The following code concerns the process of the non-evaporative sprays to extract mixing distribution through Structured Planar Laser Imaging (SPLI-2P). This code has been written in MATLAB language and only presents the necessary steps to process the two phases and extract the radiated intensity on the specific plane. This has to be repeated for all the planes in order to three-dimensionally account for light extinction between laser-sheet and acquisition system.

```
function [Intensity_Prof, SPLI2P] = Spray_SPLI2P(AvgImg, Shift1, Offaxis);

% This function processes the images taken with the Sine pattern filter.
% This technique used has been called SPLI (Structured Planar Laser
% Imaging) and removes the out-of-focus scattered photons.
% "Spray_SPLI2P" is the processed image with scattering correction and
% background removed.
% "AvgImg" is used to see if the images have been averaged already. "0" means
% the function will average the images of the structured illumination and
% save them into "Last_LIF.mat". if "1", the function will use the saved
% "Last_LIF" images from a previous process.
% "Shift" is the phase adjustment in pixels from the original picture to
% the shifted image to correct the phase and get a pi difference (e.g. 8).
% "Offaxis" refers to the position of the laser sheet with respect to the
% axis of the spray. For thos tests, it could either be "1" or "2" mm off-axis
% (towards CCD). If no "offaxis", the processing is done on the axis of the
% jet.

Pixmm = 22;
Tip = [12, 452];
if AvgImg == 0;
    names = getfiles('*.tif');
```

```

L=length(names);
av_pict_bgp1 = zeros(864,1216);
for i=(L/3+1):(L/3+19)
    pict_bg = names{i};
    disp(pict_bg)
    image_bg = imread(pict_bg);
    image_bg = double(image_bg)/65535;
    av_pict_bgp1 = av_pict_bgp1 + image_bg;
end
av_pict_bgp1 = av_pict_bgp1 / 19;

av_pict_sprayp1 = zeros(864,1216);
for j=(L/3+20):(2*L/3-1)
    pict_spray = names{j};
    disp(pict_spray)
    image_spray = imread(pict_spray);
    image_spray = double(image_spray)/65535;
    av_pict_sprayp1 = av_pict_sprayp1 + image_spray;
end
av_pict_sprayp1 = av_pict_sprayp1 / 100;
ImgStructp1 = av_pict_sprayp1;

av_pict_bgp2 = zeros(864,1216);
for i=1:19
    pict_bg = names{i};
    disp(pict_bg)
    image_bg = imread(pict_bg);
    image_bg = double(image_bg)/65535;
    av_pict_bgp2 = av_pict_bgp2 + image_bg;
end
av_pict_bgp2 = av_pict_bgp2 / 19;

av_pict_sprayp2 = zeros(864,1216);
for j=20:(L/3-1)
    pict_spray = names{j};
    disp(pict_spray)
    image_spray = imread(pict_spray);
    image_spray = double(image_spray)/65535;
    av_pict_sprayp2 = av_pict_sprayp2 + image_spray;
end
av_pict_sprayp2 = av_pict_sprayp2 / 100;
ImgStructp2 = av_pict_sprayp2;

save ImgStruct2P.mat ImgStructp1 ImgStructp2
else
load ImgStruct2P.mat;
end

ImgStructp1sht = zeros(864, 1216);
ImgStructp1sht(:,(Shift1+1):1216) =
    ... mean2(ImgStructp2)/mean2(ImgStructp1)*ImgStructp1(:,1:(1216-Shift1));

ImgDiff = sqrt((ImgStructp1sht - ImgStructp2).^2);
BG_level = mean2(ImgDiff(750:850,75:1150));
Deviation = std2(ImgDiff(750:850,75:1150));
ImgDiffadj = ImgDiff - BG_level + Deviation;

```

```

for l = 1:864
    for c = 1:1216
        if ImgDiffadj(l,c) <= 0
            ImgDiffadj(l,c) = Deviation;
        end
    end
end

px = [Tip(1), 1100];
py = [Tip(2), Tip(2)];
x0 = round(px(1)-20);
X0 = x0;
y0 = round(py(1));
Y0 = y0;
x1 = x0+20;
X1 = x1;
y1 = round(y0+0.02*(px(2)-px(1)));
Y1 = round(y0-0.02*(px(2)-px(1)));
x2 = round(px(1)+0.65*(px(2)-px(1)));
X2 = x2;
y2 = round(py(1)+0.2*(px(2)-px(1)));
Y2 = round(py(1)-0.2*(px(2)-px(1)));
x3 = round(px(1)+0.95*(px(2)-px(1)));
X3 = x3;
y3 = y2+0.1*(y1-y0);
Y3 = Y2+0.1*(Y1-Y0);
if px(2)+0.1*(px(2)-px(1)) < 1216;
    x4 = round(px(2)+0.1*(px(2)-px(1)));
else
    x4 = 1216;
end
X4 = x4;
y4 = round(py(2));
Y4 = y4;
Pointsx = [x0 x1 x2 x3 x4];
Pointsy = [y0 y1 y2 y3 y4];
PointsX = [X0 X1 X2 X3 X4];
PointsY = [Y0 Y1 Y2 Y3 Y4];

contb = [];
contb(1:Pointsx(1)) = Pointsy(1);
for j = 1:length(Pointsx)-1
    if Pointsy(j+1)-Pointsy(j) ~= 0
        slope = (Pointsx(j+1)-Pointsx(j))/(Pointsy(j+1)-Pointsy(j));
        intercept = Pointsx(j)-slope*Pointsy(j);
        if j == 1
            contb = [contb round(((Pointsx(j):Pointsx(j+1))-intercept)/slope)];
        else
            contb = [contb round(((Pointsx(j)+1:Pointsx(j+1))-intercept)/slope)];
        end
    elseif (Pointsy(j+1)-Pointsy(j)) == 0
        end
    end
end

contb(Pointsx(end):1216) = Pointsy(end);
contt = [];

```

```
contt(1:PointsX(1)) = PointsY(1);
for j = 1:length(PointsX)-1
    if PointsY(j+1)-PointsY(j) ~= 0
        slope = (PointsX(j+1)-PointsX(j))/(PointsY(j+1)-PointsY(j));
        intercept = PointsX(j)-slope*PointsY(j);
        if j == 1
            contt = [contt round(((PointsX(j):PointsX(j+1))-intercept)/slope)];
        else
            contt = [contt round(((PointsX(j)+1:PointsX(j+1))-intercept)/slope)];
        end
    elseif (PointsY(j+1)-PointsY(j)) == 0
        end
    end
contt(PointsX(end)-1:1216) = PointsY(end);

BG_stripe = [];
for i = 1:1216
    BG_stripe(:,i) = ImgDiffadj(contt(i)-5:contt(i)+4,i);
end
BG_Int = mean2(BG_stripe);

SprayReg = BG_Int * ones(864,1216);
for i = 1:1216
    SprayReg(contt(i):contb(i),i) = ImgDiffadj(contt(i):contb(i),i);
end

SPLI2P = BG_Int * ones(864,1216);
Axis = 1:1216;
if nargin == 2
    Sinex = [300 400];
elseif Offaxis == 1
    Sinex = [500 600];
elseif Offaxis == 2
    Sinex = [700 800];
else
    disp('Wrong position of the jet , verify off-axis position')
end
Siney = [Y0 Y0];
Sine = improfile(SprayReg, Sinex, Siney);
SineFlt = filter(ones(1,8)/8, 1, Sine);
[Peaks, Abs] = findpeaks(SineFlt);
Diff1 = Abs(2) - Abs(1);
Diff2 = Abs(3) - Abs(2);
if abs(Diff1 - Diff2) > 10*(Pixmm*2)/100
    Period = max(Diff1, Diff2);
else
    Period = ((Abs(3) - Abs(2)) + (Abs(2) - Abs(1))) / 2;
end
Margin = round(Period/3);

for l = min(contt):max(contb)
    AxialProf(1:1216) = BG_Int;
    Peaks = [];
    Position = [];
    [Max, Loc] = findpeaks(SprayReg(l,:));
    Peaks(1) = BG_Int;
```

```

Position(1) = round(Loc(1) - round(Period/2));
if Position(1) < 1;
Position(1) = 1;
end
Peaks(2) = Max(1);
Position(2) = Loc(1);
for c = 3:round(1216/Period)+3
C = Position(c-1);
if C+Period+Margin > 1215
Peaks(c) = BG_Int;
Position(c) = 1216;
break
else
SprayProfFlt = medfilt1(SprayReg(1,:), 3);
[Peaks(c), LocPos] = max(SprayProfFlt(round(C+Period-Margin):
... round(C+Period+Margin)));
Position(c) = round(LocPos + C + Period - Margin);
end
end
SineEval = interp1(Position, Peaks, Position(1):Position(end), 'spline');
AxialProf(Position(1):Position(end)) = SineEval;
SPLI2P(1,:) = AxialProf;
end

x = [1 1216];
y = [Y0 Y0];
x2 = 1:1216;
ProfStructp1sht = improfile(ImgStructp1sht, x, y);
ProfStructp1flt = filter(ones(1,8)/8, 1, ProfStructp1sht);
ProfStructp2 = improfile(ImgStructp2, x, y);
ProfStructp2flt = filter(ones(1,8)/8, 1, ProfStructp2);
ProfDiff = sqrt((ProfStructp1flt - ProfStructp2flt).^2);
ProfSPLI2P = improfile(SPLI2P, x, y);
Axial_Axis = (1/Pixmm)*(1-Tip(1):1216-Tip(1));

Thresh = graythresh(SPLI2P)/40;

Penetration = px(2) - px(1);

Prof25 = round(25*Pixmm + px(1));
X25 = [Prof25 Prof25];
Y25 = [1 864];

Laser_stripe25 = [];
for k=1:864
Laser_col25 = SPLI2P(k, Prof25-4:Prof25+5);
Laser_stripe25 = [Laser_stripe25; Laser_col25];
end
Laser_Prof25 = mean(medfilt2(Laser_stripe25, [5 5]), 2);

for p = contb(Prof25):-1:contt(Prof25)
if Laser_Prof25(p) > Thresh;
B_Boundary25 = p - 1; break;
end
end
T_Boundary25 = 2*Tip(2) - B_Boundary25;

```

```

Spray_center25 = (T_Boundary25 + B_Boundary25) / 2;
Radial_Axis25 = (1/22)*(2 - Spray_center25:864+1 - Spray_center25);

Prof45 = round(45*Pixmm + px(1));
X45 = [Prof45 Prof45];
Y45 = [1 864];

Laser_stripe45 = [];
for k=1:864
    Laser_col45 = SPLI2P(k, Prof45-4:Prof45+5);
    Laser_stripe45 = [Laser_stripe45; Laser_col45];
end
Laser_Prof45 = mean(medfilt2(Laser_stripe45, [5 5]), 2);

for p = contb(Prof45):-1:contt(Prof45)
    if Laser_Prof45(p) > Thresh;
        B_Boundary45 = p - 1; break;
    end
end
T_Boundary45 = 2*Tip(2) - B_Boundary45;
Spray_center45 = (T_Boundary45 + B_Boundary45) / 2;
Radial_Axis45 = (1/22)*(2 - Spray_center45:864+1 - Spray_center45);

Spray_boundariesT = [T_Boundary25 - Tip(2), T_Boundary45 - Tip(2)];
Spray_boundariesB = [B_Boundary25 - Tip(2), B_Boundary45 - Tip(2)];
x = [Prof25, Prof45];
EqT = robustfit(x, Spray_boundariesT, 'bisquare', 4.685, 'off');
EqB = robustfit(x, Spray_boundariesB, 'bisquare', 4.685, 'off');
X = 1:1216;
Spray_shapeT = EqT*(X - Tip(1)) + Tip(2);
Spray_shapeB = EqB*(X - Tip(1)) + Tip(2);
Spray_bisect = ((EqT+EqB)/2)*(X - Tip(1)) + Tip(2);

SP_halfangleT = (180/pi)*atan(EqT);
SP_halfangleB = (180/pi)*atan(EqB);
Spray_Angle= SP_halfangleB - SP_halfangleT;

end

%% *****
%%***** Appendices functions *****
%%*****

function file=getfiles(pauta)

switch nargin
    case 0
        N=dir;
    case 1
        N=dir(pauta);
    otherwise
        error('Incorrect number of argument(s)')
end

L=length(N);

```



```
j=1;
file={};
for i=1:L
    if N(i).isdir==0
        word=N(i).name;
        file(j)=cellstr(word);
        j=j+1;
    end
end

file=file';

end
```


Appendix C

Planar Laser Rayleigh Scattering function

The following code concerns the process of the evaporative sprays to extract mixing distribution through Planar Laser Rayleigh Scattering (PLRS). This code has been written in MATLAB language and only presents the necessary steps to process the images and extract The ratio of number density in 2-D, the mixture fraction can be obtained thanks to the molecular mass of the ambient and fuel.

```
function [NFAglobal,NFAavg,Tnglobal,Tnavg] = Final_Rayleigh(imgNum,preproc ,
    ... imgfile , savefile);

% The background images have to be supplied to the function (e.g.
% '15psi0PolarN2_12.spe') and the threshold level of the inpainting
% function must be adjusted not to cut quantitative data. The correspondent
% NFAFit and the Dark Current .mat have to be used to get accurate results.
% The Mirrorreg have to be adjusted as well depending on the experiments.
% Eventually , the location where the preprocess files have to be taken or
% the location where to save the results might be changed.
% This function processes the images taken with the Pixis camera (Princeton
% Instrument) of the Rayleigh signal emitted by the vaporized jet and the
% ambient.
% The preprocess is switchable and is generally used to select the pattern
% of the jet on every single image. It saves the matrix of the selected
% countour to be processed thereafter.
% Then the total process of the images taken for Rayleigh scattering first
% corrects the raw image with DC, then it calculates the ambient intensity
% outside of the jet , it compares the values with the empty vessel to make
% a correction thanks to a scale factor and the global background in finally
% subtracted from the raw image in order to obtain the Rayleigh signal only.
% The background, i.e. the Rayleigh signal emitted by the ambient is
% rebuilt by taking the laser sheet region above and below the spray
% (before and after) in order to correct the laser striping due to beam
```

```

% stirring (density gradient changes).
% A process called inpainting removes the particles that bleed in the image
% not to make the intensity level wrong. The threshold of the inpainting
% process has to be tuned in the appendices functions directly.
% The division of both images provides finally the NFA map by adjusting
% quantitatively with the temperature estimation from an adiabatic
% assumption. The temperature map is also calculated and everything is
% saved.
% "imgNums" is the number of the image that has to be processed.(eg:001)
% "preproc" is an option (0 or 1) to set that the function has to go
% through the Rayleigh preprocess or if it has been done already.(eg:1)
% "imgfile" is the raw file of the Rayleigh scattering signal emitted by
% both the ambient and the spray.(eg:'bildn')
% "savefile" is another option to set if the function has to save the
% results or not.(eg:0)

load ('...\NFAfit_rho228Ta900.mat');
load ('...\Dark.mat');
Dark = drk;
mirrorreg = [210 709];
rect = [1 120 899 719];

if preproc;
disp('Rayleigh preprocess begins');
for i = imgNum;
    file1 = sprintf('%s%.3d.spe',imgfile,i);
    Ray_img = readspe(file1);
    [Intensity,avg_img] = Average_Int('bg0polar07',0,9);
    raw_img_lvl = mean2(Ray_img(200:750,800:1000));
    bg_img = avg_img - Dark;
    bg_img_lvl = mean2(bg_img(200:750,800:1000));
    bg_adj = bg_img*(raw_img_lvl/bg_img_lvl);
    img_corr = double(Ray_img) - double(bg_adj);

    [img_woutpart] = inpainting_Rayleighpp(img_corr);

    ls_int = mean2(medfilt2(Ray_img(650:800,250:650), [12 12]));
    [bx,by] = ginput();
    bx(1) = 1;
    bottom = [bx by];
    [tx,ty] = ginput();
    tx(1) = 1;
    tx(end) = bx(end);
    ty(end) = by(end);
    top = [tx ty];
end
else disp('The image has been preprocessed already');
end

disp('Rayleigh scattering process begins');
m = 0;
for i = imgNum
    Matppfilename = sprintf('%s%.03dpp.mat',imgfile,i);
    file1 = sprintf('%s%.3d.spe',imgfile,i);
    Matppfilepath = '...';
    Matppfile = [Matppfilepath Matppfilename];

```

```

load(Matppfile);
yvb = yval(bx,by);
yvt = yval(tx,ty);
disp(file1);
Ray_img = double(readspe(file1));
Ray_img2 = Ray_img - Dark;
[Intensity,avg_img] = Average_Int('bg0polar07',0,9);
raw_img_lvl = mean2(Ray_img2(200:750,800:1000));
bg_img = avg_img - Dark;
bg_img_lvl = mean2(bg_img(200:750,800:1000));
bg_adj = bg_img*(raw_img_lvl/bg_img_lvl);
img_corr = double(Ray_img2) - double(bg_adj);

Zero_ident = img_corr > 0;
Ray_signal = Zero_ident.*img_corr;

[img_woutpart] = inpainting_Rayleighpp(Ray_signal);

Lsheetts = []; Lsheetbs = [];
for k=1:1024
    Lsheettc = img_woutpart(yvb(k)-4:yvb(k)+5,k);
    Lsheetts = [Lsheetts Lsheettc];
    Lsheetbc = img_woutpart(yvt(k)-5:yvt(k)+4,k);
    Lsheetbs = [Lsheetbs Lsheetbc];
end

I_Lsheetts = mean(Lsheetts(:,mirrorreg(1):mirrorreg(2)));
I_Lsheetbs = mean(Lsheetbs(:,mirrorreg(1):mirrorreg(2)));

lstm = mean(Lsheetts);
lsbm = mean(Lsheetbs);

ffimg = img_woutpart;
for k = mirrorreg(1):mirrorreg(2)
    slopels = (lsbm(k)-lstm(k))/double(yvb(k)-yvt(k));
    interceptls = lstm(k)+slopels*double(yvb(k));
    ffimg(yvt(k):yvb(k),k) = (-slopels*double(yvt(k):yvb(k))+
    ... interceptls)';
end

Image = zeros(1024,1024);
Image = img_woutpart./ffimg;
for l = 1:1024
    for c = 1:1024
        if Image(l,c) < 0.5;
            Image(l,c) = 0.5;
        end
    end
end

img_inpntd = zeros(1024,1024);
[img_inpntd] = inpainting_Rayleigh(Image);

img_inpntd(:,1:mirrorreg(1)-1)=1;
img_inpntd(:,mirrorreg(2)+1:1024)=1;

```

```

Ray_image = medfilt2(img_inpntd, [6 6]);
Ray_image(isnan(Ray_image)) = 1;

NFA = interp1(IJALUT, NfNaLUT, Ray_image);
Tn = interp1(IJALUT, TmixLUT, Ray_image);

if savefile
    Matfilename = sprintf('%s%.3d.mat', imgfile, i);
    Matfilepath = '...';
    Matfile = [Matfilepath Matfilename];
    save(Matfile, 'NFA', 'Tn', 'mirrorreg');
else
end

m = m + 1;
NFAGlobal(:, :, m) = single(NFA);
Tnglobal(:, :, m) = single(Tn);
close all

end

NFAavg = double(mean(NFAGlobal, 3));
Tnavg = double(mean(Tnglobal, 3));

end

%% *****
%%***** Appendices functions *****
%%*****

function [Intensity, avg_img] = Average_Int(bgfile, firstbgimg, lastbgimg);

Intensity = []; img_raw = [];
for i = firstbgimg:lastbgimg
    file = sprintf('%s%.3d.spe', bgfile, i);
    image = readspe(file);
    avg_int_img = mean2(image(150:780, 75:1000));
    Intensity = [Intensity avg_int_img];
    Intensity = mean(Intensity);
    j = i-1-firstbgimg;
    img_raw(:, :, j) = image;
    avg_img = mean(img_raw, 3);
end

end

%-----

function [img_woutpart] = inpainting_Rayleighpp(pict);

Imagewop = zeros(1024, 1024);
for r = 1:1024;
    for c = 1:1024;
        if pict(r, c) > 6000;
            Imagewop(r, c) = NaN;
        else

```

```

        Imagewop(r,c) = pict(r,c);
    end
end
end

img_woutpart = inpaint_nans(Imagewop);

end

%-----

function [yv]=yval(x,y)

yv = [];
sz = length(x);

for j = 1:sz-1
    if y(j+1) - y(j) ~= 0
        slope = (x(j+1)-x(j))/(y(j+1)-y(j));
        intercept = x(j) - slope*y(j);
        if j == 1
            yv = [yv round((x(j):x(j+1))-intercept)/slope)];
        else
            yv = [yv round((x(j)+1:x(j+1))-intercept)/slope)];
        end
    elseif y(j+1) - y(j) == 0
        if j == 1
            yv(x(j):x(j+1)) = round(y(j));
        else
            yv(x(j):x(j+1)) = round(y(j));
        end
    end
end
end
yv(round(x(end)-2):1024) = y(end);
yv = uint16(yv);

end

%-----

function [img_inpntd] = inpainting_Rayleigh(pict);

NFATn_wop = zeros(1024,1024);
for r = 1:1024;
    for c = 1:1024;
        if pict(r,c) > 12;
            NFATn_wop(r,c) = NaN;
        else
            NFATn_wop(r,c) = pict(r,c);
        end
    end
end
end

img_inpntd = inpaint_nans(NFATn_wop);

end

```

```

%
function New = inpaint_nans(nan)

[n,m] = size(nan);
nan = nan(:);
nm = n*m;
k = isnan(nan(:));

nan_list = find(k);
known_list = find(~k);

nan_count = length(nan_list);

[nr,nc] = ind2sub([n,m],nan_list);

nan_list = [nan_list,nr,nc];

if (nargin<2) || isempty(method)
    method = 0;
elseif ~ismember(method,0:5)
    error 'If supplied, method must be one of: {0,1,2,3,4,5}.'
end

fda = spalloc(n*m,n*m,size(nan_list,1)*9);

% -1,-1
L = find((nan_list(:,2) > 1) & (nan_list(:,3) > 1));
nl = length(L);
if nl>0
    fda=fda+sparse(repmat(nan_list(L,1),1,2), ...
        repmat(nan_list(L,1),1,2)+repmat([-n-1, 0],nl,1), ...
        repmat([1 -1],nl,1),n*m,n*m);
end

% 0,-1
L = find(nan_list(:,3) > 1);
nl = length(L);
if nl>0
    fda=fda+sparse(repmat(nan_list(L,1),1,2), ...
        repmat(nan_list(L,1),1,2)+repmat([-n, 0],nl,1), ...
        repmat([1 -1],nl,1),n*m,n*m);
end

% +1,-1
L = find((nan_list(:,2) < n) & (nan_list(:,3) > 1));
nl = length(L);
if nl>0
    fda=fda+sparse(repmat(nan_list(L,1),1,2), ...
        repmat(nan_list(L,1),1,2)+repmat([-n+1, 0],nl,1), ...
        repmat([1 -1],nl,1),n*m,n*m);
end

% -1,0
L = find(nan_list(:,2) > 1);

```

```

nl = length(L);
if nl>0
    fda=fda+sparse(repmat(nan_list(L,1),1,2), ...
        repmat(nan_list(L,1),1,2)+repmat([-1, 0],nl,1), ...
        repmat([1 -1],nl,1),n*m,n*m);
end

% +1,0
L = find(nan_list(:,2) < n);
nl = length(L);
if nl>0
    fda=fda+sparse(repmat(nan_list(L,1),1,2), ...
        repmat(nan_list(L,1),1,2)+repmat([1, 0],nl,1), ...
        repmat([1 -1],nl,1),n*m,n*m);
end

% -1,+1
L = find((nan_list(:,2) > 1) & (nan_list(:,3) < m));
nl = length(L);
if nl>0
    fda=fda+sparse(repmat(nan_list(L,1),1,2), ...
        repmat(nan_list(L,1),1,2)+repmat([-1, 0],nl,1), ...
        repmat([1 -1],nl,1),n*m,n*m);
end

% 0,+1
L = find(nan_list(:,3) < m);
nl = length(L);
if nl>0
    fda=fda+sparse(repmat(nan_list(L,1),1,2), ...
        repmat(nan_list(L,1),1,2)+repmat([n, 0],nl,1), ...
        repmat([1 -1],nl,1),n*m,n*m);
end

% +1,+1
L = find((nan_list(:,2) < n) & (nan_list(:,3) < m));
nl = length(L);
if nl>0
    fda = fda+sparse(repmat(nan_list(L,1),1,2), ...
        repmat(nan_list(L,1),1,2)+repmat([n+1, 0],nl,1), ...
        repmat([1 -1],nl,1),n*m,n*m);
end

% Eliminate knowns
rhs = -fda(:,known_list)*nan(known_list);

New = nan;
k = nan_list(:,1);
New(k) = fda(k,k)\rhs(k);

New = reshape(New,n,m);

end

%
```

```

function neighbors_list = identify_neighbors(n,m,nan_list,talks_to)

if ~isempty(nan_list)
    nan_count=size(nan_list,1);
    talk_count=size(talks_to,1);

    nn=zeros(nan_count*talk_count,2);
    j=[1,nan_count];
    for i=1:talk_count
        nn(j(1):j(2),:)=nan_list(:,2:3) + ...
            repmat(talks_to(i,:),nan_count,1);
        j=j+nan_count;
    end

    L = (nn(:,1)<1)|(nn(:,1)>n)|(nn(:,2)<1)|(nn(:,2)>m);
    nn(L,:)=[];

    neighbors_list=[sub2ind([n,m],nn(:,1),nn(:,2)),nn];

    neighbors_list=unique(neighbors_list,'rows');

    neighbors_list=setdiff(neighbors_list,nan_list,'rows');

else
    neighbors_list=[];
end

end

```